Title	Wideband vibration energy harvesting using electromagnetic transduction for powering internet of things
Author(s)	Mallick, Dhiman
Publication date	2017
Original citation	Mallick, D. 2017. Wideband vibration energy harvesting using electromagnetic transduction for powering internet of things. PhD Thesis, University College Cork.
Type of publication	Doctoral thesis
Rights	© 2017, Dhiman Mallick. http://creativecommons.org/licenses/by-nc-nd/3.0/ ![CC BY NC ND]
Embargo information	No embargo required
Item downloaded from	http://hdl.handle.net/10468/4072

University College Cork, Ireland
Coláiste na hOllscoile Corcaigh

Wideband Vibration Energy Harvesting using Electromagnetic Transduction for Powering Internet of Things

A thesis undertaken

at the

Tyndall National Institute

And presented to the

National University of Ireland,

University College Cork

In partial fulfillment of the

requirements for the degree of **Doctor of Philosophy (PhD)**

by

Dhiman Mallick, M.Tech.

Supervisor: Prof. Saibal Roy

Head of the Department: Prof. William P. Marnane

May 2017

Abstract

The huge potential of the so called 'Internet of Things (IoT)' has opened up a scope of realizing intelligent and responsive environment through a connected world of tiny, autonomous, self-powered Wireless Sensor Nodes (WSNs). This is envisaged based on the recent developments in low power electronics and sensors which have led to the possibility of deployment of WSNs. However, this is restrained by lack of reliable and robust power sources capable of providing energy to the sensors perpetually. This issue has surged the research to investigate the prospect of harvesting the energy out of ambient mechanical vibrations during the last decade. While linear resonant systems can generate a significant amount of power at resonance, the response drops drastically as the external vibration shifts slightly from the resonant frequency. This is inevitable as most of the ambient vibrations are either random or frequency varying. Consequently, widening/tuning the operational frequency of the transducers is essential for efficient energy harvesting.

In this series of works, bidirectional electrical tuning of Electromagnetic Vibration Energy Harvesters (EM-VEHs) using two different complex load topologies is reported. The capacitive and inductive loads are used to tune in the lower and higher frequency ranges respectively. Different meso-scale linear EM-VEH devices (volume less than few cm^3) are designed and fabricated using low Young's modulus FR4 as the resonating spring material to operate in the low frequency (<100 Hz) regime. Using the electrical tuning concept, the working frequencies of the devices are successfully tuned bi-directionally which agrees well with the theory. The developed linear EM VEH device is demonstrated using off-the-shelf LTC3588-1 power management circuit.

However, the tuning mechanism is strongly dependent on the electromechanical coupling. To be able to operate at different frequencies using a MEMS scale device where the aforementioned coupling is inherently small, design modifications are performed to activate various vibration modes of the resonators within close proximity. Single and double degree-of-freedom devices are developed using MEMS technology (volume ~0.14 cm^3) where the novel thin spring configurations are fabricated using Silicon-on-Insulator (SOI) wafers. High efficiency double layer electroplated coils are fabricated to induce the voltage due to relative movement of a bulk magnet, bonded to the spring. Operating below 300 Hz, these devices produce normalized power densities up to 0.0643 kg.s/m^3.

To further widen the bandwidth of the transducers, the concept of incorporating nonlinear effect in the system dynamics is investigated. Nonlinearity is introduced into the EM-VEH devices through specific design of the spring arms. It is shown analytically that the stretching strain in addition to bending strain of the fixed-fixed configured spring arms give rise to cubic nonlinearity leading to a wider bandwidth. The meso-scale device results in ~10 Hz bandwidth at 0.5g input acceleration which is almost 5 times higher than a comparable linear counterpart. By further exploiting the interaction between the electrical and the mechanical degrees-of-freedom of the device, the power output is improved over a large frequency range. This improvement is quantified using a new figure of merit based on a suitably defined 'power integral (P_f)' for wideband VEHs. While in the MEMS scale, the nonlinear effect is combined with activation of different vibration modes, which further widens the output response. By topologically varying the spring architectures, around 80 Hz operational bandwidth is obtained from a MEMS nonlinear EM-VEH.

However, hysteresis and multistability are fundamental phenomena of driven nonlinear oscillators, which restrict the VEH efficiency. An electrical control mechanism is introduced to switch from the low to the high energy output branch of nonlinear energy harvesters by exploiting the aforementioned interaction. This method improves the energy conversion efficiency over a wide bandwidth in a frequency-amplitude varying environment using only a small energy budget. The underlying effect is independent of the device scale and the transduction method, and is explained using a modified Duffing oscillator model.

One of the key requirements in realizing fully integrated EM-VEHs is the CMOS compatible batch fabrication of permanent magnets with large energy products. In the final module of the works, micro-patterns of nano-structured CoPtP hard magnetic material with large coercivity (>3 kOe) are developed at room temperature using pulse reverse electrodeposition technique up to a thickness of 26 μm. It is observed using analytical and FEM analysis that stray magnetic fields from a thin magnetic structure (of the order of tens of micron thickness) are only obtained from the edges due to the demagnetization effect, leading to the conclusion that micro-patterned structures can be used to improve the output power of a completely integrated EM-VEH device. Initial micro-patterned structures are fabricated on Si, which could be further optimized and potentially be used for developing fully integrated, high performance EM VEH devices.

Acknowledgement

supervisor Dr. Anirban Bhattacharyya for introducing me to the world of MEMS and for his advices whenever I needed.

Finally, I must express my very profound gratitude to my parents, Murari Mohan Mallick and Krishna Mallick, my elder brother, Vaskar Mallick and my sister-in-law, Srirupa Goswami for providing me with unfailing love, support and encouragement throughout my life and particularly during this thesis work. This accomplishment is the sole result of their sacrifice and belief in me.

Thank you.
Dhiman

To my family & my teachers

Declaration

I, Dhiman Mallick, declare that this thesis titled 'Wideband Vibration Energy Harvesting using Electromagnetic Transduction for Powering Internet of Things' is the result of my own research except as cited in the references. This thesis has not been submitted for another degree, either at University College Cork or elsewhere.

Signature:

Date:

List of Publications

Peer-Reviewed Journal Publications: (Average I.F. – 3.2)

1. **D. Mallick**, A. Amann, S Roy, A nonlinear stretching based electromagnetic energy harvester on FR4 for wideband operation, **Smart Mat. Struc. 24 (1)**:015013 (2015). (I.F. – 2.8)

2. **D. Mallick**, S. Roy, Bidirectional Electrical Tuning of FR4 based Electromagnetic Energy Harvesters, **Sens. Actuators A, 226**:154-162 (2015). (I.F. – 1.9)

3. **D. Mallick**, A Amann, S Roy, Interplay between mechanical and electrical domains of a high performance nonlinear energy harvester, **Smart Mat. Struc. (Fast Track Communication) 24 (12)**:122001 (2015). (I.F. – 2.8)

4. S. Roy, P. Podder, **D. Mallick**, Nonlinear Energy Harvesting using Electromagnetic Transduction for Wider Bandwidth, **IEEE Mag. Lett., 7**:5701004 (2016). (I.F. – 1.7).

5. **D. Mallick**, A. Amann, S. Roy, Surfing the High Energy Branch of a Nonlinear Energy Harvester, **Phys. Rev. Lett., 119:**197701 (2016). (I.F. – 7.7).

6. **D. Mallick**, A. Amann, S. Roy, High Figure of Merit Nonlinear Microelectromagnetic Energy Harvesters for Wideband Applications, **Journ. IEEE Microelectromech. Syst., 26(1)**:273-282 (2016). (I.F. – 1.8).

7. P. Podder, **D. Mallick**, A. Amann, S. Roy, Influence of Combined Fundamental Potentials in a Nonlinear Vibration Energy Harvester, **Scientific Reports, 6**:37292 (2016). (I.F. – 5.2).

8. P. Podder, P. Constantinou, **D. Mallick**, A. Amann, S. Roy, The Effect of Magnetic Tuning in a Nonlinear MEMS Electromagnetic Vibrational Energy Harvester, **Journ. IEEE Microelectromech. Syst.,** (In Press). (I.F. – 1.8).

9. **D. Mallick**, P. Podder, P. Constantinou, S. Roy, Multi-frequency MEMS Electromagnetic Energy Harvesting, (under review).

10. **D. Mallick**, S. Roy, Development and Integration of Nano-structured CoPtP Hard Magnetic Material for MEMS Energy Harvesting, (under preparation).

International Conference Publications:

1. **D. Mallick**, A. Amann, S. Roy, Analysis of Nonlinear Spring Arm for Improved Performance of Vibrational Energy Harvesting Devices, Journ. Phys.: Conf. Ser. 476 (1), 012088, 2013 (**PowerMEMS 2013**, 4-7 December, 2013, London, UK).

2. **D. Mallick**, S Roy, An Electrically Tunable Low Frequency Electromagnetic Energy Harvester, Proc. Engin., 87 (2014), 771-774 (**Eurosensors 2014**, 7-10 September, 2014, Brescia, Italy).

3. P. Podder, **D. Mallick**, S. Roy, Bandwidth widening in nonlinear electromagnetic vibrational generator by combined effect of bistability and stretching, Journ. Phys.: Conf. Ser. 557 (2014), 012039 (**PowerMEMS 2014**, 15-18 November, 2014, Hyogo, Japan).

4. M. Palizdar, **D. Mallick**, T. Maity, S. Roy, T. P. Comyn, T. J. Stevenson, C. M. Fancher, J. L. Jones, S. F. Poterala, G. L. Messing, E. Suvaci, A. P. Kleppe, A. J. Jehcoat, A. J. Bell, Texture analysis of thick bismuth ferrite lead titanate layers, (**ISAF/IWATMD/PFM**), 2014 Joint IEEE International Symposium on the.

5. **D. Mallick**, P. Podder, S. Roy, Wideband electromagnetic energy harvesting from ambient vibrations, AIP Conf. Proc. 1665, 020001 (2015) (**59th DAE Solid State Physics Symposium**, December 2014, Vellore, India).

6. S. Roy, **D. Mallick**, P. Podder, Nonlinear Energy Harvesting Using Electromagnetic Transduction for Wider Bandwidth, **ICMAT 2015 and IUMRS–ICA 2015**, 28th June-3rd July, 2015, Singapore.

7. **D. Mallick**, A. Amann, S. Roy, MEMS Based Nonlinear Monostable Electromagnetic Vibrational Energy Harvester for Wider Bandwidth, Journ. Phys.: Conf. Ser., 660 (012115), 2015 (**PowerMEMS 2015**, 1-4 December, 2015, Boston, USA).

8. P. Podder, P. Constantinou, **D. Mallick**, S.Roy, Silicon MEMS bistable electromagnetic vibration energy harvester using double-layer micro-coils, Journ. Phys.: Conf. Ser., 660 (012124), 2015 (**PowerMEMS 2015**, 1-4 December, 2015, Boston, USA).

9. T. Maity, **D. Mallick**, S. Roy, First observation of positive (anticlockwise) and negative/inverse (clockwise) hysteresis loop formation in the Ni,Fe film, (**Joint MMM-Intermag Conference 2016**, 11-15 January, 2016, San Diego, USA).

10. **D. Mallick**, S. Roy, Integrated CoPtP permanent magnets for MEMS energy harvesting applications, **27th Micromechanics and Microsystems Europe workshop (MME 2016)**, 28-31st Aug, 2016, Cork, Ireland.

11. **D. Mallick**, S. Roy, Development and Integration of Nano-structured CoPtP Hard Magnetic Material for MEMS Applications, **IEEE International Conference on Magnetics – Intermag 2017**, 24-28 April, Dublin, Ireland.

Book Chapters:

1. "**Vibrational Energy Harvesting**" by Larcher, L., Roy, S., **Mallick, D.**, Podder, P., de Vittorio, M., Todaro, T., Guido, F., Bertacchini, A., Hinchet, R., Keraudy, J. and Ardila, G., in the book titled "**Beyond-CMOS Nanodevices 1 (ed F. Balestra)**", *John Wiley & Sons, Inc.*, Hoboken, NJ, USA. (2014);
doi: 10.1002/9781118984772.ch6; ISBN: 9781848216549.

Patents:

1. 'Vibrational energy harvesting device combining multiple nonlinearity' – S. Roy, P. Podder, **D. Mallick,** A. Amann- **PCT Filed** 16th June 2016, PCT/EP2016/063940.

Awards:

1. **IEEE Student Travel Grant** for IEEE International Magnetics Conference, INTERMAG 2017.
2. Tyndall National Institute **Chief Scientist Award 2017.**
3. **Tyndall Bursary Award** for best postgraduate student 2015/16.
4. **UCC Strategic Research Fund Student Program (2014-15) winner.**

Contents

"The present is theirs; the future, for which I really worked, is mine."

- Nikola Tesla

List of Figures

List of Tables

Chapter 1

Background and Motivation

1.1. Introduction:

Energy harvesting or energy scavenging refers to the process that captures small amounts of energy from ambient sources which would otherwise be wasted and converts it into some usable form of energy – usually electrical. There has been a rapid growth in research within the fields of different energy harvesting methods over the last few decades. The root of such prompt initiative lies in the current technological advancements blended with socio-economic and environmental requirements. However, the history of energy harvesting goes back long in the past, even before the time of industrial revolution. Since the ancient times, sailboats and sailing ships have been using wind power which can be described as an earliest means of energy harvesting from an ambient energy source. The use of ambient energy to generate mechanical power came relatively later in the forms of windmill and waterwheel. The most common uses of windmill were to grind grains in milling plants and for water irrigation purposes [1]. The waterwheels were also used for agricultural, mining and tide prevention purposes in addition to the aforementioned circumstances [2-4]. In both these machines, the ambient and wasted energy sources like free-flow of air and water are converted into mechanical motion that can be purposefully utilised.

As the wave of industrial revolution hit the human civilization during the 18th century, energy harvesting found new applications with similar working principles. Flywheels and cogs were vital components of almost every coal-powered machine built in this time. With the industrial revolution, the human civilization found new and important developments as electricity became the backbone of modern lives. In the late 19th century, Charles F. Brush - a U.S. inventor, entrepreneur and philanthropist, was the first person in recorded history to produce the engineering marvel by harnessing the natural power of wind to generate electricity using a wind dynamo [5]. This dynamo was built by his

engineering company at his home in Cleveland, Ohio which operated from 1886 to 1900. The Brush wind dynamo had a rotor with diameter of 17 metres which was mounted on an 18 metres tower and was only rated at 12 kW, which is quite low by today's electrical standards. The generator was used to light up and operate various motors in Brush's laboratory. Since then, wind dynamo is being used extensively on a large scale for producing electricity worldwide and, by 2014, a large number of commercial-sized wind turbines are operating throughout the planet, generating 4% of the world's electricity [6]. While these are examples of relatively primitive ideas of energy harvesting with large scale operation, the similar concepts have been explored in small scale applications too. In the latter half of 18th century, mechanical self-winding watches were successfully developed by Abraham-Louis Perrelet – a swiss horologist [7]. Two centuries later, Hayakawa of Seiko Epson Corporation filed a patent on an electrically operated self-winding watch in 1989 [8]. The same concept is behind the currently available commercial Seiko kinetic watches. This can be considered as one of the earlier examples of small scale energy harvester. An inside view of the kinetic generator in the Seiko watch is shown in Fig. 1.1, which consists of a freely rotating asymmetric proof mass, which is attached to a permanent magnet electrical generator, through high ratio gears [9]. Later in 1996, Tiemann filed a patent [10] on inertial generator where relative motion between a magnet and coil is used to generate electrical energy. The principle of such inertial generator resembles today's vibration energy harvesting devices closely.
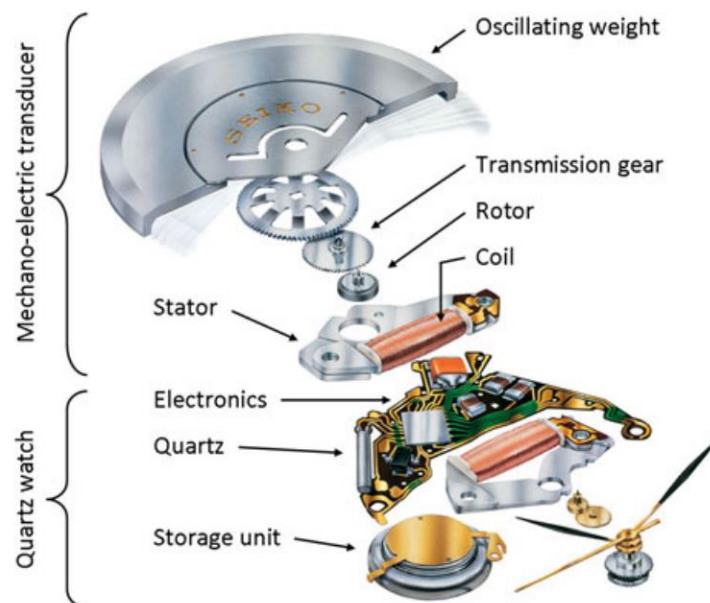
Fig. 1.1: Inside view of the Seiko kinetic powered watch [9].

So the question arises here, how this century old idea of energy harvesting from ambient sources is suddenly grabbing so much attention in the research fraternity and getting such high relevance in today's perspective. In the present time, energy is a critical issue around the world. The most common supplies of energy like fossil fuels are finite and environmentally costly. Sustainable energy can be derived from nuclear fission or captured from ambient sources. Large-scale ambient energy (e.g. solar, wind and tide), is widely available and large-scale technologies are being developed to efficiently capture it. On the other end of the scale, rapid progress in the field of low-power electronics, computation technologies and data transmission techniques have reduced the power consumption of present day electronic devices with consequential reduction in the size and cost [11-14]. These factors have encouraged the idea of ubiquitous and autonomous computation devices using long-term deployable wireless sensor networks. Lately, a major drive in this space came with the emergence of Internet of Things (IoT) technology. Therefore, low power energy harvesting from ambient sources (photovoltaic, thermal, mechanical vibration etc.) has become a topic of extensive research over the years. We start our discussion by introducing the potential application opportunities for this exciting technology.

1.2. Internet of Things (IoT) and Energy Harvesting:

It is difficult to define the concept of Internet of Things (IoT) in a precise manner covering its widespread technological aspects. In fact, different scientific and technical communities have come out with their own way of describing the Internet of Things. The initial use of 'IoT' has been attributed to Kevin Ashton, a British entrepreneur, who coined the term in 1999 while working at Auto-ID Labs (originally called Auto-ID centers, referring to a global network of objects connected to radio-frequency identification, or RFID) [15]. According to his version, IoT refers to a technological platform where the internet is connected to the physical world via ubiquitous sensors wirelessly. In other words, it refers to a computing concept where every day physical objects in nature are assumed to be connected to the internet and able to identify themselves to other devices, people and services on a global scale. IoT is expected to advance the connectivity among different embedded systems and devices that goes beyond machine-to-machine (M2M) and people-to-computer (P2M) communications. Typically an IoT network consists of physical objects, sensing devices together with

embedded electronics, software, actuators, and network connectivity that enable these objects to collect and exchange data. The vision of the IoT has evolved due to the widespread emergence of a number of technologies, such as wireless communication, embedded system electronics to Micro Electro Mechanical Systems (MEMS) and all of these fields contribute to enable such a technical platform.
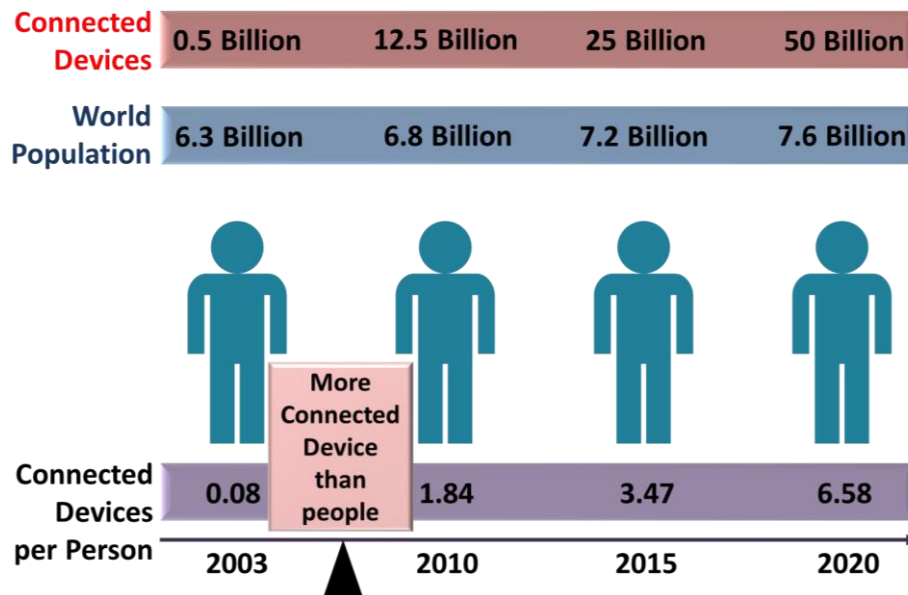
Fig. 1.2: Number of connected devices will be more than six times the number of people by 2020 [16].

This concept of connected objects makes 'things' smart, intelligent and responsive. The potentials of such a wirelessly connected 'smart' world are huge as it would flourish the information and communications technology market, save time and resources, and provide opportunities for innovation and economic growth. The IoT is expected to make our environment safer and responsive by providing a wealth of information through new forms of automation. According to Cisco Systems (an American multinational company on networking), there will be nearly 50 billion connected devices on the IoT by 2020 [16]. A perspective of that number is shown in graphical form in Fig. 1.2. It shows that there will be more than six times connected devices (50B) compared to the population on earth (7.6B) in another few years' time.

Since we are talking about a technological platform that eventually connects 'everything', the application of this budding concept is manifold too. IoT is likely to advance the conventional cyber-physical systems and will encompass technologies such as smart grids, smart homes, intelligent/autonomous transportation and smart cities. However, the application of IoT is not restricted to the above mentioned areas only. Other specific

application scenarios may exist too. Some of the most prominent application areas of IoT are provided here [17]:

- **Home/building Automation:** It involves remote control and monitoring of the Heating, Ventilation and Air Conditioning (HVAC), lighting and appliances control, remote monitoring of the smoke and CO_2 detection unit, water or gas leak detection, indoor positioning system in the office or market buildings and importantly home automation for elderly and disabled.

- **Wearable Technology:** Wearable devices are among the fastest growing terminologies and getting popular with the common people. These include clothing or accessories including sensors electronics. Wearable technologies are particularly used as activity tracking devices for monitoring of – fitness, health issue, sports activities, hearing impairments to name a few. Gadgets like smart watches and fitbit fitness tracker are already popular in this sector.

- **Smart City:** Smart city is another highly anticipated application area with a wide variety of use cases. This includes traffic management to water distribution, to waste management, urban security and environmental monitoring. Particularly with extensive deployment of IoT, problems like traffic congestion, noise pollution, air pollution can be significantly reduced to develop cleaner and safer urban areas.

- **Industrial Internet (IIoT):** The industrial internet is again one of the explorable IoT applications. Though its popularity presently has not reached the common people like smart home or wearables but the market potential is huge which has attracted multinational companies like AT&T, Cisco, Bosch, General Electric, IBM, and Intel. This can potentially advance the long established M2M communication technologies, enabling the smart machines and manufacturing on the industrial scale.

- **Autonomous Automobiles:** This sector is already getting much attention in the last few years. An autonomous automobile is a vehicle that is capable of sensing its environment and navigating without human input using a variety of techniques such as radar, lidar, GPS and computer vision. In the IoT era, the automobiles will not only be driverless but they will be connected to the other vehicles in the surroundings too. This sector includes connected avionics too.

- **Smart Agriculture:** With rapid growing human population, food and agriculture are one of the most challenging areas. With wide scale deployment of IoT, issues like water

shortages, limited land availability and cost management can be addressed, increasing the quality, quantity, sustainability and cost effectiveness of agricultural production.

Beside these prominent fields, sectors like smart retail, smart supply chain, connected health, pet animal monitoring are also growing fast. With so much of application opportunities, the market potential for IoT is huge too. According to IDC (International Data Corporation), the worldwide IoT market will grow from $655.8 billion in 2014 to $1.7 trillion in 2020 with a compound annual growth rate (CAGR) of 16.9% [18]. By 2020, majority of the IoT market will be made up by the devices, connectivity, and IT services. Together, they are projected to account for over two-thirds of the worldwide IoT market in 2020, with devices (modules/sensors) solely representing 31.8% of the total.
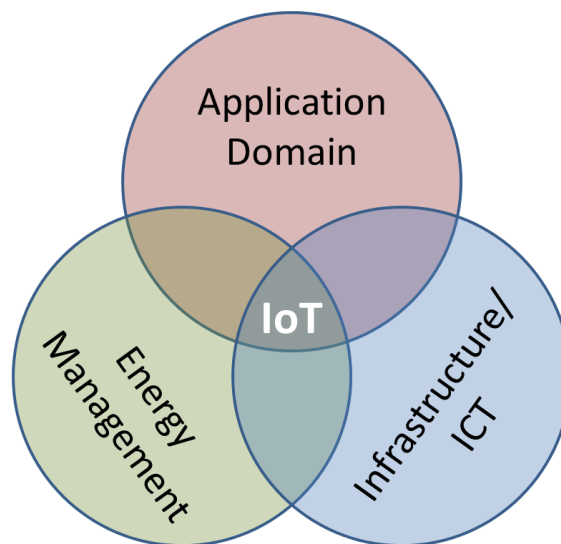
Fig. 1.3: IoT domains

Providing internet connectivity – anything, anytime, anywhere – is the key feature of IoT and leads to three main categories as network of things as shown in Fig. 1.3. Application domain defines the application areas of IoT that is already discussed. Providing suitable infrastructures such as cloud computing, embedded electronics development are another important aspect of IoT. On the other hand, energy management for IoT becomes crucial as engineers are trying to figure out how to power the billions of devices continuously in order to provide uninterrupted service – leading to the concepts of energy harvesting, energy transmission, management and storage. However, before jumping on this particular domain it is worth to discuss about the Wireless Sensor Nodes (WSNs) which are deployed all over to sense, process and transmit data.

1.2.1. Wireless Sensor Nodes (WSNs): While IoT does not focus on a particular communication method, wireless communication technologies will play a major role, and in particular, WSNs will flourish in many applications and many industries. The reason for this development is the small size, rugged operation, reduced cost and low power requirement of WSN sensors which will bring the IoT to even the smallest objects installed in any kind of environment, at reasonable costs. Integration of these objects in the IoT network will be significant evolution for the WSN technologies as well. The research on WSNs started back in the 1980s. But the proliferated interest on this topic came around the year 2000 from both the industrial and research communities.
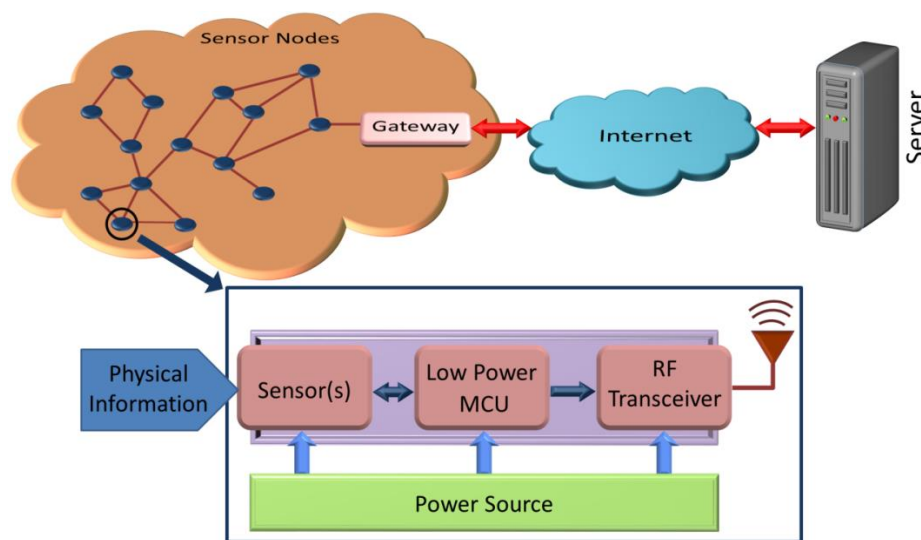
Fig. 1.4: Illustration of a typical Wireless Sensor Network [19]. Architecture of a sensor node is shown in the inset.

In general, A WSN can be defined as a network of nodes that are deployed in nature and that cooperatively sense and control the environment, thereby enables the exchange of information between persons or computers and the surrounding environment [19]. As shown in Fig. 1.4., the network usually includes sensor nodes, gateways and a host server which is connected to the nodes using wireless connectivity. A large number of sensor nodes positioned randomly inside of or near the monitoring area, form networks among themselves. The sensor nodes process the collected data to transmit along to other sensor nodes. As shown in the inset of Fig. 1.4., the hardware of a sensor node mainly includes four parts: (i) sensor(s) – to collect the information from the surroundings, (ii) a low-power microcontroller unit – to process the received information and to control the operation of the sensors, (iii) RF transceiver – to transmit and collect data among the

neighbouring nodes and (iv) power source – for powering of all the three aforementioned modules.

Though the wired technologies have been used in the communication world for a long time now, wireless sensing offers much more sophistication, ubiquity and simplification in the installation and operation of the sensor nodes as they can be deployed in really hostile and inaccessible locations for long term operation. This implementation of WSNs is enabled by the recent technological progress in low power integrated circuits, MEMS technologies and wireless communications that have made available energy efficient, tiny, low cost, low power devices for sensing applications [11-14]. The contribution from all these factors has improved the feasibility of employing a sensor network consisting of a large number of intelligent sensors, enabling the collection, processing, analysis and distribution of valuable information, assembled in a variety of environments.

However, there is one major concern that might risk the 'fit-and-forget' operation of these wireless sensors. All the above mentioned components of sensor nodes (sensors, microcontroller, and transceiver) require power for their operation. According to Boisseau et al. [40], a typical sensor node requires 1-5 μW in standby mode, 500 μW – 1 mW in active mode and 50 mW (peak) in transmission mode. Therefore a total energy of 50-500 μJ is required to perform a complete measurement. The most common source for powering these devices is batteries. However, a battery is a finite source of energy which need to be recharged or re-installed over time in order to maintain the continuous supply of power [20]. Additionally, the large numbers of WSNs are deployed in every location which are not always easy to access or where human intervention is quite cumbersome. Therefore, the replacement cost also goes up exponentially. Among other cases, if the battery is placed with a human implantable device such as artificial pacemaker, the replacement is not only costly but risky too [21]. Sometimes the batteries are too large in size compared to the devices it is powering like MEMS sensors, microcontrollers and RF antennas which restrains the miniaturization aspect of the WSNs. A comparison of the continuous power density ($\mu W/cm^3$) variation with different device lifetime is provided by Roundy et al. [22], which is reproduced in Fig. 1.5. According to this analysis, the energy densities of different battery technologies fall rapidly with time. Lifetime of a battery refers to either the length of time a device can run on a fully charged battery or the number of charge/discharge cycles possible before the cells fail to operate satisfactorily for a rechargeable battery. For a non-rechargeable one, these two lives are equal since the

cells last for only one cycle by definition. Fig. 1.5 also shows that the output power from the energy harvesters (such as vibration and solar) are independent of the device lifetime as they are assumed to generate energy forever provided the ambient conditions does not vary much (like change of light intensity in the surroundings or reduction in the mechanical vibration intensity). According to their analysis, if the required operation time of the installed sensor node varies between few months to few years, then batteries provide the easiest and most versatile power source. However, if long term operation is needed, then the only alternative is to replace or co-install the energy harvesters together with the batteries for uninterrupted supply of energy. In the following section, a comparative study of different energy supplying devices is provided.
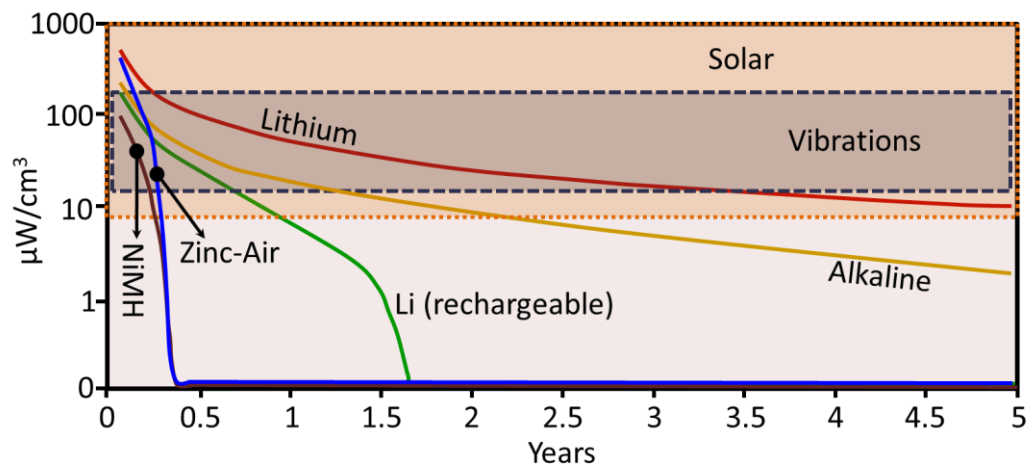
Fig. 1.5: Continuous power density variation with lifetime of different battery technologies and some other sources, reproduced from [22].

1.3. Comparison of Potential Energy Sources:

The problem of long term powering the WSNs can be addressed through two different approaches, as Soliman [23] described in his PhD thesis. In the first approach, the energy density of the energy storage systems (energy reservoirs) is enhanced to increase their lifespan. Such systems are called constant energy sources. The second technique is to develop novel techniques (energy harvesting) that can potentially capture otherwise wasted energy from the application's environment and convert it to useful electrical energy - such systems are called constant power sources. The output power from a constant energy source is a function of the amount of the energy stored. It means that the source can supply power to the load as long as the stored energy is high enough to power it and thus the efficiency of the constant energy source is measured using its energy density. When the stored energy falls below a particular level, the source can no longer

supply energy to the load and the source needs to be replaced or recharged. The delivered energy from a constant power source is a function of the amount of converted power. As long as the energy is generated from the ambience using a suitable conversion method, power will be supplied. Therefore, as it is mentioned before, constant power sources or energy harvesting methods are more suitable for long span application environments.

1.3.1. Constant Energy Sources: As described, these sources primarily rely on the micro-energy storage element. Energy can be stored in the form of electrochemical energy in batteries/micro-batteries, in a chemical energy storage mechanism like combustion fuel systems or as electrical energy storage such as capacitors.
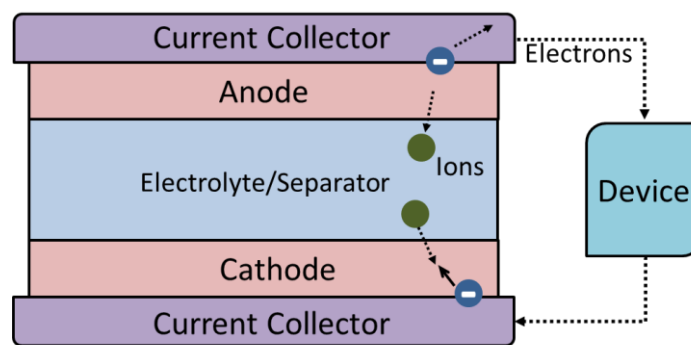
Fig. 1.6: Schematic of Battery operation, reproduced from [24].

- **Batteries and micro-batteries:** Batteries are basically galvanic cells where chemical energy due to the electrochemical reactions is converted into electrical energy. The basic operation principle of batteries can be understood from Fig. 1.6., which is reproduced from [24]. It has an ion-conducting electrolyte which is placed between two electrodes having different chemical potentials. Under open circuit condition, a potential drop develops between these two electrodes due to the tendency for chemical reactions to occur. When it is electrically connected to a load, chemical reactions occur and ions travel across the electrolyte. This results in a spontaneous flow of electrons in the externally connected circuit from the negative to the positive potential electrode, and can therefore be used to charge an external load. If the battery is rechargeable, the reverse reactions can be induced with an input of energy. The energy stored in an electrochemical storage is typically reported in units of joules (J) or watt-hours (Wh) and is quantified in terms of the specific energy (Wh/g), the amount of energy stored per unit volume (Wh/cm^3), and the energy stored per unit footprint area occupied on a substrate (Wh/cm^2).

Though non-rechargeable (primary) batteries are most widely used for powering a range of electrical devices, they tend to get overshadowed by the emergence of secondary or rechargeable batteries. Particularly when it comes to powering of billions of devices in the IoT networks, rechargeable batteries (Li-ion, NiMH, 3D printed zinc batteries etc.) are considered as the primary energy storage element.
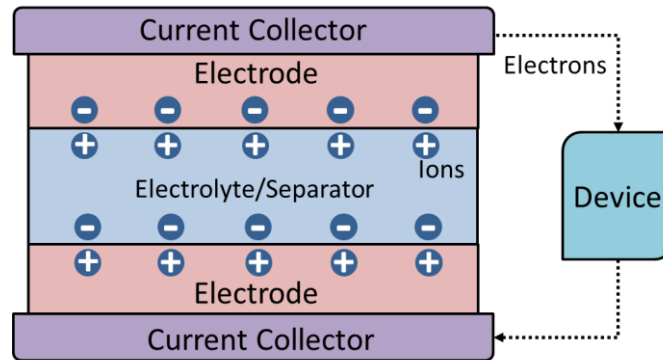
Fig. 1.7: Operation principle of Ultracapacitors, reproduced from [24].

- **Ultracapacitors:** An Ultracapacitor, also called a supercapacitor, is an electrochemical device with energy density much greater than a standard capacitor and less than a rechargeable battery [35]. However, these ultracapacitors provide very low current and thus can be used as a secondary power source, but not as the primary power source for applications with long lifespan. The operating principle of an ultracapacitor is shown in the Fig. 1.7. An ultracapacitor consists of a porous electrode, electrolyte and a current collector. The membrane, which separates the positive and negative plates is called the separator. When a voltage is applied to positive plate, it attracts negative ions from the electrolyte. When the voltage is applied to negative plate, it attracts positive ions from electrolyte. Therefore, there is a formation of a layer of ions on the both side of plate. This is called 'Double layer' formation and for this reason the ultracapacitor is also called an electric double-layer capacitor.

The normalized energy and power densities of different constant energy sources are summarized in Fig. 1.8, where the respective quantities are normalized w.r.t. their weight. The energy density of batteries is one to two orders higher than electrochemical capacitors which in turn can contain an order higher magnitude of energy than conventional electrolytic and ceramic capacitors. Power densities of batteries and fuel cells are quite low due to their slow reaction kinetics. Other constant energy sources include micro-fuel cells [30-34], micro-heat engines (static − thermoelectric devices, and

dynamic – Brayton, Rankine cycle devices) [36-37] and radioactive power sources [38-39].
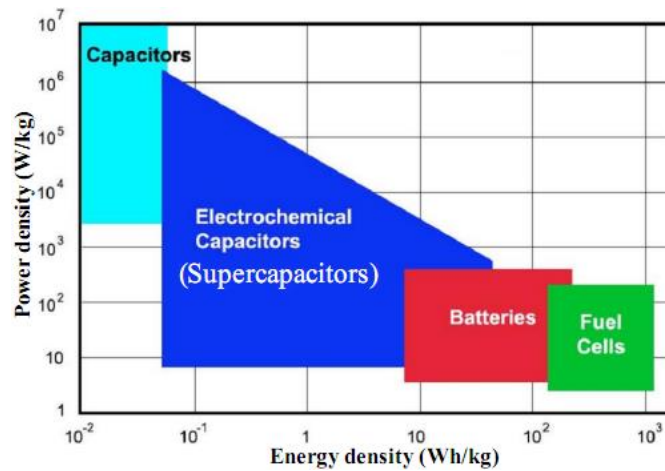
Fig. 1.8: Comparison of energy and power densities of different constant energy sources [35].
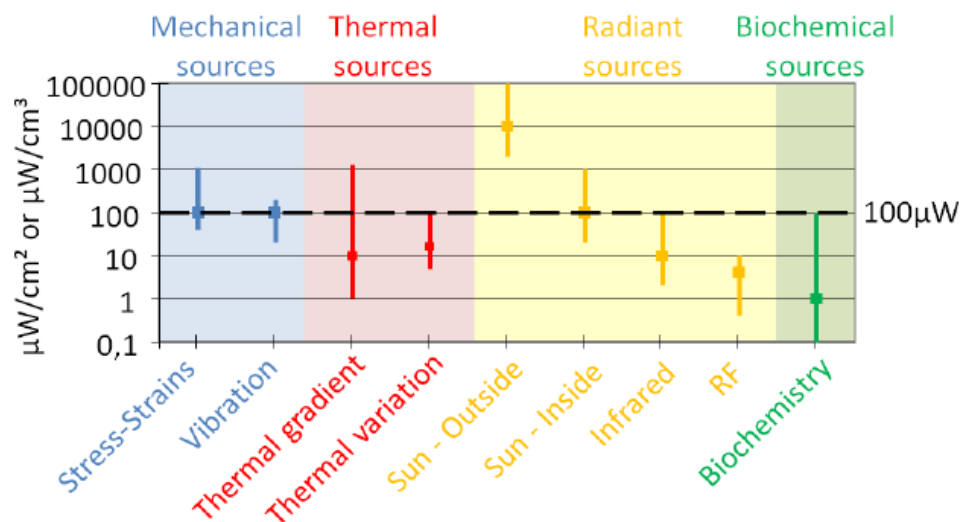
Fig. 1.9: Ambient sources power densities before conversion [40].

2. Constant power sources: As opposed to energy reservoirs (constant energy sources), constant power sources are based on energy harvesting techniques. In this approach, an energy converter or micro-power generator is used to harvest or scavenge and convert the energy that exists in the application's environment into useful electrical form that can be exploited by an external system. The most challenging part of designing an energy harvesting system is that each application environment is unique. Therefore, the power generation technique has to be compatible with the use case. But the advantage of energy harvesting is that the lifespan of the sensor node powered by such a source is limited only by the node's own longevity. However, energy harvesting might be the most difficult

realizable powering technique because the environment is unique to each application. Consequently, no one solution will fit all or even most applications. Among the different available ambient energy sources, photovoltaic energy, temperature gradient energy, fluid flow energy, RF radiation energy and mechanical vibration energy are the most common. These sources are characterized by different power densities [40] (before conversion) as shown in Fig. 1.9.
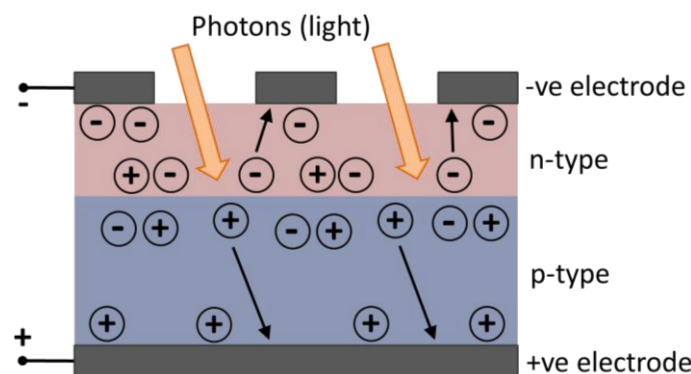
Fig. 1.10: Operation principle of a photovoltaic cell, reproduced from [31].

- **Photovoltaic Energy:** A Solar cell is the most basic form of photovoltaic energy converter, which is made of p-n type semi-conductor materials. The p-type and n-type semiconductors are positioned such that they form a p-n diode junction close to the top surface of the solar cell, as shown in Fig. 1.10. The energy conversion in a solar cell occurs in two steps [41]. Absorption of photon (light) creates electron-hole pairs. The electrons and holes are then separated by the structure of the device - electrons go to the negative terminal and holes to the positive terminal—thus generating DC electrical potential. The advantage of using solar cell is that a single solar cell has an open circuit voltage of about 0.6 V but multiple cells can easily be placed in series to obtain almost any desired voltage and can be placed in parallel to increase the current. Therefore, this energy conversion technique is widely accepted, even at large scale.

However, there are certain considerations which must also be taken into account while discussing about solar energy scavengers. The first and most obvious is that since the sun is only in the sky for half of the day, the cells won't be active in the other half of the day. Hence, some sort of secondary storage, such as batteries, will be required to store and use the energy throughout the day. Also, in case of cloud cover and shadowing, sun will be blocked and the level of incident radiation will drastically reduce. If the sensor node is deployed in a location which has no direct sun ray, like inside of a building, the magnitude level of the incident radiation on a solar cell is typically three orders of

magnitude less than outside, directly under the sun [42]. Single crystal silicon solar cells are convenient for outdoor applications as they have a spectral response close to that of outdoor light whereas thin film amorphous silicon solar cells provide higher efficiency in case of indoor based applications. The energy conversion efficiencies of commercial solar cells range from a low of approximately between 8% and 20%, with in some cases reported as high as 35% [43]. The available power density from solar cells varies between 100 mW/cm^2 for outdoor to 100 μW/cm^2 for indoor applications [44].
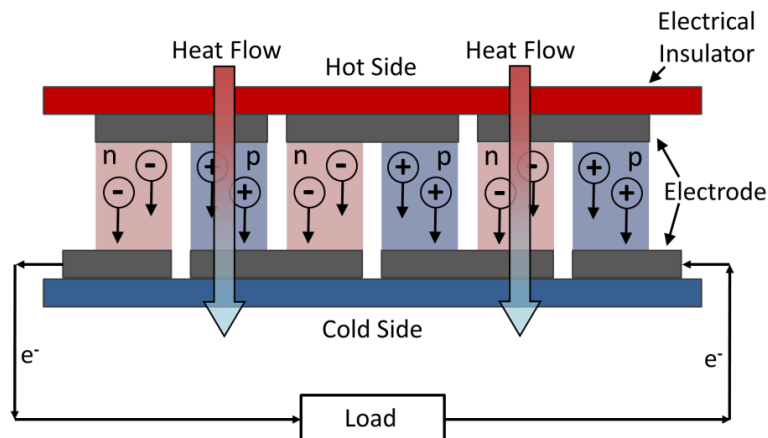
Fig. 1.11: Operation of thermoelectric generator, reproduced from [28].

- **Thermoelectric Energy:** It is well-known facts that if there exists a temperature difference between two different points, heat energy will flow from the hot to the cold point in order to maintain thermal equilibrium between them. This heat flow is utilized in miniaturized devices to harness electrical energy using the thermoelectric Seebeck effect [45]. In this effect, a thermoelectric potential difference is created across two different metals or semiconductors when their junctions are placed across a temperature gradient. The working principle of modern thermoelectric generators is depicted in Fig. 1.11. It consists of n-type and p-type semiconductor materials which are electrically connected in series and thermally connected in parallel. Bismuth telluride, a narrow gap, layered semiconductor material is mostly used in today's thermoelectric generators due to its high Seebeck co-efficient [46]. The generator has one end exposed to a heat source while the other end is attached to cooler side to form a thermocouple. Due to this temperature difference across the semiconductors, heat energy flows through it and charged carriers are diffused across the junction. The charge carriers in the n-type are negatively charged which results in flow of current from the cold to the hot side and vice-versa for the p-type semiconductor. The resultant electron current flows clockwise around the circuit as

shown. However, this method requires the generator to be placed in a region of temperature gradient, which imposes certain restrictions on the usefulness of the method. At a temperature difference of 10-200°C, electrical energy can be generated by commercially available thermoelectric generators [47]. In an experimental study, a power density of 100 μW/cm^2 is generated for a temperature difference of 5°C which rises to 3.5 mW/cm^2 for a temperature difference of 30°C [48]. Due to limitations of present thermoelectric materials (BiTe, PbTe etc.), it is difficult to generate electric power from low grade heat. Currently, considerable research efforts are being made to overcome this difficulty.

Energy Sources	Characteristics	Implementation Techniques	Amount of harvested energy	Typical Application
Solar	Uncontrollable, predictable	Solar cell	15 mW/cm^2	WSNs, household appliances
Wind	Uncontrollable, unpredictable	Anemometer	100 W (rotor diameter 1m, wind speed 8 m/s)	WSNs, household appliances
Environmental Vibration	Uncontrollable, unpredictable	Electromagnetic Induction	0.2 mW/cm^2	WSNs, consumer electronics
Human Motion	Controllable, predictable	Piezoelectric	Finger motion: 2.1 mW; footfalls: 5W	On-body monitoring; portable devices
Thermal	Uncontrollable, unpredictable	Thermopiles	~ 40 mW	WSNs
Ambient RF signal	Uncontrollable, unpredictable	Rectification and Filtering	< 0.2 mW	RFID
Biomass	Controllable, predictable	Microbial Fuel Cell	153 mW/m^2	Underwater sensor

Table 1.1. Comparison of existing energy harvesting techniques, reproduced from [52].

- **RF Energy:** Radio Frequency waves are currently broadcasted from billions of radio transmitters across the world, including mobile telephones, handheld radios, mobile base stations, and television/ radio broadcast stations. The energy from these ambient

electromagnetic waves can be converted into electrical energy for potential applications. At a distance of 25-100m from a GSM base station, 0.01-0.1 $\mu W/cm^2$ can be harvested using a RF energy harvester at a single frequency [49]. Generated power reduces significantly as the distance from the source increases, like, only 0.1 $\mu W/cm^2$ is generated at a distance of 4 km from a television station [50]. Commercial RF energy harvesting devices generate up to 15 mW when they are placed at a distance of 30 cm from a transmitting station with a transmitted power of 2-3 W at 906 MHz [51].

- **Mechanical Vibrations:** Mechanical vibrations have emerged over the years as one of the most attractive ambient sources for harnessing electrical energy due to its abundance in nature. Literally everything vibrates. When a car starts, the entire body of the car vibrates. When we run, jog or even walk, different parts of our body shake – generating mechanical energy. When an automobile goes through the road or bridge, different parts of the automobiles and the surface of the road vibrate. When home appliances like a microwave or washing machine work, they produce mechanical energy in terms of vibrations which is completely wasted. These are just some instances of the huge availability of mechanical vibrations around us. Therefore, the application scope is huge too. As will be discussed in detail later, a transducer can be attached to the vibrating host structure to convert mechanical energy into usable electrical form. Different transduction mechanisms – electromagnetic, piezoelectric, electrostatic, triboelectric – are used for this purpose as will be discussed in the following section.

Among the other energy harvesting techniques, air/fluid flow energy harvesting and biochemical energy harvesting are popular methods. A comparison of the existing energy harvesting techniques is provided in Table 1.1 by using the data accumulated by Mao et al [52].

1.4. Vibration Energy Harvesters – Different transduction mechanisms:

A transducer can be defined as a mechanism or a device that takes energy in one form and converts it into another form. An electromechanical transducer is one of the most common and important transducers in modern microelectronics and microsystems, which converts mechanical energy into electrical form and vice versa. The core of mechanical energy harvesters, like micro-power generators from ambient vibrations, is such a mechanical-to-electrical transducer. The basic inertial based Vibrational Energy Harvester (VEH) can be modelled as a second order mass damper and spring system, as proposed by Williams et. al. [53]. As shown in Fig. 1.12., the system consists of a mass

(m) mounted on a spring with a spring stiffness k, which vibrates relative to a housing (fixed frame) when subjected to an external mechanical force. It is assumed that the moving mass (m) is much smaller compared to the mass of the generator frame. Hence, the movement of the frame is unaffected by the movement of the generator. Under an external vibration of the form, $y(t) = Y_0 Sin(\omega t)$ (Where, Y_0 = vibration amplitude and ω = frequency of vibration), the mass along with the spring moves harmonically.
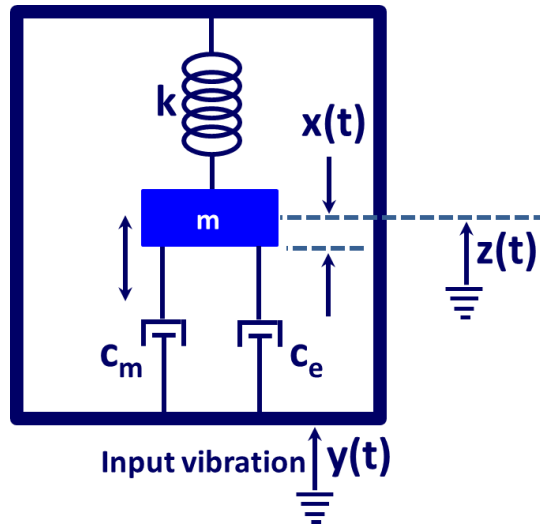
Fig. 1.12: Basic Spring-Mass-Damper model of vibration energy harvesters.

Energy losses within the system consist of two parts − (i) mechanical or parasitic losses and (ii) electrical energy extracted by using a transduction mechanism (for electromagnetic). These energy losses are represented by corresponding damping co-efficients c_m and c_e. The total damping co-efficient $c_T = c_m + c_e$. If the displacement of the mass, m, with respect to the ground is x(t) and the displacement of the frame with respect to the ground is y(t), then the net displacement of the mass (m) w.r.t. the frame is

$$z(t) = x(t) - y(t) \tag{1.1}$$

By balancing all forces acting on the system described in Fig 1.12, the equation of motion can be written as

$$m\ddot{z}(t) + c_T \dot{z}(t) + kz(t) = -m\ddot{y}(t) \tag{1.2}$$

A detailed steady-state solution of equation (1.2) is given in chapter 4. For piezoelectric and electrostatic cases, an additional force term appears which accounts for the respective effects. The most commonly used mechanisms are discussed below:

1.4.1. Piezoelectric Generators: Piezoelectrics are a special class of materials which can produce voltage across them due to the change in electric polarization when mechanical stress is applied, or vice versa. The linear constitutive equations for piezoelectric materials, which describe their mechanical and electrical behavior, are given in equation (1.3) [54-55].

$$\begin{cases} S_{ij} = s^E_{ijkl} T_{kl} + d_{kij} E_k \\ D_i = d_{ikl} T_{kl} + \varepsilon^T_{ik} E_k \end{cases} \tag{1.3}$$

where the subscripts i, j, k and l have the values of 1, 2, and 3. S and T are respectively the strain and stress tensors. The stress tensor (T) indicates the stresses that are induced by the mechanical and electrical effects and has the unit of N/m^2. D and E are the electric displacement and electric field vectors, with SI units of C/m^2 and V/m, respectively. The matrix s^E represents the elastic compliance evaluated at a constant electric field with SI units of m^2/N, d is a matrix of piezoelectric strain coefficients with SI units of m/V and matrix ε^T represents permittivity values at a constant stress with SI units of N/V^2. The piezoelectric coupling term (d) represents the charge produced by a given force in the absence of an applied electric field (short circuit electrical condition), or the deflection caused by an applied voltage in the absence of an applied force (stress free mechanical condition). Equations (1.3) represent an elastic dielectric material if the piezoelectric coupling term (d) is left out and made uncoupled.
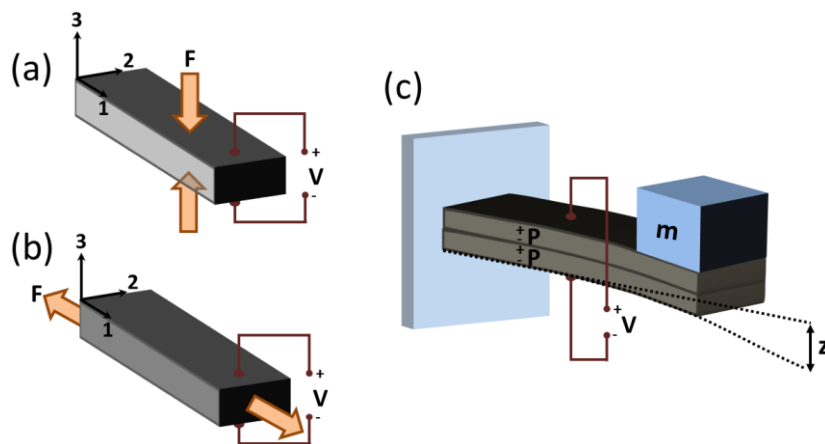
Fig. 1.13: Different modes (a) 33-mode and (b) 31-mode of piezoelectric material. (c) operational principle of a bimorph structure.

Power generation from mechanical vibration is possible due to mechanical-to-electrical coupling. Figs. 1.13 (a) and (b) depict the two most common loading conditions in which a piezoelectric material may be used. The x, y and z directions are labelled as 1, 2, and 3.

In 33 loading, the polarizing direction is denoted as the '3' direction and charge collection occurs on the electrode surface normal to the polarization direction under a tensile or compressive mechanical force which is applied along the polarization axis. When a material experiences '31' loading, mechanical force is applied perpendicular to the polarization axis and the charge is collected on the electrode surface perpendicular to the polarization direction. The electromechanical coupling factor of the 33-mode is higher than 31-mode. Therefore, the 33- mode can be employed to obtain higher energy conversion. However, larger strains can be produced with smaller mechanical forces in case of 31-mode. Hence, the 31-mode conversion may be more suitable for energy harvesting with a low amplitude source and smaller device size. The electrical energy stored in a piezoelectric material is dependent on the strain tensor, electromechanical coupling along with material's flexural modulus. The piezoelectric effect is obtained from different types of materials such as single crystals, ceramics, polymers, composites, thin films and relaxor-type ferroelectric materials. The piezoelectric properties of some commonly used piezoelectric materials are given in Table 1.2.

Material	d_{31} (pC/N)	d_{33} (pC/N)	$\varepsilon_{33,r}$	Y (GPa)	ρ(kg/m^3)
PZT	-130	290	1300	96	7.7
AlN	2	3.4	10.5	330	3.26
ZnO	-4.7	12	12.7	210	5.6
PVDF	22	-30	10-12	8.3	1780

Table 1.2. Comparison of piezoelectric properties of some commonly used materials.

Commonly used piezoelectric structures include unimorphs, bimorphs, multilayered stacks, rainbows, s-morphs, moonie and cymbal [56]. Unimorphs are the basic building block for bimorph and multi-layer stack structures. A unimorph consists of a piezoelectric material sandwiched between two electrodes. However, the most common type of piezoelectric elements is a bimorph, in which two separate piezoelectric plates are bonded together to form series or parallel type generators. When the two layers are polarized in such a way that the voltage across the two layers adds, series operation is obtained. Alternatively, they might be poled in such a way that the charge adds then parallel operation is obtained. Fig. 1.13 (c) depicts the operation of piezoelectric bimorphs. Further complicated structures like multi-layer, moonie or cymbal, consist of different combinations of basic unimorphs.
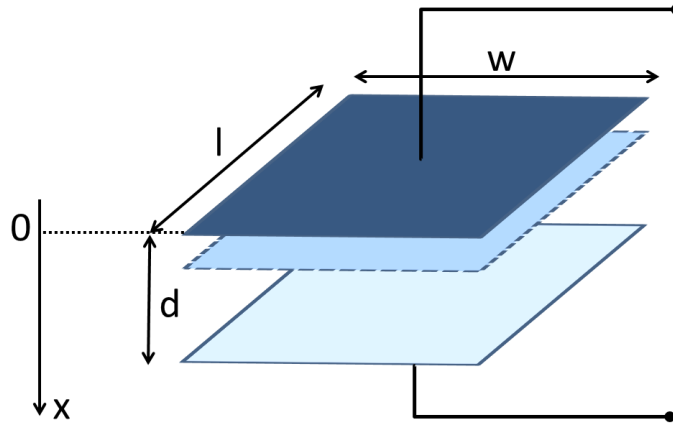
Fig. 1.14: Operation principle of a capacitive (electrostatic) transducer, reproduced from [57].

1.4.2. Electrostatic Generators: The electrostatic energy harvesters use variable capacitors as the electromechanical transducers [57]. Let us consider a parallel plate capacitor (Fig. 1.14), where one of the two plates is fixed and the other one can move. If the distance d between the plates is allowed to vary, the capacitance C_t of this capacitor will change as follows:

$$C_t = \frac{\epsilon_0 \epsilon_r A}{d} \tag{1.4}$$

where ε_0 is the permittivity of free space, ε_r is the relative permittivity of the medium (SI unit: Farad/m) between the plates and A is the area (SI unit: m^2) of each of the plates. If Q_t is the amount of charge provided to the capacitor, the energy of the electric field stored in it is given as

$$E_t = \frac{Q_t^2}{2C_t} \tag{1.5}$$

Now let us assume that the movable plate shifted further from the fixed plate keeping the charge Q_t constant, so that the new distance between the two plates becomes d_1 ($d_1 > d$). According to equation (1.4), the capacitance will decrease and the stored energy will consequently increase according to equation (1.5). In this case, the energy stored in the electrical domain is changed by manipulating a mechanical parameter (the distance d) of the transducer. Such a kind of electromechanical transducer is called capacitive or electrostatic. The major advantage of the electrostatic conversion mechanism is the simplicity of the fabrication process using silicon micromachining techniques.
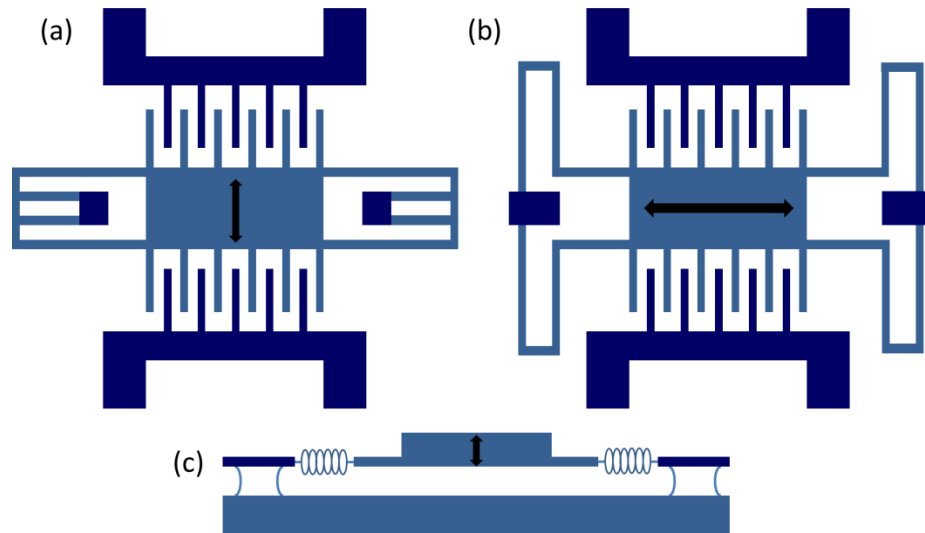
Fig. 1.15: (a) In-plane overlap (b) In-plane gap closing and (c) Out-of-plane gap closing configuration of an electrostatic generator, reproduced from [22].

Three basic configurations [22] for electrostatic transducers are shown in Fig. 1.15. The dark parts are fixed, whereas the light parts are free, released structures which can move under external excitation. The first configuration (Fig. 1.15 (a)) is referred as an in-plane overlap structure as the change in capacitance rises from the changing overlap area of the many interdigitated fingers. The overlap area changes when the central plate moves, which results in a change of capacitance between the finger arms. The second configuration (Fig. 1.15 (b)) is referred as the in-plane gap closing structure where the capacitance changes due to the change in the gap between the fingers as the central plate moves perpendicular to the finger orientations. The third configuration is known as the out-of-plane gap closing converter (Fig. 1.15 (c)) where the device moves perpendicular to the device plane, changing the gap between two plates. This configuration has the highest maximum capacitance but suffers from two major disadvantages – (i) maximum mechanical damping as the squeeze film damping becomes high due to two large plates and (ii) surface adhesion between two large area plates. The first issue can be resolved by using advanced packaging techniques but the second point makes the use of such a configuration quite limited. Among the in-plane moving structures, the gap closing configuration has a larger maximum capacitance. However, it requires a mechanical stopper in order to avoid the stiction problem which is not required for the overlap configuration. On the other hand, the stability of the structure is a critical issue for the overlap configuration under large deflections of the plate. However, the electrostatic generator needs to be charged or voltage must be provided initially to start its operation.
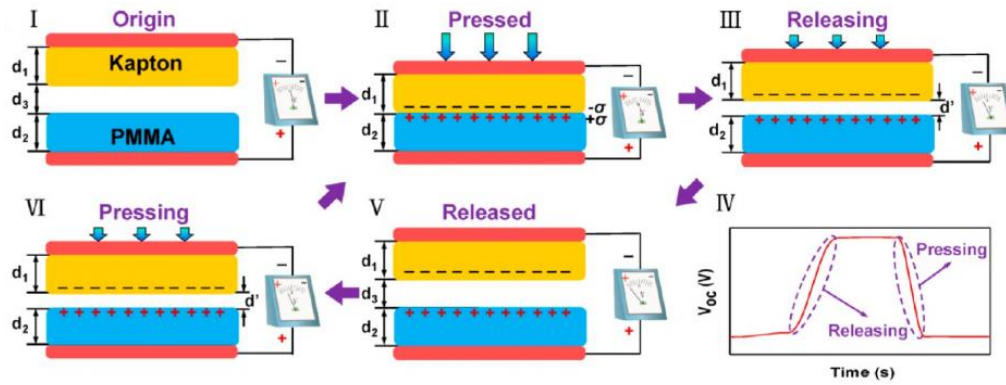
Fig. 1.16: Illustration of the contact-separation mode of triboelectric generators [58].

1.4.3. Triboelectric Generators: One of the newest mechanisms for converting mechanical energy into electrical form is triboelectrification [58-60]. The triboelectric effect is a type of contact-induced electrification in which certain materials become electrically charged after they come into frictional contact with a different material. It is one of the most common phenomena of electrostatics that is experienced in everyday life. The polarity of the charges that is carried by a material is relative to the material with which it is in contact. When two different materials come into contact, a chemical bond is formed between some parts of the two surfaces, known as adhesion. As a consequence, charges transfer from one material to the other to equalize their electrochemical potential in the form of electrons or ions/molecules. When the two materials get separated, some of the bonded atoms have an inclination to keep extra electrons and some bonded atoms tend to give them away. This phenomenon produces triboelectric charges on surfaces. Usually insulators or less conductive materials possess strong triboelectric effect. These materials can usually capture the transferred charges and hold them for a longer period of time, creating electrostatic charges. This effect is usually considered as a negative effect in many electronics applications but can potentially be useful in power generation applications. Using the triboelectric effect, electric potential is produced due to charge transfer between two thin organic/inorganic films with contrary tribo-polarity. When the generator is connected to an external circuit, electrons are forced to flow between two electrodes which are attached to the back sides of the films in order to balance the potential. Triboelectric generators operate in three basic modes [58]: vertical contact-separation mode, in-plane sliding mode, and single-electrode mode.
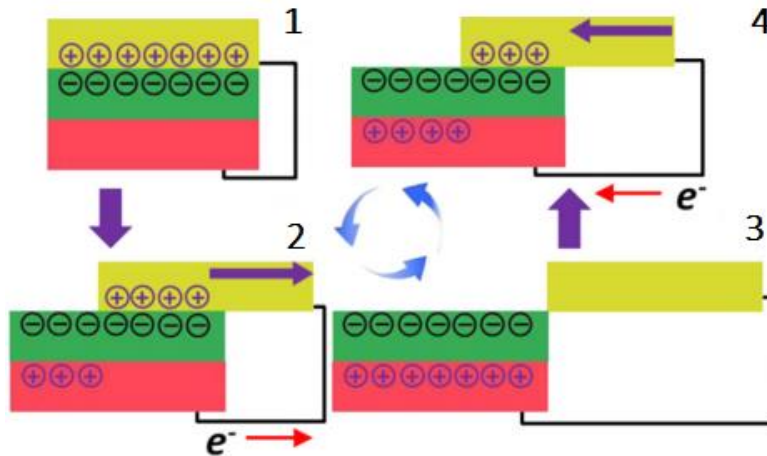
Fig. 1.17: Illustration of the sliding mode of triboelectric generators [58].

For the contact-separation mode (Fig. 1.16), no triboelectric charges are generated in the initial state. Due to an externally applied force, the two materials are brought into contact and surface charge transfers between them due to triboelectricity. Depending on their position in the triboelectric series, negative charges are injected in one material, leaving positive charges on the surface of the other. As the two structures separate, an electric potential difference is introduced between the two electrodes. As the distance between two layers increases, the open circuit voltage reduces and drops to zero by the time the next contact is made. The open-circuit voltage is dependent on the relative position of the two charged layers. If the separation distance is fixed, the output voltage can be made stable.

In case of the sliding mode (Fig. 1.17), two electrodes are normally electrically connected. Under the displacement of one, uncompensated triboelectric charges distribute in the two electrode surfaces. The electron flow continues until the displacement reaches a maximum. At the fully displaced position, the positive triboelectric charges are completely balanced out. As the relative displacement is reduced by a countering force, the induced electrons flow back till the fully aligned position is restored again which is the same as the initial position. Therefore, alternating current is produced through the external load in this process.

There is a vast choice of materials in the triboelectric series including polymers, metal and fabrics. Depending upon their position in the series, they either gain or lose charges. The first reported work on triboelectric generators for micro/nano scale applications was in 2012. The output efficiency of this method is quite good with a reported area power

density of 313 W/m^2 and volume density up to 490 kW/m^3, which leads to a conversion efficiency of ~60% [59].

1.4.4. Electromagnetic Generators: The operating principle of electromagnetic energy harvesting devices is based on Faraday's law [56], which states that a relative motion between a magnetic field and an electrical coil or a change in the flux linkage with a coil induces an electromotive force (EMF) in that coil (Fig. 1.18). The EMF depends on the strength of the magnetic field, the length of the coil, and the relative velocity (or flux linkage rate) between the magnetic field and the coil. The following equation represents this relationship:

$$EMF\ (V) = \frac{d\Phi}{dt} = Bl\frac{dx}{dt} \tag{1.6}$$
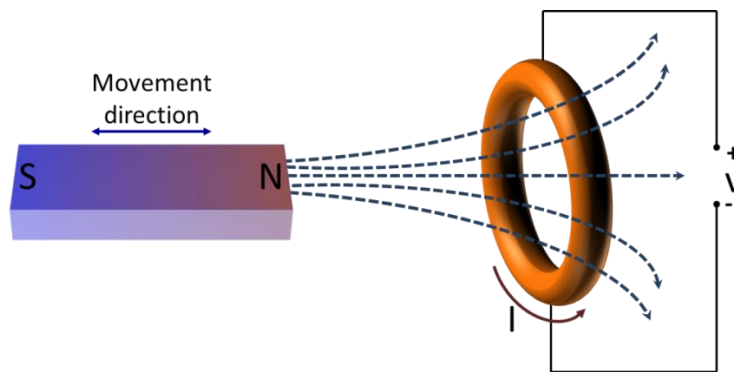
Fig. 1.18: Illustration of Faraday's law that governs electromagnetic generators.

Where Φ is the total flux linkage in Weber; t is the time in seconds, and B, l, and x are the flux density in Tesla, the effective length of the wire in metres and the relative motion between the magnets and the coil in metres respectively. The relative motion between the magnetic field and the coil can be produced by moving the magnets with respect to the coil or vice versa. The coil can be either wire-wound or micro-fabricated. The electromagnetic energy harvesters which have been researched are either macro-sized structures or miniaturized structures utilizing micro electro mechanical system (MEMS) fabrication techniques. In general, the operational principle of electromagnetic induction based generators can be grouped into three types [61]: resonant, rotational, and hybrid devices, as shown in Fig. 1.19. The operation of the resonant generators is oscillation based where the relative motion between the permanent magnets and the coil is used to produce electrical power from environmental vibrations. On the other hand, rotational generators operate in the same way as the operation of large-scale magnetic generators.

Under a steady driving torque, continuous rotational motion is produced which help to produce the large movement between the magnet and coil. Lastly, hybrid devices convert linear motion into rotational motion using an imbalanced rotor. Based on different operating conditions, the power generated by rotation from these devices may be continuous, resonant, or chaotic.
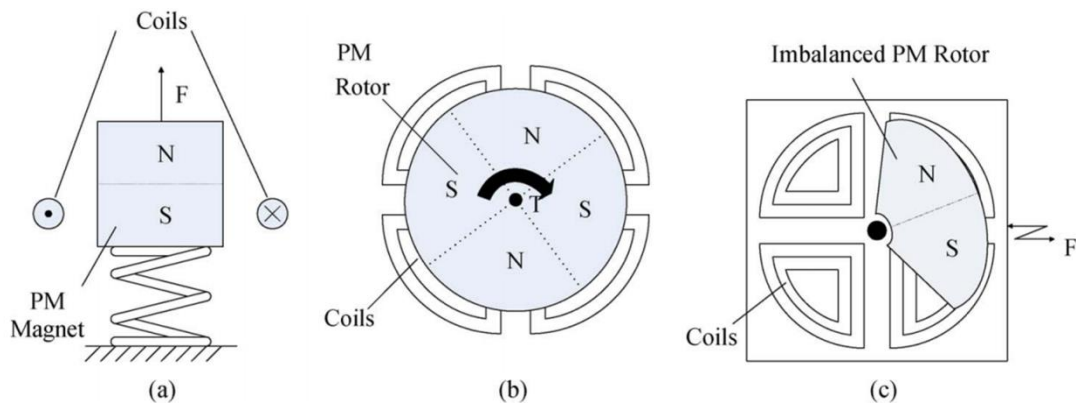
Fig. 1.19: Different types of electromagnetic generator configuration: (a) Resonant generator (b) Rotational generator (c) Hybrid generator - convert linear motion into rotational motion [61].

1.5. Research Objective:

The work reported in this thesis is part of a Science Foundation Ireland (SFI) Principal Investigator (PI) project, titled, 'Vibration based **W**ideband **E**lectromagnetic **M**icro-**P**ower **G**enerators' ('Wideband EMPG'). The project addresses the challenges of harvesting ambient energy for powering of low-power ICT technologies using electromagnetic transduction mechanism and addressing corresponding issues.

As has been described earlier, mechanical vibration is abundant in nature and can be found everywhere. Therefore, the application opportunities are huge too. Fig. 1.20 shows some of the available ambient vibration spectra (which are obtained from different resources as mentioned in the caption of the figure). A close inspection of the vibration spectra reveals that, while some of the ambient sources produce narrow band vibrations (where mechanical energy is concentrated within a narrow region of frequencies), the majority of the vibration sources are wideband/multi-frequency in nature. Therefore, extractable energy is distributed over a wide range of frequencies. The efficiency of conventional resonance based generators is significantly reduced in such cases. Hence, the main objective of this work is to develop low-frequency, wideband electromagnetic micro-power generators at a miniaturized scale (Meso/MEMS).
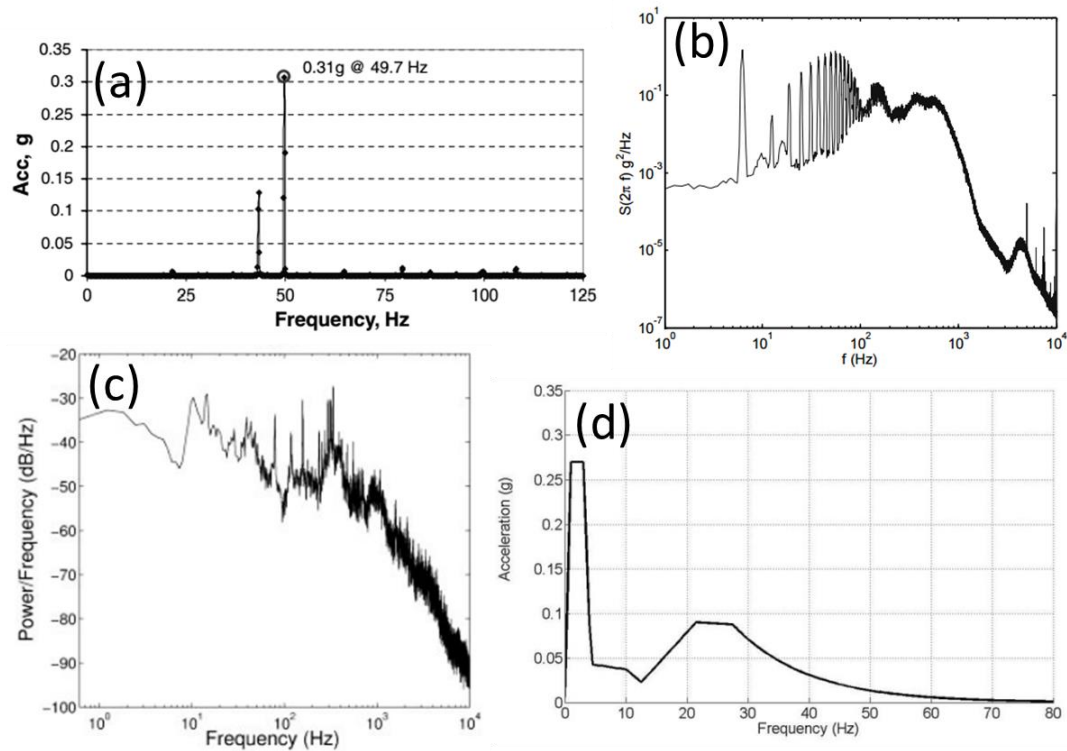
Fig. 1.20: Vibration spectra (a) from an air-compressor [62], (b) from inner liner of a car tyre driven at 50km/h [63], (c) from a running train floor [64] and (d) from right atrium of human heart [65].

In this series of works, single and double degree-of-freedom devices are developed using MEMS technology, which operating below 300 Hz. Bidirectional electrical tuning of narrow-band Electromagnetic Energy Harvesters (EMEHs) using two different complex load topologies is also reported. To widen the bandwidth of the transducers, the concept of incorporating nonlinear effect in the system dynamics is investigated. Nonlinearity is introduced into the EMEH devices through novel structural design of the spring arms. An electrical switching mechanism is introduced to switch from the low to the high energy output branch to address the fundamental phenomenon of hysteresis/multistability which limits the application of nonlinear energy harvesters. One of the key requirements for fully integrated EMEHs is the CMOS compatible batch fabrication of hard magnetic materials with large energy products. In the final module of the works, a nano-structured CoPtP hard magnetic material with large coercivity (>3 kOe) is developed at room temperature with optimized structures, using current modulated electrodeposition technique.

The work can be divided into three major categories:

(a) Design, theoretical analysis and numerical simulation

(b) Device fabrication and material development

(c) Device characterization and validation with simulated/modelled data

The mechanical structures are studied using finite element analysis (FEA) in COMSOL Multiphysics software whereas the electromagnetic simulations are performed using the Maxwell Ansoft software package. The dynamical analysis of the systems is performed numerically in MATLAB.

The developed devices are miniaturized using a number of approaches. The meso-scale mechanical structures are developed using computer-controlled laser micromachining technology which can be extended for batch fabrication aiming at large scale production. MEMS scale prototypes are fabricated on a Silicon-on-Insulator (SOI) wafer using standard MEMS processing techniques. Multilayered copper coils are fabricated on silicon too using an electroplating technique. For complete integration of the EM transducer, nano-structured, high energy product CoPtP hard magnetic materials is developed using an optimized current modulated electrodeposition method.

The developed devices are characterized using a LDS V455 permanent magnet shaker with a vibration control mechanism. The devices and materials are structurally characterized using Scanning Electron Microscopy (SEM), Electron Dispersive X-Ray (EDX) analysis and X-Ray Diffraction (XRD) methods. The magnetic characterization of the developed magnetic materials is performed using the SQUID Magnetometry (MPMS XL 5) technique.

1.6. Thesis structure:

The contents of the following chapters in this thesis are given below:

- **Chapter 2** provides a state-of-the-art literature review in the field of VEH with particular focus on EM generators both at meso- and micro-scales. A large section of the chapter is also dedicated to different wideband techniques for VEH in the literature. Also, interface electronics for EM generators are discussed briefly.

- **Chapter 3** discusses the operating principles of different simulation, fabrication and characterization techniques which are throughout the course of these works.

- **Chapter 4** discusses conventional linear (resonance based) electromagnetic energy harvesters. The chapter provides an introduction to the basic theory of electromagnetic generators followed by their implementations at meso-scale. A bidirectional electrical tuning mechanism is also discussed in this chapter. Initial work on a power

management circuit is also discussed for complete demonstration of one of the developed EM VEH devices.

- **Chapter 5** analyses multi-frequency MEMS EM energy harvesters employing two different topologies. The first system is single mass, where different fundamental modes are obtained within a close range through spring design innovation and by using a large magnetic proof mass. The second system is dual mass, which inherently has two major vibration modes corresponding to the movement of each of the masses.

- **Chapter 6** is dedicated to a novel wideband technique for VEH using the nonlinear oscillation principle. Introduction to nonlinear oscillation theory is provided in this chapter, followed by a complete theoretical analysis on the stretching strain induced nonlinearity. Prototypes in the meso-scale are first studied as a proof-of-concept before going towards micro-scale, where new innovations are introduced to further increase the operational bandwidth.

- **Chapter 7** deals with a particular, fundamental problem of nonlinear oscillators, namely hysteresis/multistability, which restricts its operation in a number of areas including energy harvesting. An electrical switching mechanism is introduced and the background physics of the mechanism is investigated thoroughly to improve the efficiency of wideband nonlinear generators.

- **Chapter 8** describes the development of nanostructured, stress-free Co-rich CoPtP films required for fully integrated electromagnetic generators using an electrodeposition technique. The self-demagnetization effect of thin magnetic films is minimized by developing an optimized micro-patterned structure for efficient MEMS scale integration.

- **Chapter 9** summarises the work reported in this thesis and suggestions for future work are discussed.

Chapter 2

Vibration Energy Harvesting: State-of-the-art

2.1. Introduction:

As described in the previous chapter, the field of vibration based energy harvesting has been recognized as an area of intensive research in the last decade for an alternate robust, reliable and sustainable power source. Also, the basic architecture of a VEH device comprises mainly of a mechanical-to-electrical transducer, which can usually be modelled as a second order spring mass damper system. The form of the electrical damping factor is dependent on the nature of the transduction mechanism. This chapter provides a state-of-the-art review of the literature of the different reported vibration based energy harvesting devices and underlying mechanisms. The review is divided in two major categories –

- Different VEH devices based on their operational dynamics will be discussed. This will cover reported resonant and non-resonant approaches. As mentioned in the previous chapter, the application/operational condition of a VEH is often unknown and the harvester with fixed resonant frequency is not suitable for a number of practical applications. Hence, a number of techniques have been adopted in the literature to suit such excitation frequency variations. This section will revisit those methods. Since the primary focus of this thesis is EM generators, a detailed review of miniaturized/MEMS scale EM harvesters will be provided. Various integration approaches and the effect of size scaling of the device on the output performance will be discussed. Finally, different commercially available VEH products will be reviewed.

- Introduction to the basic power conditioning circuits for VEH devices will be provided in this section. Different reported topologies, particularly differentiating the requirements for piezoelectric and EM VEH devices, will be discussed here.

2.2. Vibration based Energy Harvesters:

2.2.1. Resonant and Non-resonant Energy Harvesters: Equation (1.2), reported in the previous chapter, represents a second order spring mass damper system. When solved in the frequency domain, it shows resonance characteristics [66] i.e., the maximum output response is obtained at a particular resonance frequency but the response drops on both sides of this resonance point. This is particularly applicable for linear systems i.e., the systems for which the spring force is linearly proportional to the spring displacement. Such systems are well-known and are realized in a number of MEMS and non-MEMS applications [67-70] using either cantilevered or spring architectures. Regardless of the transduction mechanisms, most of the earlier reported works in the field of vibration based energy harvesting are also focussed on such designs which are suitable for single frequency excitation. While a typical non-resonant type generator has no specific operating frequency and mainly consists of freely moving objects such as a rolling sphere. Such generators are easy to realize using the electromagnetic transduction method.
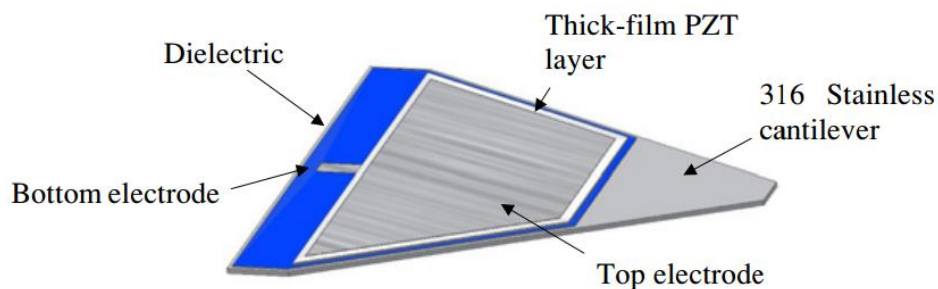
Fig 2.1: Tapered thick-film PZT generator by Glynne-Jones et. al. [72].

- **Piezoelectric Generators:** A piezoelectric cantilever is the most common structure of VEH devices with either a unimorph or bimorph configuration. Detailed modelling and experimental results of a piezoelectric bimorph cantilever generator have been given by Roundy et. al. [71] where PZT-5A patch is attached on both sides of a steel cantilever and a proof mass made of nickel and tungsten alloys is attached to the free end. At an acceleration of 0.25g and vibration frequency of 120 Hz, the device produced a maximum output power of 80 μW using a load resistance of 250 kΩ. Glynne-Johnes et. al. [72] developed a tapered cantilever piezoelectric generator (Fig. 2.1.) where the piezoelectric

material (PZT-5H) is screen printed on a steel beam. The tapered profile ensures the constant strain along the length of the piezoelectric material. At a frequency of 80.1 Hz, the device produced 3 μW output power for a load resistance of 333 kΩ. The screen printing of thick-film piezoelectric material is a low cost batch process but the power generated is limited by the reduced piezoelectric properties of the material compared to that of bulk piezoceramics. Similar screen printed bimorph configuration is used by Zhu et. al. [73] for a T-shaped cantilever which produced 240 μW power across a 57 kΩ load resistance with an input vibration of 66.2 Hz frequency and 0.29g rms acceleration.
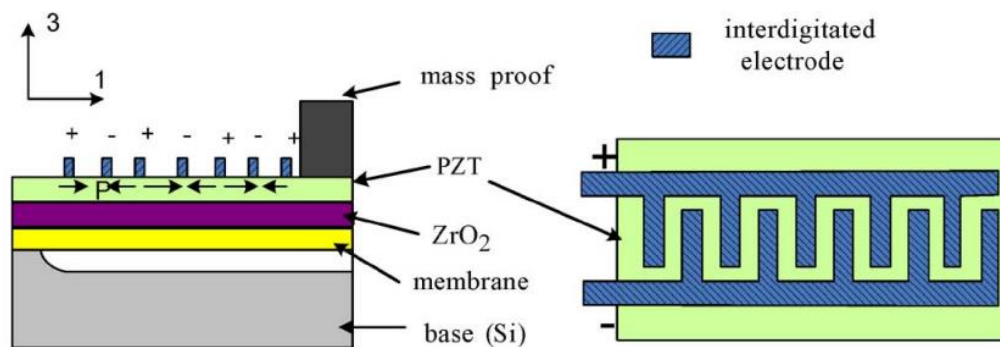
Fig 2.2: Cross-sectional and top views of d_{33} mode piezoelectric device [74].

A number of works have also been reported on miniaturized MEMS piezoelectric generators. One of the earlier MEMS piezoelectric energy generators has been designed and fabricated by Jeon et. al. [74]. The structure of the cantilever generator and the electrodes shapes are shown in Fig. 2.2. The cantilever is formed from a membrane comprised of layers of thermally grown silicon oxide, deposited silicon nitride, and sol–gel deposited zirconium dioxide, which acts as a buffer layer. The inter-digitated Ti/Pt electrode pattern enables the device to convert the d_{31} mode into the d_{33} mode as the beam bends. The d_{33} co-efficient is 2– 2.5 times larger than the d_{31} coefficient [75]. A thick layer of polymer SU8 photoresist forms the proof mass for the generator. Driven at a fundamental resonant frequency of 13.9 kHz with about 1g acceleration magnitude, the generator produces 1.01 μW across a 5.2 MΩ load. Marzencki et. al. [76] developed a micromachined MEMS piezoelectric cantilever. It consists of an inertial mass of 1.5 mm × 0.75 mm area, which is deep reactive-ion etched from a Silicon-on-Insulator (SOI) wafer with a 400 μm thick handle layer, 2 μm buried oxide, and 5 μm thick top silicon layer. The cantilever is fabricated from the top silicon layer and has a length of 750 μm. The structure is modelled for a piezoelectric layer of 1 μm thick Aluminum Nitride (AlN)

and PZT respectively. The modeling results predict 100 nW for the AlN device and 600 nW for the PZT device at a resonant frequency of approximately 900 Hz.

Jackson et. al. [77] developed CMOS- and bio-compatible AlN material whose c-axis is aligned to the (0 0 2) orientation for optimal performance. They compared the performances of narrow width beam, wide width beam and tapered beam cantilever structures (Fig. 2.3.) using their developed material. The wide beam generator produces a maximum output power of 3.07 µW for an acceleration of 0.2g with a matched load around 1 MΩ. The device cross-section consists of a 550 µm Silicon-on-Insulator (SOI) wafer with a 25 µm device layer, 3 µm thermally deposited oxide, 0.1 µm Ti bottom electrode, 0.5 µm AlN sputtered piezoelectric layer and 1 µm thick Al top electrode layer.
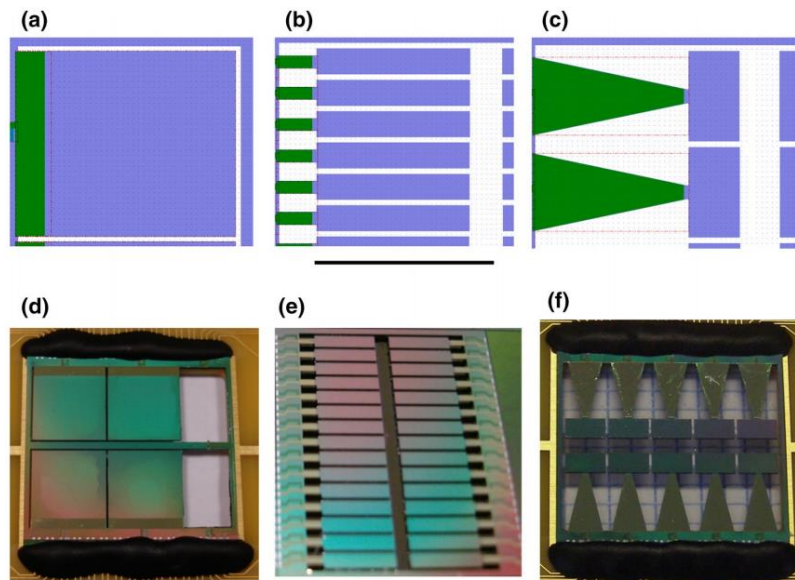
Fig. 2.3: Schematics (a-c) and Fabricated (d-f) cantilever beam structures - wide beam, narrow beam and trapezoidal beam. Beam is green and the mass is purple, scale bar is 7 mm.

Piezoelectric devices are more suitable for human wearable and implantable devices as harvesting power from bending strain/movement of the limbs using piezoelectric mechanism is more suitable. Human movements are normally characterized by large-amplitude motions at ultra-low (sub 10 Hz) frequencies [78]. Therefore, it is difficult to design a miniature resonant energy harvester to work on humans due to the scaling effect. But since the piezoelectric material just needs to be stressed in order to generate electrical voltage, the piezoelectric patch is coupled either through direct straining or by impacting the kinetic driving source for human based applications. Shenck and Paradiso [79] reported two approaches to designing a shoe-mounted piezoelectric kinetic energy

harvester which is installed at the heel of a navy work boot to harvest the parasitic energy of heel strike (Fig. 2.4.).

Shoe-Mounted Piezoelectrics
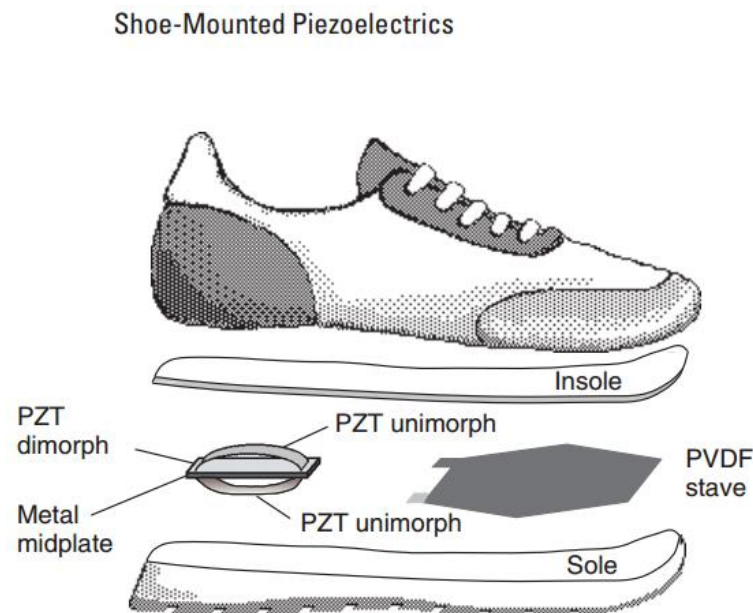
Fig 2.4: Two approaches to unobtrusive d_{31} piezoelectric energy scavenging in shoes: a PVDF stave under the ball of the foot and a PZT dimorph under the heel.

In the first approach, a hexagonal-shaped poly-vinylidene fluoride (PVDF) sheet working in d_{31} mode takes advantage of the bending movement of footfall to produce charge on the electrodes. In the second approach, a bimorph PZT plate is under the heel which captures the energy dissipated when the heel strikes the ground. In both the approaches, piezoelectric material experiences mechanical strain as the wearer walks and generates electrical power. Around 1.3 mW and 8.4 mW of average power is generated under matched resistive loads for two methods. Ramsay et. al. [80] suggested the idea to use a piezoelectric membrane exposed to blood on one side and to a chamber with constant pressure on the other side to utilize the blood pressure fluctuations for generating electrical power. They used a square PZT-5A membrane to extract energy from the fluctuating blood pressure in their modelling. For the typical blood-pressure change of 40 mmHg at a frequency of 1 Hz, a maximum power of 2.3 µW is obtained by maximizing the area and minimizing the plate thickness. Sohn et. al. [81] provided an investigation of the circular and square PVDF plates for use in harvesting energy from changes in blood pressure using a finite element study. However even with optimized device parameters, the estimated output power is quite low (0.03 µW). Mo et. al. [82] subsequently optimized the parameters for unimorph diaphragms and deciphered an optimal ratio between the radius of the supporting substrate and the radius of the piezoelectric layer

coverage for given parameters (Fig. 2.5.). Experiments with a PZT-5H layer epoxy-bonded to an Al substrate produced up to 128 μJ per loading cycle (Δp = 40 mmHg).
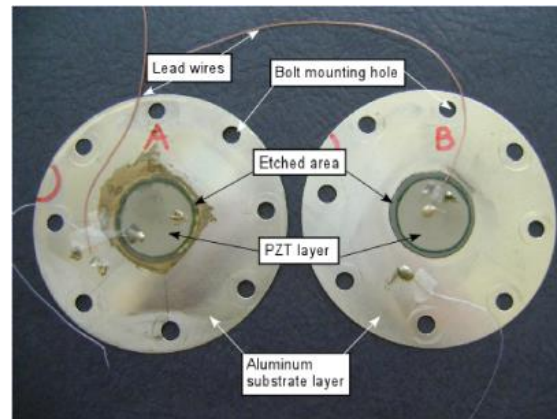
Fig. 2.5: Photograph of fabricated PZT harvester as reported by Mo et. al. [82].

Heart motion is another interesting source which generates a continuous supply of energy. Therefore, usable energy can be extracted using a number of approaches from the heart beat motion for powering implantable devices such as pacemakers and implantable cardioverter defibrillators (ICD). Karami et. al. [83] reported a zigzag shaped brass cantilever with 254 μm thick PZT-5A material epoxy bonded to it for power generation. The maximum power of 10 μW corresponds to 1800 μm substrate thickness. The reported linear meso-scale device can generate 10 times the power requirement of a pacemaker, excited at nominal heart rate. However, power reduced to only 39 nW for an optimized micro-scale prototype.

- **Electrostatic Generators:** As described in the previous chapter, there are mainly two variants of electrostatic energy harvester architectures based on the way the capacitor's plates are charged: battery-based and electret-based. Among the battery based harvesters, there are three types which are popular – in-plane overlap, in-plane gap closing and out-of-plane gap closing. Also, most of the reported electrostatic generators are integrated devices due to their ease of fabrication using MEMS processing. Meninger et. al. [84] investigated an in-plane overlap generator with a comb-driven structure which generates 8 μW output power at 2.5 kHz excitation frequency. Using a charged floating gate generator, Ma et. al. [85] estimated an output power of 1 μW for an optimum load of 58 MΩ at 4.3 kHz and an acceleration of 182.5g. The monolithic integrated device uses an insulated poly-silicon floating gate to provide the required bias voltage. The floating gate is charged by electron tunnelling and power is generated by a variable capacitor of which

one plate is a moving gold proof mass and the other is the fixed floating gate. Using an array of 20 devices, a maximum power of 65 nW is generated at 76.6g.

Despesse et. al. [86] reported an electrostatic in-plane gap closing structure with a charge constrained cycle. In their design, the electrostatic force is linearly proportional to the inertial mass displacement like the mechanical spring force, allowing the two forces to be balanced for all displacements of the inertial mass. This results in high electrical damping as the electrical stiffness is chosen close to the mechanical stiffness. Using a silicon microstructure with a 2×10^{-3} kg inertial mass and excited by a vibration of 0.93g at 50 Hz, the device is predicted to produce a scavenged power of 70 µW.
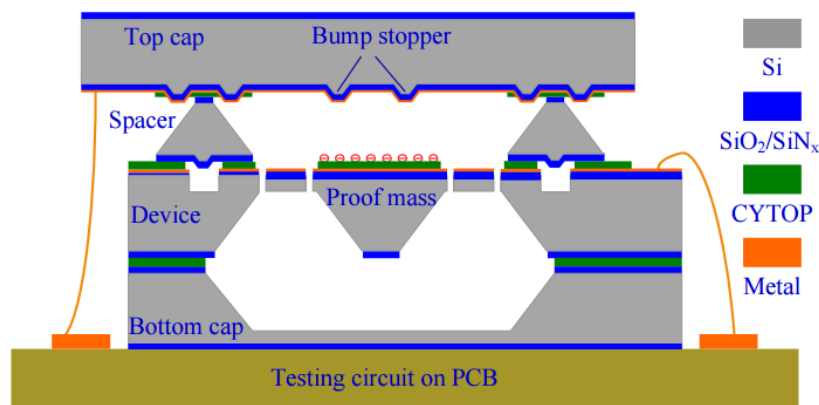
Fig 2.6: Cross-sectional scheme of the electrostatic energy harvesting device with a four wafer stack, reported by Wang et. al. [87].

Wang et. al.. [87] developed an electrostatic energy harvester with an out-of-the-plane gap closing scheme (Fig. 2.6.). The energy harvesting devices with a four wafer stack are batch fabricated and fully packaged at wafer scale. CYTOP polymer is used both as an electret material and an adhesive layer for low temperature wafer bonding. With an external load of 13.4 MΩ, a power output of 0.15 µW is achieved when vibration at an acceleration of 1g is applied at a frequency of 96 Hz.

There are a number of reported electrostatic generators which employ wideband techniques like nonlinear oscillation or frequency up-conversion. However, we have restricted the review to resonant devices in this section.

- **Electromagnetic Generators:** The electrical potential in an EM VEH device is dependent on relative motion between the magnet and the coil. Therefore, ultimately the performance of an EM VEH device depends on factors like the strength of the magnetic field, the number of turns in the coil and the relative velocity (or flux linkage rate) between the magnetic field and the coil. The relative motion between the magnetic field

and the coil can be produced by either using a static coil while the magnet is moving with respect to the coil or vice versa. It is well known that the performance of electromagnetic devices is not encouraging in the MEMS scale because the electromagnetic force scales down drastically with volume [88]. Therefore, EM VEH devices have been researched extensively over the years using macro to meso-sized structures assembled with discrete components along with miniaturized MEMS scale prototypes. The coil can be either wire-wound or micro-fabricated. However, macro-sized permanent magnets are used to provide the required magnetic field in most of the reported devices, because the maximum residual flux in permanent micro-magnet ranges from 0.2 T to 0.4 T and the coercive force ranges from 80 to 400 kA/m [89]. Unfortunately, these parameters are not comparable to those associated with the available rare-earth permanent magnets (1.27 T residual flux and ~12 kOe coercivity). The utilization of such micro-magnets produces a generator with very low power density. A detailed review of various permanent magnetic materials is provided in Chapter 8.
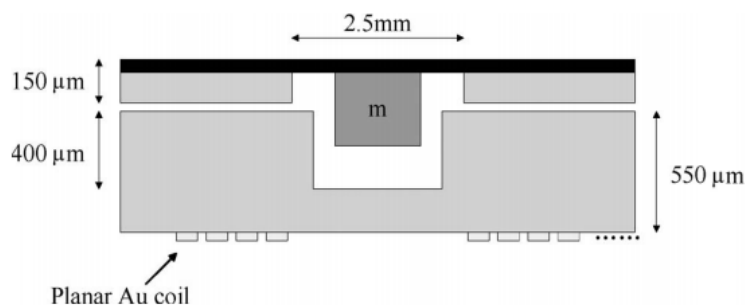
Fig. 2.7: Schematic of the electromagnetic generator by Williams et. al. [90].

In 1995, Williams et. al. [90] at the University of Sheffield were the first to propose a resonant electromagnetic generator for low-power applications. The generator, as shown in Fig. 2.7, has overall dimensions of 5 mm × 5 mm × 1 mm with a typical generated power of 1 µW at an excitation frequency of 70 Hz and 100 µW at 330 Hz. Sherwood et. al. [91] later fabricated a generator based on this design which comprises a flexible circular membrane micro-machined on a GaAs substrate coated with 7 µm polyimide layer. A SmCo magnet (weight = 2.4×10^{-6} Kg) was attached to the membrane whereas a planar Au coil of 13 turns was patterned on a separate wafer. This generator produced 0.3 µW output power at an excitation frequency of 4.4 kHz and an acceleration of 39g. From that time, research on EM VEH devices has sparked. The research has focussed on separate entities such as resonating spring structure, efficient magnetic arrangement, and proficient coil development for overall improvement of EM generators. Amirtharajah et.

al. [92] developed an EM generator using off-the-shelf spring, wire, and permanent magnets. They reported 400 µW of power generation at 2 Hz for 2 cm amplitude vibrations due to humans walking, which is equivalent to an acceleration of 0.3g. The main disadvantage of this design is the presence of an open loop magnetic circuit i.e., the magnetic field produced by the north pole of the magnet has to return to the south pole through a huge air reluctance. This reduces the magnetic flux linkage with the coil significantly. Additionally, such an open magnetic circuit can affect the surrounding electronics due to the relatively large magnetic field. Also, the size of the prototype is quite large, making it unsuitable for miniaturized applications. El-hami et. al. [93] reported a moving magnet generator with a cantilever spring. A C-shaped soft magnetic core is used in the design as the return path for the magnetic field so that the flux density in the air gap is increased to overcome the aforementioned problem. A fixed copper coil with 27 turns allows relative displacement between the coil and the magnets under external excitation. They reported an output power of 530 µW at 322 Hz at an excitation acceleration of 10.23g, which reduces to 40 µW at 1.2 g.
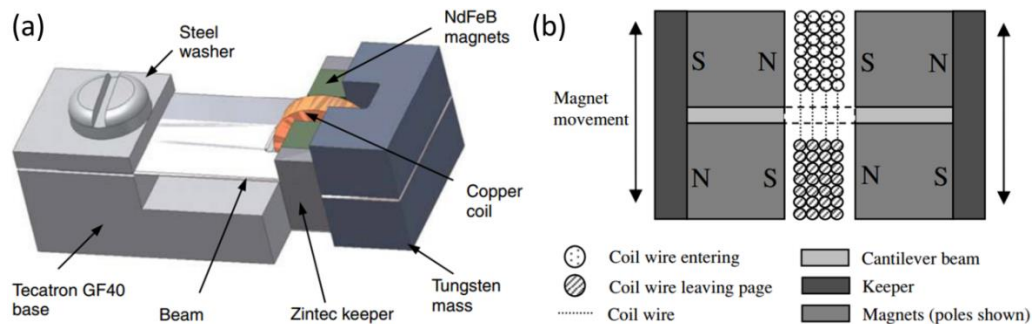
Fig. 2.8: (a) BeCu cantilever generator [62]. (b) Closed magnetic circuit used in the prototype to maximize the flux gradient.

The group working at the University of Southampton and Tyndall National Institute developed a new configuration of magnetic circuit with a closed magnetic field path for optimizing the structure of a moving magnet generator with cantilever [94, 62]. As shown in Fig. 2.8 (a), an optimized EM harvester consists of a Beryllium Copper (BeCu) cantilever with a magnetic arrangement attached to the free end while the wire wound copper coil is fixed vertically through a slot in the cantilever. The magnetic circuit (Fig. 2.8 (b)) consists of two pairs of oppositely polarized NdFeB magnets forming a closed path for the magnetic field while two soft magnetic steel keepers at the end guide the flux lines. The reported generator with a volume of only 150mm^3 still has one of the highest

reported power densities. The device generates 46 µW at an excitation frequency of 52Hz and a 0.059g acceleration level.

While the above mentioned magnetic arrangement has been used in a number of reported works [95-96] for getting optimum flux linkage for an out-of-plane moving device, several topologies have also been used for an in-plane moving EM harvester. In 2012, a group from Southampton University developed an interesting magnetic arrangement by introducing the concept of a Halbach array in energy harvesting [97]. The Halbach array consists of two sets of magnets, i.e. main magnets and transit magnets, which is depicted in Fig. 2.9 (a). The superimposition causes the concentration of field on one side of the array with cancellation of field on the other side. Fig. 2.9 (b) shows the construction of the planar electromagnetic energy harvester using a Halbach array.
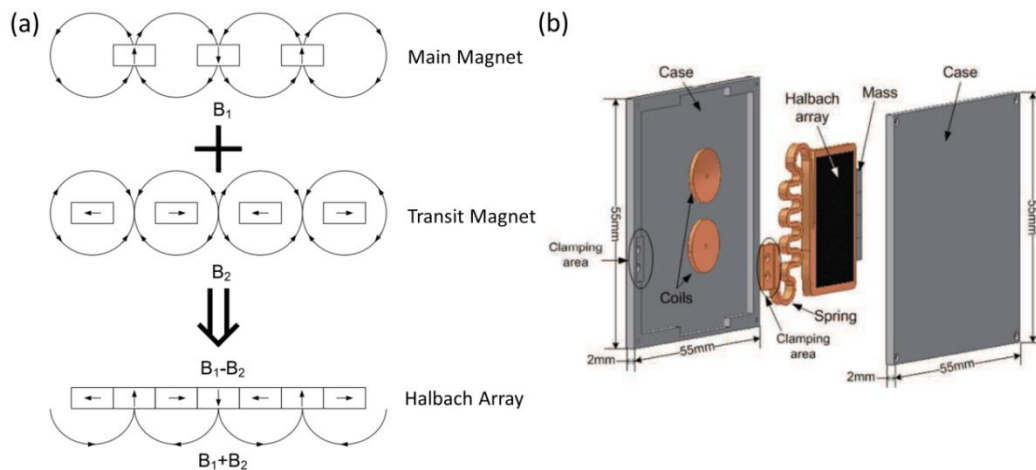
Fig. 2.9: (a) Principle of the Halbach array (b) Breakdown of different components in the planar EM generator [97].

With external vibration, the Halbach array moves laterally due to the particular geometry of the meander spring. The magnetic flux line cut by the coil induces a voltage. Field strength at the active-side of the Halbach array is measured to be about 9 times than that at the quiet-side. Thus the electromagnetic field strength of the Halbach array is greater than that of conventional layouts of magnets of the same total volume. At low vibration level, the Halbach array does not show any advantage over conventional layouts. However, when the vibration level is increased so that the displacement of the magnets is comparable to the outer diameter of the coil, the energy harvester with a Halbach array has a 40% higher output power. The Halbach arrangement can improve electromagnetic coupling in a limited space. Another benefit of the Halbach array is that due to the existence of an almost-zero magnetic field zone, electronic components can be placed

close to the energy harvester without any chance of interference, which can potentially reduce the overall size of a self-powered device. Roundy and Takahashi [98] reported on the development of a new planar EM transducer which is realized with low cost printed circuit board (PCB) coils, multi-pole magnetic sheets and springs which suspend the magnet over the PCB and maintain the gap between them. A schematic diagram of the device topology is shown in Fig. 2.10 which has a resonance frequency of 260 Hz.
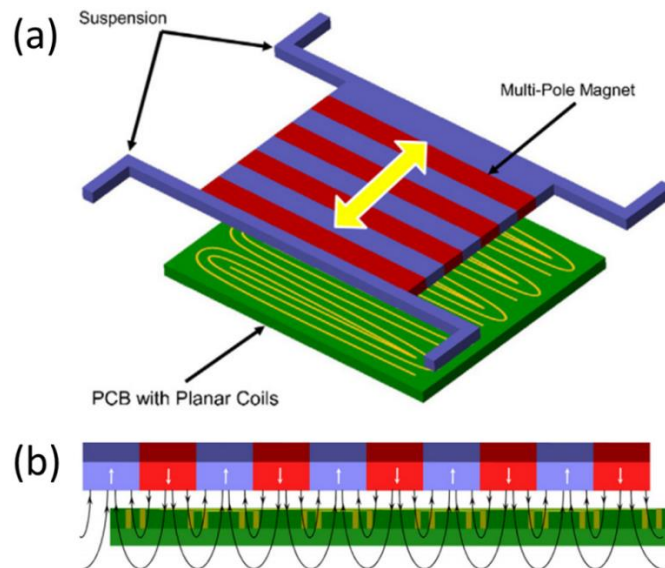
Fig. 2.10: (a) Schematic of multi-pole magnet transducer concept. (b) Illustration of the magnetic flux captured by the planar coils on the PCB [98].

The prototype is intended for direct force input. When the proof mass is displaced with a force of 12 N, it results in a 2 mm displacement. Across a matched load of 20Ω, the generated energy is 1.1 mJ from 12 mJ of input energy, which results in an efficiency of 9%. In many of these above mentioned prototypes, BeCu is used as the spring material due to its suitable mechanical properties, in particular excellent fatigue characteristics. On the other hand, polymeric materials with lower flexural modulus have been used for resonator development in a number of reported works.

Sardini et. al. [99] reported a power harvesting device (Fig. 2.11) which is constituted by two sets of magnets with a thin moveable structure between each set. The moveable structure, over which a flat inductor is fabricated, oscillates between the two sets. The magnets and the outer circular edge of the resonator are bounded rigidly to the case structure by circular supports. Five polymers were chosen for the resonator structure: PTFE (Teflon), Vulkollan, Silicone, Latex, Para. The last four materials are elastomers, more commonly known as gums. These materials are isotropic, elastic and

incompressible defined by the hyper-elastic law. All the generators made with a polymeric resonator showed a lowering of the resonant frequencies from about 100 Hz to about 30–40 Hz. Measurements on this system show that it is possible to generate a maximum instantaneous power and voltage of 290 µW and 183 mV for the linear resonator at 102 Hz, while with the nonlinear resonator (Latex) it is possible to generate a maximum instantaneous power and voltage of 153 µW and 378 mV respectively at 41 Hz.
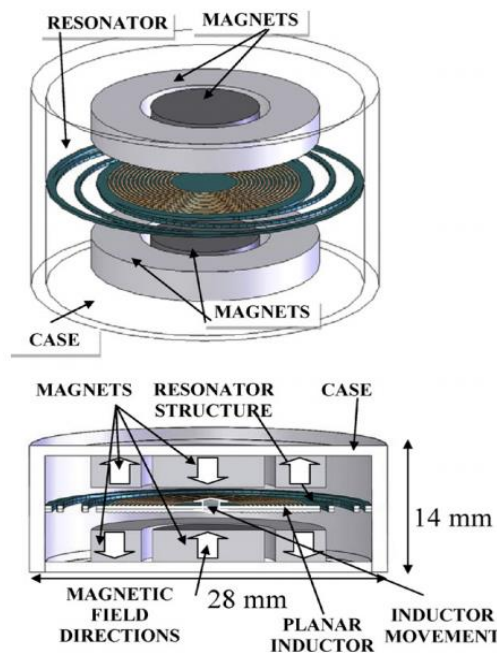
Fig 2.11: EM Generator structure developed Sardini et. al. [99], who investigated different polymers as spring materials.

The EM harvester reported in [100] uses a flexible PCB-part as a mechanical resonator which is sandwiched between two rigid PCB-parts (FR4) that serve as a frame. The device consists of stacked layers of housing, coil, spacer and mechanical resonator. The flexible part of the resonator is a polyimide film that is 50µm thick. A copper layer of 35µm thickness is electro-deposited on each side of the film. Two permanent magnets, which also provide the required proof mass, are magnetically attached to both sides of the flexible parts to generate the magnetic field. Two copper wire-wound coils are used as electrical transducers that convert the deflection of the resonator into an electrical signal. The fabricated energy harvester has a power density of 44 µW/g and weighs 8.12 g.

A popular approach to derive energy from ultra-low frequency human movements using an EM generator is to employ a magnetic levitation based harvester. In general, such a

levitation based harvester consists of two similar magnets having the same polarity fixed on the two ends of a hollow channel. In the middle, there is another freely moving magnet which is suspended in the channel due to the repulsive force with the fixed magnets. A coil is wrapped around the housing of the generator. When the housing vibrates, the suspended magnet starts to move, inducing an EMF in the coil. Saha et. al. [101] were among the first to report such a magnetic levitation based EM generator. As mentioned, the mechanical resonator in this generator is replaced by a magnetic spring based on the repulsion force between same-polarity magnets. The experimental results show that the device could generate 300 μW to 2.5 mW power from the motion of a human body operating in the sub-ten Hz frequency regime. Following this, a number of works have been reported on a similar concept for both vertical moving [102-104] and horizontal moving [105] magnetic spring structures to obtain optimized performance. Recently, Salauddin et. al. [106] reported a magnetic-spring-based, low-frequency generator comprising a dual Halbach array. The device, as shown in the cross-sectional diagram in Fig. 2.12., is composed of a rectangular-shaped dual-Halbach-array structure suspended between two magnetic springs and a series of three connected copper coils. Each Halbach array concentrates the magnetic- flux lines on one side of the array while suppressing the flux lines on the other side. Therefore, a dual Halbach array allows for interaction between the concentrated magnetic flux lines and the coils to produce the maximum flux linkage. The device is capable of delivering a maximum average power of 1093 μW to a 44 Ω optimum load, at an 11 Hz resonant frequency and under 0.5g acceleration.
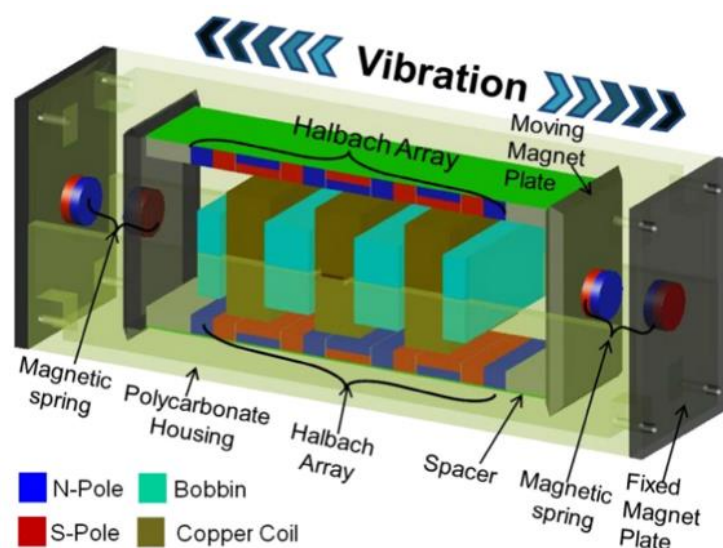
Fig. 2.12: 3D drawing of the magnetic spring based low-frequency VEH device comprising a dual Halbach array [106].
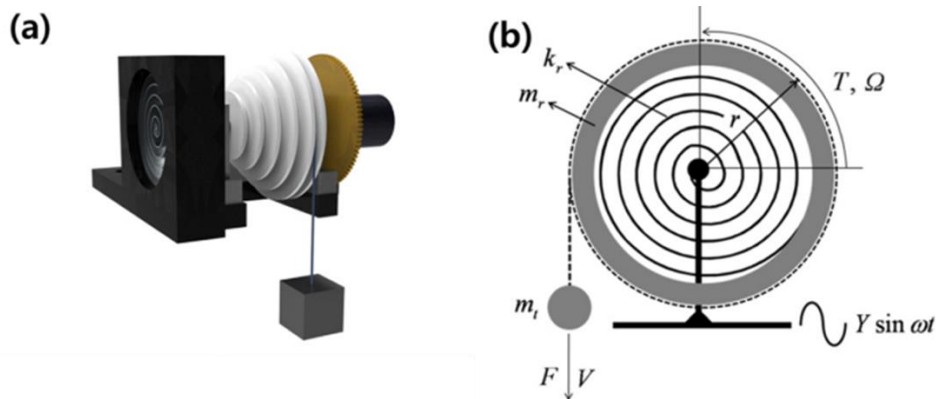
Fig 2.13: (a) Schematic of the tunable rotational energy harvester [107]. (b) The simplified mechanical model where spiral spring with rotational stiffness of k_r and the mass, m_t, is attached to it. The reel radius is r. The rotational velocity torque are X and T and the translational velocity and force are V and F respectively.

Jang et. al. [107] concluded that the maximum harvested electrical power from a resonant device with translational motion is limited by the internal travel range of the inertial mass within the generator. Under the low frequency and large amplitude excitation such as human motion and civil structures vibration, its efficiency is greatly reduced. The use of devices with rotational motion is advantageous in such cases. They proposed a tunable single degree of freedom rotational energy harvester which combines the rotational motion along with the translational motion of a proof mass suspended by the string and attached to the rotational body. The schematic diagram and simplified mode of the proposed device are shown in Fig. 2.13 (a) and (b) respectively. Its natural frequency can be adjusted by manipulating the size of the reel. However the built prototype is quite bulky, the proof mass itself being 1 kg. By changing the radius of the reel as 30, 25 and 20 mm, the natural frequencies are modified from 0.9, 1.03 to 1.19 Hz and the output powers are 37.85, 21.55 and 9.27 W respectively.

Moss et. al. [108] developed a hybrid rotary-translational VEH approach that exploits cycloidal motion to realize relatively high power density from an oscillatory device operating at frequencies below 10 Hz. The schematic model of the device is shown in Fig. 2.14, which shows that the magnetic sphere in this case is rolling around its axis while experiencing translational motion. The authors investigated that for a rolling magnetic sphere, the magnetic pole is travelling with twice the velocity compared with a non-rolling (i.e., sliding) magnetic sphere. This increase in velocity of the magnetic pole produces a corresponding increase in EMF induced in the coil. Ma and Zhang [109] used

a pendulum type system subjected to parametrical excitation. When the dynamics of the device is outside the potential well and stays in stable orbits of period-one rotations, the harvested energy is proportional to the energy level of the orbit. It is dependent neither on the natural frequency of the device nor on the intensity of the excitation. For low-level vibrations, the effectiveness of the proposed method is limited to relatively low frequencies.
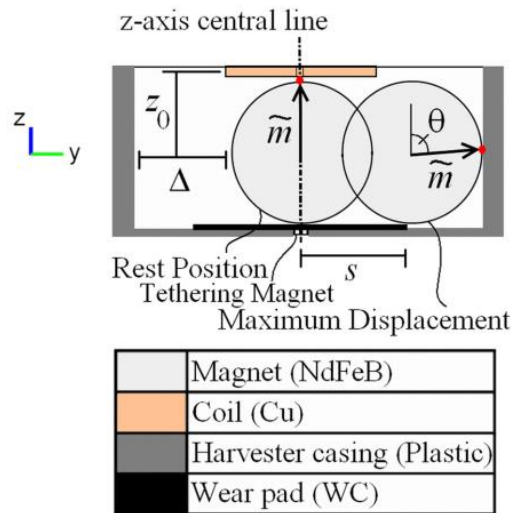
Fig 2.14: Schematic showing a side-elevation of the cycloidal vibration energy harvester as proposed by Moss et. al. [108].
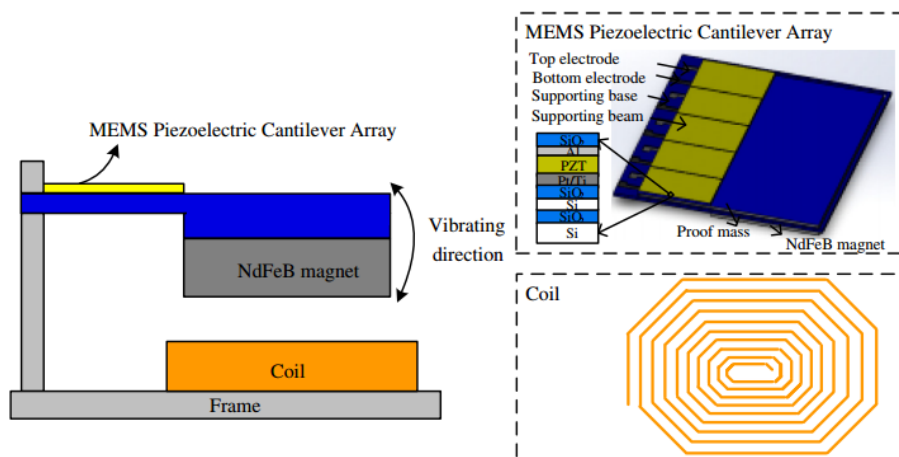
Fig 2.15: Hybrid micro-piezoelectric-electromagnetic energy harvester [110].

- **Hybrid Generators:** A hybrid generator combines multiple transduction mechanisms in a single device. A number of reported works have combined piezoelectric and electromagnetic transductions. Normally a piezoelectric device produces large output voltage whereas an electromagnetic device provides high current output. Therefore, the hybrid devices should potentially gain from both this advantages while increasing the overall output power. Yu et. al.. [110] reported a hybrid micro piezoelectric-

electromagnetic generator as shown in Fig. 2. 15. The harvester is composed of MEMS piezoelectric cantilever arrays with a NdFeB magnet attached to the free end proof mass, and two micro copper coils fabricated using screen printing technique placed on the two fixed bases. The device produces a load power of 40.67 μW across a matched load at 0.2g acceleration and 55.9 Hz frequency, which is quite high for micro-scale devices. Xu et. al. [111] reported a tunable multi-frequency hybrid energy harvester combining piezoelectric and electromagnetic mechanisms, which are coupled with magnetic interaction. Using a hybrid device, the authors find an increase of 16.7% and 833.3% in the peak power compared with that of the multi-frequency EMEH and the multi-frequency PEH devices. Khaligh et. al. [112] proposed and analyzed a novel hybrid VEH topology for human movement applications. In this structure (Fig. 2.16.), the moving mass with permanent magnets attached to it is connected to four serpentine piezoelectric beams on four sides, and the copper coil is fixed in the middle of the moving mass. The device is made to work under low frequency by attaching a proof mass of tungsten alloy having a volume of 4.9 cm^3. With a vibration frequency of 2 Hz and an acceleration of 0.47g (vibration amplitude of 3 cm), 37 and 6 mW can be generated from the EM and piezoelectric parts, respectively. As two separate outputs from a hybrid generator need to be merged after the transduction, additional complexity may arise such as phase correlation of outputs, impedance matching between different transducers etc.
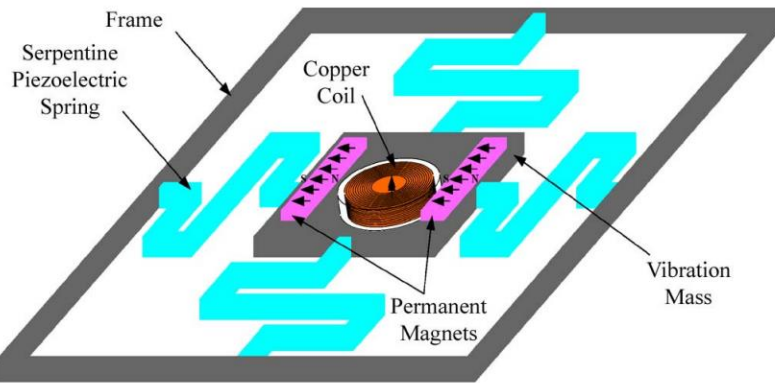
Fig 2.16: Topology of the hybrid generator reported by Khaligh et. al. [112].

Comparing different VEHs is not straightforward as the amount of data presented in published works varies considerably in terms of their operating conditions and device sizes. Hence, just comparing the output parameters like voltage, current or power is not justified. Beeby et. al. [62] derived a figure-of-merit for resonant VEH devices called, Normalized Power Density (NPD), which is simply the output power (P) of the device

normalized w.r.t. input acceleration level (A) and volume (V) of the device. Frequency is not considered in the figure-of-merit as resonant generators are fixed in frequency whereas acceleration levels applied during testing can be varied. The NPD can be defined as

$$NPD = \frac{P}{A^2V} \qquad (2.1.)$$

It is to be noted that acceleration (A) is taken in equation (2.1) in square form as the power varies with the square of the acceleration. A comparative study of the different reported vibration based energy harvesting devices is given in Table 2.1. For non-resonant generators, there is no such fixed frequency of operation. Hence the corresponding column is left blank there. In some cases, information like the volume of the device or the excitation acceleration or load power is not mentioned explicitly. Approximations are made in such cases.

Transduction Mechanism	Reference	Volume (cm³)	Acceleration (g)	Frequency (Hz)	Output Power (µW)	NPD (kg. s.m⁻³)
Piezoelectric	Roundy [71]	1	0.25g	120	80	19.2
	Glynne-Jones [72]	0.04	20.3g	80.1	3	0.0018
	Zhu [73]	14.03	0.4g	67	240	0.0134
	Jeon [74]	-	10.7g	13900	1	-
	Marzencki [76][1]	0.002	1g	900	0.1	0.5
	Jackson [77]	0.029	0.2g	149	3.07	26.5
	Shenck [79][2]	371.6	-	0.9	8400	-
	Ramsay [80][2]	-	-	1	2.3	-
	Sohn [81][2]	0.00087	-	-	0.61	-
	Karami [83][2]	4.38	-	-	10	-
Electrostatic	Meninger [84]	0.075	-	2520	8	-
	Ma [85]	-	182.5g	4300	1	
	Despesse [86]	0.032	0.93g	50	70	25.29
	Wang [87]	-	1g	96	0.15	
Electromagnetic	Williams [90]	0.025	1g	70	1	0.43
	Shearwood [91]	0.005	38.2g	4400	0.3	0.0004
	Amirtharajah [92]	23.5	0.32g	2	400	1.66
	El-hami [93]	0.24	10.23g	322	530	0.21
	Beeby [62][3]	0.15	0.06g	52	46	851.9
	Zhu [97]	0.1	0.5g	45	150	0.5
	Roundy [98]	-	-	260	-	-
	Sordini [99][4]	8.6	0.56g	41	153	0.57

Transduction Mechanism	Reference	Volume (cm^3)	Acceleration (g)	Frequency (Hz)	Output Power (μW)	NPD (kg. s.m^{-3})
	Sordini [99][5]	8.6	3.4g	102	290	0.029
	Bouendeu [100]	1.45	1g	98	356	2.45
	Saha [101]	12.7	0.038g	8	14.55	7.93
	Zhang [102]	120	0.05g	4	250[6]	8.33
	Berdy [103]	12	0.1g	6.7	410	69.72
	Apo [104]	5.88	1g	16	12900	34.17
	Palagummi [105]	85	0.005g	1.9	9.47	44.56
	Salauddin [106]	32.76	0.5g	11	1093	1.33
	Jang [107]	-	0.15g	0.9	37.85×10^6	-
	Moss [108]	59.7	0.5g	5.4	33000	22.11
	Ma [109][7]	13	0.14g	4	2800	109.9
Hybrid	Yu[110]	-	0.2g	55.9	40.67	-
	Xu [111]	-	0.2g	25.6	2820	-
	Khaligh [112][8]	19.6	0.47g	2	37000	85.45
	Khaligh [112][9]	19.6	0.47g	2	6000	13.85

Table 2.1. Comparative study of different resonant and non-resonant VEH devices using various transduction mechanisms.

[1]AlN device (simulated result)
[2]Devices work on direct application of force, no acceleration is present
[3]Mk2 EM generator
[4]Latex resonator
[5]FR4 resonator
[6]Estimated from Power vs Acceleration curve in Ref [38]
[7]Winding A – Ref [45]
[8]Electromagnetic Part
[9]Piezoelectric Part

2.3. Wideband Techniques for VEH:

Resonance based energy harvesters are suitable for single frequency excitation applications where they are designed in such a way that the natural frequency of the resonator matches with the external vibration frequency. But the response drops considerably with little shift of the ambient frequency from the resonance. In a number of practical applications, the operational condition is often unknown and the harvester with a fixed resonant frequency is not suitable for such cases. Thus in order to address this problem, a number of strategies have been reported in the literature to improve the efficiency of the energy harvesters in a frequency varying environment, which can be

categorized mainly under three headings - resonance frequency tuning, multi-frequency techniques and nonlinear energy harvesting.

2.3.1. Resonance Frequency Tuning: The most common approach to match the resonance frequency of a resonator with a changing external vibration frequency is to tune it. The resonance frequency of a generator can be tuned by altering either its mechanical or electrical characteristics. According to Roundy et. al. [113] the mechanical characteristics can be changed either through passive or active tuning. In passive tuning, energy is supplied in an intermittent manner so that when the generator frequency is matched with the external frequency then no further supply of energy is needed until the mismatch appears again. Whereas, the energy is supplied continuously in active tuning regardless of the resonance frequency of the system. Roundy et. al. [113] assumed the actuation force to be proportional to either resonator displacement (i.e. altering stiffness) or acceleration (i.e. altering mass) and performed the net maximum power output calculation for both types of tuning mechanisms. They concluded that the generators using an active tuning mechanism can never produce an overall gain in the power output as the power required to tune the resonance frequency is always greater than the output power resulting from the tuned system. However, Zhu et. al. [114] later revised this calculation by considering the average power and inferred that there is no generalized rule for such a conclusion as the tuning mechanism is often not connected to the movement of the resonator.
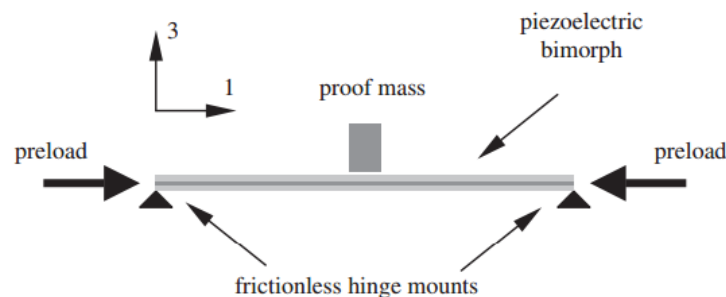
Fig. 2.17: Schematic of a simply supported piezoelectric bimorph with axial preload tuning scheme.

Leland and Wright [115] presented one technique to reduce the resonance of a simply supported piezoelectric bimorph by applying an axial compressive preload, which actually altered the stiffness of the harvester. The method is schematically shown in Fig. 2.17. By using compressive axial pre-load, the resonance frequency can be tuned up to 19-24% of the initial unloaded value while the damping rises continuously. However, the

output power does not fall significantly, being 65-90% of the untuned value. Hu et. al.. [116] showed that the resonance can be adjusted either higher or lower with a tensile or compressive load. The same can also be done by applying pre-stress [117]. The resonance frequency can be tuned by adjusting the center of gravity of the tip mass, as demonstrated by Wu et. al. [118]. They presented a cantilevered energy harvester by realizing a movable tip mass. The center of gravity of the whole proof mass can be adjusted by driving the movable screw. In their prototype, the adjustable resonance frequency range could cover 130-180 Hz by tuning the center of gravity of the tip mass up to 21 mm.

Challa et. al. [119] employed magnetic force to manipulate the effective stiffness and demonstrated bidirectional tuning of the harvester, which is schematically shown in Fig. 2.18. They used magnets on the top and on the bottom of the piezoelectric cantilever. Two other magnets were fixed on the top and bottom of the housing of the device. The effective stiffness could be changed by changing the distance between these magnets, which in turn alters the attractive and repulsive force between them. The output power of the device varies between 240-280 µW operating at an acceleration of 0.8g over the frequency range of 22-32 Hz. Later on, the concept of variable magnetic force has been utilized by many researchers to tune the resonance frequency [120-121]. All of the above mentioned methods need manual tuning and are passive. There are some reported active tuning mechanisms [122-123] using piezoelectric methods that are automatic. But the power needed to tune is often greater than the power actually harvested.
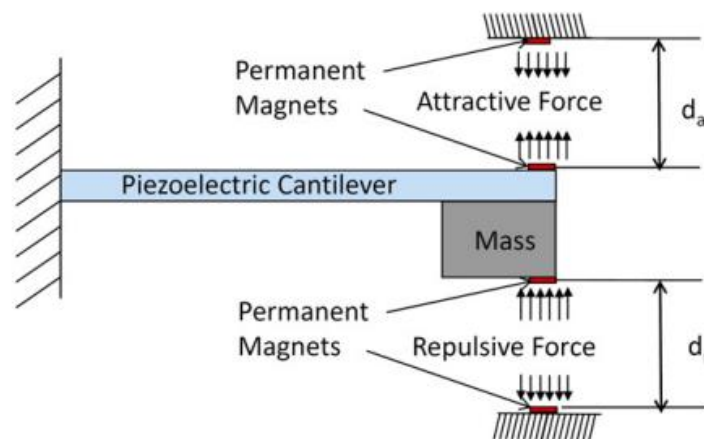
Fig. 2.18: Bidirectional frequency tuning scheme proposed by Challa et. al. [119].

The resonance frequency of a VEH can also be altered by modifying the electrical load of the system. This could also be categorized as an electrical method of tuning. Charnegie [124] tuned the bimorph piezoelectric energy harvester by modifying the load

capacitance. The concept of using a complex load instead of a resistive load to tune an electromagnetic energy harvester was first demonstrated by Cammarano et. al. [125]. Later, Zhu et. al. [126] provided a more generalized model to investigate the influence of different system parameters on the performance in the case of a capacitive load. A more elaborate study on the different resonant frequency tuning methods is reported by Tang et. al. [127].
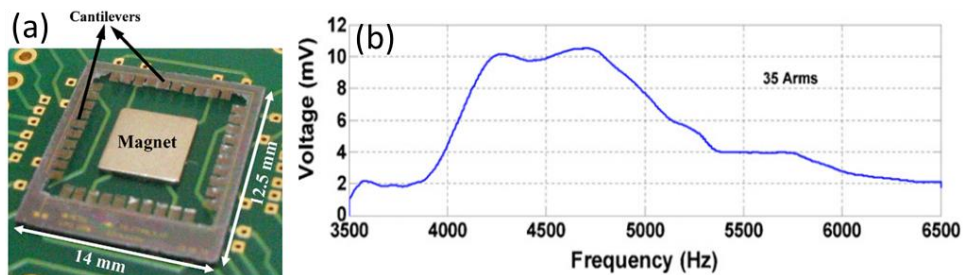
Fig. 2.19: (a) Array of parylene cantilevers with different dimensions. (b) Measured output voltage from the 35 cantilevers connected in series [129].

2.3.2. Multi-frequency Generators: Multi-frequency techniques are most suitable for MEMS scale integration due to relatively simple development methods. The reported multi-frequency approaches can be divided into two major groups. The first group is of array of generators with different dimensions [128-129] or different mass [130-131] to achieve separate resonance frequencies. However, use of an array significantly increases the overall volume of the device. Sari et. al. [129], utilized an array of 35 parylene cantilevers with different lengths which are connected serially, as shown in Fig. 2.19. An output power of 0.4 μW is obtained from the device with an electromagnetic transduction mechanism working at the operating frequency range between 4.2 – 5 kHz. Ferrari et. al.. [131] reported a similar array of cantilevers with a piezoelectric bimorph structure which works at different frequencies below 300 Hz. The other group comprises a single structure with closely spaced vibration modes. Tadesse et. al. [132] reported a multimodal generator with multiple (piezoelectric and electromagnetic) transduction mechanisms. The power output from the device is significantly increased as the electromagnetic transduction produces more power in the low frequency mode (20 Hz), whereas the piezoelectric method generates higher power in the second mode (300 Hz), due to the specific design of the device. Liu et. al. [133] reported a MEMS EM multimodal generator where both in-plane and out-of-plane vibration modes are excited within a single structure where all of the modes are above 1 kHz. The same group reported another multi frequency MEMS EM structure [134] with similar mechanical functionality but a

different magnet coil arrangement. In a recent work [135], both the above mentioned approaches are combined so that an array of multi-frequency VEHs are reported where nine different frequency peaks are activated between 189 – 662 Hz within a single chip. The concept of coupled resonators with more than one proof mass was first proposed by Petropoulos et. al. [136] in order to obtain a flat response over a significant operating range by optimizing the different structural parameters. Wu et. al. [137] reported a macro-scale, compact two degrees of freedom piezoelectric generator, where two vibration modes are developed due to two cantilever beams, one placed inside another, both operating at low frequencies. Tao et. al. [138] recently reported a MEMS EM two degree of freedom VEH, which comprises a primary subsystem for power generation and an accessory subsystem for frequency tuning which is depicted in Fig. 2.20. The device has two frequency peaks at 326 and 391 Hz, but the output power is lowered due to lower electromechanical coupling.
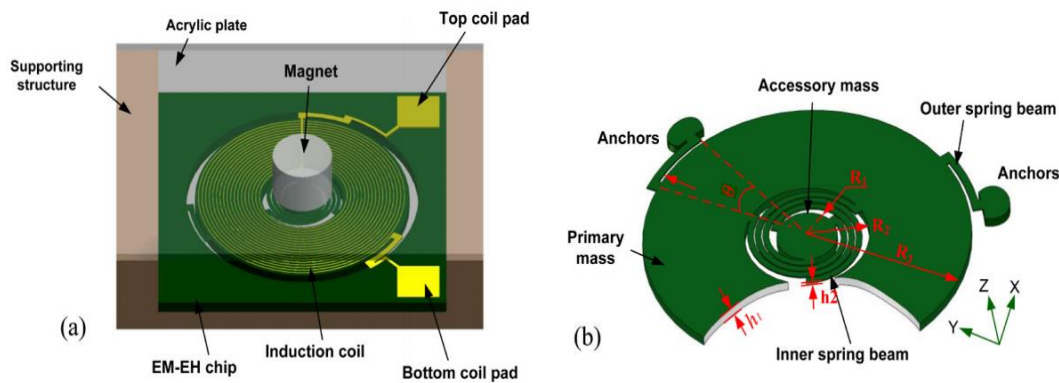
Fig. 2.20: (a) 3D schematic of proposed 2DOF EM-EH device; (b) trimetric view of spring-mass resonant configuration [138].

2.3.3. Nonlinear Energy Harvesting: The generalized equation of motion of a forced oscillator is given as

$$m\ddot{x} + c\dot{x} + F(x) = -m\ddot{z} \tag{2.2}$$

where m is the inertial mass, x is the position of the oscillator, c is the damping co-efficient, z is the input vibration applied to the frame and F(x) is the generalized spring force. For Duffing oscillator based nonlinear energy harvesters, the generalized restoring force and potential energy (U(x)) can be expressed as

$$F(x) = -kx - k_n x^3 \tag{2.3}$$

$$U(x) = -\int F dx = \frac{1}{2}kx^2 + \frac{1}{4}k_n x^4 \tag{2.4}$$

where k and k_n are the linear and nonlinear stiffness constants of the oscillators. Depending on the nature of k and k_n, the potential energy function can be classified in three major categories as shown in Fig. 2.21. For a linear oscillator (i.e., restoring force is linear function of displacement), the nonlinear stiffness constant k_n is equal to zero and k is positive. Such systems are reviewed extensively in the previous sections. For a non-zero k_n, a cubic nonlinearity comes into play in the energy harvesting system which can be introduced through the additional modulation of the stiffness of the spring. The nonlinear potential function is monostable for $k>0$ and bistable for $k<0$. The phrase 'stable' is utilized w.r.t the number of minima in the corresponding potential energy functions. Thus the monostable potential systems are single potential well systems where the point of minimum potential occurs at $x=0$ whereas the bistable potential function consists of two potential wells and the two corresponding minima exist at $x = \pm\sqrt{k/k_n}$ respectively, which are separated by a potential barrier at $x = 0$.
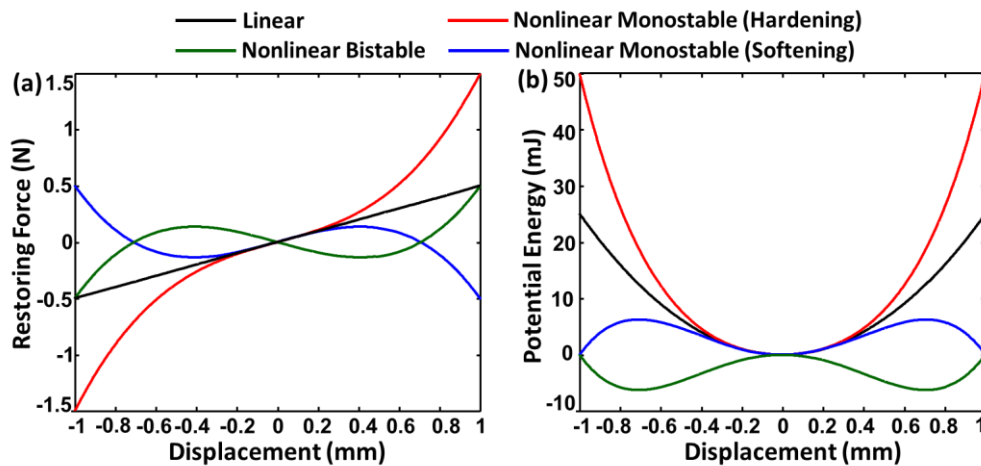
Fig 2.21: (a) Restoring forces and (b) Potential energy functions for different VEH configurations.

When $k>0$ and $k_n>0$, the restoring force increases with the displacement and is said to be a the hardening type nonlinear monostable. On the other hand, when $k>0$ and $k_n<0$, the restoring force decreases with the displacement and is said to be of the softening type nonlinear monostable nature, as depicted in Fig. 2.21(a). The corresponding potential energy functions of different configurations are shown in Fig. 2.21(b). The amplitude dependant nonlinear restoring force expressed by equation (2.2), forces the resonance frequency to track the external frequency under harmonic excitations. This results in the wideband output response of the energy harvesters. If an EM generator is considered, then the damping term in equation (2.2) also includes the viscous damping caused by

electromagnetic coupling. For a piezoelectric generator, the damping caused by piezoelectricity cannot be modelled as damping term and the equation of motion should be modified by adding a coupling term as mentioned in chapter 1.
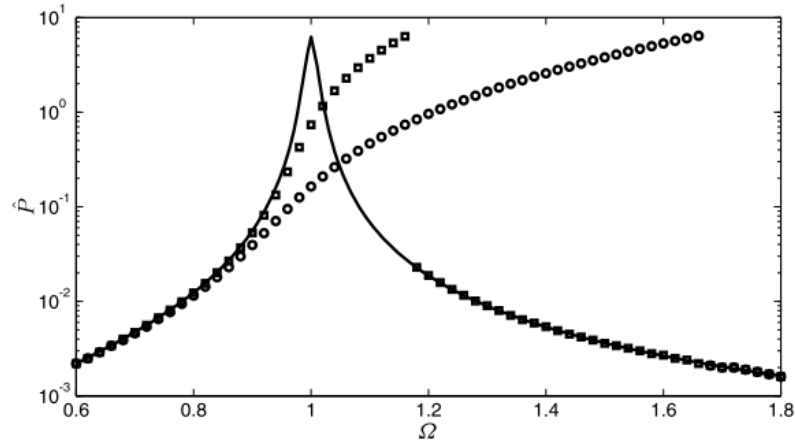
Fig. 2.22: Numerical simulation solutions, showing power ($\hat{P}$) vs. frequency (Ω), for linear (solid line) and nonlinear hardening responses (square and circle mark). The response bends more with increase in degree of nonlinearity [139].

The monostable hardening mechanism in a nonlinear energy harvester and its merits have been investigated by Ramlan et. al. [139]. They reported that the maximum output power generated by a system with a monostable nonlinearity is the same as the maximum power derived from a linear system, irrespective of the degree of nonlinearity (value of k_n). However, this might occur at a different frequency, depending on the degree of nonlinearity, as shown in Fig. 2.22. The bend in the frequency response results in the larger bandwidth of operation. It is often observed that the magnetic levitation based systems [140] described in the previous section, produce a monostable nonlinearity under large deflection. Stanton et. al. [141] proposed another monostable nonlinear piezoelectric device where both hardening and softening effect can be obtained through necessary adjustments and hence the frequency response can be broadened bidirectionally. As shown in Fig. 2.23, the device consists of a piezoelectric beam with a magnetic end mass interacting with the field of oppositely poled stationary magnets. By tuning nonlinear magnetic interactions around the end mass, both hardening and softening responses may occur. The geometric nonlinearity arising due to the stretching strain based monostable systems [142-147] are rather easy to implement in the MEMS scale as the source of nonlinear stiffness in such a system is from the special design of the spring arms. In such systems, nonlinear effects become prominent only under large deformation conditions which require higher excitation forces.

A critical issue associated with nonlinear energy harvesters is the presence of multiple solutions [139-147] at a single excitation frequency over a certain frequency region which gives rise to a hysteresis region. The advantage imparted in the nonlinearity depends on realizing the high energy branch. A linearly decreasing (softening type) or increasing (hardening type) frequency sweep can capture the high energy branch in the case of a monostable nonlinear system. Unfortunately, such conditions cannot be guaranteed in practice. The output power is significantly reduced in the low energy states. Daqaq et. al. [148] demonstrated that under white Gaussian excitation, monostable nonlinear devices do not provide any advantage over a linear system in terms of the output power. Under colored Gaussian excitations, the output power even reduces further.
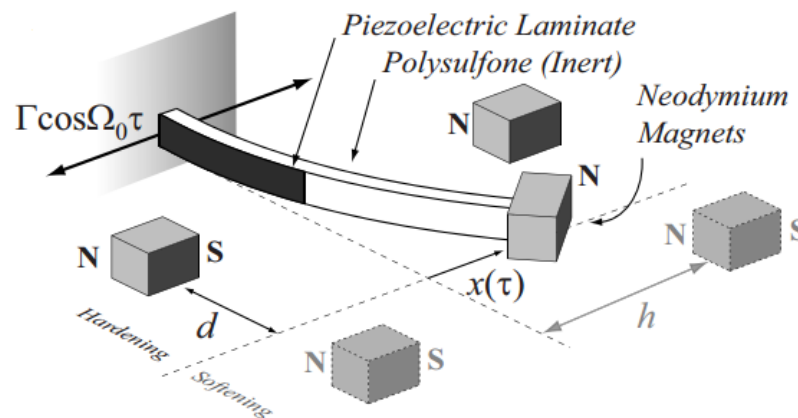
Fig. 2.23: Schematic of the nonlinear energy harvester, proposed by Stanton et. al. [141] where both hardening and softening nonlinearities can be obtained through adjustments.

Due to the presence of the double potential well, the dynamics of bistable oscillators is much more complicated. Even with periodic forces, they can undergo various types of motion, including intra-well motion (oscillation confined within one of the potential well) and intra-well motion (oscillator can move between two potential wells) [142]. The nature of oscillation depends on the initial conditions and on the magnitude and the frequency of the external excitation force. When the magnitude of the external force is small, the oscillator shows inter-well motion and the output characteristics are similar to a monostable system. However, in this case the potential well is asymmetric. Once enough energy is provided through the external forces, the oscillator is able to break the potential barrier and initiate the inter-well motion. Further increase in the external force magnitude leads to the different complicated bifurcation phenomenon and chaotic oscillation [142]. At one stage, the high energy periodic solution becomes unique over a certain range of

frequencies, allowing the oscillator to undergo large amplitude motions for any set of initial conditions.
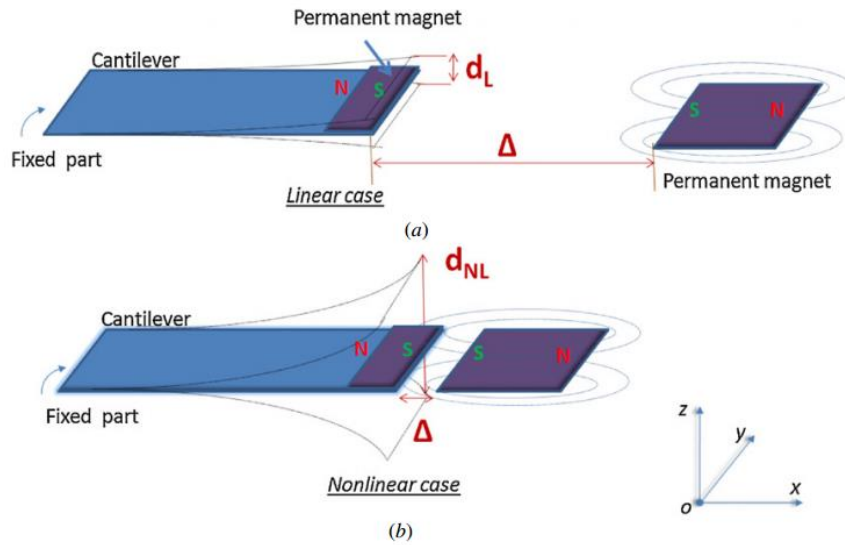
Fig. 2. 24: Cantilever beam (a) immune to magnetic repulsive force, therefore linear and (b) subject to magnetic repulsive force; d_L and d_{NL} represent the displacement of the beam in the linear and nonlinear cases, respectively [152].

Nonlinear bistable stiffness can be created by using magnets (Fig. 2.24). Erturk et. al.. [150] designed a broadband piezomagnetoelastic generator which consists of a ferromagnetic cantilevered beam with two permanent magnets located symmetrically near the free end, and subjected to harmonic base excitation. For an initial deflection at one of the stable equilibria, the voltage response could be chaotic strange attractor motion or large-amplitude periodic motion (limit cycle oscillation), under small or large excitation amplitude. Cottone et. al. [151] realized a piezoelectric inverted pendulum using the bistable mechanism through oppositely polarized magnet interaction. By changing the distance between these two interacting magnets, the potential energy can be modified. Under noise input, the maximum power for a specific distance (11.2 mm) can exceed the power obtained when the magnets were far away by four to six times. A similar idea was adopted by several other researchers [152-153] later. Ramlan et. al.. [139] proposed a concept of nonlinear bistable energy harvesting via a snap-through mechanism. The model consists of two linear oblique springs connected to a mass and a damper, yielding a nonlinear restoring force. Using numerical results, they showed that this mechanism can provide much better performance than the linear mechanism, when the excitation frequency was much less than the natural frequency. The similar concept of buckling force has resulted in a number of reported works [154-155].

Due to the presence of inter-well motion, a suitably designed bistable oscillator can outperform a linear or monostable nonlinear oscillator under stochastic or noisy input vibrations. This is due to the fact that the oscillator can initiate the large amplitude motion as soon as it gets the minimum energy from the external source to cross the potential barrier. However, it is observed that in most of the bistable generators, extra components or external intervention is required to realize the system which is undesirable.
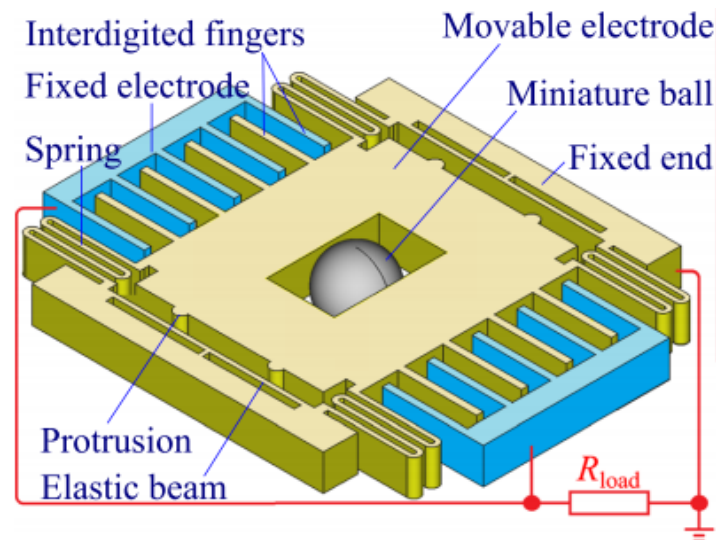
Fig. 2.25: Schematic of the electrostatic generator employing frequency up-conversion technique for generating power from human motion [157].

Other than these three major wideband techniques, another topic in this area is frequency up-conversion [156-157] or mechanical amplification where the system consists of two components – one at very low frequency and other at high frequency. The low frequency vibrating unit vibrates due to the external excitation which in return transfers the energy to the high frequency component through some mechanism, impact in most cases. The frequency up-conversion technique can be more significant in the design of micro-scale energy harvesting devices, in which the resonance frequency of the structure can be at the level of 1 kHz, while the ambient vibration frequency is generally below 100 Hz. Lu et. al.. [157] recently reported an electrostatic MEMS generator using a similar concept for transducing the power from human motion (Fig. 2.25). Thanks to a miniature tungsten ball impacting with a movable proof mass of silicon. The motion of the silicon proof mass is confined by nonlinear elastic stoppers on the fixed part standing against two protrusions of the proof mass.

In the following Table 2.2, different broadband techniques are summarized in terms of their bandwidth and peak frequency of operation. Since many of the techniques require

extra components or adjustments, the volume or output power is left out of the comparison. However, an estimation of the volume can be made from the scale of the device like macro ($>10cm^3$), meso (1-10 cm^3) or MEMS ($<1cm^3$).

Mechanism	Reference	Device Scale & Transduction	Peak Frequency (Hz)	Operating Frequency Range (Hz)[1]	Remarks
Resonance Frequency Tuning	Leland [115]	Macro, Piezoelectric	250	250→200	Axial Compressive Pre-load (up to 65N)
	Hu [116]	Macro, Piezoelectric	129.3	58.1↔169.4	Axial Tensile/ Compressive Pre-load (± 50N)
	Eichhorn [117]	Macro, Piezoelectric	380	380→292	Mechanical Pre-stress (22.75N)
	Wu [118]	Macro, Piezoelectric	180	180→130	Manual Tuning the Gravity Center of the Tip Mass up to 21 mm.
	Challa [119]	Macro, Piezoelectric	26	22↔32	Magnetic Force Tuning
	Reissman [120]	Meso, Piezoelectric	88	88→99.38	Magnetic Attractive Force Tuning
	Zhu [121]	Meso, Electromagnetic	45	47.72→87.84	Magnetic Attractive (distance changed 13→2 mm) Force Tuning
	Peters [122]	Meso, Piezoelectric	78	65↔90	Piezo Actuation (±5V) (active control circuit – 150 mW consumption)
	Wischke [123]	Macro, Electromagnetic	299	267↔323	Piezo Actuation (-100 to 260V)
	Cammarano [125]	Macro, Electromagnetic	62	57.4↔66.5	Load Reactance Tuning (150 μF to 57 mH)
	Zhu [126]	Meso, Electromagnetic	70.05	70.05→69.9	Load Capacitive Tuning (up to 10 μF)
	Zhu [126]	Macro, Electromagnetic	95.5	95.5→90.5	Load Capacitive Tuning (up to 1.6 μF)

Mechanism	Reference	Device Scale & Transduction	Peak Frequency (Hz)	Operating Frequency Range (Hz)[1]	Remarks
Multi-frequency Generators	Sari [129]	MEMS, Electromagnetic	-	4200↔5000	Diof
	Xue [128]	MEMS, Piezoelectric	-	87↔115	Different Thicknesses of Piezoelectric Layers
	Liu [130]	MEMS, Piezoelectric	-	226, 229, 234	Different Proof Mass
	Ferrari [131]	Meso, Piezoelectric	-	113, 183, 281	Different Proof Mass
	Tadesse [132]	Meso, Hybrid	-	19.38, 175, 265	Multiple Vibration Modes of a Cantilever
	Liu [133]	MEMS, Electromagnetic	-	1285, 1470, 1550	Multiple Vibration Modes of a Resonator
	Liu [134]	MEMS, Electromagnetic	-	840, 1070, 1490	Multiple Vibration Modes of a Resonator
	Liu [135]	MEMS, Electromagnetic	-	189, 280, 348, 379, 382, 406, 479, 563, 662	Combination of Three Multi-modal Structures
	Wu [137]	Macro, Piezoelectric	-	17.4, 19.6	Two degrees-of-freedom System
	Tao [138]	MEMS, Electromagnetic	-	326, 391	Two degrees-of-freedom System
Nonlinear Energy Harvesters	Mann [140]	Macro, Electromagnetic	12.2	2.2	Magnetic Levitation System (at 0.84g).
	Stanton [141]	Macro, Piezoelectric	23.5	10	Mangetic Interaction – Hardening Configuration (at 0.4g)
	Liu [142]	MEMS, Electromagnetic	146.5	26.5	Geometric Nonlinearity (at 3g)
	Liu [143]	MEMS, Electromagnetic	383.7	57.7	Stretching Strain Nonlinearity (at 1g)

Mechanism	Reference	Device Scale & Transduction	Peak Frequency (Hz)	Operating Frequency Range (Hz)[1]	Remarks
	Gafforelli [144]	Macro, Piezoelectric	69	6	Stretching Strain Nonlinearity (at 0.5g)
	Marinkovic [145]	MEMS, Piezoelectric	400	240	Stretching Strain Nonlinearity (at 63g)
	Nguyen [146]	MEMS, Electrostatic	556	31	Geometric Nonlinearity (at 0.135g)
	Hajati [147]	MEMS, Piezoelectric	2750	350	Stretching Strain Nonlinearity (1V driving voltage)
	Nguyen [155]	MEMS, Electrostatic	400	587	Bistable Buckling Force (at 0.208g)
	Kaur [158]	MEMS, Electrostatic	670	40	End Stop Nonlinearity (at 0.5g)

Table 2.2: Comparative study of different wideband techniques reported for VEH devices.

[1]Operating frequency range – Tuning range for resonance frequency tuning; Peak frequencies for multi-frequency generators; Half-power bandwidth for Nonlinear generators.

2.4. MEMS based Electromagnetic Energy Harvesters:

Electromagnetic (EM) energy harvesters have the advantages of low output impedance and high output current levels, but the micro-scale implementation is found to be challenging. It is a well-known fact in MEMS that surface related phenomenon have a favorable scaling effect as compared to volume related effects [159]. This is due to the fact that surface (S) scales as the square of length (L) whereas volume (V) scales as the cube of length. Therefore, as L decreases, its S/V ratio increases. Unfortunately the strength of a magnetic flux depends on its volume, even though the magnetic flux density available from a permanent magnet is independent of its size. Therefore electromagnetic force is less favorable to scale down compared to electrostatic or piezoelectric forces [159]. There are a number of reported works that have already demonstrated the effect of

scaling laws on the performance of EM generators [160-162]. Arnold [162] derived the power scaling law for an oscillatory linear EM generator as

$$P \propto \frac{L^7 Z^2}{L^2 + 1} \tag{2.5}$$

where Z is the base acceleration. Two asymptotic relations are obtained due to the summation in the denominator.

$$P \propto L^5 Z^2 \; for \; L \to \infty \tag{2.6}$$

$$P \propto L^7 Z^2 \; for \; L \to 0 \tag{2.7}$$

Arnold also explained that if electrical damping dominates over mechanical damping, the power scales according to equation (2.6) whereas if electrical damping is dominant then the power scales according to equation (2.7). By comparing the dimension of the two damping terms, it was concluded that at very small scale the mechanical damping will be dominating and electrical damping will dominate at very large scale. Hence, the power output from a MEMS scale oscillatory generator is restricted by large mechanical damping as the mass and velocity decrease. This indirectly owes to the inability to produce large electromagnetic coupling at the MEMS scale. The advances in MEMS technology have resulted in a variety of micro-fabricated structures that can be coupled with permanent magnets in order to develop miniaturized MEMS based EM VEH devices. But practical implementation of a MEMS based micro-power generator involves a number of challenges like the realization of multiple-turn coils and permanent magnets using MEMS techniques.

Most attempts to incorporate permanent magnets using microfabrication techniques such as sputter deposition [163-164], electrodeposition [165-166] or magnetic powder bonding [167-170] in EM VEH have resulted in very low output power (few pW - nW) level. Jiang et. al. [163] reported a fully MEMS EM device by bonding a vibrator with embedded micro-magnets and a stator with integrated micro-coils. The micro-magnets are fabricated by using sputtering deposition of NdFeB/Ta multilayered magnetic films with a thickness of 10 μm. A schematic diagram of the device is shown in Fig. 2.26. The maximum power output of the energy harvester at 115 Hz is approximately 12 nW at an input acceleration of 1.17g. Han et. al. [165] reported an in-plane moving MEMS EM generator where CoNiMnP hard magnetic alloy is electroplated onto the vibration plate instead of manually assembling bulk magnets. The in-plane device (Fig. 2.27) with integration approach condenses the device's volume to 67.5 mm^3. The proposed structure

with an integrated magnet array can generate 11.2 nW maximum output power at a frequency of 48 Hz with a matched load of 15.8 Ω.
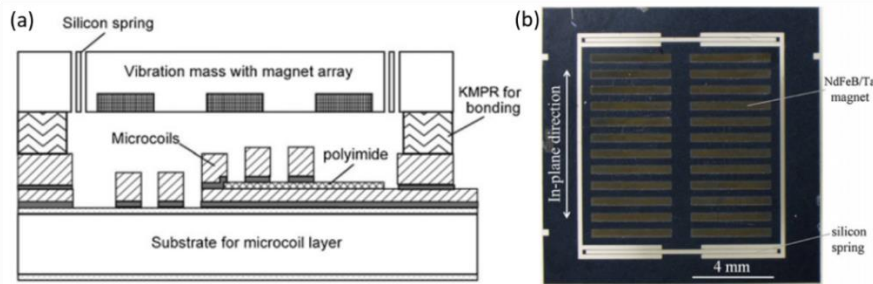
Fig 2.26: (a) Structure of the sputtered magnet EM energy harvester [163]. (b) Micrograph of the vibrator layer with integrated micro-magnet array and silicon micro-springs.
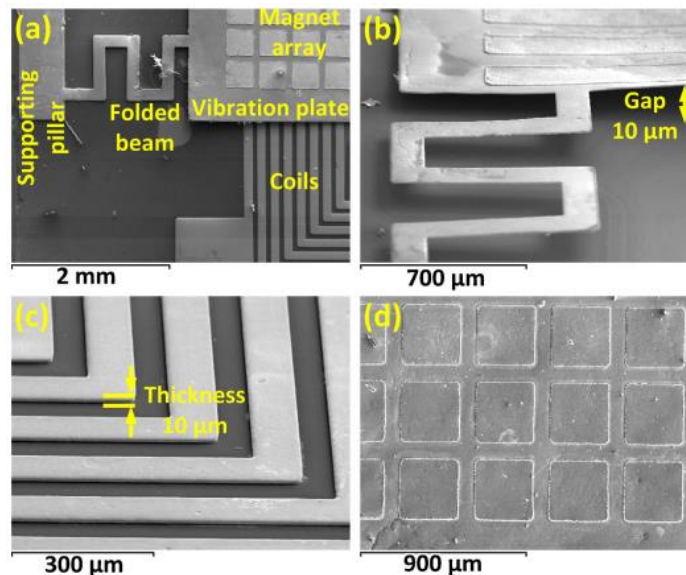
Fig. 2.27: SEM images of the fabricated fully MEMS device [165] (a) top view of the device, (b) the folded beam and 10 m gap,(c) the electroplated copper coil, and (d) the electroplated CoNiMnP magnet array.

Wang and Arnold [167] reported three different designs of integrated EM harvester that utilize embedded NdFeB powder micro-magnet technology whereas a PDMS diaphragm acts as the resonator. The structures with among the smallest volume (4 – 15 mm^3) magnetic generator reported to date, produce very little load power even at a reasonably high acceleration. A novel fully integrated micro-scale EM device using micro-patterning of bonded magnets was reported by Tao et. al. [168]. The magnetic material utilized is a polymer composite, consisting of a commercially available NdFeB powder dispersed in epoxy. The prototype (20 mm³), which is shown in Fig. 2.28, is fabricated using UV-LIGA technology and microelectroplating technology. The fabricated device can generate

a maximum peak-peak voltage of 20.9 µV at the device's resonance frequency of 365 Hz and input acceleration of 1g.
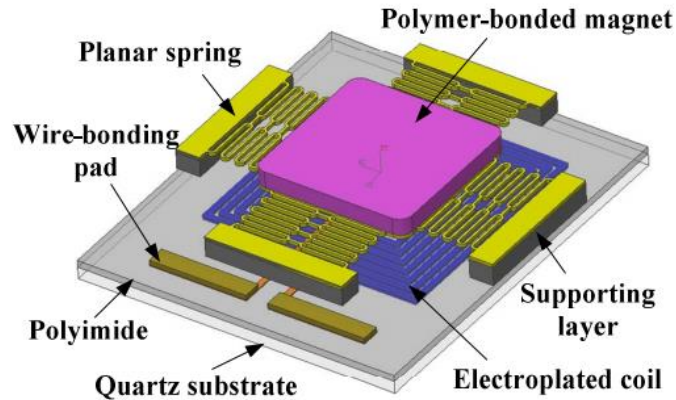
Fig. 2.28: Schematic of the device with micro-patterned, NdFeB powder bonded magnets [168].

In other approaches, the micro-coil is integrated on to the moving silicon paddle which experiences a varying magnetic field due to the relative motion with respect to static NdFeB bulk magnets [133-135, 138, 142-143, 171-172]. The output power is also found to be low in such cases due to poor magnetic flux linkage and smaller proof mass. Liu et. al.. [142] reported a micro-scale ultra-wide bandwidth device (Fig. 2.29) where nonlinear effects from different vibration modes are utilized to produce a wideband output. In spite of the wideband nature, the peak output power from the device is significantly low due to the above mentioned reasons.

The same group from the National University of Singapore has reported a number of other topologies [133-135, 143], where in spite of the interesting device dynamics, the final output power is quite low due to the above mentioned drawbacks. Recently, Zhang et. al. [171] developed two micro-fabricated devices (one with a coil proof mass and the other with a magnet proof mass) suspended by silicon springs, as shown in Fig. 2.30(a) and Fig. 2.30(b). Rapid spatial variations of magnetic field are produced by alternately polarized NdFeB magnet array, and are coupled and aligned to an array of multiple-turn spiral coils. Experimental results show that the energy harvester with a coil proof mass generates an induced peak-peak voltage of 18.2 mV with 0.75 µW power output (into 13.8 load) when it is vibrated at 410 Hz with a vibration amplitude of 6.7 µm (corresponding to 4.5 g acceleration). The other device with a magnet array proof mass generates a voltage of 16.8 mV with 0.82 µW power output (into 10.8 load) when it is vibrated at 350 Hz with a vibration amplitude of 9.1 µm (corresponding to 4.5 g acceleration).
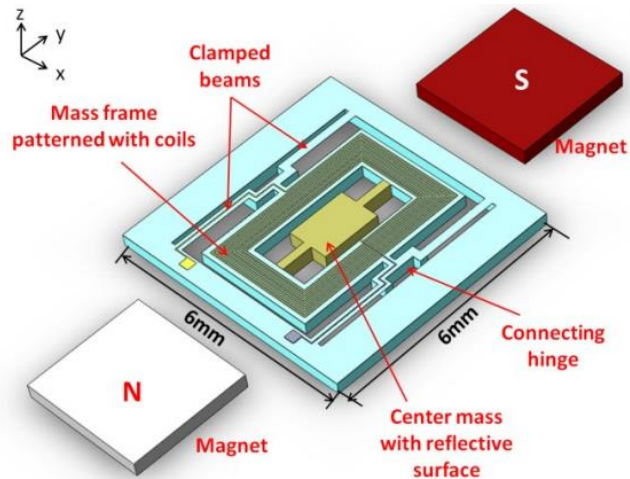
Fig. 2.29: Schematic of the ultra-wide EM generator reported by Liu et. al. [142].
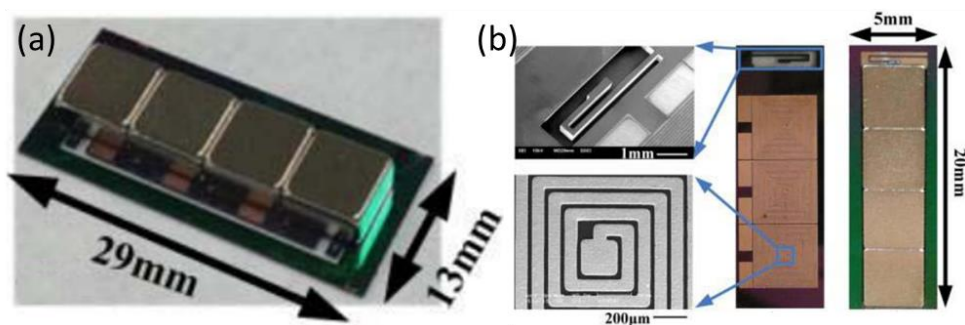
Fig. 2.30: (a) The fabricated VEH device with coil proof mass. (b) Photos of front side and backside of the fabricated EM harvester with magnet proof mass [171].

Another key element for efficient EM transductions is the micro-fabricated pick-up coils. Liu et. al. [142] reported in-plane moving EM harvesters where two layers of aluminum coil are sputtered onto the movable silicon structure. A similar sputtered, double layer coil is used in other works as well [133-135, 143]. Recently, Tao et. al.. [138] have used a planar Cr/Au sputtered coil (350 nm thick). The thickness of the sputtered metallic layers is normally small due to the slow deposition rate and reported sputtered metals such as Al or Au has higher resistivity than copper. Eletroplated planar copper coils were previously used [171-172] as opposed to sputtered coils in order to develop thick conducting layers. Zorlu et. al. [173] reported electroplated double layer copper coils with each layer having 41 turns, integrated on a parylene cantilever. A smaller proof mass in the developed structure resulted in a high (> 1 kHz) resonance frequency. Other than low Young modulus polymer materials like parylene [129, 173] and PDMS [167, 174], researchers have exploited other materials for developing the resonating spring in a MEMS compatible process. These include an electroplated Ni spring [175-176], and wet-etched copper foil [177] to name a few. It can be concluded from this review is that high flux linkage through proper configurations of magnet and coil, along with development of

suitable MEMS components, are essential to improve the performance of micro-electromagnetic energy harvesters.

Table 2.3 summarizes the performance parameters of all the different MEMS EM generators discussed so far. Again, like Table 2.1, the NPD metric is used for comparison. However, there are a number of devices which are wideband or multi-frequency. Hence it is not perfect to compare the peak output power for them as a significant amount of power is generated over a wideband. But for initial comparison, still the NPD parameter is considered.

Reference	MEMS Component	Volume	Input Acceleration (g)	Frequency (Hz)	Output Power (μW)	NPD (kg.s.m^{-3})
Jiang [163]	Fully MEMS	0.1	1.17g	115	1.2×10^{-4}	8.8×10^{-7}
Tanaka [164]	Fully MEMS	0.08	15.79g	100	12×10^{-3}	6.01×10^{-6}
Han [165]	Fully MEMS	0.0675	1.2g	48	11.2×10^{-3}	1.2×10^{-3}
Han [166]	Fully MEMS	0.0125	1g	64	3.75×10^{-4}	3×10^{-4}
Wang [167]	Fully MEMS (PDMS membrane)	0.014	1g	530	2.3×10^{-5}	1.64×10^{-5}
Tao [168]	Fully MEMS	0.02	1g	365	-	-
Zhang [169]	Fully MEMS	0.22	6.31g	400	0.55×10^{-3}	6.28×10^{-7}
Miki [170]	Fully MEMS	0.1	1.7g	94.9	0.76×10^{-3}	2.63×10^{-5}
Liu [143]	MEMS spring & coil	0.158	1g	383.7	0.59×10^{-4}	3.73×10^{-6}
Liu [142]	MEMS spring & coil	0.032	3g	146.5	2×10^{-3}	6.9×10^{-5}
Liu [133]	MEMS spring & coil	0.032	1g	840	5.5×10^{-3}	1.7×10^{-3}
Liu [134]	MEMS spring & coil	0.036	1g	1285	16×10^{-3}	4.4×10^{-3}
Tao [138]	MEMS spring & coil	0.29	0.12g	391	0.96×10^{-3}	2.3×10^{-3}
Zhang [171][1]	MEMS spring & coil	0.67	4.5g	410	0.75	6.01×10^{-4}
Zhang [171][2]	MEMS spring & coil	0.09	4.5g	350	0.82	4.5×10^{-3}
Kulkarni [172][3]	MEMS spring & coil	0.1	1g	9830	23×10^{-3}	2.3×10^{-3}
Sari [129]	MEMS spring (parylene) & coil	1.4	~60g	4500	0.4	7.93×10^{-7}
Zorlu [173]	MEMS spring (parylene) &	0.17	1g	10	18.5×10^{-3}	1.1×10^{-3}

Reference	MEMS Component	Volume	Input Acceleration (g)	Frequency (Hz)	Output Power (µW)	NPD (kg.s.m^{-3})
	coil					
Khan [174]	MEMS spring (PDMS)	2.25	3g	108.4	68	33.6×10^{-3}
Wang [175]	MEMS spring (electroplate nickel) & coil	0.31	0.8g	280.1	21.2	1.06
Dai [176]	MEMS spring (electroplate nickel) & coil	0.11	0.8g	180	-	-
Khan [177]	MEMS spring (etched copper foil) & coil	1	13.5g	371	10.7	5.87×10^{-4}

Table 2.3: Comparative study of different wideband techniques reported for VEH devices.

[1]Coil proof mass; [2]Magnet proof mass; [3]Prototype B
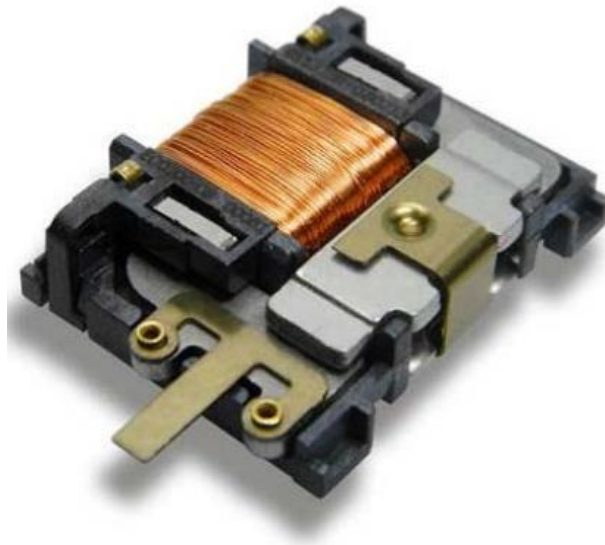
Fig. 2.31: EnOcean energy harvester ECO 200 [178].

2.5. Commercially Available VEH Products:

Vibration based energy harvesting have been recognised as one of the promising topics due to its potential to power low-power electronic devices. During the last years, different harvesters have been designed not only for academic research but also by a number of

industrial companies for a range of specifically selected applications. Probably the best known harvester is the device of EnOcean GmbH [178] that is usually installed into light switches. The device (Fig. 2.31) harvests energy (typical energy output 120-210 μJ at 2V) for sending three radio telegrams when the switch is pressed and allows a plug-and-play switch design.
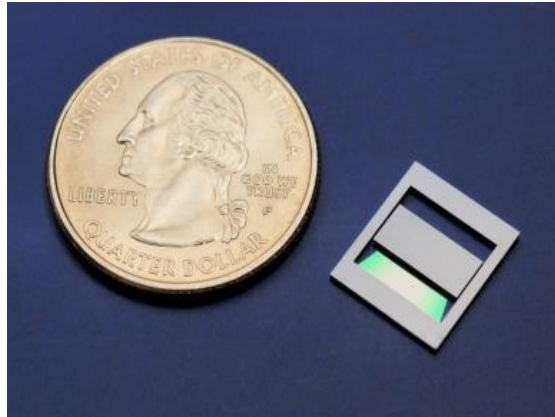
Fig. 2.32: Microgen Piezo-MEMS VEH device [180].
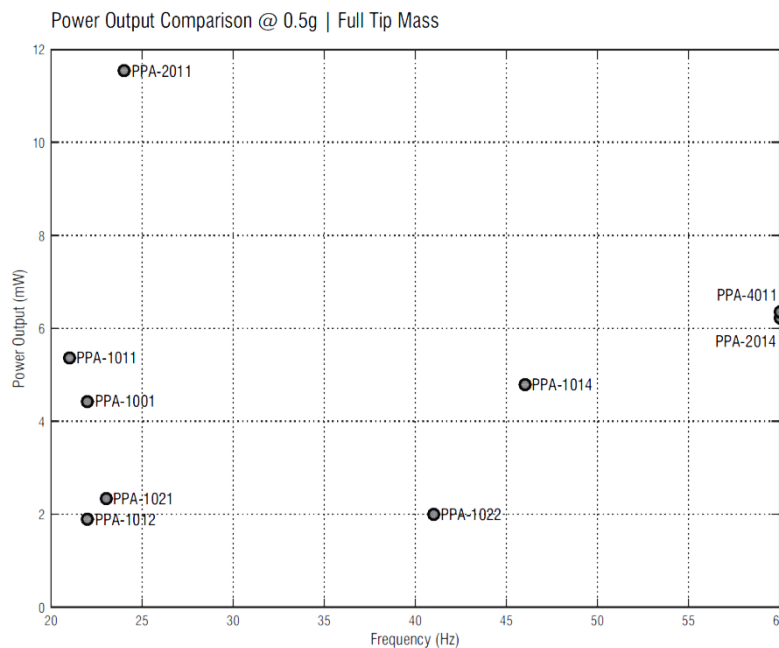
Fig. 2.33: MIDE PPA products comparison in terms of output power when tuned to 60 Hz [181].

Perpetuum Ltd. [179], a spin-off company from the University of Southampton, has specialized in developing linear EM generators for a number of low frequency applications including rail sensor nodes and industrial WSNs. According to their claim, the energy harvesters are designed to last over 100 years without maintenance, and the sensor nodes 20 years, easily outlasting other battery-only powered systems. The low frequency (25, 30, 50, 60, 100, 120 Hz respectively) harvesters are quite bulky (mass = 1

kg) including some basic power conditioning circuits and are capable of generating high output power at two standard output voltages (5V and 8V).

Microgen Systems has specialised in Piezo-MEMS generators (Fig. 2.32) having a volume of 1.2 cm^3. They have three different 'BOLT' family products [180] operating at 100 Hz, 120 Hz and 500 Hz respectively. Each of the devices can generate an open circuit AC output of >15V and optimal output power of 75 μW at <0.1g acceleration. The devices use an AlN piezoelectric layer for power generation.

Mide Technologies PPA standard products [181] utilize the piezoelectric PZT 5H to convert mechanical energy in the form of vibration or shock into electrical energy. All of the PPA products can be tuned to a wide range of frequencies by changing the tip mass. Fig. 2.33 compares the power output for each product when there is the maximum tip mass added, which represents the lower limit of the products frequency range if the clamping configuration is not changed.

While all of these products are linear or narrow-band, recently Flexous [182], a Dutch company, developed a wideband nonlinear generator operating below 100 Hz. Their product, HiPER-D, can generate up to 79 mW output power with a DC output voltage between 3.4 – 5.6V. The product uses EM transduction, and weighs only 82 gm.

2.6. Power Management Electronics for Electromagnetic Energy Harvesters:

2.6.1. Introduction: Since the VEH devices generate a time-varying voltage, it needs to be rectified before applying to some battery system or modern sensor devices. Additionally, the constant power and voltage levels may be required under varying load conditions, so power/voltage regulation must also be included in the power electronics. In short, power management is as important as power generation for efficient and effective operation of an energy harvesting module. In addition to efficient performance, the power electronics should be relatively small in size compared to the generator device. Arnold [162] reviewed micro-scale magnetic generators with a brief overview of typical interface circuits and addressed the need for advanced power processing circuits, particularly for low-power and low-voltage applications. Similar conclusions are found in the review of piezoelectric harvesters and their associated interface circuitry by Anton and Sodano [183], emphasizing the importance of complete system optimization. Dicken et. al.. [184]

also reported different power extraction circuits, particularly for piezoelectric generators, and found that the single-supply pre-biasing circuit has the highest power density among the reported topologies. Szarka et. al.. [185] summarizes the state-of-the-art in power electronics circuits within the field of energy harvesting. They pointed out the corresponding challenges as:

− Development of topologies which can start at very low voltage output from the harvester (few to few hundred millivolts).

− Controlling the input impedance of the interface electronics circuit in order to match it with the output impedance of the transducer.

− Improving the conversion efficiencies of switching converters at microwatt power levels.

− Developing power efficient control techniques that optimize harvester utilization using system-level power management concepts.

An important point that is mentioned by Szarka et. al. [185] is that the challenges associated with energy harvesting systems designed for naturally occurring vibrations that are complex, non-sinusoidal excitations whose magnitude and frequency spectrum vary significantly over time require more attention before kinetic energy harvesting can be used as an alternative power source in a wider range of applications.
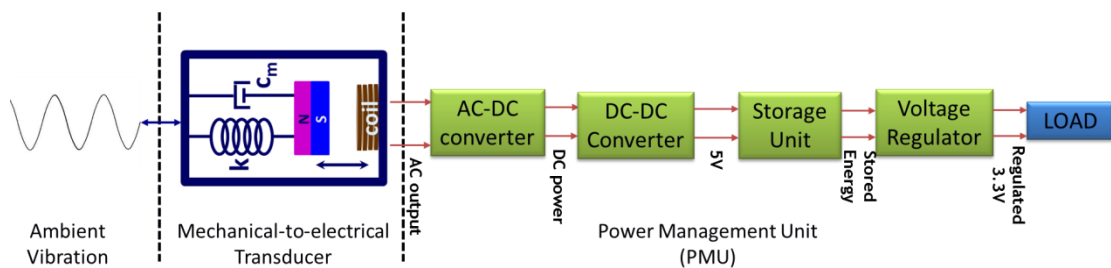
Fig. 2.34: Block diagram of complete energy harvesting system.

The generic block diagram of an energy harvesting system is shown in the Fig. 2.34 which consists of two major components – a mechanical-to-electrical transducer (which is basically the energy harvesting device) and a Power Management Unit (PMU). This shows that not only conversion of power from mechanical to electrical domain is important but also the efficient conversion of raw power from the transducer to usable form is equally important. The term 'efficiency' in the PMU is used in terms of power conversion/transfer efficiency.

2.6.2. Equaivalent Circuit Model of EM VEHs: It is known from circuit analysis theory that maximum power transfer from a DC voltage source to a pure resistive load occurs

when the source resistance is equal to the load resistance. In the case of an AC voltage, the same happens when the load impedance is the complex conjugate of that of the source. An EM generator can be primarily considered as a AC voltage source with some source impedance where the impedance accounts for the coil resistance and inductance and the voltage source represents the time varying EMF generated at the coil as relative motion between magnet and coil occurs. However, the actual representation of energy harvesters is not as simple as that. This is because the source impedance is directly dependent on the type of the harvester and on the operating condition which changes continuously. Hence, matching the harvester output impedance under all operating conditions is extremely difficult. Besides that the impedance of vibration driven harvesters are also linked to the mechanical characteristics of the device like damping, spring stiffness, mass, etc. Typically, the generated voltage from EM VEH devices are low (few mV to few V) compared to that of piezoelectric or electrostatic (few to tens of V) ones. While the sources impedance of EM VEHs ($< 10 \text{ k}\Omega$) are significantly low compared to that of other counterparts ($\geq 100 \text{ k}\Omega$). Hence to model the input of the PMU efficiently, a number of equivalent circuits of VEH devices have been reported in the literature. Two different configurations of equivalent circuits have been demonstrated for EM VEH devices based on second order spring mass damper approximations.
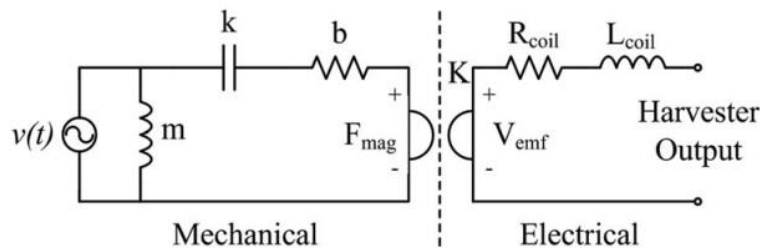
Fig. 2.35: First equivalent circuit of EM energy harvesters [185-186].

In the first circuit [185-186], a series connection of a resistance (b - damping) and a capacitance (k - spring constant) model the most significant effects. The series connection in the mechanical domain is preceded by a parallel connection of voltage source v(t), representing the velocity and a inductance (m – proof mass). As shown in Fig. 2.35, the mechanical and electrical energy domains are a linked gyrator. An ideal gyrator neither stores nor dissipates energy; it serves to interface different energy domains. The portion to the left of the gyrator represents the mechanical domain, and the portion to the right of the gyrator represents the electrical domain.

Another form of equivalent circuit model [53, 126] for EM generator is given in Fig. 2.36. Here the electromechanical transducer is represented by a parallel RLC circuit where the capacitive, resistive and inductive components account for the mass, damping and mechanical stiffness parameters. The input force is modelled using a current source which is dependent on the base acceleration. A load resistance is connected externally to model the harvesting devices, which is not an actual case when the same is interfaced with some load electronics. Instead load resistors overestimate the power which can be actually delivered. Therefore a number of works have been reported in order to develop an efficient power management circuit keeping in mind the different operating conditions of the harvester.
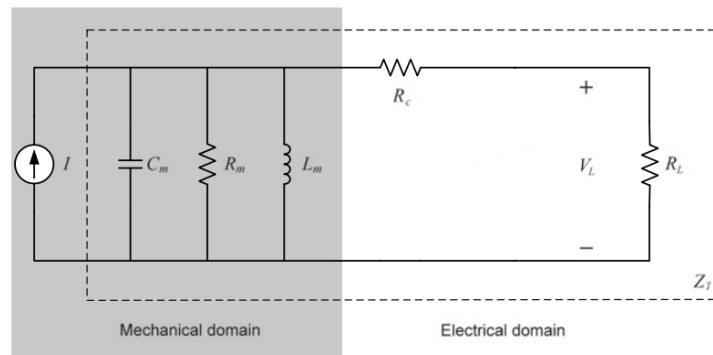
Fig. 2.36: Second equivalent circuit of EM energy harvesters [53, 126].
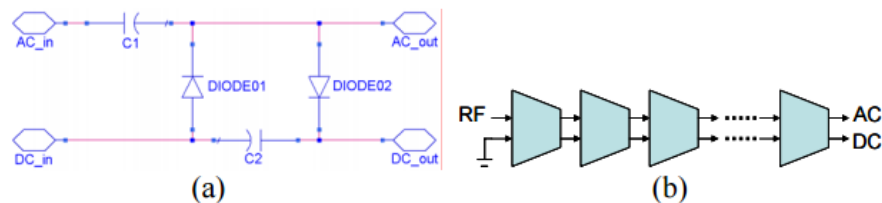
Fig. 2.37: (a) Single Villard voltage double and (b) cascaded Villard voltage multiplier [199].

2.6.3: Reported Topologies: The simplest AC/DC converters that are reported are normally consists of half-wave [187] or bridge [188] rectifier and smoothing capacitors for processing the generated AC signal. Often a step-up transformer is used in order to increase the low output voltage from an EM generator. But the AC/DC conversion efficiency tends to be low as a significant part of the generated power is used to turn on the rectifying diodes. Some works on piezoelectric transducers with relatively high output voltage have reported sophisticated power processing implementations for AC/DC conversion [188-190]. There are a few examples in the literature that combine an electromagnetic energy harvester with customized power electronics for a full system

solution [191-195]. An improved version of the passive rectifier is the gate cross coupled rectifier [196] where a pair of diode connected transistors is replaced with a pair of cross-connected NMOS transistors, which have lower drain-to-source voltage drop (compared to the threshold voltage) which increases the conversion efficiency. In another study, a passive full wave rectifier configuration is proposed which employs the cross connected configuration and a boot-strap rectifier (BSR) in order to reduce the threshold voltage of the diode connected transistors, increasing the conversion efficiency to reach a maximum of 65%. Alternatively, active rectifiers can be used to rectify the AC voltages with a very high efficiency; however, they need an extra battery to power up their internal circuitry [197-198].
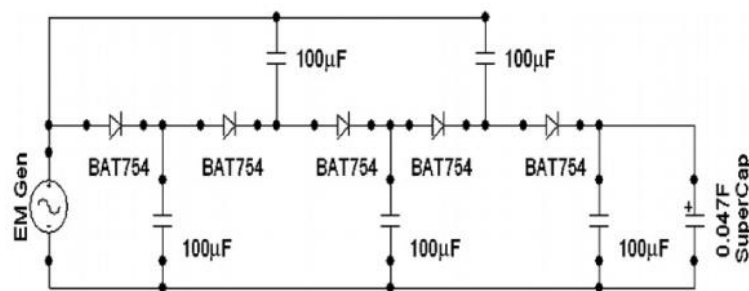
Fig. 2.38: Five stage Dickson charge pump reported by Torah et. al. [200].

On the other hand, to comply with the load electronics or to utilize sufficient efficiency of the power conditioning circuits, the amplitude of the rectifier circuit must also be increased. A common approach is to use a charge pump or voltage multiplier circuit. There are two main configurations of voltage multiplier, namely, the Villard cascade and the Dickson configuration. The circuits operate by charging a capacitor in one half of the AC input cycle and then discharging it into the next stage of the circuit during the second half of the cycle. The number of stages in the circuit determines the multiplication level of the original input signal. Furthermore, the circuit behaves as a rectifier and therefore the final output is DC. In [199], cascading multiple stages of the Villard multiplier (Fig. 2.37) results in a boost of the voltage from the transducer. The advantage of such multiplier circuits over transformers is the ability to step-up without using any magnetic components, which reduces the effects of component parasitics and simplifies the integration techniques. Torah et. al. [200] reported the development and implementation of an energy-aware autonomous wireless condition monitoring sensor system (ACMS) where voltage rectification and multiplication is obtained using a five stage Dickson charge pump (Fig. 2.38). The switching loss is minimized by using Schottky diodes. The

rectified voltage is stored in a super-capacitor. It is found that the regulator tried to operate before the input voltage reached the specified minimum value, resulting in the regulator sinking current from the super-capacitor at a rate that increased with applied voltage. As a result, the voltage of the super-capacitor stops increasing beyond a certain minimum value with the result that the regulator can never switch on properly. To overcome this problem a cold start circuit is used. It consists of a low power voltage detector Torex XC61C (power consumption around 1.4 W) with a specified switching voltage of 2V and an N-channel MOSFET ZXMN2B01F. Due to hysteresis in the switching value of the Torex XC61C, it will not immediately turn off when the super-capacitor voltage temporarily drops below 2V.

Mitcheson et. al. [201] proposed a dual-polarity boost converter to separately process the positive and negative half cycles of the generated voltage. Diode rectification is replaced in the circuit by alternate activation of one of two voltage boost circuits. This is a form of synchronous rectification which avoids a series connection of a separate rectifier and voltage converter. To limit the step-up ratio, the two circuits will provide half the output voltage each. As shown in Fig. 2.39, among the two boost converter sub-circuits, one is configured to produce the top half of the output voltage when the generator voltage is positive and the other is configured to produce the lower half when the generator voltage is negative. As the harvested voltage is small, it is not able to forward bias the parasitic diodes of the MOSFETS. Hence, to prevent conduction in the negative polarity boost converter when the generator voltage is positive, it is enough to hold off the MOSFET of the negative polarity converter. The efficiency of this topology is limited up to 50% due to the power loss of the MOSFET.
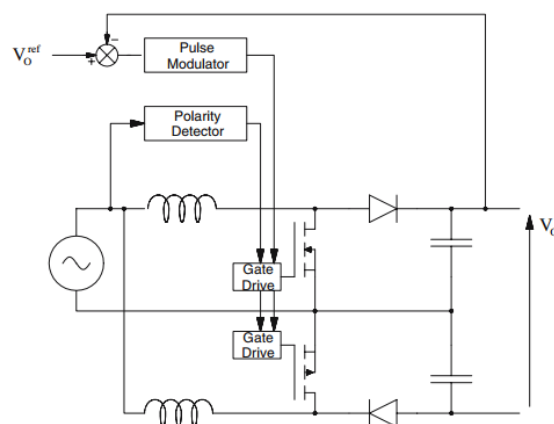
Fig. 2.39: Dual-polarity boost converter, proposed by Mitcheson et. al. [201].

Dayal and Parsa [202] proposed a topology (Fig. 2.40) based on a buck-boost configuration (using a single inductor only, where the main advantage is that the power extracted from the input only) depends on the duty cycle of the converter and not on the load characteristics. The converter uses a bidirectional switch to perform the voltage conversion. As the diodes D1 and D2 in this converter are on the output side, the average current through them is low, resulting in the significantly lowered loss. The converter is operated in discontinuous conduction mode (DCM) to reduce switching losses and to enable simple feedback control. The efficiency of the converter is estimated to be around 61%.
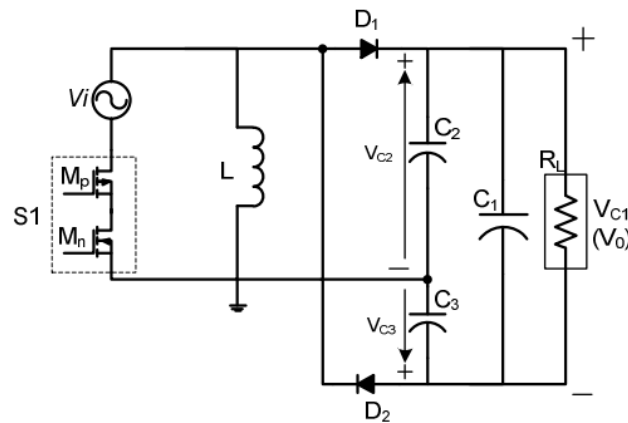
Fig. 2.40: Single inductor buck-boost converter for electromagnetic generators [202].
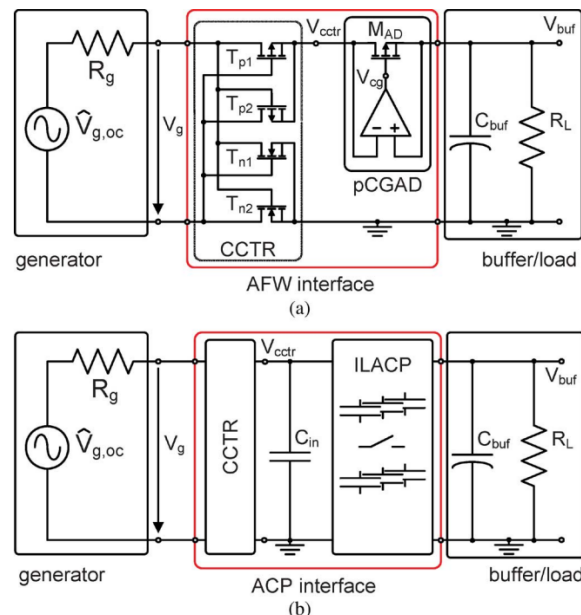
Fig. 2.41: (a) The active full-wave rectifier configuration uses an active diode, (b) the adaptive charge pump interface comprises the input-load adapting charge pump.

For efficient ultra-low voltage rectification, Maurath et. al. [203] introduced ab active full-wave rectifier (Fig. 2.41(a)) that comprises a cross-coupled transistor rectifier and an

active diode, which prevents reverse current flows. To overcome the drawbacks of full-wave rectifiers i.e. limited conduction angle and lack of maximum power point tracking, an input load adapting charge pump (Fig. 2.41(b)) replaces the active diode. The adaptive charge pump interface provides maximum power point tracking by adaptation of its input load. While the active rectifier offers low voltage drops, low complexity and ultra-low power consumption, the adaptive charge pump allows dynamic maximum power point tracking with implicit voltage up-conversion. The active full wave rectifier has the high efficiency of over 90%, over a very wide operation range between 0.5 V and 3.3 V while the adaptive charge pump with dynamic maximum power point tracking has limited efficiency of 48% due to intrinsic charge pump losses. Here it is to be mentioned that a maximum power point tracking (MPPT) circuit is used to increase the harvested power by optimizing the load to extract maximum available power from the device.

Szarka et. al. [204] later developed a fully autonomous circuit for a low power EM generator which can start up at zero energy storage. Zero-energy start-up is provided by a passive voltage multiplier circuit that is automatically disconnected when the active power converter circuit becomes operational. The main power converter is a nonsynchronous full-wave boost rectifier, as shown in Fig. 2.42, which provides rectification and voltage boosting in a single stage. The parasitic coil inductance, which is considered to be negligible at the mechanical resonance frequency, is significant at the switching frequency of the power converter and is used to eliminate the need for an additional boost inductor. The proposed circuit also uses MPPT to control the input impedance of the converter, preserving maximum output power. Consequently, near-optimum damping conditions for the energy harvester are maintained independently of variations in the output voltage, the conduction mode, and the excitation magnitude. A harvester utilization of up to 89% is achieved through the proposed circuit, which leads to an overall system effectiveness up to 70%.

The purpose of the above review is to highlight the current trends in power management electronics for electromagnetic energy harvesters. One thing which is clear from the above discussion is that efficient voltage rectification and step-up of the generated voltage is a key challenge for electromagnetic transducers because of the low AC output voltages (typically mV order) from the harvester. A generic problem with energy harvesters is that not always sufficient energy is available from an energy storage device to start the voltage regulation circuit properly. Hence, a cold start circuit is needed for low energy conditions.

On the other hand, a maximum power point tracking circuit with boost converter can possibly optimize the load condition at steady state under varying operation conditions. However, an efficient combination of all of these components is not much reported in the literature.
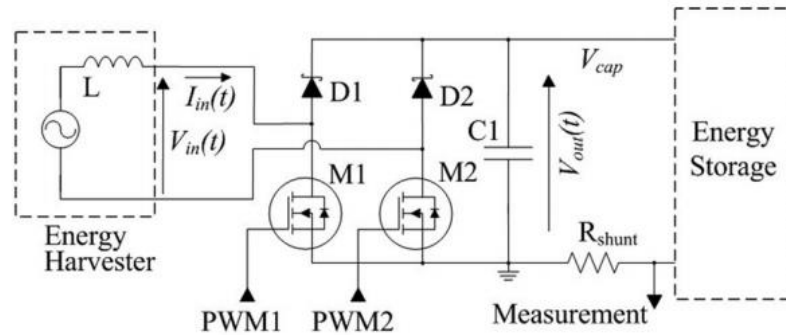
Fig. 2.42: Circuit schematic of a nonsynchronous, full-wave boost rectifier that uses the parasitic coil inductance as the boost inductor.

2.7. Conclusions:

This chapter has reported the state-of-the-art literature in the vibration energy harvesting field with particular emphasis on EM generators. While earlier reported generators are mostly resonant or low frequency non-resonant using various transduction mechanisms like electromagnetic, piezoelectric and electrostatic, the miniaturization of the devices has remained an open problem in this field. This is due to the fact that power density drops drastically with scaling. This problem is significant for EM devices due to unfavourable scaling effects. Additionally, the challenges faced in integration of EM transducers due to presence of permanent magnets and the requirement for a high efficiency micro-coil have evoked a significant number of research works. Thus devices with different sizes (macro, meso and MEMS scale) have been reported.

To operate the device over wide range of frequencies, a number of approaches have been undertaken like resonance frequency tuning, multi-frequency generator development and nonlinear energy harvesting. Among these, nonlinear techniques are attractive as comparatively large bandwidth can be obtained from a single device without any external supply of energy as in the case of resonance frequency tuning. Multi frequency generators are suitable only if discrete frequency peaks are available in the operating environment. However, nonlinear oscillator based devices also suffer from the disadvantage of multi-stability where a number of steady states with different output amplitudes are available

over a certain frequency range. Thus practical implementation of nonlinear generators is still a question.

On the other hand, efficient power management of the harvester is equally important for overall improvement of the system. Particularly for EM harvesters where the generated voltage is low, AC/DC conversion is a major concern. Along with that, the start-up problem and optimal performance at steady state need to be addressed in the future.

Chapter 3

Theoretical and Experimental Techniques

3.1. Introduction:

This chapter describes the different theoretical and experimental techniques that are used throughout this thesis for the design, fabrication and characterization of different devices, materials and systems. In general, the development of EM VEH devices is carried out in three steps. First, the device is designed and simulated to predict the output response and its further optimization. The simulation is carried out in three steps. The mechanical structure of the device is simulated using the Finite Element Method (FEM) analysis software package COMSOL Multiphysics. The electromagnetic behaviour of the designed device is analysed using FEM in the Maxwell Ansoft software package. Different mechanical (stiffness, natural frequency) and electrical (electromagnetic coupling) static parameters are thus obtained through FEM simulations have been used to perform the dynamical modelling of the devices by using numerical solvers in MATLAB. Then, the designed devices are fabricated. In this thesis, devices at two different scales – Meso (1-10 cm^3) and MEMS (<1 cm^3), are reported. Hence the devices are developed in different routes as well. The meso-scale devices are assembled using discrete components like commercially available miniaturized bulk NdFeB magnets (Magnet Sales Ltd., UK), tiny wire-wound copper coils (Recoil Ltd., UK) and fabricated spring structures. The meso size spring structures are fabricated using a Laser micromachining process and the service is outsourced from an Irish based company, ShipCo Circuit Ltd. The Laser micromachining provides better performance in terms of resolution and reduced edge roughness compared to the Computer Numerically Controlled (CNC) machining technique. On the other hand, the MEMS scale devices are fabricated using standard microfabrication techniques using the state-of-the-art Tyndall National Institute cleanroom fabrication facilities. Finally, the fabricated and fully packaged devices are

characterized. The imaging of the different components of the device is performed either under high resolution optical microscope or using Scanning Electron Microscopy (SEM) imaging. The VEH devices are characterized using a permanent magnet shaker. The electrical outputs are recorded using a digital oscilloscope. A detailed description of the experimental setup is given later in the chapter. This thesis also reports the development of high performance hard magnetic material. The material is deposited using the electrodeposition method. The structural and compositional analysis of the material is done using SEM, EDX (Energy Dispersive X-Ray) and XRD (X-Ray Diffraction) techniques, while the magnetic characterization is performed using SQUID (Superconducting Quantum Interference) Magnetometer in a variable temperature platform. In the following sections, all these methodologies are described briefly under three headings – theoretical modelling techniques, major fabrication techniques and major characterization techniques.

3.2. Theoretical Modelling Techniques:

3.2.1. Mechanical Simulation using COMSOL Multiphysics: COMSOL Multiphysics [205] is a finite element analysis (FEA) solver and simulation package for solving different physics and engineering applications, especially coupled or multiphysics phenomena involving mechanical, electrical, magnetic, thermal, acoustic and chemical domains. It covers multi-domain packages like MEMS as well. Over the years, the use of this software package has increased extensively within both academic and industrial worlds. Here, COMSOL Multiphysics is utilized to study the mechanical characteristics of the different designed transducers. Static, eigen-frequency and time-domain problems are mainly solved using the MEMS module of the software package. The software provides an automated solution process where the user provides the geometry, material, boundary conditions and solution conditions. The in-built solvers inside the software provide both graphic as well as numeric outputs. In the following, a step-by-step overview is given to create a 3D design (for a typical case in the reported work, Fig. 3.1).

Insertion of a 3D model: 3D model space dimension is selected from the model wizard. Selection of Physics: The physics of the problem is selected (as an example, Solid Mechanics (solid)). Selection of Study: the study domain of the problem is selected (eigen-frequency, static, time-domain etc). Creating the Work plane: An X-Y work plane is created to draw a projection of the desired geometry. Drawing the Geometry: The

desired geometry is drawn using different default shapes like rectangle, square, circle, polygon, beizer curve, straight line etc and using different Boolean actions. Extruding the Geometry: The work plane is extruded along the z-axis to define the z- or vertical dimensions. Different entities can be extruded for different distances to develop a complicated design. Defining the Material: COMSOL has a built-in library for a large number of materials. Required materials are assigned to the drawn geometries. Setting the Boundary Conditions: Boundary conditions of the problem are defined. The fixed constraint is used to fix different edges, points or domains. Prescribed displacement can be used to set motion in a particular direction. Point/boundary/volume load can be applied to insert mechanical force at different levels. Using the parametric study option, user defined loads can also be inserted. Setting Mesh Operation: The design is divided in a number of meshes for FEM analysis. Computation: The problem is studied to obtain the result.
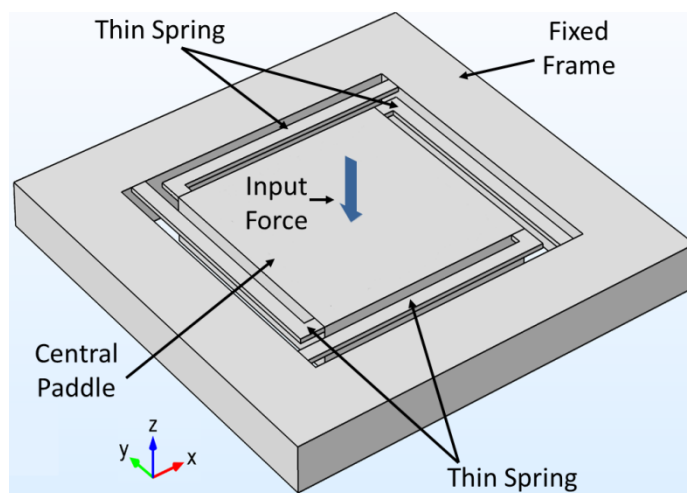
Fig. 3.1: Example of a mechanical structure designed in COMSOL Multiphysics.

The resonance frequencies of different mechanical structures are simulated using COMSOL. Also the force-displacement curves, stress analysis, damped transient studies are performed for the purpose of design.

3.2.2. Electromagnetic Simulation using Ansys Maxwell Ansoft: Ansys Maxwell [206] is an interactive software package that uses finite element analysis (FEA) to solve two- or three-dimensional (2D/3D) electrostatic, magnetostatic, eddy current, and transient parameters. This particular software package is extensively used to design inductors, transformers, electromagnetic motors, actuators, sensors and other electromagnetic and electromechanical devices while using FEM to solve static, time-domain and frequency-

domain electromagnetic and electric field problems. Like COMSOL, the advantage of Maxwell is its automated solution process which requires the user only to specify the geometry, materials and other design parameters. Maxwell automatically generates an appropriate mesh for solving the problem. In the following, a step-by-step overview is given to create a 2D design (as a typical case in the reported work, Fig. 3.2).
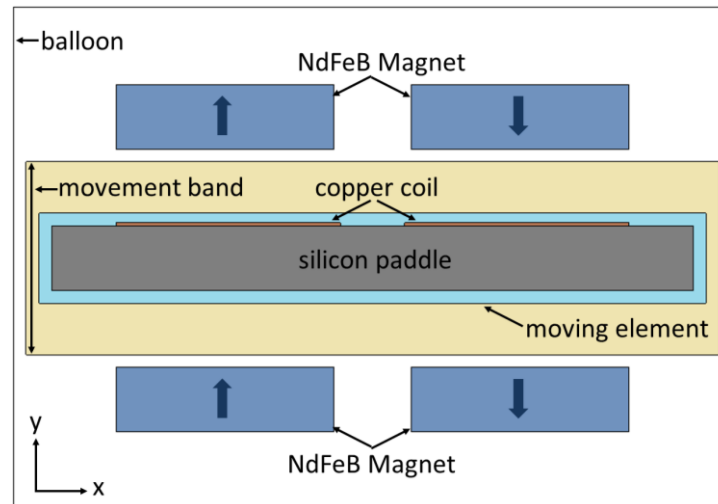
Fig. 3.2: Example of electromagnetic 2D model designed in Maxwell Ansoft.

Insertion of a 2D design: An X-Y plane graphic interface is used to create a 2D design. Setting solution type to transient: This is done in order to perform a time dependent solution. Setting solution depth: This defines the dimension of the design in the perpendicular or z-direction. Drawing magnet and coil designs: The design is created using different drawing tools with specific dimensions and location. Assigning coil and magnet materials: This step is used to choose the coil and magnet materials. Copper is chosen as the coil material in all cases whereas NdFeB is used as the magnet material in most cases unless otherwise stated. The orientation of the magnet is specified by modifying the coercivity vector. Defining the number of coil turns and polarity on each side: The polarity on each side of the magnet is used to specify the direction of current flow in the coil. The number of coil turns (n) is also defined at this stage. Adding winding to the coil and define coil resistance: The coil windings are set to stranded for voltage properties and coil resistance is defined. Defining the movement band: The movement band defines the limit of the displacement of the moving element. Either magnet or coil can be included within the moving band. As only one moving object is allowed inside a moving band, two sides of a moving coil or different moving magnets must be included inside another enclosure to define a single moving element. Creation of balloon: A

rectangle is drawn around the complete design as a boundary known as a balloon. All results and properties of the design such as magnetic field vectors will be calculated and shown inside this boundary. Setting eddy effects: This step is used to analyse the eddy current effects of the designed structures. Setting analysis setup: simulation run time is selected in this step. Setting Mesh Operation: The design is divided into a number of meshes for FEM analysis. Setting coil motion properties: The direction and expression for coil movement is defined and the limits to the displacement are also set. Running validation check: This step is required to make sure that all necessary steps have been carried out prior to analyse the problem. Analysing all: simulation is performed to obtain the result.

Mainly the flux linkage co-efficient is derived from Maxwell simulation by calculating displacement and flux linkage over the simulation time and calculating their slopes.

3.2.3. Numerical Simulation in MATLAB using ode45 Package: This routine uses a variable step Runge-Kutta Method to solve differential equations numerically [207]. The generalized code for ode45 integration is

[t, y] = ode45(odefun, tspan, y0), where tspan = [t0 tf]

which integrates the system of differential equations y'=f(t,y) from t_0 to t_f with initial conditions y_0. Each row in the solution array y corresponds to a value returned in column vector t. This method is widely used for numerically solving first and second order differential equations. The backbone of this algorithm is Runge Kutta 4th order (RK4) solver. Let us consider the generalized initial value problem

$$\dot{y} = f(t, y), \qquad y(t_0) = y_0$$

where y is an unknown function of t. Considering h (h>0) as the step size in the RK4 algorithm, the approximated solution can be written as

$$y_{n+1} = y_n + \frac{h}{6}(k_1 + 2k_2 + 2k_3 + k_4) \text{ where } t_{n+1} = t_n + h \tag{3.1}$$

For n=0,1,2,3,…. Using the following values

$$k_1 = f(t_n, y_n); \quad k_2 = f\left(t_n + \frac{h}{2}, y_n + \frac{h}{2}k_1\right); \quad k_3 = f\left(t_n + \frac{h}{2}, y_n + \frac{h}{2}k_2\right); \quad k_3 = f\left(t_n + \frac{h}{2}, y_n + hk_3\right).$$

Here y_{n+1} is the RK4 approximation of $y(t_{n+1})$, which is determined by the present value plus the weighted average of four increments according to equation (3.1), where each increment is the product of the size of the interval, h and an estimated slope specified by function f on the right-hand side of the differential equation. In averaging the four increments, greater weight is given to the increments at the midpoint. Examples of MATLAB code of the ode45 solver for different differential equations are given in the Appendix section.

3.3. Major Fabrication Methods:

In the following sub-sections, a brief description of the different fabrication techniques is provided for both Meso- and MEMS-scale devices.

3.3.1. Laser Micromachining: Laser micromachining is a cost-effective alternative to lithography and crystallographic etching process for the development of different MEMS devices. A high degree of flexibility, contact- and wear-less machining, the possibility of high automation, as well as easy integration are some of the most attractive features of laser micromachining that allows this tool to be used in a wide field of macro machining processes for many materials including silicon, ceramics, metal and polymer [208]. Depending upon the fineness of the impact caused by the laser, this machining technique can be categorized either as micro- or macro. Normally, a pulsed laser is used for micromachining with a power below 1 kW, whereas a continuous wave laser with several kW power is used for macromachining purposes. A wide variety of lasers can be used for micromachining purposes – from microsecond pulsed (wavelength 9-13 μm) to nanosecond pulsed (wavelength 157-353 nm) lasers are used. Presently, laser micromachining is accomplished using two major techniques [209]: (i) Direct Laser Writing (DLW) using solid state lasers and (ii) Mask Projection (MP) technique using conventional masks and excimer lasers.

DLW [209] is normally used for the so called hard or low sensitivity materials where solid state lasers with galvanometer scan heads are required to machine over the surface. Optimized beam focussing optics is also used to minimize the beam diameter. This method is quite easy and flexible. The design can be easily made in conventional software formats like *.DXF or *.GDS and can be transferred to the equipment. However, speed limitation and limited applicability to the sensitive materials are major concerns of DLW.

Excimer lasers with a shorter wavelength are used for the mask projection (MP) technique. This technique, which is mainly used for sensitive materials, is much like photolithography. The information is written in a transmissive mask and the laser beam is collimated and concentrated before hitting the mask. This process is faster compared to DLW but requires a new mask for each new process making it expensive.
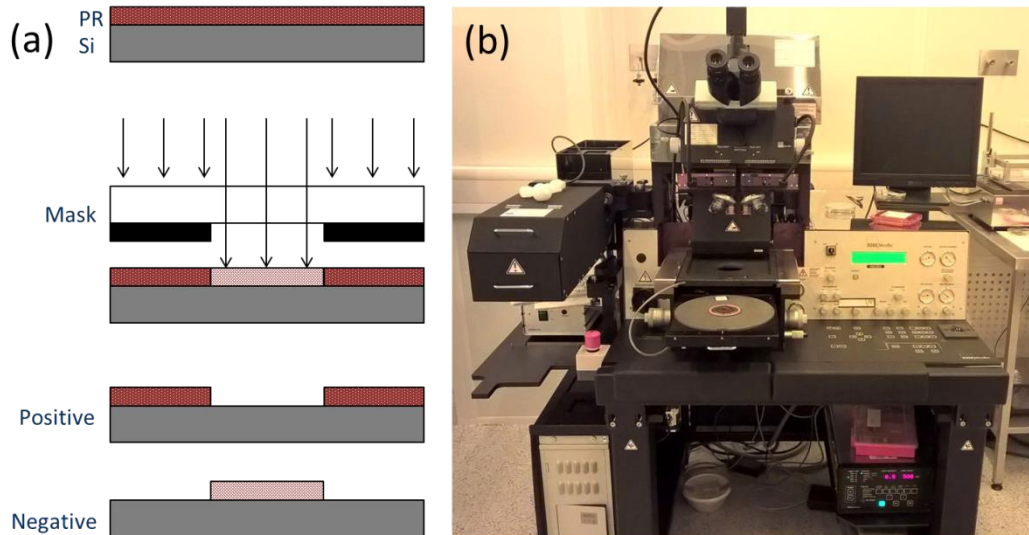
Fig. 3.3: (a) Process flow for photolithography. (b) EV 420 double side mask aligner at Tyndall National Institute.

3.3.2. Photolithography: Photolithography or optical lithography is a common process step in CMOS and MEMS microfabrication which is used to transfer a geometric pattern from a photomask to a light-sensitive chemical, called 'photoresist (PR)', on the substrate [210-211]. This process selectively removes light sensitive (positive PR) or non-sensitive (negative PR) parts of the chemical polymer. The steps of this process are shown in Fig. 3.3 (a). Photolithography shares same operation principles with photography in the sense that the pattern in the etching resist is created by exposing it to light through a photo mask. A single process run of photolithography combines several steps in sequence in a cleanroom environment using automated or robotic wafer track systems to coordinate the process. First the wafer is cleaned using standard wafer cleaning procedures like RCA cleaning [212] to remove the contaminations. Then the wafer is heated to a temperature that is sufficient to remove any moisture that may be present on the wafer surface. The wafer is covered with photoresist by spin coating and the photo resist-coated wafer is then prebaked to drive off excess photoresist solvent. After prebaking, the photoresist is exposed to a UV light through photomask using a mask aligner. The exposure to light changes the PR chemically so that some of the photoresist can be removed by a developer

solution (by analogy with photographic developer). Before developing, the wafer is baked again (post-bake) to reduce the effect of standing waves caused by the destructive and constructive interference patterns of the incident light. For MEMS device fabrication reported later in this thesis, the photolithography is performed using the Electronic Visions EV420 mask alignment system (Fig. 3.3 (b)). This is an H-line system with double-sided mask alignment capabilities and is used for 100 mm (4 inch) wafer processing. This mask aligner has the facility for wedge error compensation (WEC) for better planarity between the mask and the wafer surface. The top side alignment objectives can be changed to a higher magnification (4X) for more precise alignment. The following parameters can be changed: exposure time, side of alignment, separation gap of 6-130µm, proximity gap of 6-130µm, and process type (exposure or bonding). Exposure settings can be soft contact, vacuum contact, hard contact or proximity. The illumination uniformity for a 4 inch wafer is better than ±3%.
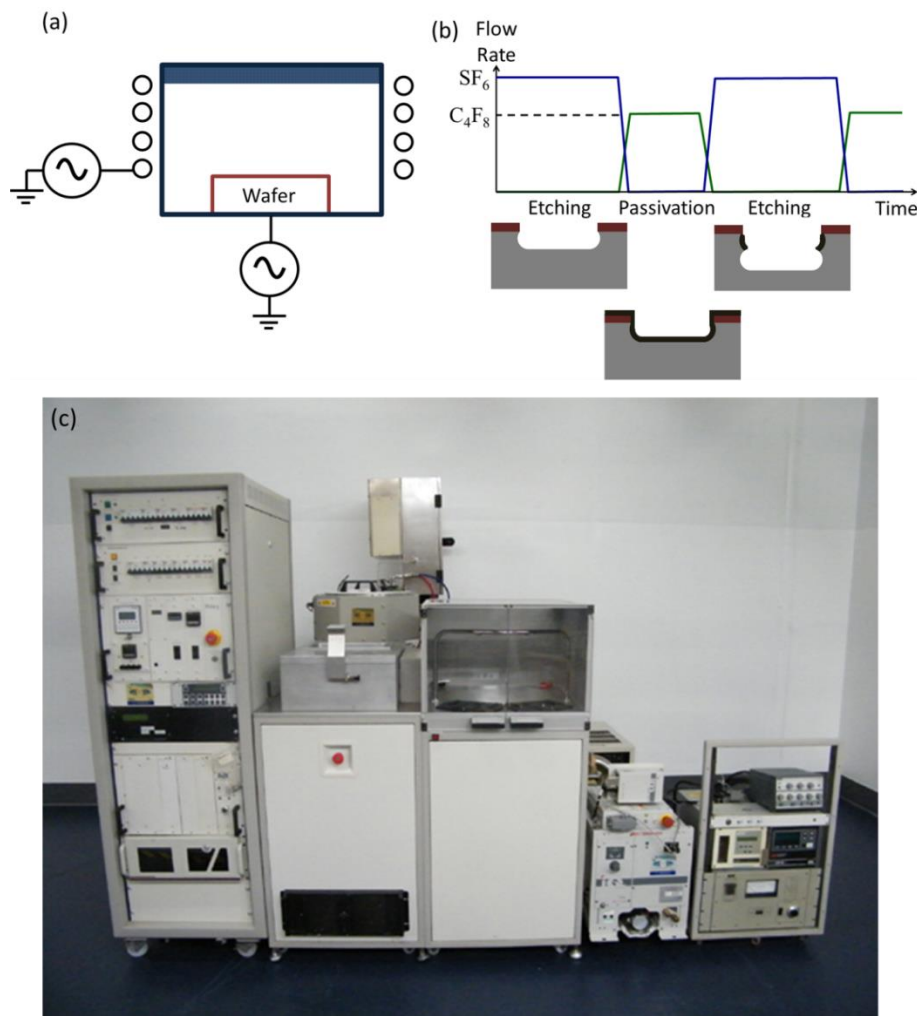
Fig. 3.4: (a) RF chamber. (b) Time multiplexed Bosch etch process. (c) STS ASE Bosch etcher.

3.3.3. Deep Reactive Ion Etching - Inductively Coupled Plasma (DRIE-ICP)/ Bosch Etching:

Creating high aspect ratio deep, flat surface holes and trenches are key for many MEMS applications. Deep Reactive Ion Etching (DRIE) is an anisotropic etching process that is used for those purposes [210]. However, the application space for DRIE extends beyond MEMS and is used also for creating trenches for high-density capacitors for DRAM, for through silicon via (TSV) technology, etc. There are two main technologies for high-rate DRIE: cryogenic and Bosch. But the Bosch process [213] is the most commonly recognised technique. Both Bosch and cryo processes can fabricate 90° (truly vertical) walls, but often the walls are slightly tapered, e.g. 88° (re-entrant) or 92° (retrograde). The Bosch process is also known as pulsed or time-multiplexed etching as two modes of the etching process are alternately repeated to achieve nearly vertical structures. The entire process is done inside a chamber (Fig. 3.4 (a)) where inductively coupled plasma (ICP) is generated through RF coils. The first mode is nearly isotropic plasma etch, where a plasma containing ions of sulphur hexafluoride (SF_6) attacks the wafer from a nearly vertical direction and etch the exposed part of the wafer. Often a thin layer of silicon dioxide is used as the mask layer. The second mode is the deposition of a chemically inert Octa-fluoro-cyclo-butane (C_4F_8) passivation layer. Each phase normally persists for a few seconds (Fig. 3.4 (b)). The passivation layer protects the sidewalls from further chemical attack during the following etch step and prevents further etching. During the etching step, the directional ions that bombard the substrate attack the passivation layer at the bottom of the trench but not much on the sides. Hence, the bombarding ions remove the passivation layer from the bottom and expose the substrate to the chemical etchant. The cycle is repeated a number of times until the desired etching is obtained. For creating thin movable beam structures in MEMS as required in VEH applications, the Bosch etching is a key processing step. The dry etching in the fabrication steps reported later is done using STS ASE Bosch etching instrument (Fig. 3.4 (c)).

3.3.4. Sputtering:

The metal deposition in the fabrication processes reported later are using the sputter deposition technique. Sputter deposition [210-211] is a method of physical vapour deposition for depositing thin films by sputtering material from a target and depositing it on to a substrate kept a few cm apart. Sputtered atoms are ejected by the striking of Ar ions on the target, into a gas phase and tend to deposit on all surfaces of a vacuum chamber. The advantage of sputtering is that a uniform thickness and composition of the deposited film can be maintained. There are low levels of

contamination in the deposited film. The disadvantage of this technique is that it is slow for depositing thick (few microns) films. There are two types of sputtering techniques available, RF sputtering and DC magnetron sputtering (Fig. 3.5).
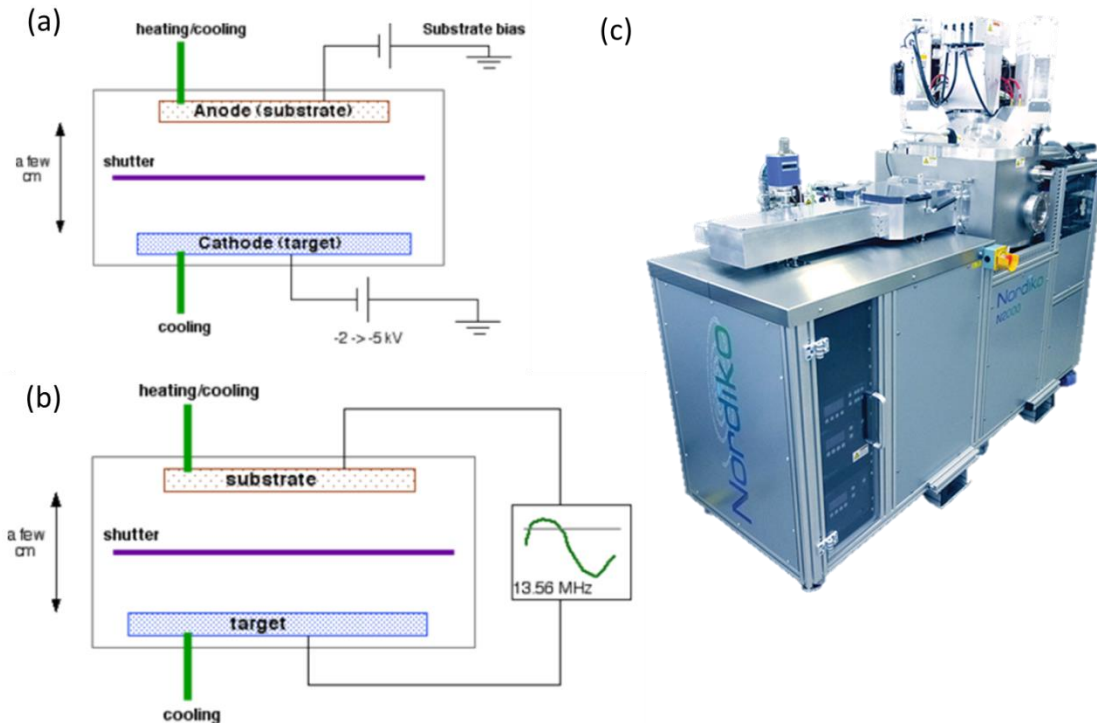
Fig. 3.5: (a) DC Sputtering. (b) RF Sputering. (c) Nordiko N2000 Compact Sputtering System.

In the DC magnetron sputtering technique, the substrate and target are charged using a DC supply in the presence of a magnetic field; this increases the ionization of argon ions, further improving the deposition rates. Here, there has to be a compromise on the maximum number of Ar ions used for striking the target because an increase in Ar ions leads to an increase in collisions between target ions and Ar ions. A positive field is applied to the target plate which acts as the anode and a negative field is applied to the silicon wafers, which act as cathode. For this work, DC magnetron sputtering was used to deposit thin seed layers of copper and titanium on insulated silicon wafers. The process is done using the Nordiko N2000 compact sputtering system in the Tyndall fabrication laboratory (Fig. 3.5 (c)). The disadvantage of DC sputtering is that a positive charge builds up at the cathode with depositing electrons and ions. In order to overcome this problem, a different approach to charging the target and the substrate is required; this is done by RF sputtering. RF sputtering uses an RF source to charge the substrate and the target. The electrons and ions move depending on the charging and discharging of the plasma. The heavy ions cannot follow the quick switching of charges, thus reducing the

number of collisions and leading to lower working pressures for deposition. RF sputtering is used to deposit on dielectric substrates.
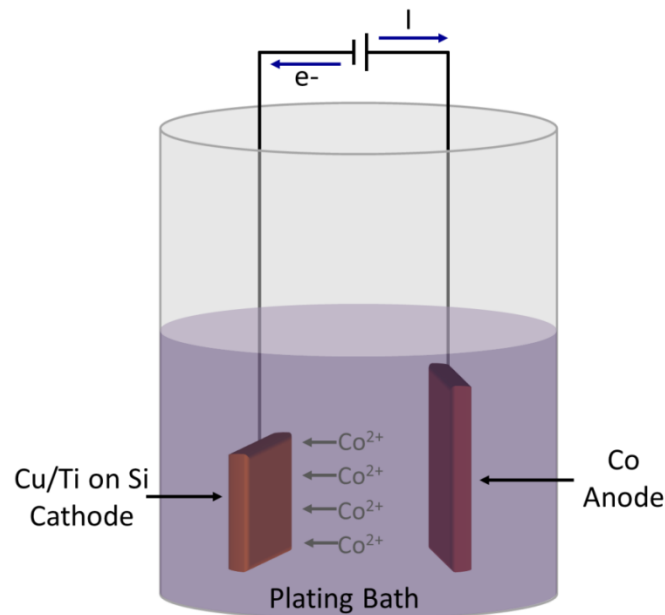
Fig. 3.6: Illustration of the electrodeposition process.

3.3.5. Electrodeposition: Electrodeposition, also called electroplating or electrolytic deposition, is one of the well-known method for deposition of metal or metallic alloy [214]. In this process, the substrate to be plated forms the cathode and the anode is made of the metal to be plated on the cathode. Both electrodes are immersed in a solution called an "Electrolyte" containing one or more dissolved metal salts as well as other ions that permit the ionic flow. A direct current source supplies a current to the anode causing the metal ions in the electrolyte solution to lose their charge and plate out on the cathode. As the electrical current flows through the circuit, the anode slowly dissolves and replenishes the ions in the bath. A schematic of the electrodeposition process is shown in Fig. 3.6. The thickness of the electrodeposited layer on the substrate is controlled by the time duration of the plating and the applied current/ potential. The longer the time the substrate remains in the operating plating bath, the thicker the resulting electroplated layer will be. The thickness depends on the applied current/ potential across the two electrodes as well.

3.4. Major Characterization Methods:

3.4.1. Microstructural Characterization using Scanning Electron Microscopy (SEM) coupled with Energy Dispersive X-Ray Spectroscopy (EDS):
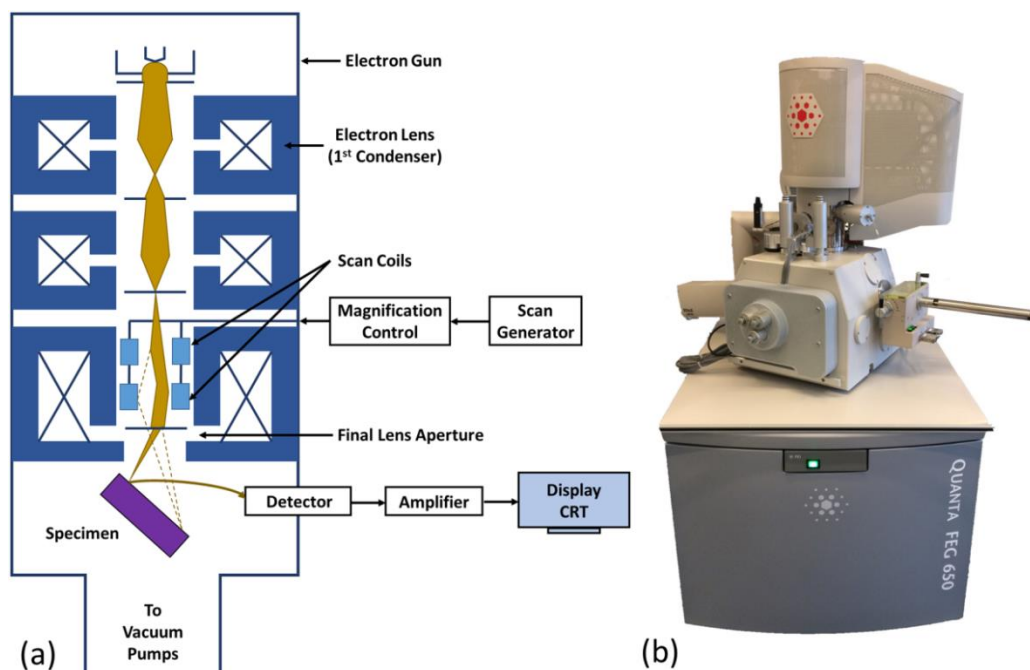
Fig. 3.7: (a) Operation principle of SEM. (b) FEI Quanta 650 SEM.

A scanning electron microscope (SEM) is a type of electron microscope that produces images of surfaces or three-dimensional objects by scanning it with a focused beam of electrons. It is widely used to examine microscopic details of surfaces and sectioned samples and to identify and analyse required features for a wide range of investigation applications. The main components of a typical SEM are electron column, vacuum system, scanning system, detector, and electronics controls [215]. The electronic consoles have control blocks that allow for instrument adjustments such as filament current, accelerating voltage, focus point, magnification, brightness, contrast, etc. As shown in Fig. 3.7 (a), the electron column of the SEM consists of an electron gun which generates free electrons under vacuum, accelerates to high energy (1-40 keV) and focused to a small diameter using two or more electromagnetic condenser lenses to probe small, focused electrons on the specimen. The lower portion of the column is called the specimen chamber. The secondary electron detector is located above the sample stage inside the specimen chamber. Specimens are securely mounted on the stage which is controlled by a goniometer. The stage is capable of undergoing x-, y- and z-directional movement, 360° rotation and tilting for the convenience of the user.

The SEM provides a collimated electron beam under vacuum pressure of $\geq 5\times10^{-5}$ Torr. The high vacuum pressure is needed to control the temperature of the filament as the current passes through it, to maintain a clean environment for the column optics to operate and to ensure that the electrons can reach the sample chamber without any interference from dust particles. Most SEMs can generate an electron beam with a spot size less than 10 nm with a probe diameter in the range of 1 nm to 1 μm and a probe current of pA to μA. Electromagnetic radiation is generated from the surface of the specimen due to accelerated electrons. There are different kinds of signals produced due to the electron's interaction with the sample. In SEMs, an electron source is used instead of light as the illumination source, which improves the resolution considerably compared to conventional microscopes. Due to the nature of interaction between the electron beam and the specimen, a number of signals can be used to gather information from or near the surface of the specimen. In SEM, visual examination of the surface of a sample utilizes two types of signals: (a) secondary electrons (low energy, result of inelastic collision and scattering of incident and specimen electrons). These are used for high resolution inspection of the surface structure (~10 nm). (b) back scattered electrons: (resulting from elastic collision and scattering between incident electrons and the specimen nuclei or electrons). They are generated from the surface of the material and are used to study the topological variations and atomic ratio contrast with a resolution of > 1 μm. Among the other types of signals, the generated x-ray signal from the above mentioned interaction is the only other signal that is used for SEM. The recombination interactions between free electrons and positive electron holes that are generated within the material emit the x-ray signal and it can originate from further inside the surface of the specimen, allowing determination of elemental composition through EDS (Energy Dispersive X-ray Spectroscopy) analysis. This is possible due to the fundamental principle that each element has a unique atomic structure allowing a unique set of peaks on its electromagnetic emission spectrum, which is also the basis for any kind of spectroscopy. Throughout this thesis, the microstructural and elemental analysis is performed using the FEI Quanta 650 SEM instrument which is shown in Fig. 3.7 (b).

The electron microscopy of non-conductive materials is difficult due to charging effect. Hence, those samples are attached to a conductive specimen holder (carbon substrate/ copper tape) or sputter coated with a very thin layer of conductive material (Au, Pt, Pd, their alloys) or carbon.

3.4.2. Microstructural Characterization using X-Ray Diffraction (XRD):

X-ray Diffraction (XRD) is one of the most well-known, non-destructive and rapid analytical techniques [216] which are primarily used for phase identification of a crystalline material and are also used to gather information about unit cell dimensions. The analyzed materials in XRD can be powder, homogenized and average bulk in composition. The XRD technique is based on the Debye-Scherrer method.
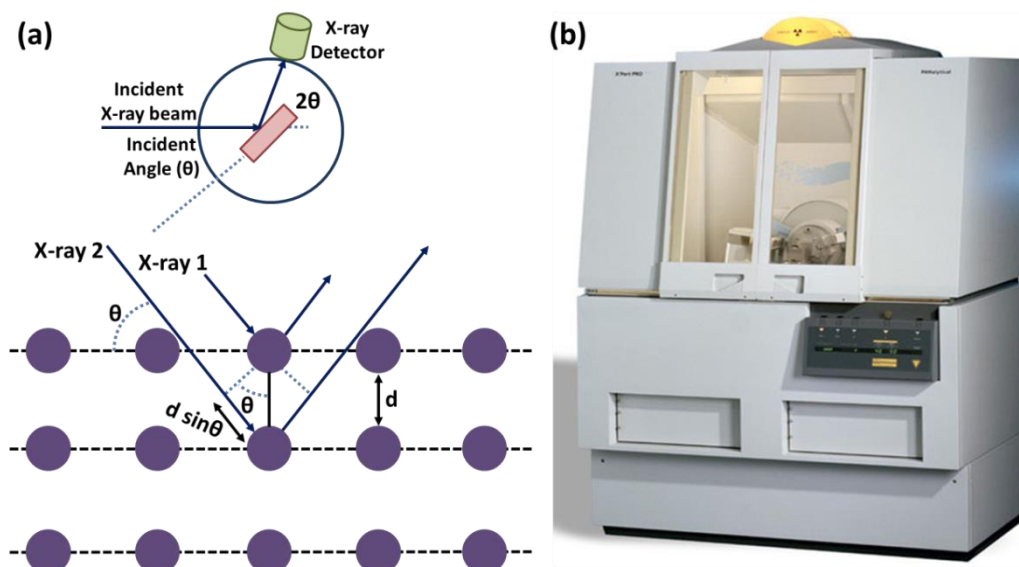
Fig. 3.8: (a) Illustration of the operating principle of X-Ray Diffraction (XRD) method. (b) PANalytical X'Pert Pro MPD X-ray Diffractometer (XRD).

In 1912, Max von Laue, a German physicist discovered that x-rays can be diffracted using an ordered array of atoms in a crystal and thus crystals can be used as a 'diffraction grating' for x-rays. X-ray diffractometers have three major parts: an x-ray tube, a sample holder, and an x-ray detector. The monochromatic radiation of x-rays is generated by a filtered cathode ray tube by heating a filament to produce electrons, which is then collimated and concentrated by applying a voltage, and directed toward the sample. When electrons have sufficient energy to disrupt the inner shell of electrons of the target material, characteristic x-ray spectra are produced. The interaction of the incident rays with the sample produces constructive interference (and a diffracted ray) when conditions satisfy Bragg's Law (Fig. 3.8 (a)). According to Bragg's law, if the spacing between reflecting planes is d and the glancing angle of the incident x-ray beam is θ, then the path difference for waves reflected by successive planes is $2d\ sin\theta$. Hence the condition for diffraction (the Bragg condition) is $n\lambda = 2d\ sin\theta$ where n is an integer and λ is the x-ray wavelength. These diffracted X-rays are then detected, processed and counted. The

sample is scanned through a range of 2θ angles, for all possible diffraction directions of the lattice obtained due to the random orientation of the material. Conversion of the diffraction peaks to d-spacings allows identification of the crystal phase because each phase in a material has unique d-spacings. This is done by comparing the d-spacings with standard reference patterns.

The x-ray spectra consist of several components, the most common being K_α and K_β. K_α in turn consists of $K_{\alpha 1}$ and $K_{\alpha 2}$. $K_{\alpha 1}$ has a somewhat shorter wavelength and double intensity compared to that of $K_{\alpha 2}$. These specific wavelengths are characteristic of the target material. $K_{\alpha 1}$ and $K_{\alpha 2}$ are sufficiently close in wavelength and therefore a weighted average of the two is used. Commonly, x-rays are collimated and directed onto the sample using Cu K_α radiation with a wavelength of 1.5418 Å. The detector records and processes the x-ray signal data and converts it into a count rate which is then output to the user interface. The geometry of the x-ray diffractometers are such that as the sample rotates in the path of the collimated x-ray beam at an angle θ, the detector which is mounted on an arm of the instrument maintains an angle of 2θ with the incident beam. The instrument used to maintain the angle and rotate the sample is termed a goniometer. The count rate output from the measurements is plotted against 2θ, which is called the X-ray diffraction pattern or diffractogram of the material. The diffractograms are unique for every material from which one can analyze the crystallographic structure of the material and characterize them by comparing with diffractograms from known standards databases. For characterization of materials in this thesis, the PANalytical X'Pert Pro MPD X-ray Diffractometer (XRD) instrument is used.

3.4.3. Magnetic Characterization using SQUID Magnetometer: The magnetic property characterization of the developed hard magnetic materials is performed in the Quantum Design Superconducting Quantum Interference Device (SQUID) magnetometer (Field Range: 5T) Magnetic Properties Measurements System (MPMS-XL5). The main components of this measurement system [217] consist of (a) Temperature control system (to precisely control the sample temperature between 1.8 - 800K). (b) Magnet control system (current from a power supply is used to generate a magnetic field between +5T to -5T in the coil). (c) Superconducting SQUID amplifier system (The RF SQUID detector is the most crucial part which provides reset circuitry, auto-ranging capability, a highly balanced second-derivative sample coil array and EMI protection). (d) Sample handling system (to move the sample smoothly through detection coils). (e) Computer operating

system (for automation and user interface). Using superconductivity at liquid Helium temperature is a key technology for SQUID MPMS which allows for the generation of a very large, stable magnetic field and at the same time detection of very small changes in the field.
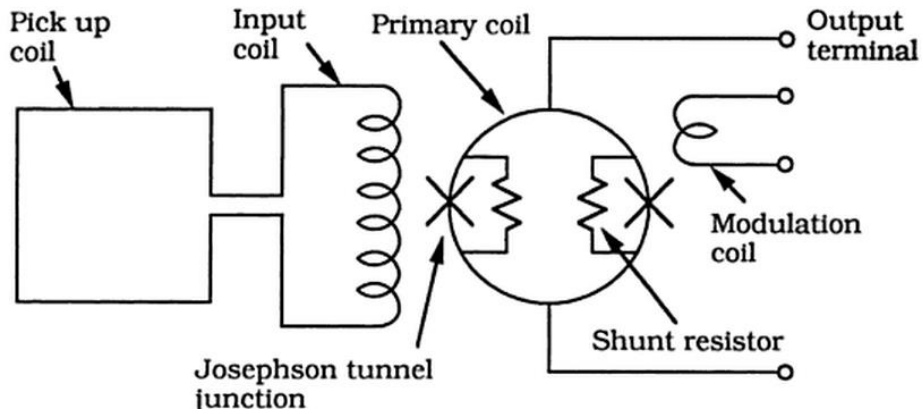
Fig. 3.9: The equivalent circuit of a SQUID magnetometer.

A SQUID magnetometer comprises two superconductors separated by thin insulating layers to form two parallel Josephson junctions. The operational principle of a SQUID magnetometer is based on magnetic flux quantization in a superconducting cylinder which makes measurements of very highly sensitive voltage, current and magnetization possible. According to the Josephson Effect, the electrical current density through a weak electric contact between two superconductors depends on the phase difference $\phi(t)$ between the two superconducting wave functions. The voltage across this weak contact is related to the time derivative of the aforementioned phase difference as $U(t) = \frac{\hbar}{2e}\frac{\partial\phi}{\partial t}$. The phase difference $\phi(t)$ is additionally influenced by the magnetic flux Φ through this ring. Hence, this arrangement can be used to convert magnetic flux into an electrical voltage.

The equivalent circuit of a SQUID magnetometer [217] is shown in Fig. 3.9. When the sample is moved up and down it produces an alternating magnetic flux in the pick-up coil .The magnetic signal of the sample is obtained via a Superconducting pick-up coil with four windings which receives this magnetic signal. The magnetic flux is transferred from the measuring sample to an RF SQUID device which is at liquid helium temperature. This part of the equivalent circuit works as magnetic flux to voltage converter. The converted voltage is amplified and read out by the magnetometer's electronics. The output voltage gradually changes due to the change of magnetic field resulting from quantum interference in the Josephson junctions. Later this output signal is refined through a

modulation coil and converted to a magnetic moment. The whole SQUID unit is enclosed within a superconducting lead to avoid vibrations, and is cautiously shielded against external magnetic fields. The external and internal design of a SQUID MPMS system is shown in Fig. 3.10 (a) and Fig. 3.10 (b) respectively (Courtesy: Quantum Design).

The samples are diced or cut into size of 3×3 mm^2 for measurement in the SQUID. The square shape is maintained as much as possible to avoid the shape anisotropy contribution. The sized samples are inserted inside the instrument using a straw and the SQUID is calibrated to take account of the magnetic contribution of the straw, which may distort the measurements. Then the sample is centered w.r.t. the pick-up coil by applying a magnetic field that is sufficiently high so as to saturate the sample (up to 5T) and moving the sample through the SQUID's measurement chamber. The center point is chosen by visually inspecting the maxima of the magnetic moment vs. position plot. After centering, finally, the magnetic fields are applied to the sample between positive to negative 5T and the resultant magnetization of the sample is measured in the unit of emu (electromagnetic units, 1000 emu/cm^3= 1 A/m).

01. Sample Rod
02. Sample rotator
03. Sample Transport
04. Probe assembly
05. He level Sensor
06. Superconducting Solinoid
07. Flow impedance
08. Squid capsule
09. Superconducting pick-up coil
10. Dewar Isolation cabinet
11. Dewar
12. Printer
13. Magnetic power supply
14. Temp. controller
15. Console Cabinet
16. Power distribution unit
17. MPMS controller
18. Gas/Magnet control unit
19. Computer
20. Monitor

Fig. 3.10: (a) SQUID MPMS XL5. (b) Internal configuration of the instrument [217].

The magnetic measurements in the SQUID are considered optimum in terms of time and accuracy due to the elaborate measurement algorithm. In each measurement in the SQUID, the magnetic moment is measured a number of times and statistical techniques are applied to decide whether subsequent measurements are required to ensure a certain percentage of the resultant magnetic moments is within the standard deviation limit of the mean response. Theoretically the SQUID has a measurement sensitivity of 10^{-8} emu, but in practice it takes a long time and consumes a large amount of liquid helium to measure very low moment samples.

The magnetic moment of a sample can be measured in the SQUID as a function of temperature and external magnetic field using different measurement protocols. In this thesis, the magnetic moments of different samples are measured for varying the applied field (M-H measurement) which constitutes the magnetic hysteresis loop.
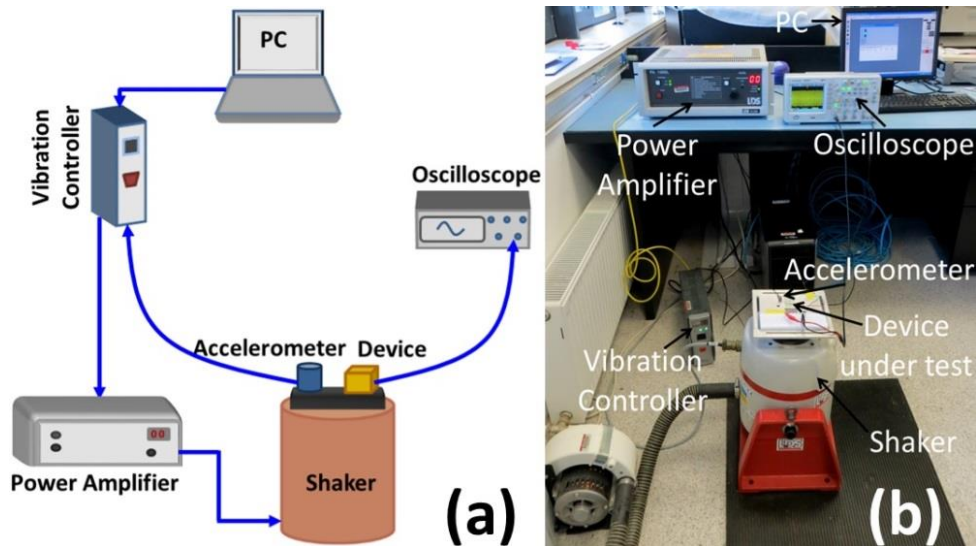
Fig. 3.11: (a) Schematic of the experimental set-up. (b) The actual test set up for experimental study of the system.

3.4.4. Electromechanical Characterization of the VEH devices using Permanent Magnet Shaker: The fabricated EM energy harvesting prototypes reported in this thesis are electromechanically characterized using the experimental test set up as shown in Fig. 3.11. The device is excited by a Brüel & Kjær LDS V455 Permanent Magnet Shaker. They rely on the same physical relationships that make a loudspeaker work. When a current passes through a wire that is in a magnetic field, a force perpendicular to the wire and to the magnetic flux is induced in the wire. The amount of force is proportional to the current, to the magnetic flux and to the length of wire in the magnetic field. The wire is wound around a cylindrical coil, which is part of the shaker armature and elastically suspends it in a radial magnetic field. This results in an axial force acting on the armature in proportion to the applied current. The suspension holds the coil concentrically within the magnetic field. It allows the armature to move over limited distance axially relative to the shaker body. This limited distance is termed the shaker's displacement stroke. Characterization is performed under (i) fixed acceleration, sweeping frequency, (ii) fixed acceleration, fixed frequency and (iii) fixed frequency, sweeping acceleration modes. The sweeping sinusoidal signal is produced by the vibration controller via the power amplifier to get a constant input acceleration level which is monitored by a miniature piezoelectric

CCLD accelerometer (LDS 4394). The shaker is controlled by LDS Comet USB vibration control system which is fed to LDS PA 1000L power amplifier. The LDS V455 electro-dynamic shaker is suited for sine and random vibration and shock testing in the range 5 - 9000 Hz. The system has a maximum acceleration of 70 g (sine) and 70 g (random). The output voltage signal from the energy harvester is recorded using a Picoscope digital oscilloscope.

3.5. Conclusions:

The simulation methods, fabrication and characterization techniques reported in this chapter are utilized at different stage of this thesis to achieve the goal of developing wideband electromagnetic energy harvesting devices.

Chapter 4

Linear Energy Harvesters & Bidirectional Electrical Tuning

4.1. Introduction:

As mentioned in chapter 1 and 2, there has been a surge of research on the conversion of mechanical kinetic energy from ambient vibrations into useful electrical energy. The main motivation behind the research in this particular field is to achieve the autonomous operation for low power applications such as Wireless Sensor Nodes (WSN). The most commonly used transduction mechanisms for converting the available mechanical energy into electrical energy are electromagnetic, piezoelectric and electrostatic. Regardless of the adopted transduction mechanisms, vibration energy harvesters (VEHs) are, in general, modeled using spring-mass-damper systems as described in chapter 1. Such systems are normally characterized by their resonant behaviour i.e., the peak output response is obtained at the resonant frequency but the response drops considerably with a little shift of the ambient frequency from the resonance.

This chapter briefly introduces the basic theory of the linear resonance based VEH device model. The theory and optimization of electromagnetic power generation is provided to understand the underlying physics of the transducers. A comparison of performances of different electromagnetic generators is demonstrated by developing a number of prototypes at meso-scale. The devices are designed, fabricated, characterized and analysed. A comparative performance study of four different meso-scale EM energy harvesters is provided in terms of the effect of electrical tuning using complex loads. A general model using theoretical derivations for bidirectional tuning of the EM harvesters using two different load topologies is developed: capacitive load to tune the resonance in the lower frequency direction and inductive load to tune in the higher frequency direction. Finally, the experimental validations and comparative analysis of electrical tuning on the

four EM harvester prototypes are discussed. In the end, an initial power management circuit is developed to demonstrate a complete energy harvesting solution.

4.2. Theory of a Resonant Electromagnetic Energy Harvester:

4.2.1. Steady-state Solution: As shown in Fig. 4.1., the system consists of a mass (m) mounted on a spring with spring stiffness k, which vibrates relative to a housing (fixed frame) when subjected to an external mechanical force [53]. It is assumed that the moving mass (m) is much smaller compared to the mass of the generator frame. Hence, the movement of the frame is unaffected by the movement of the generator. Under an external vibration of the form, $y(t) = Y_0\sin(\omega t)$ (where, Y_0 = vibration amplitude and ω = frequency of vibration), the mass along with the spring moves harmonically. If the displacement of the mass, m, with respect to the ground is x(t) and displacement of the frame with respect to the ground is y(t), then the net displacement of the mass (m) w.r.t. the frame is

$$z(t) = x(t) - y(t) \tag{4.1.}$$
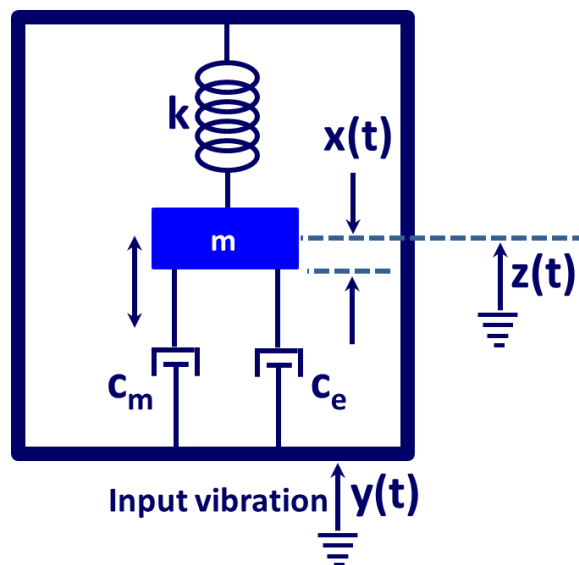
Fig. 4.1. Basic Spring-Mass-Damper model of vibration energy harvesters.

By balancing all forces acting on the system described in Fig. 4.1., the equation of motion can be written as

$$m\ddot{z}(t) + c_T\dot{z}(t) + kz(t) = -m\ddot{y}(t) \tag{4.2.}$$

where c_T is the total damping co-efficient which includes both mechanical/parasitic damping co-efficient (c_m) and electrical damping co-efficient (c_e) such that $c_T = c_m + c_e$.

Equation (2.2) can be written in vector form and replacing $\sin(\omega t)$ by $e^{i\omega t}$

$$m\ddot{z}(t) + c_T\dot{z}(t) + kz(t) = F_0 e^{i\omega t} \tag{4.3.}$$

where $F_0 = m\omega^2 Y_0$

Let's assume the solution of equation (4.3) is of the form $z(t) = Ae^{i\omega t}$. Then from the above equation,

$$(-A\omega^2 m + i\omega Ac_T + Ak)e^{i\omega t} = F_0 e^{i\omega t} \tag{4.4.}$$

which is true for all t, if,

$$A = \frac{F_0}{i\omega c_T + (k - \omega^2 m)} = \frac{F_0}{\sqrt{(c_T\omega)^2 + (k - \omega^2 m)^2}} \tan^{-1}(-\alpha) \tag{4.5.}$$

where α is the phase angle.

Then, $$z(t) = Ae^{i\omega t} = \frac{F_0}{\sqrt{(c_T\omega)^2 + (k - \omega^2 m)^2}} \sin(\omega t - \alpha)$$

Putting value of F_0, the expression for the displacement $z(t)$ of the mass (m) w.r.t. the frame can be obtained as

$$z(t) = \frac{\omega^2 Y_0 \sin(\omega t - \alpha)}{\sqrt{[(\frac{c_T\omega}{m})^2 + (\frac{k}{m} - \omega^2)^2]}} \tag{4.6.}$$

where α is the phase angle given by

$$\alpha = \tan^{-1}\frac{c_T\omega}{(k - m\omega^2)} \tag{4.7.}$$

Maximum energy can be extracted from the system when the frequency (ω) of the external vibration matches with the natural frequency (ω_n) of oscillation of the system which is given by $\omega_n = \sqrt{\frac{k}{m}}$. The amplitude of the maximum displacement of the resonant generator which occurs at resonance ($\omega = \omega_n$) is calculated to be

$$z_{max} = \frac{\omega_n Y_0}{c_T} \tag{4.8.}$$

The parasitic damping ratio of the system is given by $\rho_m = \frac{c_m}{2m\omega_n}$ which leads to an open circuit quality factor, $Q_{oc} = \frac{1}{2\rho_m} = \frac{m\omega_n}{c_m}$. The open circuit refers to the condition when no electrical transduction is made.

For an electromagnetic generator, the total damping includes the electrical damping (c_e) too. When a load is connected to the coil terminal of the generator, an electromagnetic force (F_{em}) is generated between the magnet and the coil due to the current flowing through the load. This force opposes the movement of the generator.

4.2.2. Calculation of the Electrical Damping Co-efficient (c_e): The electromagnetic force (F_e) can be calculated from the approximation of a coil moving relatively in a single direction through a magnetic field which varies in the direction of movement. Since the operating principle of an EM generator is governed by Faraday's law of induction, the voltage induced in the coil with n number of turns is

$$V = n\frac{d\varphi}{dt} = nA\frac{dB}{dz}\frac{dz}{dt} \tag{4.9.}$$

Where A is the average coil area, n is the number of turns and φ is the total flux of the magnet which is given as $\varphi = BA$, where B is the magnetic field induction.
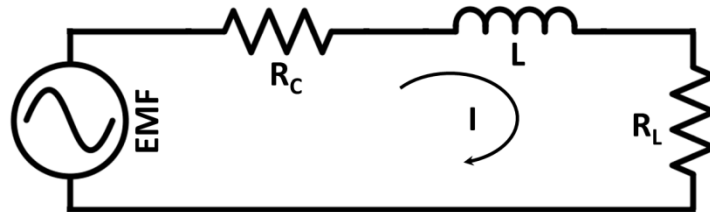
Fig. 4.2: Simplified circuit of an electromagnetic generator.

Now a simplified circuit model for EM generators can be imagined as the one depicted in Fig. 4.2, where the induced voltage in the coil (V) is considered as a voltage source with series resistance (R_C) and series inductance (L_C). A load (R_L) is connected across the coil so that a current (I) can flow in the closed loop.

Using Kirchhoff's law, the generated voltage (V_L) across the load is given as

$$V_L = V - I(R_C + j\omega L) = IR_L \tag{4.10.}$$

The instantaneous generated power in electrical domain is given as

$$P_e(t) = F_e \cdot \frac{dz(t)}{dt} = c_e \left(\frac{dz(t)}{dt}\right)^2 \tag{4.11.}$$

where $F_e = c_e \frac{dz(t)}{dt}$ is the force due to EM coupling. The same power can be expressed as a product of the voltage generated and the current in the circuit of Fig. 4.2,

$$P_e(t) = V(t) \cdot I(t) \tag{4.12.}$$

Equating (4.11) and (4.12), and substituting the values of V and I from equations (4.9) and (4.10)

$$c_e \left(\frac{dz(t)}{dt}\right)^2 = V(t) \cdot I(t) \tag{4.13.}$$

or,
$$c_e \left(\frac{dz(t)}{dt}\right)^2 = \frac{V^2(t)}{R_C + R_L + j\omega L} \tag{4.14.}$$

or,
$$c_e \left(\frac{dz(t)}{dt}\right)^2 = \frac{n^2 \left(\frac{d\varphi}{dz}\right)^2 \left(\frac{dz}{dt}\right)^2}{R_C + R_L + j\omega L} \tag{4.15.}$$

Hence,
$$c_e = \frac{n^2 \left(\frac{d\varphi}{dz}\right)^2}{R_C + R_L + j\omega L} \tag{4.16.}$$

Equation (4.16) represents the electrical damping co-efficient in an EM energy harvesting device. Normally, vibration based energy scavenging devices work in the low frequency regime, where the effect of impedance provided by the coil inductance (ωL_C) is ignored compared to that of the coil (R_C) and load (R_L) resistances. Hence, the approximated value of the electrical damping co-efficient is given as

$$c_e = \frac{n^2 \left(\frac{d\varphi}{dz}\right)^2}{R_C + R_L} = \frac{\gamma^2}{R_C + R_L} \tag{4.17.}$$

where γ is known as the electromagnetic coupling co-efficient and has the unit of Wb/m.

F_e is calculated to be $F_e = c_e \frac{dz}{dt} = \frac{\left(\frac{d\varphi}{dz}\right)^2}{(R_C + R_L)} \frac{dz}{dt}$.

4.2.3. Generated Electrical Power: Equation (4.11) provides the instantaneous electrical power that is dissipated within the electrical damper. Hence the average electrical power is given as,

$$P_{elec} = \frac{1}{T} \int c_e \left(\frac{dz(t)}{dt}\right)^2 dt \tag{4.18.}$$

From equation (4.6), taking derivatives,

$$\frac{dz(t)}{dt} = \frac{\omega^3 Y_0 \cos(\omega t - \alpha)}{\sqrt{[(\frac{c_T \omega}{m})^2 + (\frac{k}{m} - \omega^2)^2]}}$$

So, substituting this value and rearranging,

$$P_{elec} = \frac{c_e(\frac{\omega}{\omega_n})^3 Y_0{}^2 \omega^3}{2\omega_n[\{2\rho_T(\frac{\omega}{\omega_n})\}^2 + \{1 - (\frac{\omega}{\omega_n})^2\}^2]} \tag{4.19.}$$

Here ρ_T is the total damping ratio including both electrical and parasitic components. Similarly the total average energy (P_{av}) dissipated in the damper (both electrical transduction and parasitic damping) can be obtained by replacing c_e by c_T, which is written as

$$P_{av} = \frac{m\rho_T(\frac{\omega}{\omega_n})^3 Y_0{}^2 \omega^3}{[\{2\rho_T(\frac{\omega}{\omega_n})\}^2 + \{1 - (\frac{\omega}{\omega_n})^2\}^2]} \tag{4.20.}$$
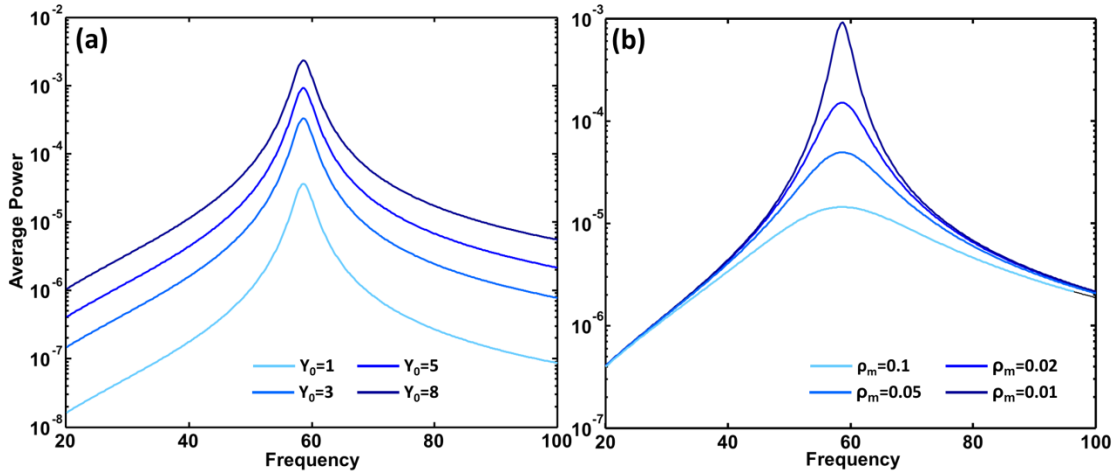
Fig. 4.3: Frequency response of a linear generator for (a) different values of the input force (Y_0) and (b) different values of the parasitic damping (ρ_m) which changes the open circuit quality factor.

Using the above formula, the response of the linear resonator is studied in Fig. 4.3 by varying the input force amplitude and the parasitic damping. For increasing force amplitude while the other parameters remains constant, the peak output power increases as expected. On the other hand, the variation of parasitic damping co-efficient is directly related to the change of open circuit quality (Q) factor according to the formula $Q_{oc} = \frac{1}{2\rho_m}$. The Q-factor indicates the sharpness of the resonance. High Q-factor gives a sharp peak whereas a low value of Q-factor accounts for a spread out resonance curve. Hence,

with increasing damping, the Q-factor decreases and this results in a wide frequency response. However, the output amplitude is reduced too as the damping is increased. It is to be noted that there is no control over an input force as that is related to external vibration. By contrast, the damping can be controlled to get the desired output response.

The maximum power dissipation at resonance $(\omega=\omega_n)$ is

$$P_{av}|_{\omega=\omega_n} = \frac{mY_0{}^2\omega_n{}^3}{4\rho_T} \tag{4.21.}$$

Similarly from equation (4.19), the maximum electrical power generated at resonance is

$$P_{elec}|_{\omega=\omega_n} = \frac{c_eY_0{}^2\omega_n{}^2}{8\rho_T{}^2} = \frac{c_em^2Y_0{}^2\omega_n{}^4}{2(c_m+c_e)^2} \tag{4.22.}$$

The maximum electrical power and optimum electromagnetic damping can be found by putting $\frac{dP_{elec}}{dc_e} = 0$.

This condition shows that maximum power occurs at $c_e = c_m$. This is the optimum electromagnetic damping condition at resonance.

4.2.4. Optimum Load Resistance for Maximum power: This can be obtained by equating the above mentioned condition for maximum power. Thus,

$$\frac{n^2(\frac{d\varphi}{dz})^2}{R_C+R_L} = c_m \tag{4.23.}$$

Therefore, the optimum load resistance, for which maximum electrical power is obtained, is given by,

$$R_L|_{opt} = \frac{n^2(\frac{d\varphi}{dz})^2}{c_m} - R_C \tag{4.24.}$$

From equation (4.24), the following conclusions can be drawn –

- Optimum load resistance may not be positive if the first term on the right is less than R_C. This can happen if c_m is large, $\frac{d\varphi}{dz}$ is low or R_C is large.

- Under such circumstances, it is not possible to generate optimum power just by varying the load resistance. This is only possible when $\frac{d\varphi}{dz}$ is low or R_C is large and

consequently c_e is much less than c_m. Under such conditions, there is not much difference of the generator displacement between the loaded and open circuit conditions. In this case, the maximum power will be delivered to the load according to the classical maximum power transfer theory when the load resistance (R_L) is matched to the source or coil resistance (R_C). Under this condition ($R_C=R_L$), half of the voltage and power is dissipated in the generator's internal resistance and the harvesting efficiency is likely to be very low.

Now the maximum generated electrical power at resonance is given in equation (4.22). The electrical power which is transferred to the load (P_L) is given by

$$P_L|_{\omega=\omega_n} = \frac{R_L n^2 (\frac{d\varphi}{dz})^2 m^2 {Y_0}^2 {\omega_n}^4}{2[c_m(R_C+R_L)+n^2(\frac{d\varphi}{dz})^2]^2} \qquad (4.25.)$$

The optimum load resistance at maximum load power can be found by setting $\frac{dP_L|_{\omega=\omega_n}}{dR_L} = 0$. This gives

$$R_L|_{P_L\ max} = \frac{n^2(\frac{d\varphi}{dz})^2}{c_m} + R_C \qquad (4.26.)$$

In the following section/chapter, linear resonant generators are developed at different scales, characterized and analysed according to the above mentioned theoretical foundation. The meso-scale devices are developed using FR4 as the spring material and by using NdFeB discrete magnets and wire wound copper coils whereas the MEMS devices are fabricated using standard microfabrication technologies.

4.3. FR4 based Linear Generators:

4.3.1. Flame Retardant 4 (FR4): Flame Retardant 4 or FR-4 in short is a composite material composed of woven fiberglass cloth with an epoxy resin binder that is flame resistant or self-extinguishing [218]. The most common use of this material is in modern Printed Circuit Boards. FR-4 glass epoxy is a popular and versatile high-pressure thermoset plastic laminate grade with good strength to weight ratios. FR-4 is a good electrical insulator possessing considerable mechanical strength. With almost zero water absorption, FR-4 can retain its high mechanical strength and electrical insulating qualities in both dry and humid conditions. These attributes, along with good fabrication

characteristics, makes FR-4 suitable for a wide range of electrical and mechanical applications.

Material	Young's Modulus (GPa)	Yielding Stress (GPa)	Density (Kg/m^3)
BeCu	130	0.35	8250
Silicon	190	7	2330
Steel	200	0.52	7500
FR4	21	0.31	1900

Table 4.1: Comparison of properties of different materials

As has been already discussed in chapter 2, a number of materials have been reported in literature for fabricating vibrating mechanical springs, such as BeCu, steel for meso scale devices and silicon for MEMS scale devices. Comparative charts of the properties of different materials are shown in Table 4.1. The low Young's modulus of FR4 (Y=21 GPa) enables a designed device to operate in the low frequency region within a smaller footprint without adding additional mass which could degrade the reliability of the devices for long term deployable applications. Further, for EM Energy Harvesters, conducting coils can easily be routed on FR4 laminates [219].

4.3.2. Design & Fabrication of the FR4 based EM Harvesters: Four different Electromagnetic VEH structures are developed using FR4 as the resonating spring material due to its suitable mechanical properties for low frequency applications. The different spring configurations considered are shown in Fig. 4.4 (a) to Fig. 4.4(d). The outer dimensions (including the frame) of the resonator of Prototype 1 (P1) and Prototype 2 (P2) are the same, 2.5×2.5 cm^2, and those of Prototype 3 (P3) and Prototype 4 (P4) are same, 2.2×2.2 cm^2.

The spring configurations of P1 and P2 are both four armed, except that the lengths of the individual arms of P2 are smaller than those of P1. Whereas for P3, U shaped arms are designed and these four arms are connected to the four corners of the central paddle. Two serpentine springs are connected at the two opposite corners of the central paddle of P4 and this particular spring design effectively increases the length of the spring within a compact space and thus reduces the spring constant, resulting in low frequency operation. The spring structures are fabricated using Laser Micromachining technology on 210 µm thick FR4.
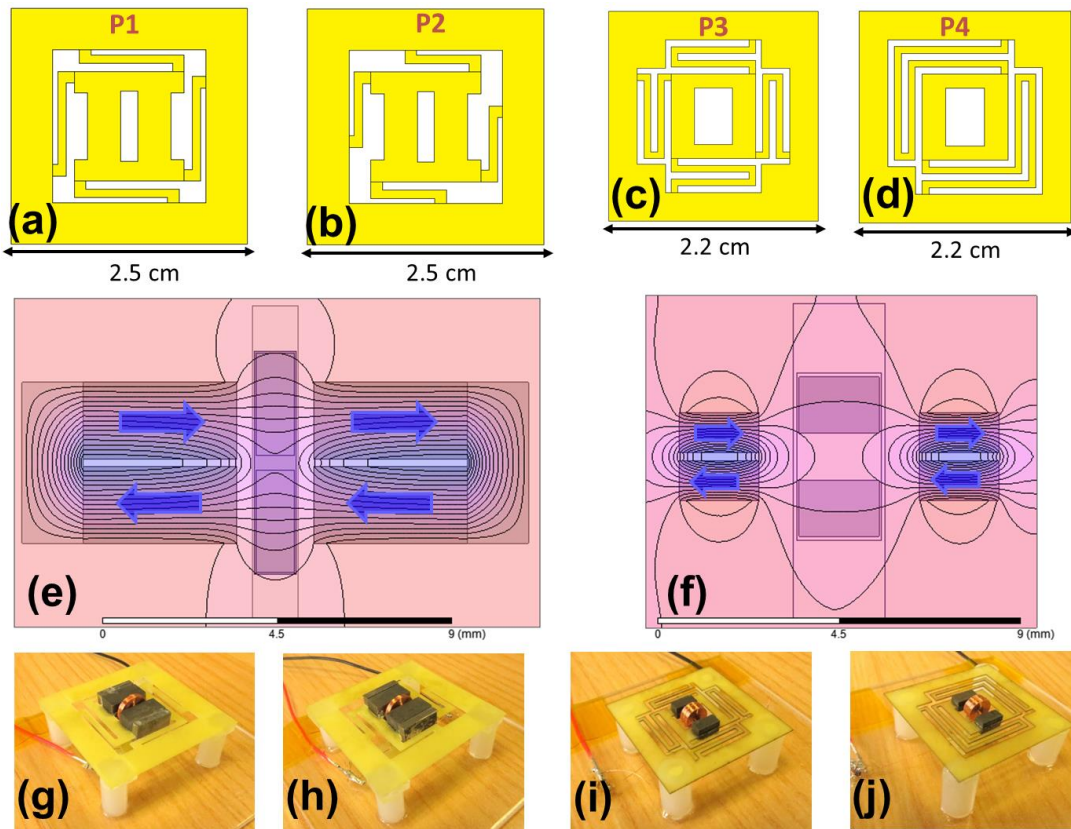
Fig. 4.4: (a) – (d) Spring configurations on FR4 for prototypes 1-4 (P1-4). (e) Magnet coil arrangement for P1 and P2, mild steel keepers are used at the two ends to maximize the flux density. (f) Magnet coil arrangement for P3 and P4. (Arrows show the polarity of the magnets). (g)-(j) Assembled prototypes P1-4.

An arrangement of two pairs of oppositely polarized sintered NdFeB N50 magnets with mild steel keepers at the ends was assembled to maximize the flux density for both P1 and P2 (Fig. 4.4 (e)) whereas for P3 and P4 the two pairs of oppositely polarized NdFeB N50 magnet configurations (Fig. 4 (f)) are used without any soft magnetic keepers. Wire wound copper coils (placed upright in a stand) are used in all the prototypes to induce voltage. The coil inductances are ignored in the following analysis.

The values of different parameters that are used in the design of the four prototypes are tabulated in Table 4.2. The sizes of the magnets are bigger for P1 and P2 compared to those for P3 and P4. The value of electromagnetic coupling co-efficient (γ) is numerically calculated using the Maxwell Ansoft software. If we consider a coil with n number of turns which moves relatively along the z-direction in a magnetic field density B then according to equation (4.17), the electromagnetic coupling co-efficient can be expressed as the following,

$$\gamma = n\frac{d\phi}{dz} \qquad (4.27.)$$

where ϕ is the flux linkage given by $\phi = \iint B.dA$ (A being the area enclosed) and $\frac{d\phi}{dz}$ is the flux linkage gradient per turn of the coil.

Parameters	P1	P2	P3	P4
Coil Outer Diameter	6.5 mm	6.5 mm	4 mm	4 mm
Coil Inner Diameter	1.2 mm	1.2 mm	1.2 mm	1.2 mm
Coil Thickness	1 mm	1 mm	2 mm	2 mm
No of Turns	2500	2500	2500	2500
Coil Resistance (measured)	717 Ω	714 Ω	770 Ω	767 Ω
Coil Inductance (calculated)	1.81 mH	1.81 mH	2.67 mH	2.67 mH
NdFeB Magnets	$8\times4\times2$ cm^3	$8\times4\times2$ cm^3	$4\times2\times1$ cm^3	$4\times2\times1$ cm^3
Soft Magnet	$8\times4.2\times1.6$ cm^3	$8\times4.2\times1.6$ cm^3	No	No
FR4 Thickness	210 μm	210 μm	210 μm	210 μm
Length of individual spring arms	12.8 mm	9.3 mm	18.72 mm	33.48 mm
Width of individual spring arms	1 mm	1 mm	0.72 mm	0.72 mm
EM Coupling Co-efficient (calculated)	11.069 Wb/m	11.057 Wb/m	1.12 Wb/m	1.13 Wb/m

Table 4.2: Values of different parameters used for design and experiments on FR4 based EM harvester prototypes.

The value of γ for the first magnetic configuration is almost 10 times higher compared to the second magnetic arrangement due to the use of soft magnetic keepers and larger hard magnets. This difference in electromagnetic coupling co-efficient provides an interesting observation later in terms of the tuning capabilities. The assembled prototypes are shown in Fig. 4.4 (g-j). The overall volumes of P1 and P2 are 4.38 cm^3 whereas those of P3 and P4 are 2.9 cm^3.
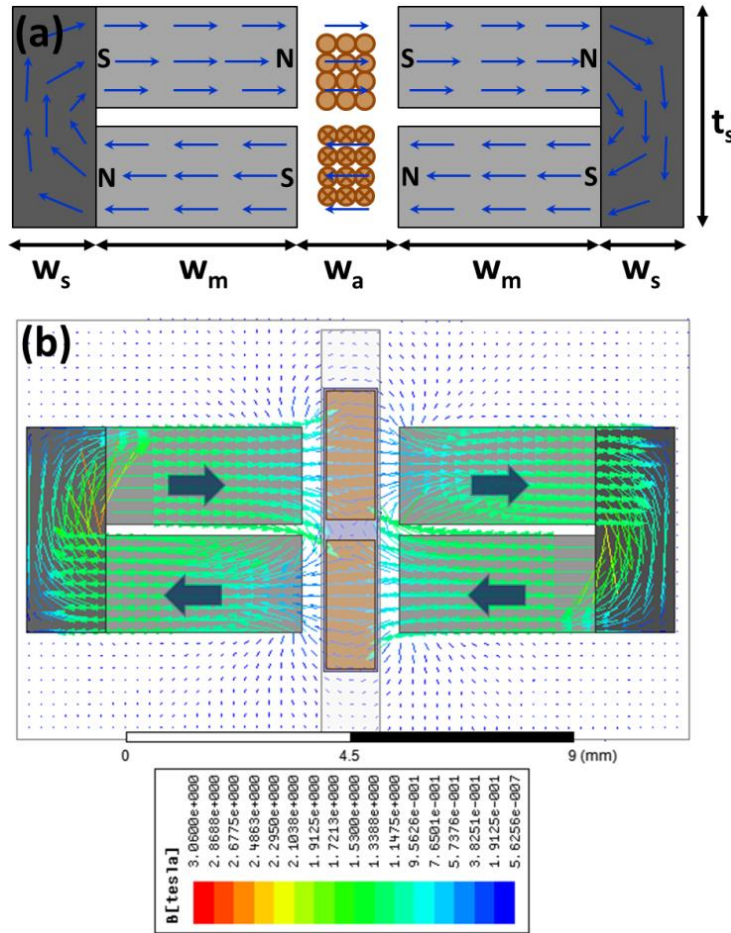
Fig. 4.5: (a) Schematic of the high efficiency magnet-coil assembly to increase the electromagnetic coupling (the arrows show the direction of the magnetic flux). Dimensions are also marked. (b) Simulated view of the magnetic field distribution for the magnet-coil assembly from Maxwell Ansoft.

The developed magnetic circuits can be analyzed in terms of the magnetic reluctance. In an analogy to electrical resistance in an electrical circuit, the magnetic reluctance should be minimized in a magnetic circuit to obtain the large magnetic flux. The magnetic flux traverses through three media – NdFeB magnets, soft magnetic iron blocks and intermediate air paths between the magnets. The total magnetic reluctance of the magnetic circuit consists of reluctances due to NdFeB magnets (χ_m), iron blocks (χ_s) and air gap (χ_a) and can be calculated as

$$\chi = \chi_m + \chi_s + \chi_a = \frac{l_m}{\mu_m A_m} + \frac{l_s}{\mu_s A_s} + \frac{l_a}{\mu_a A_a} \tag{4.28.}$$

where l is the magnetic path length, μ is the magnetic permeability and A is the cross-sectional area in the direction of the magnetic flux. The subscripts m, s and a in equation (4.28) stand for NdFeB, Iron block and air mediums. According to Fig. 4.5 (a), the

lengths of the magnetic paths through the respective media are given as $l_m = 4w_m$, $l_s = 2t_s$ and $l_a = 2w_a$ where w_m, w_a and t_s are the width of a NdFeB block, the width of the air gap and thickness of an iron block. Due to the high permeability of the soft magnets (μ_s = 0.25 H/m) [220], χ_s is negligibly small. If the soft magnetic iron blocks were not present at the ends, the second term in equation 4.28 would have been replaced by the reluctance due to the air for the corresponding space and the total reluctance of the magnetic circuit would be much higher, reducing the magnetic flux. Thus the presence of the soft iron blocks makes the entire magnetic arrangement highly efficient. However, the coil size, number of turns and magnet sizes are not optimized. Different coil shapes with optimized numbers of turns could result in better electromagnetic coupling. But as we are interested in studying output parameters such as operational bandwidth, such design and fabrication optimization is excluded from our current study.
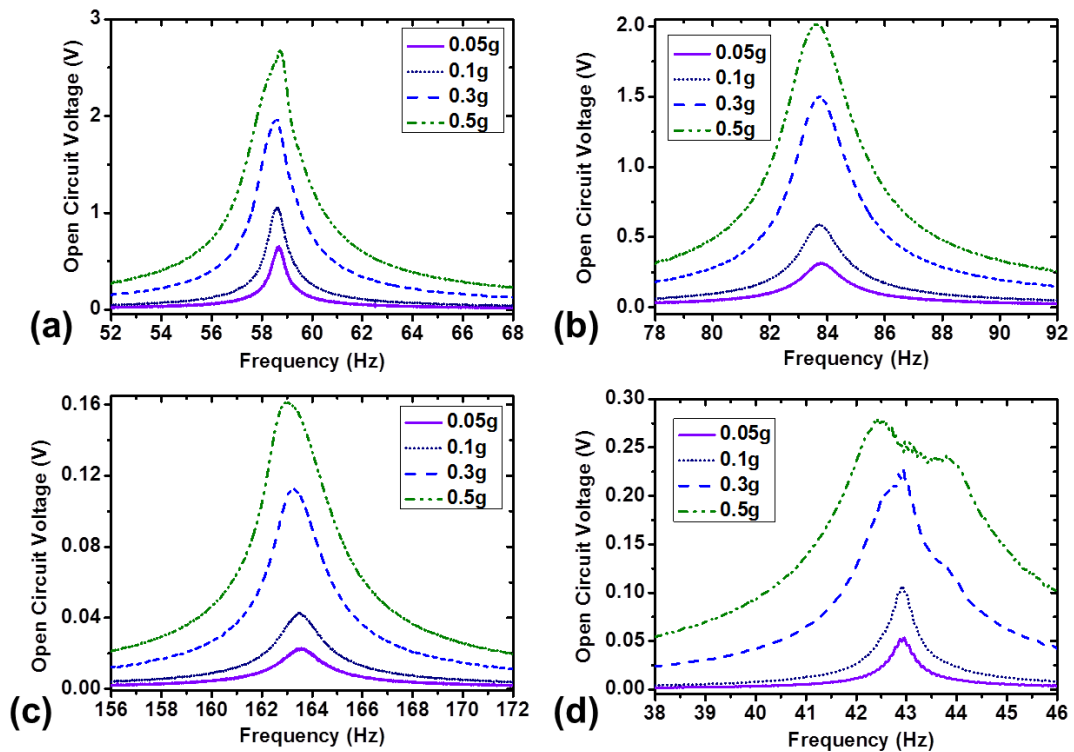
Fig. 4.6: Open Circuit RMS Voltage responses at different input acceleration of (a) Prototype 1 (P1). (b) Prototype 2 (P2). (c) Prototype 3 (P3). (d) Prototype 4 (P4).

4.3.3. Experimental Characterization of the FR4 based EM Harvesters: The fabricated devices were tested in a LDS V455 permanent magnet shaker using harmonic excitation. The open circuit output voltage performance of the EM harvesters as a function of input acceleration levels and input frequency is shown in Fig. 4.6 (a-d) and the responses are linear resonant in nature. The resonant frequencies of P1, P2, P3 and P4

are 58.6 Hz, 83.8 Hz, 162.9 Hz and 42.9 Hz respectively. The output voltage response of P1 bends slightly towards the right at higher accelerations (0.5g, g=9.8m/s^2) due to the spring hardening effect, which will be explained in detail in chapter 6. The response of P4 is flat at the top for 0.5g because the device collides with the base of the prototype at higher acceleration due to its longer spring arms and this causes abrupt changes in the system dynamics to make the output response wide [221-222]. The optimum load condition that is the resistive load across which maximum power is obtained is given in Table 4.3 for the four prototypes, measured at 0.3g for of the prototypes. As tabulated, the prototypes P1, P2, P3 and P4 produce 470 µW, 350 µW, 4.3 µW and 16.5 µW at respective optimum loads of 2400 Ω, 2100 Ω, 780 Ω and 900 Ω respectively. The variation of the load voltage and power with load resistance is shown in Fig. 4.7 for the four prototypes. The optimum output powers of P3 and P4 are lower compared to those of P1 and P2 due to smaller electromagnetic coupling co-efficients. However, each of the prototypes generates sufficient power to energize the WSNs depending upon the applications. The average load power spectra for all the devices at different acceleration levels at their respective optimum loads are shown in Fig. 4.8 (a-d).

	P1	P2	P3	P4
Optimum Load Resistance (Ω)	2400	2100	780	900
Input acceleration level	0.3g	0.3g	0.3g	0.3g
Resonance Frequency (Hz)	58.6	83.8	162.9	42.9
Power at optimum Load (µW)	470	350	4.3	16.5
Voltage across optimum Load (V)	1.06	0.9	0.06	0.12

Table 4.3: Comparison of optimum load performances of P1, P2, P3 and P4.
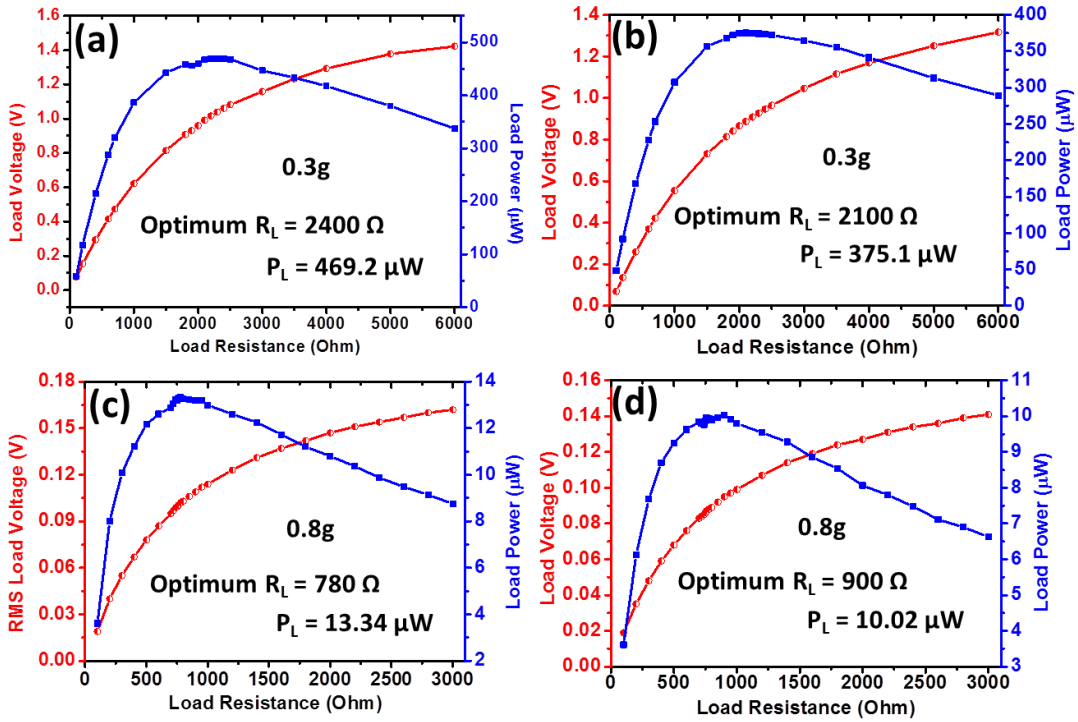
Fig. 4.7: Load voltage and load power variation with load resistance for (a) Prototype 1 (P1). (b) Prototype 2 (P2). (c) Prototype 3 (P3). (d) Prototype 4 (P4).
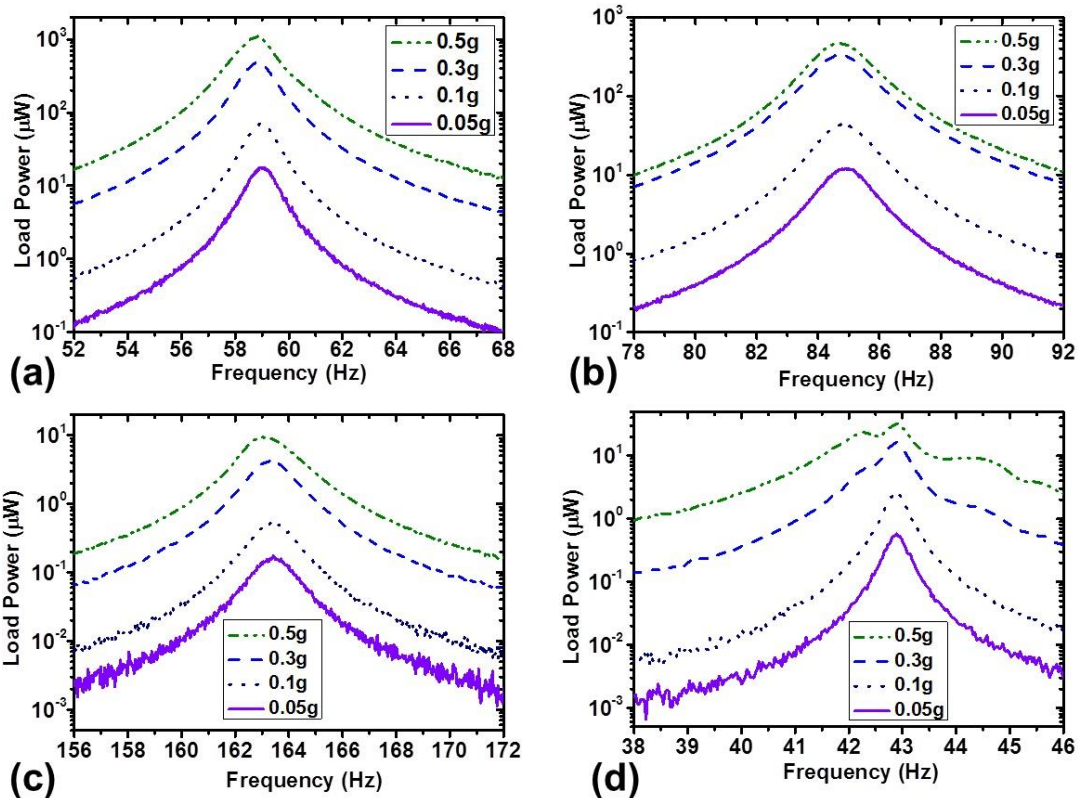
Fig. 4.8: Load power responses at different input accelerations of (a) Prototype 1 (P1). (b) Prototype 2 (P2). (c) Prototype 3 (P3). (d) Prototype 4 (P4).

4.4. Bidirectional Electrical Tuning of FR4 based Linear Generators:

4.4.1. Theoretical Framework: The dynamics of a resonant VEH are governed by the second order differential equation described in equation (4.2). Using Laplace transformation and dividing throughout by γ (where γ is the electromagnetic coupling co-efficient), this equation can be written in the frequency domain as:

$$\frac{ms^2}{\gamma}Z(s) + \frac{cs}{\gamma}Z(s) + \frac{k}{\gamma} = -\frac{ms^2}{\gamma}Y(s) \tag{4.29.}$$

Equation (4.29) can be written in circuit form if it is considered that $V = \gamma s Z(s)$ is the induced voltage, $I = \frac{ms^2 Y(s)}{\gamma}$ is the input drive current, $C_m = \frac{m}{\gamma^2}$, $R_m = \frac{\gamma^2}{c}$, $L_m = \frac{\gamma^2}{k}$ are respectively the equivalent capacitance, resistance and inductance of the mechanical system. Equation (4.29) can be rewritten as:

$$V(s)\left(\frac{1}{R_m} + \frac{1}{sL_m} + sC_m\right) = -I(s) \tag{4.30.}$$

Based on the above equation, the equivalent circuit of the EM VEH is schematically drawn in Fig. 4.9 (a) where the mechanical part of the system is represented as a parallel combination of R_m, C_m and L_m connected to a current source of generated current I. The open circuit induced voltage is represented as V. The mechanical system is connected to an electrical load to generate load voltage and the power derived to the load for different applications. If it is considered that the mechanical system is connected to a resistive load R_L (Fig. 4.9 (b)), then the resonant frequency is given by $\omega_n = \sqrt{\frac{1}{L_m C_m}}(= \sqrt{\frac{k}{m}})$, which is the natural frequency of the oscillator. But adding a variable reactive element to the load gives scope to tune the resonant frequency accordingly. When a resistive load is connected to the energy harvester, the current flowing through the load is real and it produces a restoring electromagnetic force ($F_{em} = BlI$; B is magnetic flux density and l is mean length of the conductor) to the generator which is real in nature and it does not change the mechanical resonant frequency (ω_n) of the generator. However if a reactive load is connected to the energy harvester, the current flowing through the load has imaginary components in it and, as a result, the exerted electromagnetic force on the mechanical system becomes complex in nature and thus modifies the resonant frequency of the system. Two kinds of complex load topologies are considered, namely the lossy

capacitive load that consists of a parallel combination of load capacitor C_L and the load resistance R_L (Fig. 4.9 (c)) and the lossy inductive load that consists of a series combination of load inductance L_L and the load resistance R_L (Fig. 4.9 (d)) for our analysis.
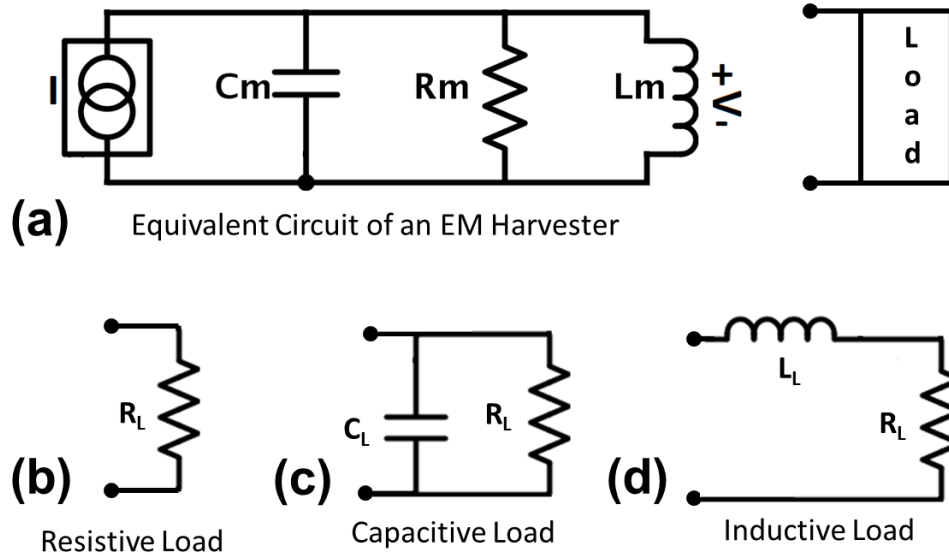
Fig. 4.9: (a) Equivalent circuit of an EM Harvester: mechanical system is represented by a parallel resonant circuit, which is connected to an electrical load. (b) Resistive Load. (c) Capacitive Load. (d) Inductive Load.

First, assume that the capacitive load is connected to the equivalent circuit of the EM harvester. The coil has a resistance R_C and the coil inductance is ignored at low operating frequency. Then the total impedance of the circuit is given by

$$Z_{TC}(\omega) = \cfrac{1}{j\omega c_m + \cfrac{1}{j\omega L_m} + \cfrac{1}{R_m} + \cfrac{1}{R_C + \cfrac{1}{\frac{1}{R_L} + j\omega C_L}}} \qquad (4.31.)$$

or,
$$Z_{TC}(\omega) = \cfrac{1}{jX_1 + \cfrac{1}{R_m} + \cfrac{1}{R_C + \cfrac{R_L}{1 + j\omega C_L R_L}}}$$

or,
$$Z_{TC}(\omega) = \cfrac{1}{jX_1 + \cfrac{1}{R_m} + \cfrac{1 + j\omega C_L R_L}{R_1 + j\omega C_L R_L R_C}}$$

or,
$$Z_{TC}(\omega) = \cfrac{1}{jX_1 + \cfrac{1}{R_m} + \cfrac{(1 + j\omega C_L R_L)(R_1 - j\omega C_L R_L R_C)}{R_1{}^2 + \omega^2 C_L{}^2 R_L{}^2 R_C{}^2}}$$

where $X_1 = \left(\omega c_m - \frac{1}{\omega L_m}\right)$, $R_1 = (R_L + R_C)$.

Considering $Y_1 = R_1{}^2 + \omega^2 C_L{}^2 R_L{}^2 R_C{}^2$,

$$Z_{TC}(\omega) = \frac{Y_1}{jX_1 Y_1 + \frac{Y_1}{R_m} + R_1 + \omega^2 C_L{}^2 R_L{}^2 R_C + j\omega C_L R_L R_1 - j\omega C_L R_L R_C}$$

Further considering $P = \frac{Y_1}{R_m} + R_1 + \omega^2 C_L{}^2 R_L{}^2 R_C$,

$$Z_{TC}(\omega) = \frac{Y_1}{P + j(X_1 Y_1 + \omega C_L R_L{}^2)}$$

or,
$$Z_{TC}(\omega) = \frac{Y_1[P - j(X_1 Y_1 + \omega C_L R_L{}^2)]}{P^2 + (X_1 Y_1 + \omega C_L R_L{}^2)^2} \tag{4.32.}$$

The modified resonant frequency is calculated by putting the imaginary part of the above mentioned impedance equal to zero and is calculated as

$$X_1 Y_1 + \omega C_L R_L{}^2 = 0$$

or,
$$X_1 Y_1 = -\omega C_L R_L{}^2$$

or,
$$(\omega c_m - \frac{1}{\omega L_m})(R_1{}^2 + \omega^2 C_L{}^2 R_L{}^2 R_C{}^2) = -\omega C_L R_L{}^2$$

or,
$$(\frac{\omega^2}{\omega_n^2} - 1)(R_1{}^2 + \omega^2 C_L{}^2 R_L{}^2 R_C{}^2) = -\omega C_L R_L{}^2 L_m$$

or,
$$(\frac{\omega^2}{\omega_n^2} R_1{}^2 - R_1{}^2 + \omega^4 \frac{C_L{}^2 R_L{}^2 R_C{}^2}{\omega_n^2} - \omega^2 C_L{}^2 R_L{}^2 R_C{}^2) = -\omega C_L R_L{}^2 L_m$$

or,
$$\mu^2 R_C{}^2 \omega^4 + (R_1{}^2 - \mu^2 R_C{}^2 \omega_n^2 + \mu^2 \eta \omega_n^2)\omega^2 - \omega_n^2 R_1{}^2 = 0$$

where $\mu = C_L R_L$ and $\eta = \frac{L_m}{C_L}$. Solving the above equation,

$$\omega = \sqrt{\frac{\pm\sqrt{(R_1{}^2 - \mu^2 R_C{}^2 \omega_n^2 + \mu^2 \eta \omega_n^2)^2 + 4\mu^2 R_C{}^2 \omega_n^2 R_1{}^2} - (R_1{}^2 - \mu^2 R_C{}^2 \omega_n^2 + \mu^2 \eta \omega_n^2)}{2\mu^2 R_C{}^2}}$$

The modified resonant frequency in this case is calculated in a similar manner as above and is given by

$$\omega_{rc} = \sqrt{\frac{\sqrt{(R_2+X-\mu\omega_n^2)^2+4R_1\mu\omega_n^2}-(R_2+X-\mu\omega_n^2)}{2\mu}} \qquad (4.33.)$$

where $R_2 = (1 + \frac{R_L}{R_C})^2$, $X = \frac{C_L}{C_m}(\frac{R_L}{R_C})^2$, and $\mu = R_L C_L$. The modified resonant frequency (ω_{rc}) is a function of load capacitance and can be tuned by changing it.

Similarly by considering that the inductive load is connected to the harvester, the total impedance of the circuit is given by

$$Z_{TL}(\omega) = \frac{1}{j\omega C_m + \frac{1}{j\omega L_m} + \frac{1}{R_m} + \frac{1}{R_C + R_L + j\omega L_L}} \qquad (4.34.)$$

or,
$$Z_{TL}(\omega) = \frac{1}{jX_1 + \frac{1}{R_m} + \frac{1}{R_C + R_L + j\omega L_L}}$$

or,
$$Z_{TL}(\omega) = \frac{1}{jX_1 + \frac{1}{R_m} + \frac{(R_C + R_L - j\omega L_L)}{(R_C + R_L)^2 + \omega^2 L_L^2}}$$

where $X_1 = (\omega C_m - \frac{1}{\omega L_m})$. If $R_1 = (R_L + R_C)$, $Y_2 = (R_C + R_L)^2 + \omega^2 L_L^2$ then

$$Z_{TL}(\omega) = \frac{Y_2}{(R_1 + \frac{Y_2}{R_m}) + j(X_1 Y_2 - \omega L)} \qquad (4.35.)$$

Like before, the modified resonant frequency is calculated by putting the imaginary part of the above mentioned impedance equal to zero and is calculated as

$$Y_2(X_1 Y_2 - \omega L_L) = 0$$

or,
$$X_1 Y_2 = \omega L_L$$

or,
$$(\omega C_m - \frac{1}{\omega L_m})(R_1^2 + \omega^2 L_L^2) = \omega L_L$$

or,
$$(\frac{\omega^2}{\omega_n^2} - 1)(R_1^2 + \omega^2 L_L^2) = \omega^2 L_L L_m$$

or,
$$(\frac{\omega^2}{\omega_n^2} R_1^2 - \omega^2 L_L^2 - R_1^2 + \frac{\omega^4 L_L^2}{\omega_n^2}) = \omega^2 L_L L_m$$

or,
$$\omega^4 \left(\frac{L_L^2}{\omega_n^2}\right) + \omega^2 \left(\frac{R_1^2}{\omega_n^2} - L_L^2 - L_L L_m\right) - R_1^2 = 0$$

Hence,
$$\omega = \sqrt{\frac{\pm\sqrt{\left(\frac{R_1{}^2}{\omega_n^2}-L_L{}^2-L_LL_m\right)^2+4\frac{L_L{}^2}{\omega_n^2}R_1{}^2}-\left(\frac{R_1{}^2}{\omega_n^2}-L_L^2-L_LL_m\right)}{\frac{2L_L{}^2}{\omega_n^2}}}$$

Considering the rational value only and denoting the modified resonant frequency as ω_{rl}, it can be written,

$$\omega_{rl} = \sqrt{\frac{\sqrt{(R_1^2-L_L^2\omega_n^2-\varepsilon\omega_n^2)^2+4L_L^2R_1^2}-(R_1^2-L_L^2\omega_n^2-\varepsilon\omega_n^2)}{2L_L^2}} \qquad (4.36.)$$

where $R_1 = (R_L + R_C)$ and $\varepsilon = L_LL_m$. The modified resonant frequency (ω_{rl}) can be tuned by changing L_L.
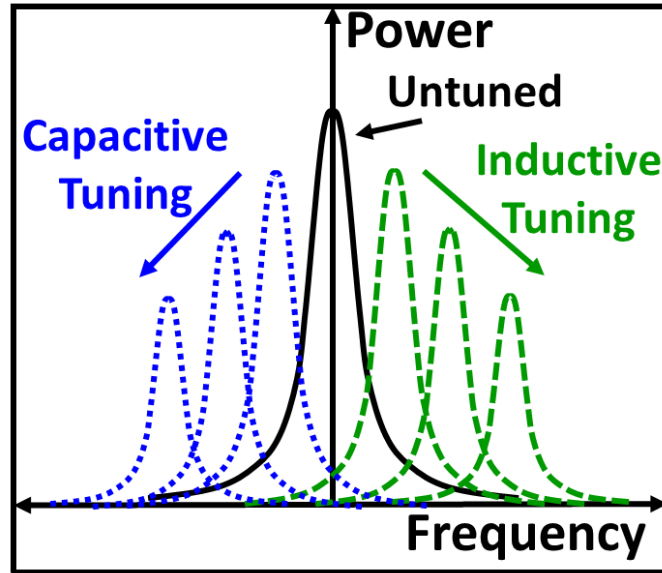
Fig. 4.10: Pictorial representation of the bidirectional tuning using two different complex load topologies. By changing inductive load, the resonant frequency has been modified in the upper direction whereas the same has been modified in the lower direction by changing capacitive load.

The effect of using capacitive and inductive loads compared to a simple resistive load is shown pictorially in Fig. 4.10. By increasing load capacitance the frequency can be tuned in the low frequency direction and similarly by increasing load inductance the resonance frequency can be tuned in the higher frequency direction. The tuning of the resonance frequency using inductive and capacitive load configurations is shown theoretically (Appendix I) in Fig. 4.11 (a) and (b) respectively. For both of these plots, the parameter values $m=3\times10^{-3}$, $\gamma=15$ and $R_C=1000$ are chosen, while the load capacitance and load

inductance are varied for different R_L values. It is to be noted that in both cases, the resonance frequency cannot be tuned for an infinite range, but can be tuned only up to a critical value beyond which the resonant frequency again comes close to its untuned value. However for increasing R_L, the capacitive tuning range widens and that critical value of maximum tuning is achieved with smaller C_L, whereas the inductive tuning range widens by lowering R_L and the maximum tuning is obtained with lower values of L_L.
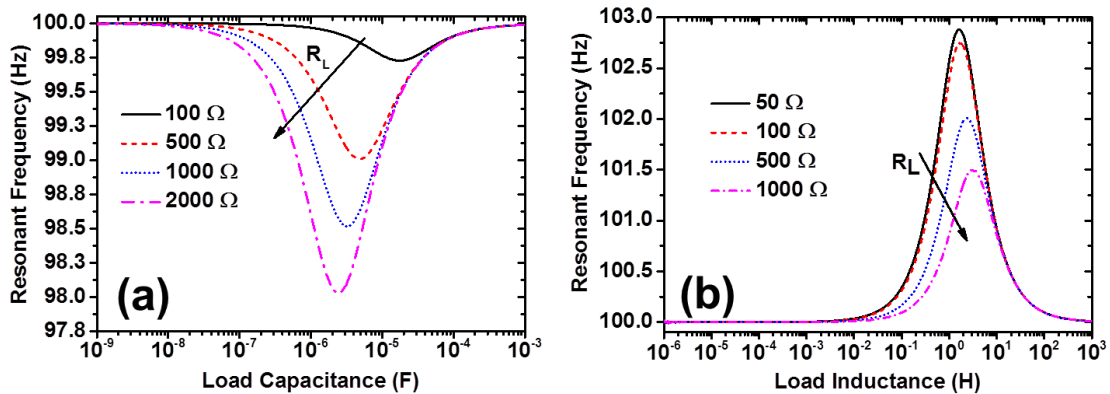
Fig. 4.11: Effect of Load Resistance on electrical tuning in case of (a) capacitive tuning, (b) inductive tuning.
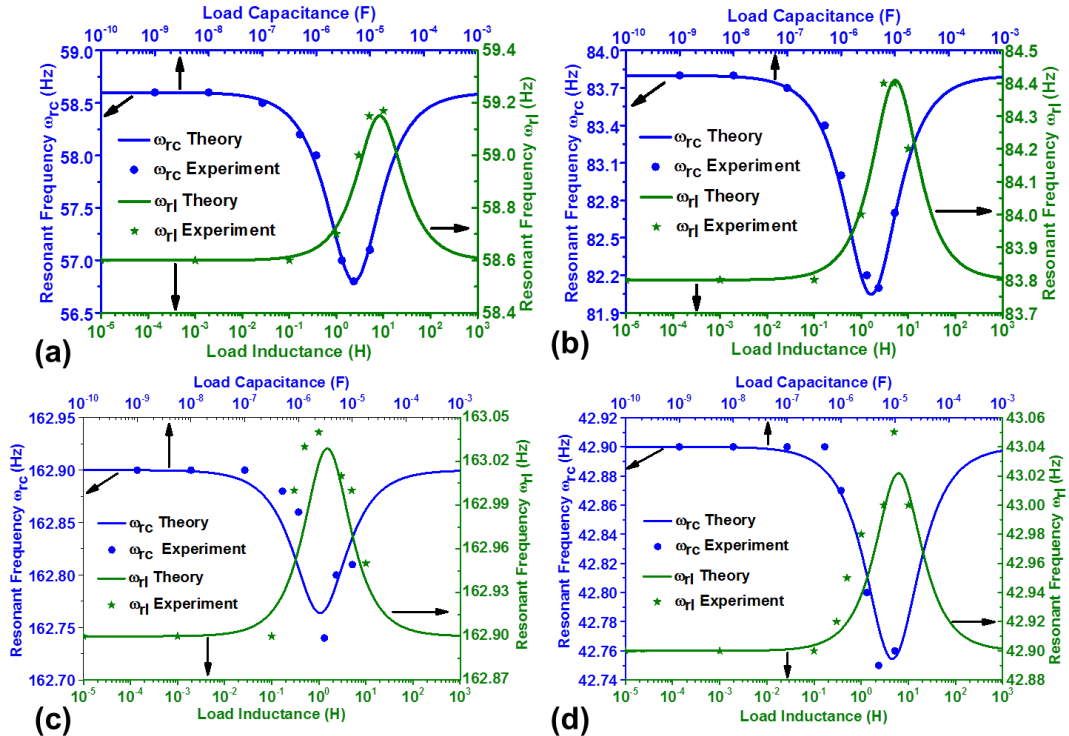
Fig. 4.12: Comparison between experimental and theoretical variation of resonant frequency at 0.3g acceleration level, with load capacitance and load inductance of (a) P1 at optimized load resistance 2400 Ω (b) P2 at optimized load resistance 2100 Ω (c) P3 at optimized load resistance 780 Ω and (d) P4 at optimized load resistance 900 Ω.

4.4.2. Experimental Study of Bidirectional Electrical Tuning and Analysis: In this section, the experimental study on the resonance frequency tuning by using two complex electrical load topologies of the four FR4 based linear EM harvesters are reported. The theoretical bidirectional electrical tuning capabilities of the four prototypes are investigated using the parameter values from Table 4.2 in equations (4.33) and (4.36) respectively and they are shown in Fig. 4.12 by the solid lines. The values of the load resistance (R_L) are maintained at their optimum values for each of the prototypes during tuning operation. Experimentally, the capacitive and the inductive loads are varied using commercially available variable capacitance (range: 100 pF - 11 µF) and variable inductance (range: 1 µH – 11 H) decade boxes while the resistive load is maintained at its optimized value. Since the electrical tuning of relatively smaller volume EM energy harvesters is addressed in this work to validate the developed model, not much attention is paid at this stage in optimizing the physical sizes of the inductors and capacitors for a given application. The load capacitance was varied between 1 nF and 100 µF and similarly the load inductance was varied between 1 µH and 11 H for each of the prototypes. As shown in the Fig. 4.12, the nature of variation of the resonance frequency has the same trend as predicted from the theoretical analysis. For P1, the maximum tuning of 1.8 Hz could be achieved in the low frequency direction using capacitive load topology at C_L = 5µF whereas a maximum tuning of 0.57 Hz is obtained in the high frequency direction using inductive load topology at L_L = 10.15 H. The same values for P2 are 1.75 Hz at C_L = 3.58 µF and 0.6 Hz at L_L = 5.47 H respectively. However, for P3 and P4 the tuning ranges are smaller and thus difficult to detect. As a result, the responses are recorded a number of times and the average was taken to reduce the error; still the matching accuracy with theoretical plots are not as high as in the case of P1 and P2. A maximum capacitive tuning of 0.16 Hz is obtained at C_L = 3 µF and a maximum inductive tuning of 0.13 Hz is achieved at L_L = 1 H for P3. For P4, those values are 0.16 Hz at C_L = 5 µF and 0.13 Hz at L_L = 5.13 H. The reason for the smaller bidirectional tuning ranges of P3 and P4 are due to very small electromagnetic coupling compared to those of P1 and P2. For Prototype 1 (P1) using capacitive and inductive tuning methods, the resonant frequencies can be tuned up to 3.07% and 0.97% of their resonant values whereas for Prototype 2 (P2) those values are 2.09% and 0.72% respectively. For P3 and P4, the tuning ranges are smaller. The percentages of capacitive and inductive tuning for

P3 are 0.01% and 0.008% whereas the same values for P4 are 0.37% and 0.30% respectively.
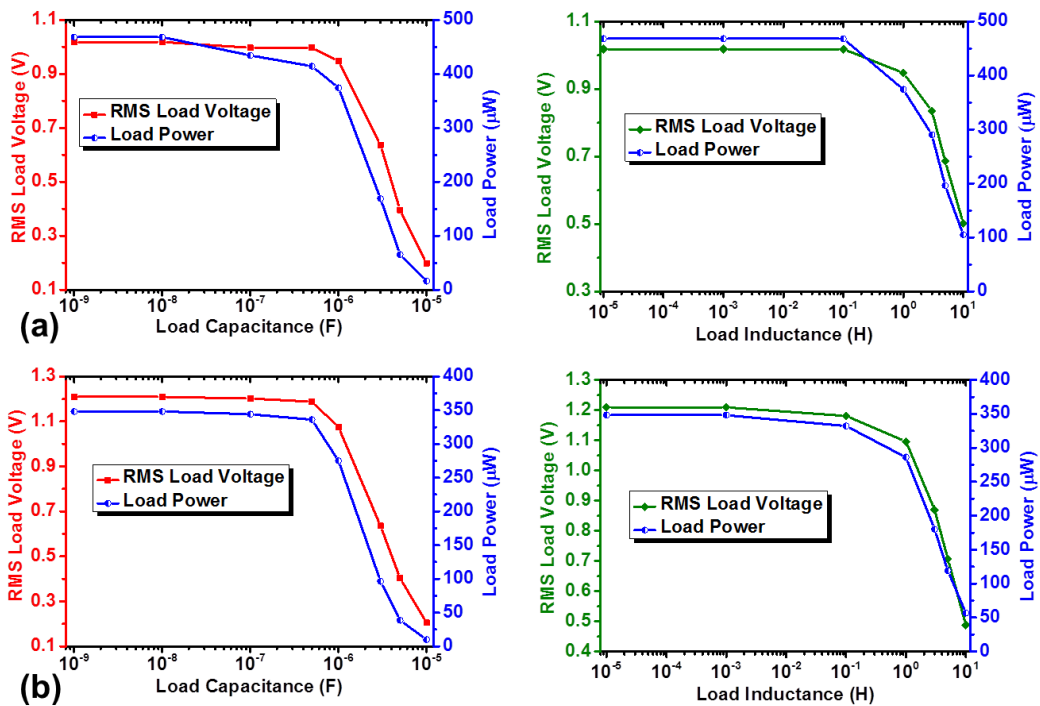
Fig. 4.13: Variation of RMS Load Voltage and Average Load Power at 0.3g with load capacitance and load inductance for (a) Prototype 1 (P1) and (b) Prototype 2 (P2).
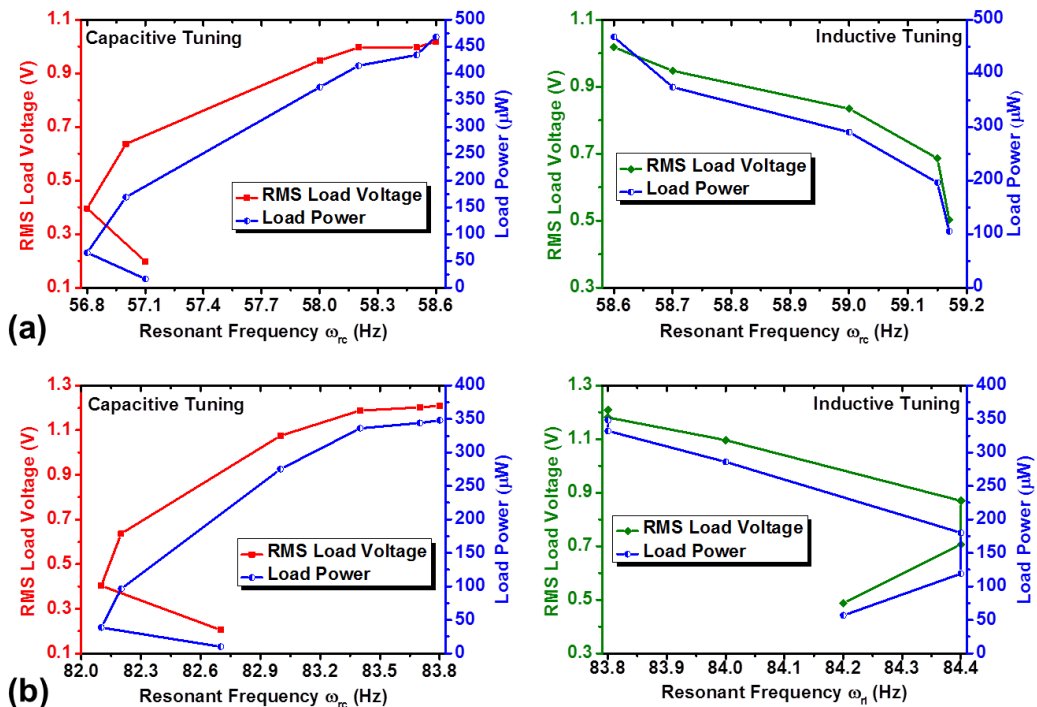
Fig. 4.14: Variation of RMS Load Voltage and Average Load Power at 0.3g with resonant frequency for (a) Prototype 1 (P1) and (b) Prototype 2 (P2).

The dependence of the rms load voltage and average load power on the load capacitance and load inductance are shown from experiment for P1 and P2 in Fig. 4.13 (a) and 4.13 (b). Both the load voltage and power remain the same almost up to 500 nF of load capacitance in both the devices, after which they start falling and become very small at large capacitance values. The same happens in the case of inductive tuning; the respective quantities remain unchanged almost up to 0.1 H and then start rising. The experimental variations of the above two mentioned quantities with resonance frequency are obtained by combining Fig. 4.12 (a), 4.13 (a) and Fig. 4.12 (b), 4.13 (b) and plotted in Fig. 4.14 (a) and 4.14 (b).
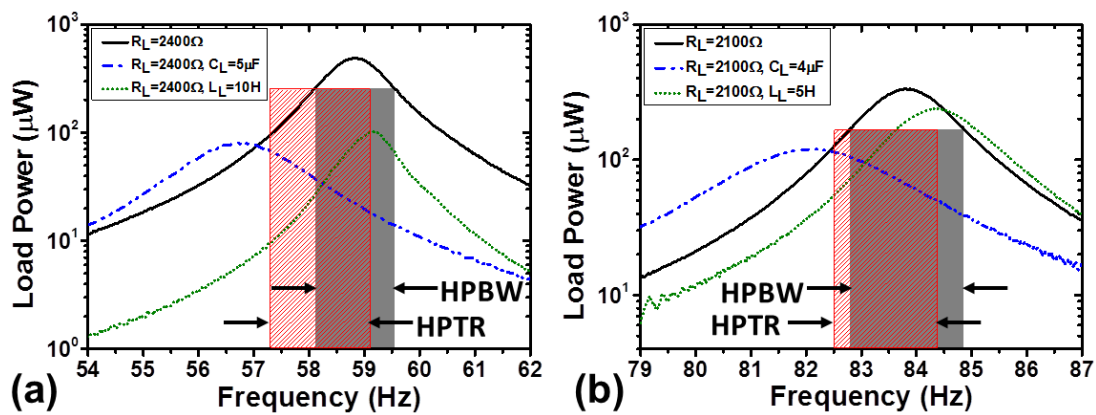
Fig. 4.15: Comparison of the load power spectra of (a) Prototype 1 (P1) and (b) Prototype 2 (P2) at untuned (resistive load only) and maximally tuned conditions (resistive and reactive load components). Half Power Band Widths (HPBW) of the untuned harvesters are shown by the shaded regions and the tuning range in which the output power doesn't drop below half of the maximum power of the untuned harvesters, Half Power Tuning Ranges (HPTR), are indicated by the red patterned regions.

Though the resonant frequency can be tuned by changing the reactive part of the generalized load, the output power and voltage also fall down also with this change. For P1, the average output power at the edge of the maximum capacitive tuning range is 65.36 μW, which is 13.96% of its untuned value, whereas the edge of the maximum inductive tuning range is 105 μW, which is 22.43% of its untuned value. Similarly for P2, the average output power drops at the maximum capacitive tuning point to 11.11% of the untuned value and that drop becomes 33.1% in the case of inductive tuning. It is apparent from Fig. 4.14 (a) and 4.14 (b) that the tuned frequency ranges over which the load powers of P1 and P2 remain above their untuned half power values are 1.89 Hz and 1.85 Hz respectively. Fig. 4.15 compares the power spectra of P1 and P2 under untuned and the maximally tuned conditions at 0.3g input acceleration. The half power bandwidths of

P1 and P2 under untuned conditions are 1.54 Hz and 2.1 Hz respectively; they are also marked in Fig. 4.15 by the shaded regions. The tuning range over which the output power doesn't drop below half of the maximum power of the untuned harvesters is also indicated by the patterned regions in Fig. 4.15. Though there has been an improvement of 0.35 Hz for P1 in terms of its half power frequency performance the same for P2 drops by 0.25 Hz. Due to tuning, not only the load power but also the Q-factor of the devices changes. The Q-factor of untuned P1 is 38.05, whereas at the edge of the capacitive tuning range the Q-factor reduces to 22.72 and at the edge of the inductive tuning range it changes to 49.29. Similarly, the untuned Q-factor of P2 is 39.9 which becomes 21.6 at the limit of capacitive tuning and 38.3 at the limit of inductive tuning. Thus electrical tuning also modulates the total damping co-efficient (ρ_T) of the energy harvesting devices ($Q = \frac{1}{2\rho_T}$).

As discussed already, the maximum value of the capacitive tuning range could be improved by increasing the value of R_L at a relatively small value of C_L, whereas the maximum value of the inductive tuning range could be enhanced by decreasing the value of R_L at a relatively small L_L. The optimized value of R_L is maintained for the untuned devices throughout the study to produce the maximum output power. Thus, there exists a trade-off between the achievable tuning range and the output power, which could be addressed with devices having large electromagnetic coupling, as discussed below.

Zhu et. al. [126] defined the electromagnetic coupling factor, E_C as:

$$E_C = \frac{\gamma^2}{R_C} \qquad (4.37.)$$

As per their derivation, higher values of E_C account for the wider tuning range. For our prototypes P1 and P2, E_C has a value of 0.17. For P3 and P4, E_C has a value of 0.0016. Maximum capacitive tuning ranges of 1.8 Hz, 1.75 Hz, 0.16 Hz and 0.16 Hz are achieved for P1 – P4 respectively, whereas maximum inductive tuning ranges of 0.57 Hz, 0.6 Hz, 0.13 Hz and 0.13 Hz are obtained for the same devices. Zhu et. al. [126] have demonstrated a tuning range of 0.15 Hz for a micro energy harvester (E_C=0.0035) and a tuning range of 4.2 Hz for a macro energy harvester (E_C=552.25) by changing load capacitance only. By modifying both the resistive and reactive elements of the load simultaneously, Cammarano et. al. [125] have tuned their experimental energy harvester, which has an electromagnetic coupling factor (E_C) of 9.50, up to 4.5 Hz in the up direction and up to 4.6 Hz in the down direction, respectively. In this study, the optimum

value of load resistance is maintained for all the devices during tuning. However, by changing R_L this tuning range could be modified as shown in Fig. 4.11. Also, it is observed that the bidirectional tuning range is high for P1 and P2 compared to that of P3 and P4 due to almost 10 times larger electromagnetic coupling. The tuning range could be widened to a greater extent with even smaller load reactance values for devices with higher electromagnetic coupling. The main advantage of bidirectional electrical tuning is that the complexity is low as compared to other tuning mechanisms. However, the limitation of this approach in real applications is that a finite number of discrete reactive load components cannot produce a system with continuously variable tuning. Thus in order to achieve efficient and continuous tuning, proper control electronics with an appropriate interface are required for realtime modification of the reactive components which could be realized using micromachined MEMS devices [223]. However, detailed study of such control unit is outside the scope of the current work and it could be the target of a future study.

4.5. Demonstration of Complete Energy Harvesting Solution including Linear Generator (P1) and Off-the-shelf Power Management:

It is mentioned in chapter 2 that power management is an integral part of energy harvesting research and is as important as power generation. The focus of this thesis is mostly oriented towards transducer development. However, for demonstration of the developed prototypes, an off-the-shelf energy harvesting power management board is used. A potential application of vibration energy harvesting could be acoustic emission monitoring of industrial machines. This intended industrial application for the developed generators can cross the limit and can be widened to include laboratory or building HVAC monitoring. This is due to the fact that the sources of vibration in most cases are similar and are related to the operation of a motor. An air compressor unit, for example, supplying several laboratories within a building was studied previously as a potential source of mechanical energy [62]. The electric motor runs continuously whilst the compressor is duty cycled to maintain the pressure within an in-line reservoir tank. The vibration levels and frequencies have been measured at various locations on the compressor and electric motor. The measured results indicate several resonances between 43 and 109 Hz with acceleration levels between 0.019g and 0.37g.

For such applications, the linear generator prototype P1 is considered, which has been studied extensively in previous sections. It has a resonance frequency of 58.6 Hz. The equivalent circuit of an EM VEH device is derived in section 4.4.1 and the circuit is shown in Fig. 4.9, where R_m, L_m and C_m are respectively the electrical resistance, inductance and capacitance equivalents of the mechanical parameters. The corresponding values for P1 are 5.72 kΩ, 421 mH and 24 μF, respectively. This equivalent circuit model is shown later in place of an EM VEH device for a complete system demonstration using off-the-shelf components.
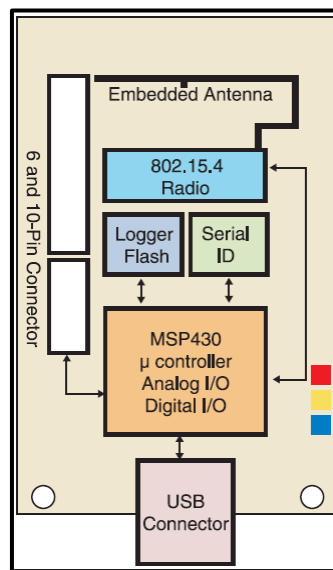
Fig. 4.16: Standard TelosB mote block diagram [224].

4.5.1. Calculation of Power Consumption by a WSN Mote:

Before working on the power electronics circuit for EM VEH devices, the average power consumption of a standard WSN mote is calculated experimentally. This gives an estimate of the power required for operation of the WSN for different applications. For such power consumption calculation, a Crossbow's TelosB mote (TPR2400) is considered, which is an open source WSN platform developed by UC Berkeley [224]. It contains a Texas Instruments MSP430F1611 low power microcontroller unit, an on board ADC controller to monitor a super capacitor voltage (2.5 – 3.5 V) and a CC2530A Zigbee Transceiver. For application purposes, it may contain the following sensors: Light Sensor (0-1000 Lux), Light Sensor (0-140K Lux), Temperature Sensor (PT100 with 0.5ºC resolution and range of -20 to 75ºC). The mote requires a regulated supply voltage of 3V. The WSN gets active twice each hour for 30 milli-seconds each, called the active mode. It requires a current of 20 mA (I_a) during its active mode. For the rest of the time, the WSN

is in sleep mode where the required current is 13 μA (I_s). The measured current requirements for the WSN mote are shown in Fig. 4.17 for active and sleep modes. The average power required by the mote is

$$P_{avg} = \frac{1}{T}\left(2 \times \int_0^{0.03} 3 \times I_a . dt + \int_0^{3599.94} 3 \times I_s . dt\right) = 46\ \mu W \qquad (1)$$

On first initialization of the mote, the high current requirement will be for more than 20 milli-seconds. On average, the current requirement is 100 μA per 2 minutes.
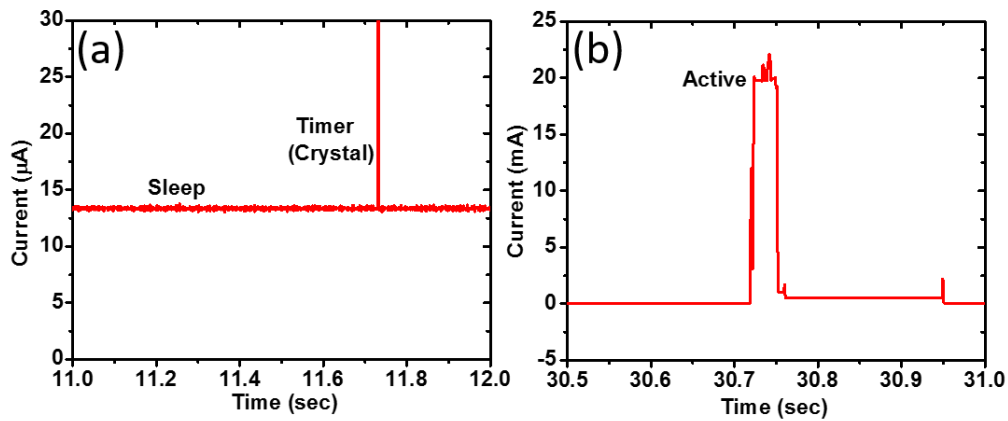
Fig. 4.17: Current consumption by TelosB mote in (a) sleep mode and (b) active mode.

4.5.2. Demonstration using off-the-shelf LTC3588-1 Nanopower Energy Harvesting Evaluation Board:

For complete demonstration of the EM VEH device, an off-the-shelf Linear Technology power management evaluation board is used. The LTC3588-1 is a nano-power energy harvesting power supply [225] from Linear Technology. It has a low-loss full-wave bridge rectifier with a high efficiency buck converter to form a complete energy harvesting solution optimized for high output impedance energy sources. Specifically this module is suitable for piezoelectric generators which are ideally characterized by high output impedance, high output voltage and low output current. Hence, this module is not particularly ideal for low output impedance transducers like EM VEH devices. However, as a first step towards a complete system demonstration, this power management module is chosen. Also, this module is designed for VEH devices and includes an in-built rectifier circuit. The block diagram [225] of the LTC3588-1 is shown in Fig. 4.18. The LTC3588-1 has an internal bridge rectifier which is accessible using the PZ1 and PZ2 input pins where the EM VEH device is connected. The rectified output is stored on a capacitor at the V_{IN} pin and can be used as an energy reservoir for the buck converter. The low-loss

bridge rectifier has a total drop of about 400mV. The EM VEH device inherently possesses low output voltage. Hence, the device is operated at a relatively high input acceleration vis-à-vis high open circuit voltage for the initial demonstration of the complete system. As V_{IN} rises above the Under Voltage Lockout (UVLO) rising threshold, the buck converter is enabled and charge is transferred from the input capacitor to the output capacitor. A wide (~1V) UVLO hysteresis is engaged with a lower threshold (approximately 300mV above the selected regulated output voltage) to prevent short cycling during buck power-up. When the input capacitor voltage is depleted below the UVLO falling threshold, the buck converter is disabled.
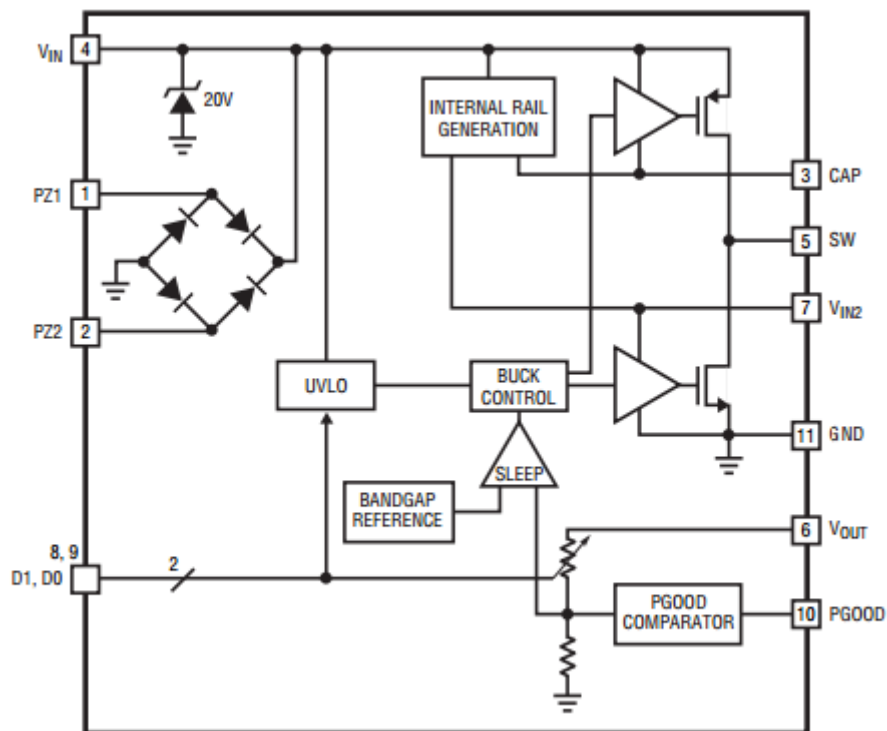
Fig 4.18: Block diagram of LTC3588-1 Nano-power energy harvesting module.

The buck regulator uses a hysteretic voltage algorithm to control the output through internal feedback from the V_{OUT} sense pin. The buck converter charges an output capacitor through an inductor to a value slightly higher than the regulation point. It does this by ramping the inductor current up to 260mA through an internal PMOS switch and then ramping it down to 0 mA through an internal NMOS switch. If the input voltage falls below the UVLO falling threshold before the output voltage reaches regulation, the buck converter will shut off and will not be turned on again until the input voltage again rises above the UVLO rising threshold. V_{IN2} serves as a logic high rail for output voltage select bits D0 and D1. A 4.7µF capacitor is connected from V_{IN2} to GND. For 0/1 values of

D0/D1, the output voltage of 3.3V is selected. A detailed operation of the LTC3588-1 power management module is available on Linear Technology website [225].
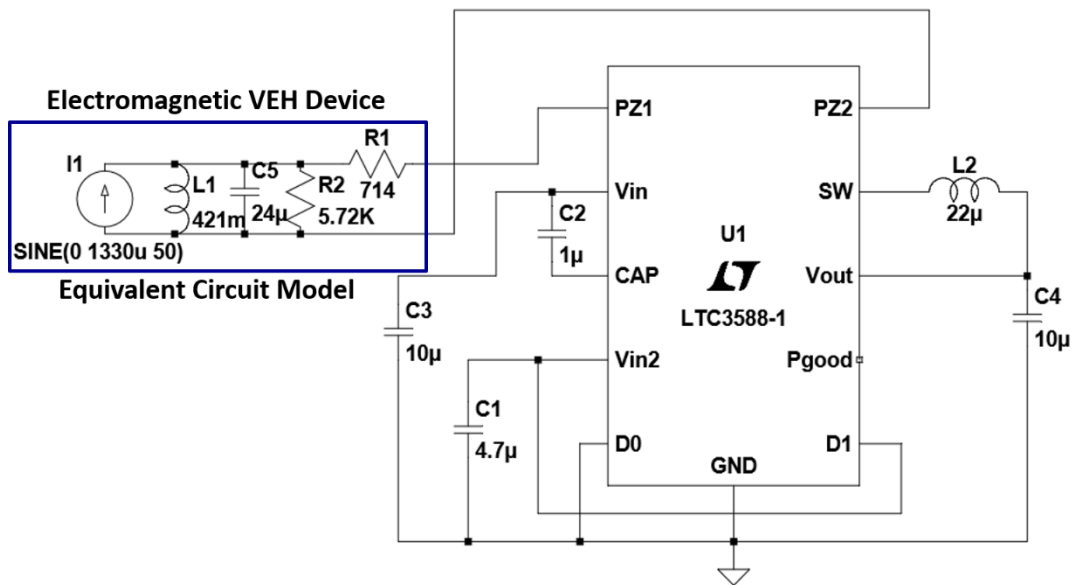
Fig. 4.19: Schematic of the circuit used for complete energy harvesting solution including linear generator (P1) and LTC3588-1 power management.
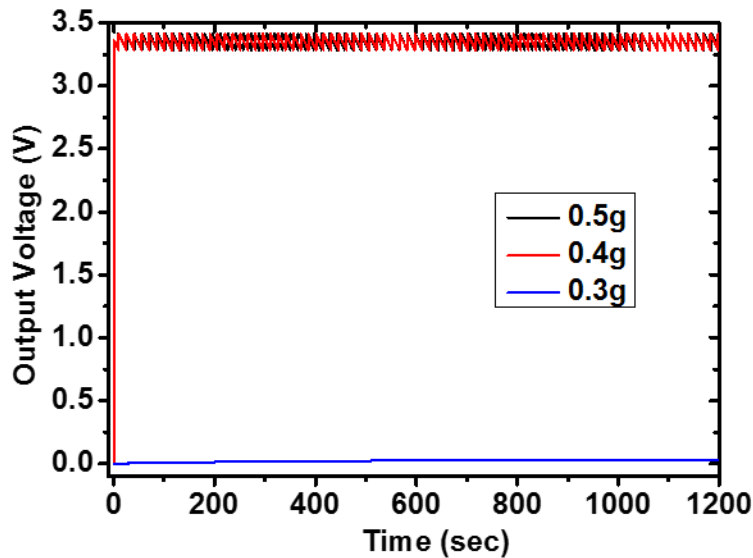
Fig. 4.20: Regulated output voltage of 3.3V at 0.5g and 0.4g from the LTC3588-1 power management circuit.

The schematic diagram of the experimental circuit used for demonstration of the EM VEH device is shown in Fig. 4.19. The EM VEH is represented using the corresponding equivalent circuit as discussed before. Fig. 4.20 shows the measured output voltage of the power management circuit. The experiment showed that the output voltage is 3.3V with low ripple. The output of 3.3V is maintained for acceleration levels of 0.5g and 0.4g, whereas the output does not reach even close to the expected value at 0.3g. This might be

due to the fact that the open circuit voltage of the generator is low at such acceleration compared to the minimum input requirement of the power management circuit. As mentioned earlier, this circuit is designed to work for high impedance sources like piezoelectric generators with high output voltage. However, the power management circuit successfully demonstrated the developed EM VEH device at higher acceleration. For efficient operation under real working conditions such as for industrial machine monitoring, a complete power management solution for low voltage, low impedance sources must be developed. This can be attributed to the future work.

4.6. Conclusions:

In this chapter, linear resonance based generators are studied. First the chapter introduced the basic theory of a resonance based inertial generator and the theory of electromagnetic power transduction. Then bidirectional electrical tuning of four different FR4 based EM harvesters was reported using two different complex load topologies: a capacitive load to tune in the lower frequency direction and an inductive load to tune in the higher frequency direction, respectively. A theoretical model has been derived for this tuning method and study shows that in the case of capacitive tuning, the tuning range widens with an increase in the load resistance whereas the tuning range broadens with a decrease in the load resistance for inductive tuning. Four EM harvesting devices are fabricated on FR4 as the resonating spring material, which differ in their spring configurations to operate at four different resonant frequencies: 58.6 Hz, 83.8 Hz, 162.9 Hz and 42.9 Hz respectively. In the untuned condition, the prototypes P1, P2, P3 and P4 produce 470 μW (at 0.3g), 350 μW (at 0.3g), 4.3 μW (at 0.3g) and 16.5 μW (at 0.3g) at respective optimum loads of 2400 Ω, 2100 Ω, 780 Ω and 900 Ω respectively. Bidirectional tuning has been implemented successfully on the four prototypes and the test results are found to agree well with theoretical predictions. A maximum capacitive tuning of 1.8 Hz, 1.75 Hz, 0.16 Hz and 0.16 Hz are achieved for P1 – P4 respectively whereas maximum inductive tuning of 0.57 Hz, 0.6 Hz, 0.13 Hz and 0.13 Hz is obtained for the same devices. Result also show that the output load power and load voltage drop with tuning as only 13.96% and 22.43% of the untuned power are obtained at the maximum tuned frequencies for capacitive and inductive tuning in case of P1 and 11.11% and 33.1% for P2. The tuning ranges could be modified by using different values of load resistance and this method could be very useful for high-Q, largely electromagnetically coupled EM harvesters.

Finally, for a complete demonstration of the linear generator (P1), an off-the-shelf power management circuit LTC3588-1 is used which has an internal low loss bridge rectifier and buck converter. Ideally such a circuit is suitable for high impedance sources like piezoelectric generators. However, the circuit is used here for demonstrating the developed linear generator (P1) in potential applications. Development of an efficient power management circuit for low voltage, low impedance sources like EM VEH devices will be undertaken in future.

Chapter 5

Multi-frequency MEMS EM Energy Harvesters

5.1. Introduction:

The previous chapter deals mainly with single degree of freedom (SDOF) resonance based meso-scale generators and their frequency tuning. In a number of applications such as industrial machines, pump and ferry vibrations, there are multiple peaks within a close frequency range of the available vibration spectra [226]. Hence, multi frequency generators could be quite useful in these applications, having different resonance frequencies of the VEH devices matched to different source frequencies. In this chapter, multi-frequency MEMS EM energy harvesters are reported employing two different topologies. The first system is single mass, where different fundamental modes are obtained within a close range through spring design innovation, realization of the spring architectures and by using a large magnetic proof mass. The second system is dual mass, which inherently has two major vibration modes corresponding to the movement of each of the masses. The output power is improved in our designs in general by using the bulk magnet as a proof mass compared to the reported MEMS scale EM generators and this high performance is benchmarked through a normalized power density parameter. The spring structures are developed using a Silicon-on-Insulator (SOI) substrate while voltage is induced on double layer electroplated copper coils that are batch fabricated on silicon. The single mass MEMS generator has different fundamental modes in a relatively low frequency (<300 Hz) region with each peak separated from the other by a comparatively small margin. However, the device relies on the different fundamental modes of a single vibrating mass, thus constituting the SDOF system. It is difficult sometimes to design the device in such a way as to bring the other modes such as torsions of a single mass system close to its vertical up-down (out-of-plane) moving mode. On the other hand, the novel

two degree of freedom (TDOF) system inherently has two major vibration modes corresponding to the movement of each of the masses. First, a theoretical model is derived for the MEMS energy harvesting devices and the design methodology and micro-fabrication of the devices are reported. Then Finite Element Method (FEM) simulations are provided to study the static and modal characteristics of the developed devices. Finally, the devices are characterized experimentally and the output responses are explained in terms of the FEM analysis provided.

5.2. Multi-frequency MEMS EM Generator (Single Mass):

5.2.1. Design of the MEMS based Generator: The spring architecture of the vibrating structure is similar to that which was developed for the meso-scale prototype 1 (P1) in the previous chapter but it is efficiently scaled down and optimized for MEMS scale development.
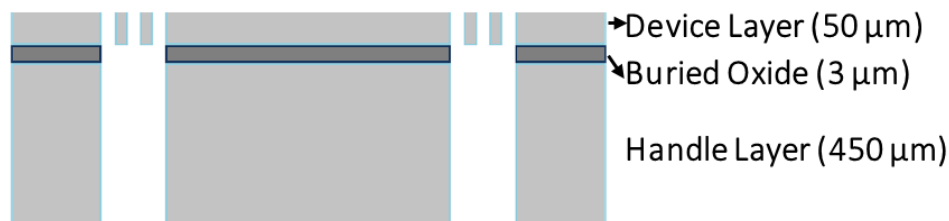
Fig. 5.1: Cross-section image of a micromechanical structure on Silicon-on-Insulator (SOI) wafer. The thin spring arms can be easily fabricated on such wafers.

The MEMS spring structures were planned for development on Silicon-on-Insulator (SOI) wafers. The SOI wafers are very popular and advantageous for developing microelectronic and micromechanical devices [227-228]. The cross-sectional image of a typical SOI wafer is shown in Fig. 5.1, which consists of a bulk silicon handle layer, a buried oxide layer (BOX) in the middle and a thin device layer of silicon on the top. The SOI wafers are mainly developed using a technique called Separation by Implantation of Oxygen (SIMOX) [229]. In this process, the initial silicon wafer is developed using the Czochralski process, followed by oxygen ion implantation on the wafer. Depending on the implantation power and dose, the depth and concentration of silicon dioxide inside the silicon can be defined. A post-deposition thermal annealing at high temperature is then performed in order to realize a uniform and relatively thin layer of silicon dioxide while the top device layer silicon gets separated from the bottom handle layer. The thin device layer of the SOI helps to accurately define many moving parts in micro-electro-

mechanical devices. However, such thinning of the silicon structures is also restricted by process technologies such as clamping issues during dry etching of the bulk silicon etc. For the fabrication described in the following section, the thickness of the spring arms was chosen to be 50 μm to match the Tyndall fabrication facilities conveniently.
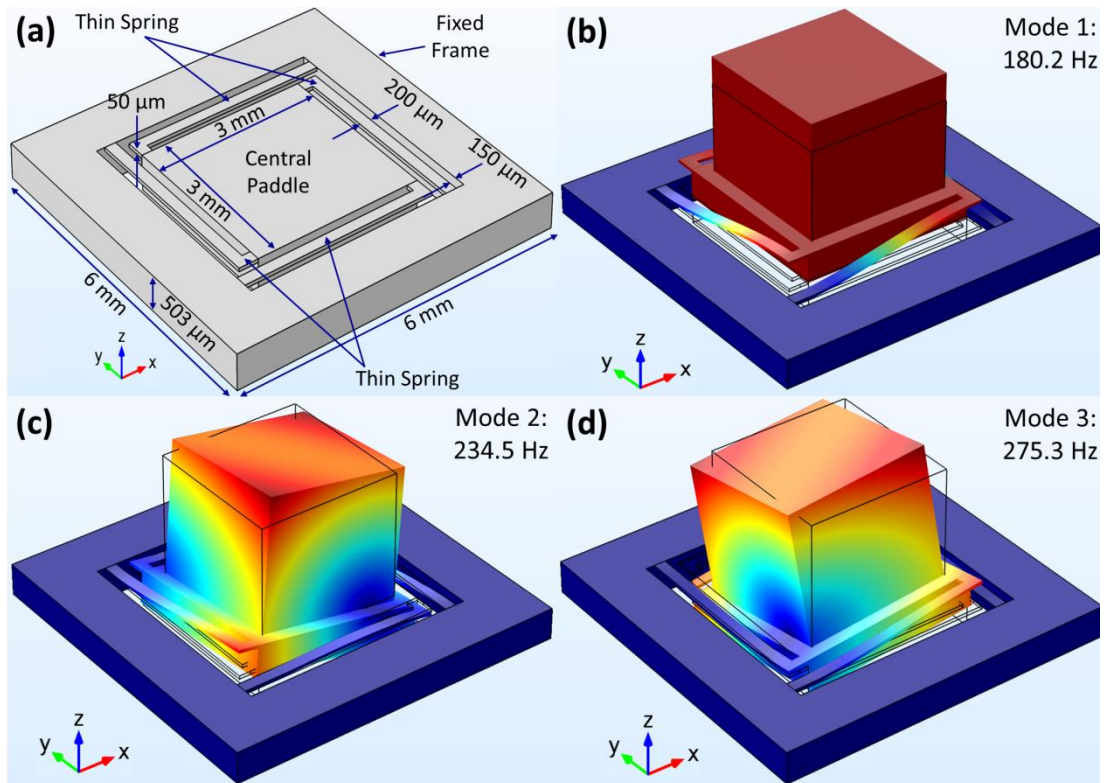
Fig. 5.2: (a) Designed linear spring structure. First three fundamental modes of A1 from COMSOL - (b) Mode 1: Vertically up and down movement, (b) Mode 2: Torsional motion, (c) Mode 3: Another torsional movement.

The designed linear spring structure is shown in Fig. 5.2 (a). The central paddle (3×3 mm^2) is connected to the fixed frame using four L-shaped thin beams. As mentioned, the thickness of the spring arms is defined by the device layer of SOI which is set to 50 μm in this case. A small NdFeB block magnet (2.5×2.5×2 mm^3) is epoxy bonded onto the movable paddle which provides mass (9.83×10^{-5} Kg) for the vibrating oscillator. Larger mass increases the generated power according to equation (4.20). In addition to increasing the power, a large mass together with thin spring arms reduces the fundamental vibration modes of the resonator. Hence, the first few modes of the designed structure are obtained at a relatively low frequency (<300 Hz). The eigen-frequencies of the designed structure are analysed using finite element analysis software COMSOL Multi Physics and are shown in Fig. 5.2 (b-d), which are obtained at 180.2 Hz, 234.5 Hz and 275.3 Hz respectively. In the first mode, the device moves vertically, orthogonal to the device

plane, whereas in the second and third modes, it shows torsional movements in different directions. The presence of multiple peaks in the close frequency range allows generating power from vibration sources with multiple peaks in their spectra. Detailed dimensions of the spring design are provided in Table 5.1.

Parameters	Values
Length of a single beam	3.45 mm
Width of the beams	0.2 mm
Thickness of the beams	50 μm
No of Turns	2500
Dimension of movable paddle	$3 \times 3 \times 0.5$ mm^3
Mass attached (magnet)	9.83×10^{-5} kg
Magnet dimensions	$2.5 \times 2.5 \times 2$ mm^3
Coil footprint	2.8×2.8 mm^2
Coil no. of turns	144
Coil Resistance (R_C)	187 Ω
Gap between magnet and coil	0.8 mm

Table 5.1: Different parameters of the MEMS based linear generator

Double layer electroplated copper coils, used for inducing the voltage due to relative movement between magnet and coil, are fabricated on a separate Silicon substrate. Such a coil consists of two layers of copper with the track width, the inter-track gap and the height of each of the coils being 10 μm, 10 μm and 15 μm respectively. The square-shaped coil has outer dimensions of 2.8×2.8 mm^2. Each of the micro-fabricated double layer coils has 144 turns with the coil resistance of 187 Ω. According to Faraday's law, the induced voltage in the coil is proportional to the rate of change of magnetic flux through the coil. Using simulations in Ansoft Maxwell, the relationship between the magnetic flux density (B) and the gap (z) between the magnet and coil along the center line of the magnet is shown in Fig. 5.3 (a), where B decreases with an increase in the gap distance. At a gap distance of 1 mm, a magnetic flux density of 0.23 T is obtained by assuming the residual magnetic flux density (B_r) of 1.4 T for the NdFeB N52 magnets. The inset figure shows the magnetic flux line distribution along the cross-section. The simulation shows that the magnetic flux density is mostly concentrated near the surface of the magnet and decreases drastically away from the magnet. However, to allow the

movement of the magnets, the gap should be adjusted according to the maximum amplitude of the displacement of the magnets. In the current design, the coil experiences the variation from dense to sparse magnetic field due to the relative motion between the magnet and coil which creates the desired flux gradient. The variation of the static magnetic flux density along the plane of the coil for different distances between the magnet and coil is shown in Fig. 5.3 (b). The change of the slope near the edge of the coil is due to the fact that the width of the coil is greater than that of the magnet.
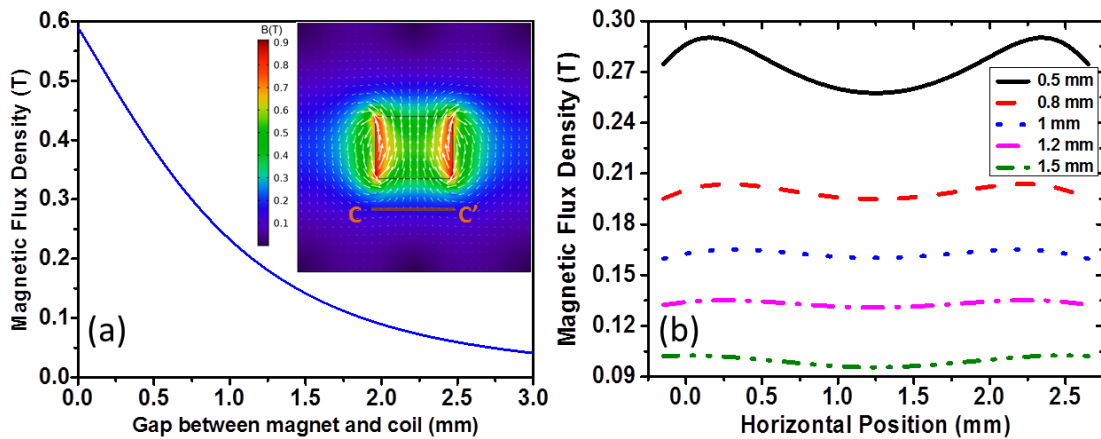
Fig. 5.3: (a) Magnetic flux density along the axis passing through the center of the magnets. The inset shows the magnetic flux line distribution with respect to the rest position of the coil (CC'). (b) Magnetic flux distribution over the plane of the coil for different gaps between the magnet and the coil.
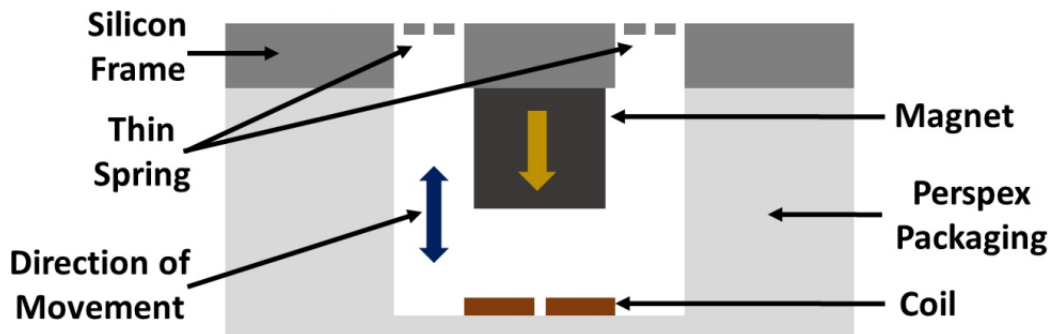
Fig. 5.4: Schematic of the packaged device

The MEMS spring structure together with the bonded magnet and the micro-coil are packaged together to form the MEMS based energy harvesting device. The cross-sectional schematic of the packaged MEMS device is shown in Fig. 5.4. An acrylic spacer is used to create a gap of 0.8 mm between the moving magnet and the fixed coil of the device to allow relative motion between the two.
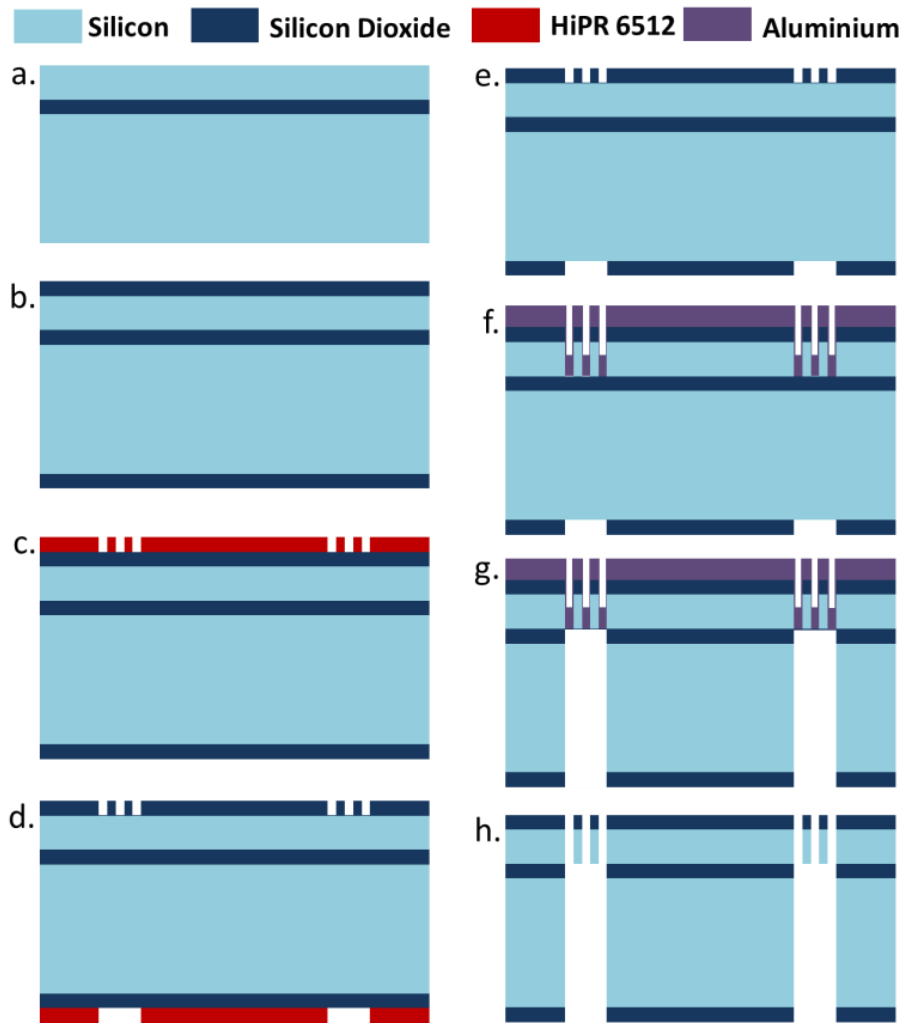
Fig. 5.5: Process flow for fabrication of MEMS nonlinear spring structures on Silicon-on-Insulator (SOI) substrate.

5.2.2. Micro-fabrication Processes: This sub-section describes the microfabrication process steps involved in the development of MEMS based linear generator which was designed and analysed in the previous sub-section. All of the other MEMS devices reported in the following chapters of the thesis are also fabricated in the same process runs in the same wafers. Hence, the fabrication steps mentioned in the following are applicable for all MEMS based devices discussed in this thesis. The device is fabricated in two steps. First, the spring structures are fabricated on an SOI wafer. Second, the double layer micro-coils are fabricated on a Si wafer using electroplating technique. Finally the two components are packaged together and a magnet is bonded on the moving silicon paddle to produce electromagnetic coupling.

The fabrication of the spring structures and micro-coils are described in the following sections.
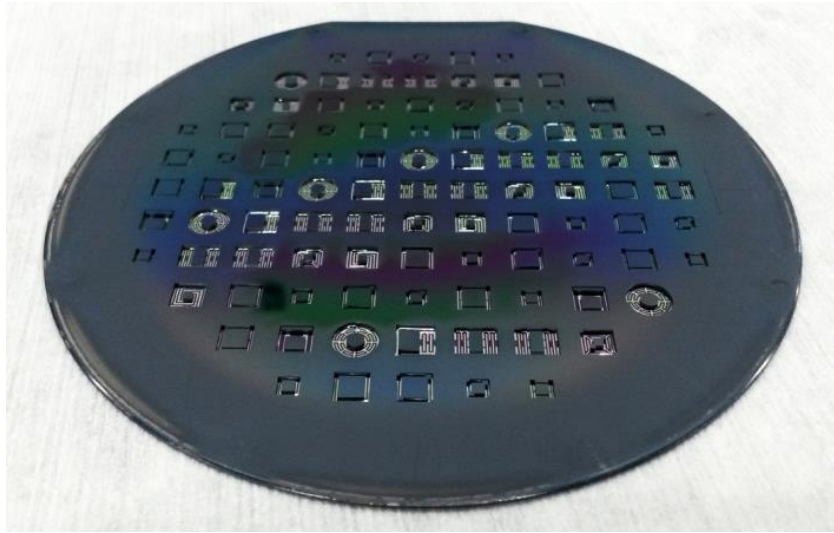
Fig. 5.6: DRIE etched SOI wafer with Sputtered Al layer on the back before dicing.

- **Fabrication of Spring Structure on Silicon-on-Insulator (SOI):** Fig. 5.5 shows the cross-sectional views of the micro-fabrication process flow of MEMS spring structures as indicated in Fig. 5.4. This is a two mask fabrication process. The details of the mask layout are shown in Appendix II, which are designed using Mentor-Graphics IC Station software. The process starts with a 500 μm thick, double side polished Silicon-On-Insulator (SOI) wafer with a device layer of 50 μm, buried oxide layer (BOX) of 3 μm and a bulk handle layer of 450 μm respectively. A 3 μm thick oxide layer is thermally grown using the wet oxidation method on the front and backside of the wafer. The front side oxide layer acts as the mask layer for the front device layer silicon etch whereas the back side oxide acts in same way for the back silicon etch. HiPR-6512 positive photoresist was spun on the front of the wafer; the pattern was transferred using the first mask (L1) and developed subsequently. This first mask is used to define the shape of the thin spring structure on the front side of the wafer. The front oxide layer is etched on the exposed sites using Plasma Enhanced Reactive Ion Etching (PERIE) to reach the device layer silicon. The resist was then stripped off. HiPR 6512 photoresist was spun on the back of the wafer and patterned using a second mask (BACK MASS) to etch the oxide layer for back silicon etching. After etching of the back side oxide layer, the resist was stripped off. The device layer silicon in the front is etched using Deep Reactive Ion Etching (DRIE) up to the BOX layer to define the thin spring structure. 6 μm thick Al layer is sputtered in the front to provide mechanical support to the front silicon spring layer while the back silicon and oxide are etched sequentially. The handle layer silicon in the back is then etched using the DRIE technique, followed by removal of the BOX layer.

The dry etched wafer is shown in Fig. 5.6, where the mechanical structures are still not free due to the presence of the Al layer. The wafer is diced and the sputtered Al layer is wet etched using a commercial etchant solution to release the mechanical structure.

The Scanning Electron Microscope (SEM) image of the spring architecture is shown in Fig. 5.7 . The thin spring arms and bulk central paddles are identified in the tilted image in the right figure.
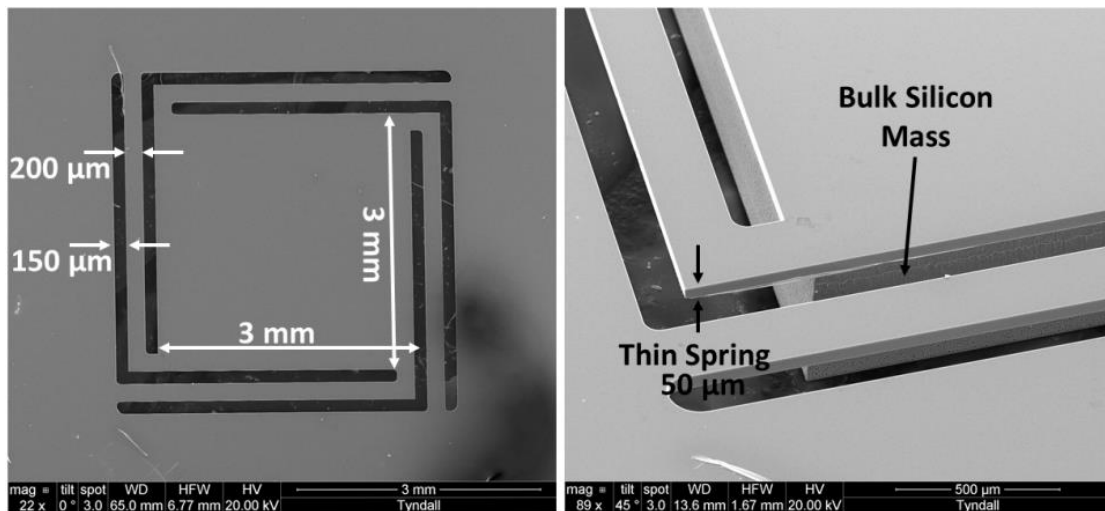
Fig. 5.7: The released mechanical structure (linear resonator). The titled image of the right shows the thin spring and the bulk silicon separately.

- **Fabrication of the double layer copper coil:** The double layer electroplated copper coil is fabricated on a separate Silicon substrate and the corresponding process flow is shown in Fig. 5.8. This is a three mask process. The details of the masks used in the process are shown in the Appendix III. The fabrication process starts by deposition of 1μm oxide layer on Si by wet oxidation followed by sputtering of Titanium/Copper (Ti/Cu) layer of 20/200 nm thickness which act as seed for electroplating. The substrate is then patterned using first mask after AZ9260 positive photoresist (18.6 μm thick) is spin coated. The first layer of copper is electroplated up to 15 μm thickness using digital matrix plating line and the resist is stripped off. Then an optimized double spin coating process is used to develop 38 μm thick AZ9260 resist layer where the via layer is patterned using a second mask. The copper is again electroplated by 10 μm to fill the via and after that the resist is stripped and seed-
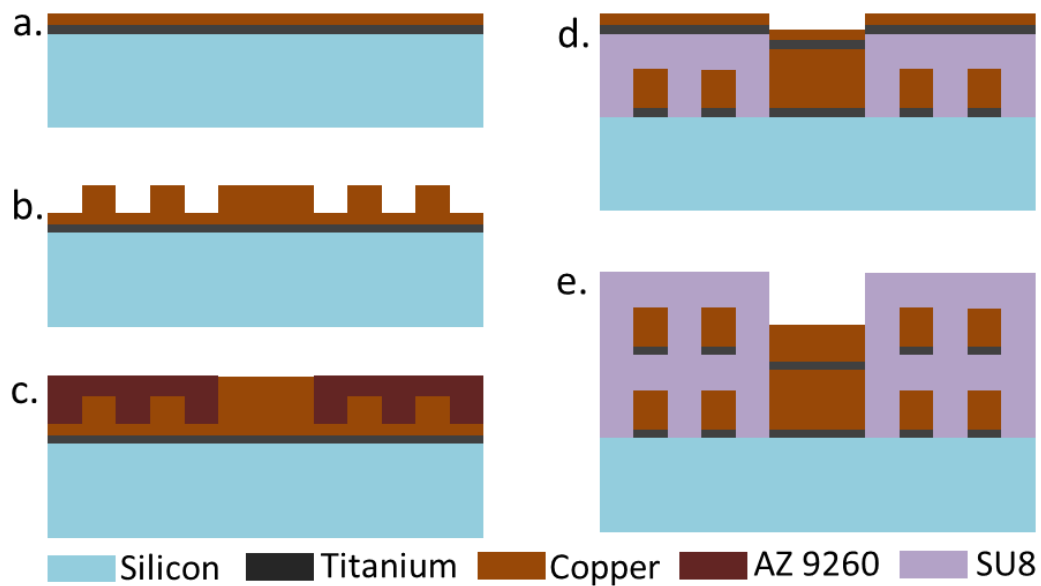
Fig. 5.8: Process flow for fabrication of double layer electroplated copper coil on silicon substrate.

- layers are etched. Next, SU-8 insulation layer is spun to a thickness of 28 μm to isolate the bottom copper tracks from the top layer. Similar seed layers (Ti/Cu) as on the bottom are sputtered again on SU-8. The corresponding layer is patterned using a third mask using AZ9260 resist (19 μm thick) again and then top layer copper is electroplated up to a height of 12.5μm. Similar to the bottom layer, the resist is stripped off and seed layers are etched using HF acid. Finally, another layer of SU-8 (28 μm thick) is spun to provide passivation for the structure. The final fabricated wafer is shown in the Fig. 5.9 (a). The electroplated copper tracks after the first layer of coil deposition are depicted in Fig. 5.9 (b) using SEM imaging. An optical image of a portion of the micro coil is shown in Fig. 5.9 (c) and a cross-sectional image using SEM is shown in the inset which clearly shows the two conductive copper layers of the coil connected at the middle.

- **Device Packaging:** At the packaging stage, the magnets are manually epoxy bonded on the silicon paddle under the optical microscope. In the manual procedure, it is difficult to guarantee exact alignment of the center of the magnet with that of the coil below. However, it is observed using finite element analysis that the slight mismatch between the centers of the magnet and coil does not affect the generated output significantly. The image of the packaged device is shown in Fig. 5.10, having a packaged volume of 0.14 cm^3.
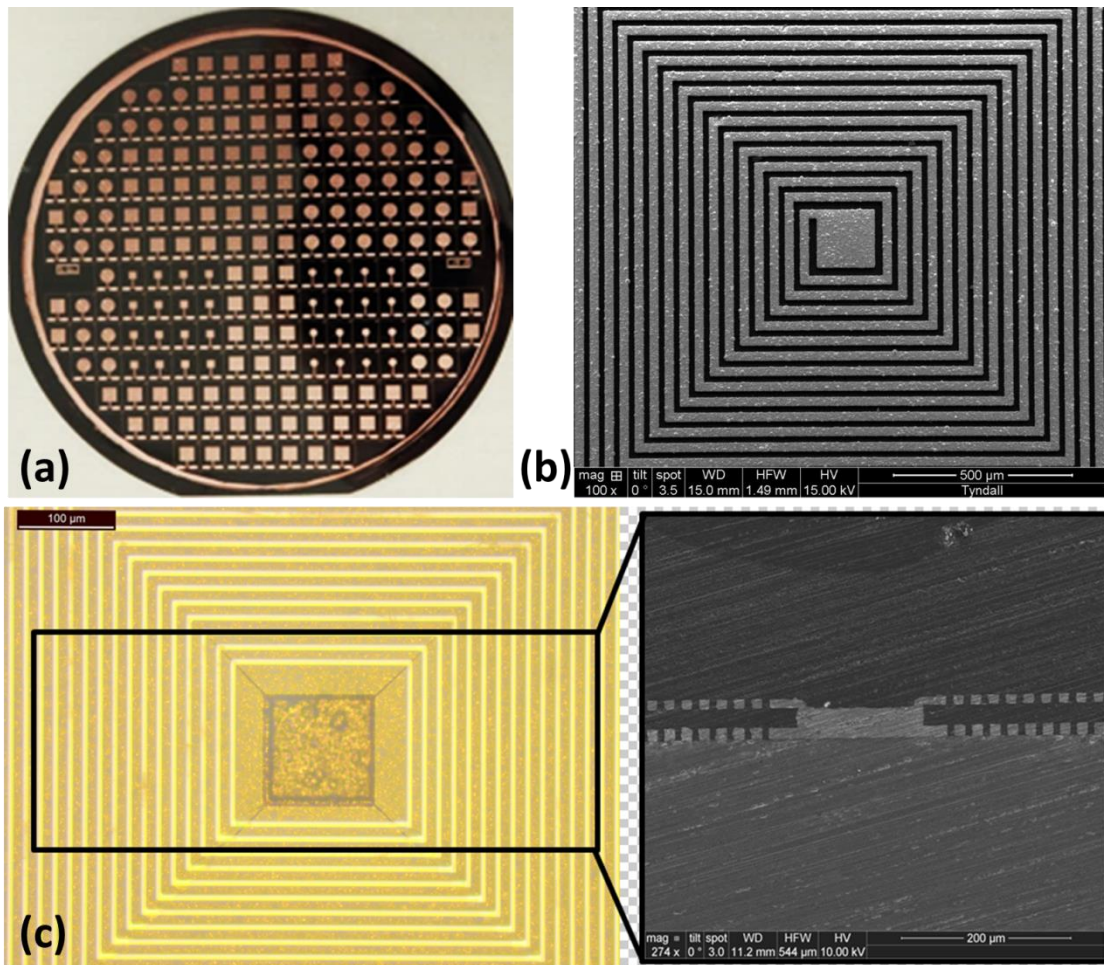
Fig. 5.9: Fabricated wafer with double layer copper coils. (b) Copper tracks after the first layer of electroplating and resist is removed. (c) Optical image of the fabricated micro-coil from the top. A SEM image of the cross-section of the coils is shown as inset. The two layers of copper are clearly visible there.
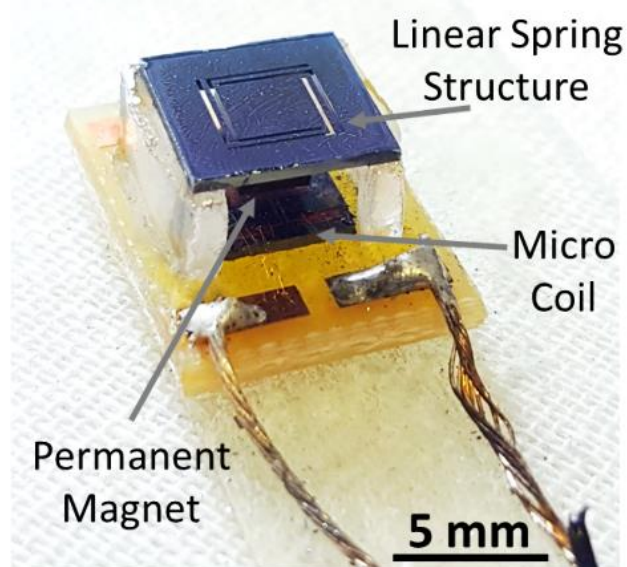
Fig. 5.10: Packaged Linear MEMS generator.
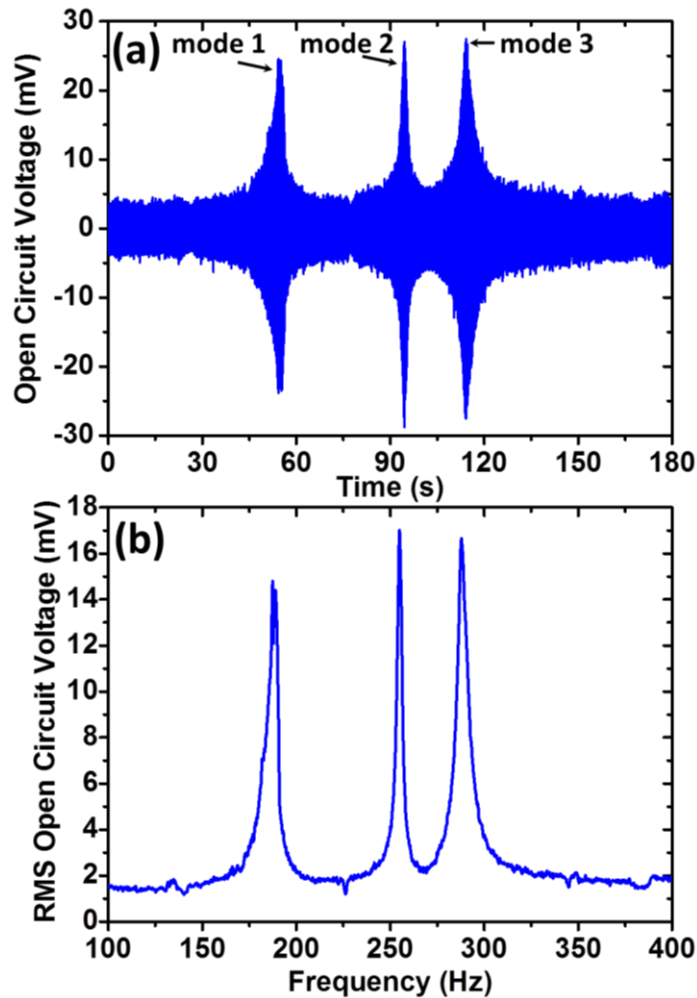
Fig. 5.11: (a) Time history for output open circuit voltage of the MEMS generator as the input frequency is swept from 100 to 300 Hz at 0.5g. (b) The corresponding frequency response.

5.2.3. Results and Discussions: The open circuit voltage time trace for the generator is shown in Fig. 5.11 (a) where the input frequency is swept from 100 to 300 Hz at 0.5g at a rate of 1.67 Hz/sec. The three peaks denote the three fundamental modes of the MEMS spring structure as predicted using the FEM analysis shown in Fig. 5.2. The corresponding RMS open circuit voltage vs. frequency response is obtained using the Fast Fourier Transform (FFT) technique of the time domain data. Three voltage peaks of 14.8, 17.05 and 16.8 mV are obtained at the resonance frequencies of 188, 255.1 and 287.9 Hz, respectively. Based on the FEM analysis results, these three frequencies actually correspond to the out-of-plane motion (mode I) at 180.2 Hz, torsion motion (mode II) at 234.5 Hz and torsion motion in another direction (mode III) at 275.3 Hz, respectively. The obtained modal frequencies match reasonably well with the experimental results but the observed deviation (4 - 10%) could be due to the geometrical variation of the spring structure during the DRIE etch process.
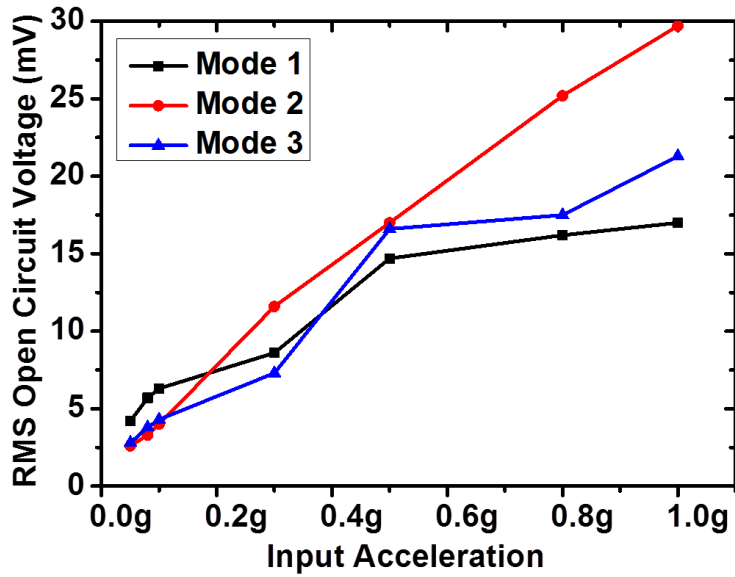
Fig 5.12: Variation of RMS open circuit voltage with the input acceleration.

The variation of the RMS open circuit voltage with the input acceleration is shown in the Fig. 5.12 where the output voltage increases with the input excitation level, as expected, being only 4.2, 2.6 and 2.8 mV at 0.05g for the three different resonance modes which increases to 17, 29.7 and 21.3 mV at 1g. It is to be noted here that the output responses from the three modes are comparable in amplitude. Whereas the device is designed to obtain large out-of-plane motion, the bonding of the large magnet mass could possibly aid the torsional movements in mode 2 and 3 which helps in getting large outputs from those two modes as well.
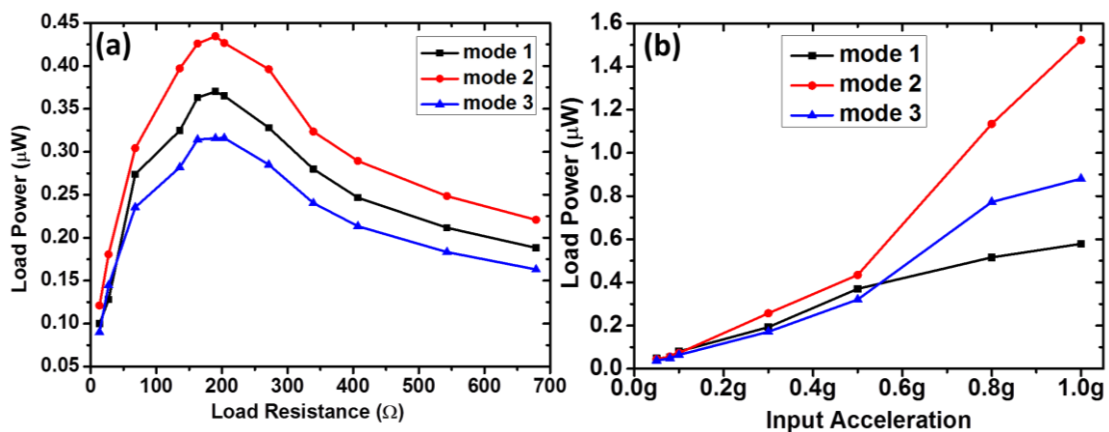
Fig. 5.13: (a) Variation of load power with load resistance and (b) variation of load power with input acceleration.

Next, load resistance is connected to the generator to dissipate electrical power. The variation of the load power of the three modes with the load resistance is shown in Fig. 5.13 (a). The matched load is found to be 190 Ω which is quite close to the coil resistance

($R_C = 187\ \Omega$) value. As described earlier, if the magnetic flux linkage is small so that the electromagnetic damping co-efficient is lower than the mechanical damping, then the maximum power is for load equal to coil resistance. The maximum powers of 0.37, 0.43 and 0.32 µW were obtained at the matched load for an input acceleration of 0.5g and rise to 0.6, 1.5 and 0.9 µW respectively at 1g, as shown in Fig. 5.13 (b). This leads to Normalized Power Densities (NPDs) of 0.04, 0.11 and 0.06 kg.s/m^3 respectively which is among the higher values for MEMS scale EM VEH devices.

5.3. MEMS Two Degrees-of-Freedom (TDOF) EM Energy Harvester:

5.3.1. Theory of TDOF EM Energy Harvester: A single degree of freedom (SDOF) vibration based energy harvesting device is generally modelled as a second order spring mass damper system which was analysed in the previous chapter. Fig. 5.14 (a) on the other hand depicts the model of two degrees of freedom (TDOF) or dual mass system which requires two independent co-ordinates to describe the motion. The system consists of a primary and a secondary spring, at the end of each of which a mass is attached which are called the primary and secondary masses respectively. The coupled second order differential equation of motion for such system can be written in matrix form as

$$\begin{bmatrix} m_1 & 0 \\ 0 & m_2 \end{bmatrix} \begin{pmatrix} \ddot{x}_1 \\ \ddot{x}_2 \end{pmatrix} + \begin{bmatrix} c_1 + c_2 & -c_2 \\ -c_2 & c_2 \end{bmatrix} \begin{pmatrix} \dot{x}_1 \\ \dot{x}_2 \end{pmatrix} + \begin{bmatrix} k_1 + k_2 & -k_2 \\ -k_2 & k_2 \end{bmatrix} \begin{pmatrix} x_1 \\ x_2 \end{pmatrix} = \begin{pmatrix} f_1(t) \\ f_2(t) \end{pmatrix} \qquad (5.1)$$

Where $x_1(t)$ and $x_2(t)$ are the relative displacements of the primary (m_1) and secondary (m_2) masses, c_1, c_2 are the damping co-efficients of the primary and secondary oscillators and k_1 and k_2 are the effective primary and secondary spring stiffness values. The secondary damping c_2 also includes the electromagnetic damping. For a sinusoidal input vibration as mentioned previously, the input forces on the right hand side of equation (5.1) can be written as $f_i(t) = -m_i \ddot{y}(t)$, i=1, 2.

Assuming a steady-state solution of equation (5.1) of the form $x_i(t) = X_i e^{i\omega t}$, it can be written,

$$\begin{bmatrix} m_1 & 0 \\ 0 & m_2 \end{bmatrix} (-\omega^2) \begin{pmatrix} X_1 \\ X_2 \end{pmatrix} + \begin{bmatrix} c_1 + c_2 & -c_2 \\ -c_2 & c_2 \end{bmatrix} (i\omega) \begin{pmatrix} X_1 \\ X_2 \end{pmatrix} + \begin{bmatrix} k_1 + k_2 & -k_2 \\ -k_2 & k_2 \end{bmatrix} \begin{pmatrix} X_1 \\ X_2 \end{pmatrix}$$
$$= \begin{pmatrix} m_1 \omega^2 Y \\ m_2 \omega^2 Y \end{pmatrix}$$

or,

$$\begin{bmatrix} -\omega^2 m_1 + i\omega(c_1 + c_2) + (k_1 + k_2) & -i\omega c_2 - k_2 \\ -i\omega c_2 - k_2 & -\omega^2 m_2 + i\omega c_2 + k_2 \end{bmatrix} \begin{pmatrix} X_1 \\ X_2 \end{pmatrix} = \begin{pmatrix} m_1 \omega^2 Y \\ m_2 \omega^2 Y \end{pmatrix}$$

or,

$$\begin{pmatrix} X_1 \\ X_2 \end{pmatrix} = \begin{bmatrix} -\omega^2 m_1 + i\omega(c_1 + c_2) + (k_1 + k_2) & -i\omega c_2 - k_2 \\ -i\omega c_2 - k_2 & -\omega^2 m_2 + i\omega c_2 + k_2 \end{bmatrix}^{-1} \begin{pmatrix} m_1 \omega^2 Y \\ m_2 \omega^2 Y \end{pmatrix}$$

or,
$$\begin{pmatrix} X_1 \\ X_2 \end{pmatrix} = \frac{\begin{bmatrix} -\omega^2 m_2 + i\omega c_2 + k_2 & i\omega c_2 + k_2 \\ i\omega c_2 + k_2 & -\omega^2 m_1 + i\omega(c_1 + c_2) + (k_1 + k_2) \end{bmatrix}}{\begin{vmatrix} -\omega^2 m_1 + i\omega(c_1 + c_2) + (k_1 + k_2) & -i\omega c_2 - k_2 \\ -i\omega c_2 - k_2 & -\omega^2 m_2 + i\omega c_2 + k_2 \end{vmatrix}} \begin{pmatrix} m_1 \omega^2 Y \\ m_2 \omega^2 Y \end{pmatrix} \tag{5.2}$$

Solving the above matrix equation, the displacements of the primary and the secondary masses are

$$X_1(\omega) = \frac{(-\omega^2 m_2 + i\omega c_2 + k_2) m_1 \omega^2 Y + (i\omega c_2 + k_2) m_2 \omega^2 Y}{\begin{vmatrix} -\omega^2 m_1 + i\omega(c_1 + c_2) + (k_1 + k_2) & -i\omega c_2 - k_2 \\ -i\omega c_2 - k_2 & -\omega^2 m_2 + i\omega c_2 + k_2 \end{vmatrix}} \tag{5.3}$$

$$X_2(\omega) = \frac{(i\omega c_2 + k_2) m_1 \omega^2 Y + (-\omega^2 m_1 + i\omega(c_1 + c_2) + (k_1 + k_2)) m_2 \omega^2 Y}{\begin{vmatrix} -\omega^2 m_1 + i\omega(c_1 + c_2) + (k_1 + k_2) & -i\omega c_2 - k_2 \\ -i\omega c_2 - k_2 & -\omega^2 m_2 + i\omega c_2 + k_2 \end{vmatrix}} \tag{5.4}$$

The absolute values of the respective displacements are derived as

$$|X_1(\omega)| = \sqrt{\frac{((k_2 - \omega^2 m_2) m_1 \omega^2 Y + k_2 m_2 \omega^2 Y)^2 + (\omega^3 c_2 (m_1 + m_2) Y)^2}{(k_1 k_2 + \omega^4 m_1 m_2 - \omega^2 (m_1 k_2 + m_2 k_1 + m_2 k_2))^2 + \omega^2 (m_1 c_2 + m_2 c_1 + m_2 c_2)^2}} \tag{5.5}$$

$$|X_2(\omega)| = \sqrt{\frac{((k_1 + k_2 - \omega^2 m_1) m_2 \omega^2 Y + k_2 m_1 \omega^2 Y)^2 + (\omega^3 c_2 (m_1 + m_2) Y + \omega^3 c_1 m_2 Y)^2}{(k_1 k_2 + \omega^4 m_1 m_2 - \omega^2 (m_1 k_2 + m_2 k_1 + m_2 k_2))^2 + \omega^2 (m_1 c_2 + m_2 c_1 + m_2 c_2)^2}} \tag{5.6}$$

The generalized time response of the primary and secondary masses is given as

$$x_i(t) = |X_i(\omega)| e^{(i\omega t + \theta_i)}, i = 1, 2, \tag{5.7}$$

where θ_i is the phase angle of the respective displacements which can be obtained from equations (5.3) and (5.4).
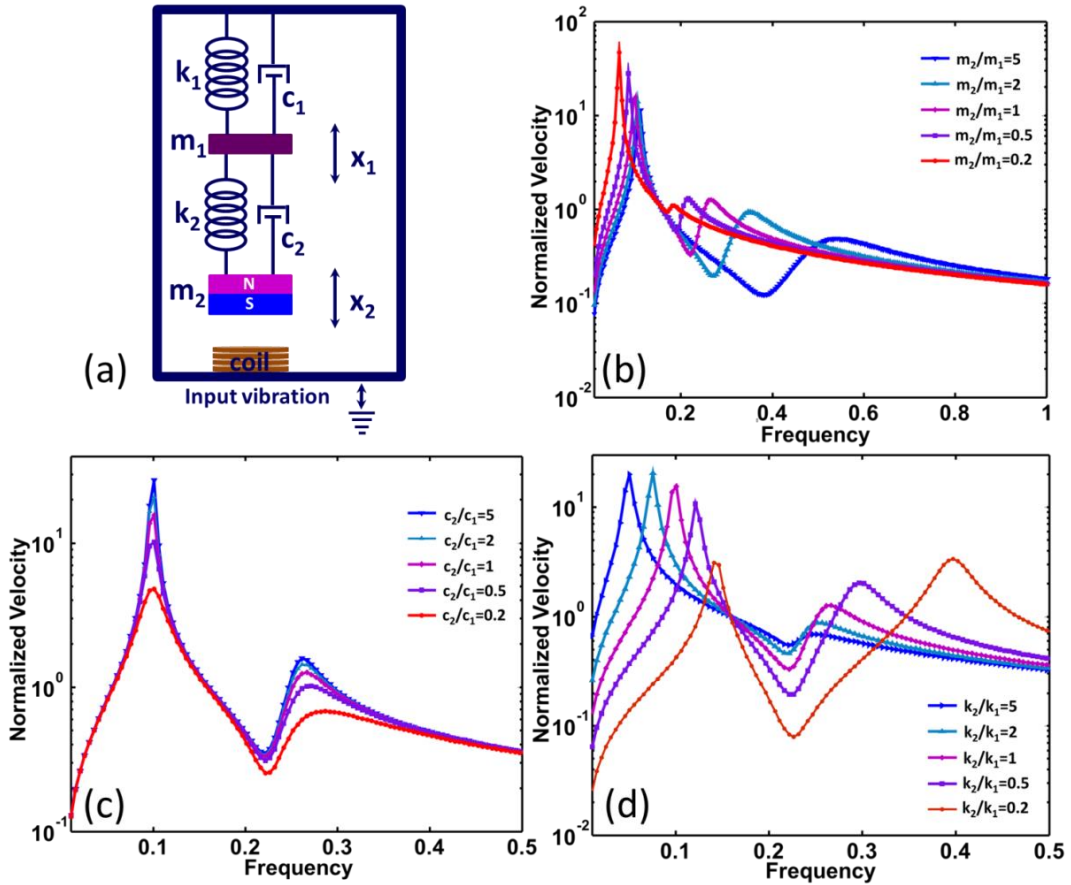
Fig. 5.14: (a) Model of a Two Degrees-of-freedom (TDOF) system. Parametric study of the TDOF system: (b) m_2/m_1, (c) c_2/c_1 and (d) k_2/k_1 are changed while other parameters are kept constant.

By setting the damping co-efficients and the external force to zero in equation (5.1), the resonance frequencies of the dual mass, two degrees of freedom system can be derived as

$$\omega_{n_{1,2}} = \sqrt{\frac{B \pm \sqrt{B^2 - 4m_1 m_2 k_1 k_2}}{2m_1 m_2}} \tag{5.8}$$

where $B = m_1 k_2 + m_2(k_1 + k_2)$. If the forcing frequency is close to any of the resonance frequencies of the system, large displacement occurs, leading to the large output power. In between the two resonances, there is one frequency where the displacement is minimum. This phenomenon of anti-resonance has been utilized in a number of engineering problems to suppress the vibration of a structure etc. The most popular practical application of such 'tuned vibration absorber' is to solve London's Millennium bridge vibration problem [230]. However, we intend to take advantage of the two separate resonances of the TDOF system and increase the energy harvesting capabilities at different input frequencies. The total converted electrical power can be expressed as

$$p_{elec}(t) = c_e \omega |X_2(\omega)|^2 \qquad (5.9)$$
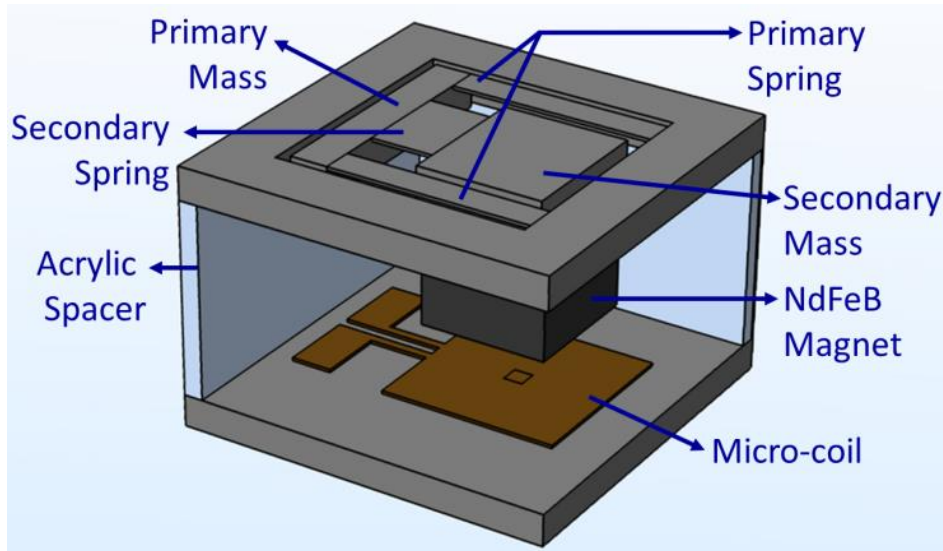
Fig. 5.15: Schematic depiction of the TDOF Device. For clarity, the spacer is not shown on the front sides.

The effect of variation of different parameters on the performance of TDOF system is shown in Fig. 5.14 (b-d). Other parameters remaining same, the first and second frequency peaks shift to higher frequencies and reduce in amplitude when the secondary mass (m_1) is significantly larger than the primary mass (m_1), as shown in Fig. 5.14 (b). On the other hand, comparatively low frequency and large amplitude peaks are obtained when m_1 is much higher than m_2, which is desirable in energy harvesting applications. It is observed from Fig. 5.14 (c) that the primary damping (c_1) changes the output response more significantly compared to the secondary damping (c_2) in terms of peak heights and quality factors. The peak amplitudes can be most effectively modulated through variation of spring constants. When the secondary spring constant (k_2) is much larger than the primary spring constant (k_1), the first frequency peak is much larger than the second peak (Fig. 5.14 (d)). The difference between these amplitudes becomes smaller as k_1 is increased. When k_1 is much higher than k_2, the two peak amplitudes are similar. Thus, by optimizing different design parameters, the output response at two different frequencies can be improved significantly for multi-frequency energy harvesting purposes.
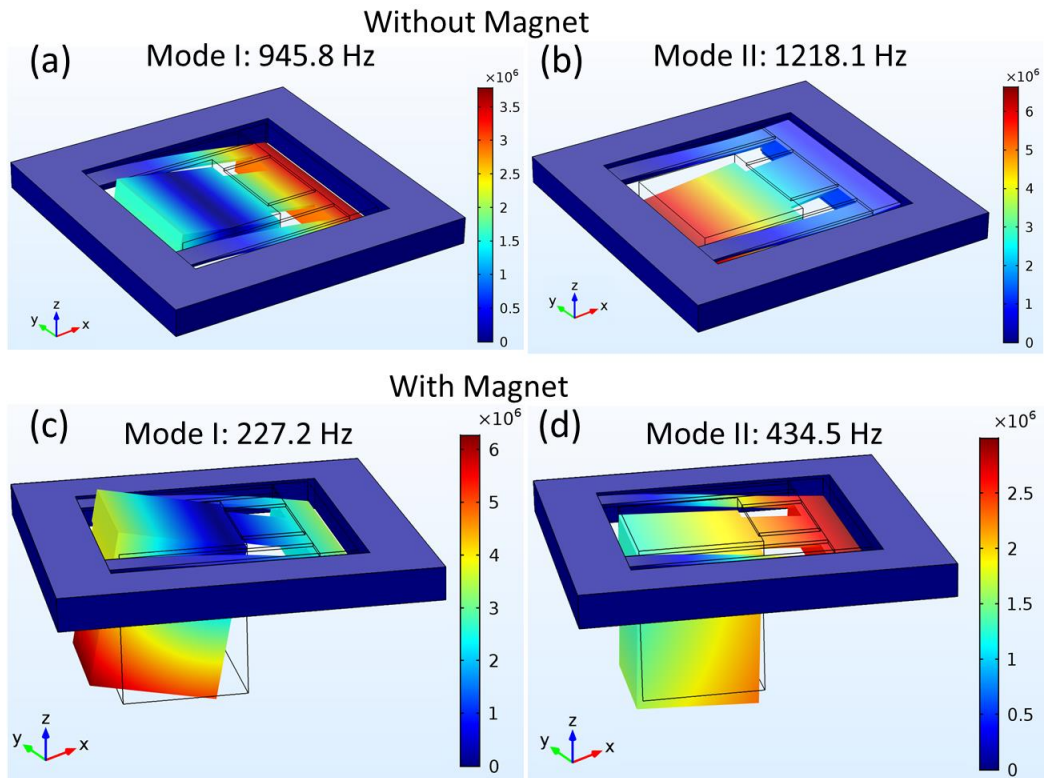
Fig. 5.16: First two fundamental modes of TDOF device without [(a) and (b)] and with [(c) and (d)] the magnet– The primary mass undergoes the maximum displacement in mode I without the magnet whereas the secondary mass undergoes maximum displacement in mode II. This reverses in the presence of the magnet mass.

5.3.2. Design of the MEMS based TDOF Generator: The dual mass system consists of two cantilevers which act as primary and secondary springs. Unlike the model shown in Fig. 5.14 (a), where the secondary spring is extended away from the primary spring tip, here the secondary cantilever is curved inside the primary cantilever. The designed dual mass system, along with the compact spring structure is shown in the Fig. 5.15. It is observed from FEM analysis that if the secondary spring is extended outward from the edge of the primary spring, the gap between the fundamental frequencies of the two cantilevers becomes very large. Like the single mass device reported before, this device is also designed to be fabricated on an SOI substrate. The bulk silicon paddle at the end of the primary spring defines the primary mass whereas the silicon paddle along with an attached NdFeB magnet ($2\times2\times2$ mm^3) defines the secondary mass, making it quite large compared to the primary mass. The eigen-frequency analysis of the dual mass harvester without and with the magnet is shown in Fig. 5.16 using COMSOL. The analysis shows that that the first two fundamental frequencies of the spring structure without the magnet are at 945.8 Hz and 1218.1 Hz, where the primary and secondary mass undergo maximum displacements respectively, whereas the same with the magnet are 227.2 Hz

and 434.5 Hz, where the secondary and primary masses undergo maximum displacements, respectively. An interesting observation here is that though the movements of the primary and secondary masses are in the out-of-plane direction, the tip of the magnet curves an arc of a circle which can be approximated as an in-plane motion. Hence, the dual mass system offers three-dimensional energy harvesting capabilities, being out-of-plane in the first mode and in-plane in the second fundamental mode. Thus energy harvesting capabilities in different directions can be obtained from the same device. Different physical parameters for the designed device are tabulated in Table 5.2.

5.3.2. Electromagnetic model: Electroplated double layer copper coils are used in our designs to induce electrical voltage which is generated due to the relative movement between a moving magnet and a static coil, according to Faraday's law. According to that law, the electromotive force (EMF) of a coil is proportional to the negative rate of change of the magnetic flux.

$$\varepsilon = -\frac{d\varphi}{dt} = -\frac{d}{dt}\sum_{i=1}^{N}(B.A_i) \tag{5.10}$$

Parameters	Values
Length of the primary beam	3.25 mm
Width of the primary beam	1 mm
Length of the secondary beam	1 mm
Width of the secondary beam	1.5 mm
Thickness of the beams	50 μm
Primary Mass	2.5×10^{-6} kg
Secondary (magnet) Mass	68×10^{-6} kg
Magnet dimensions	$2\times2\times2$ mm^3
Coil footprint	2.8×2.8 mm^2
Coil no. of turns	144
Coil Resistance (R_C)	191 Ω
Gap between magnet and coil	0.8 mm

Table 5.2: Different parameters of the MEMS the TDOF Device

where φ is the magnetic flux, N is the total number of loops in the coil, B is the magnetic flux density and A_i is the area included in the i-th loop. However, the magnetic flux is not

same for both the in-plane and the out-of-plane movement of the magnet. For the single mass device, the magnet moves out-of-plane w.r.t the coil in the different vibration modes. The magnet motion is in-plane in the first mode and out-of-plane in the second mode for the dual mass system. The variation of the magnetic flux w.r.t the magnet displacement for both in-plane and out-of-plane motion is shown in Fig. 5.17. For in-plane motion, the magnetic flux becomes maximum when the magnet is in the center position. For out-of-plane motion, the magnetic flux becomes maximum when the magnet comes closest to the coil and reduces gradually as it moves away from the coil. Both the curves are fitted using third order polynomial functions as

$$\varphi = a_3 x^3 + a_2 x^2 + a_1 x + a_0 \tag{5.11}$$
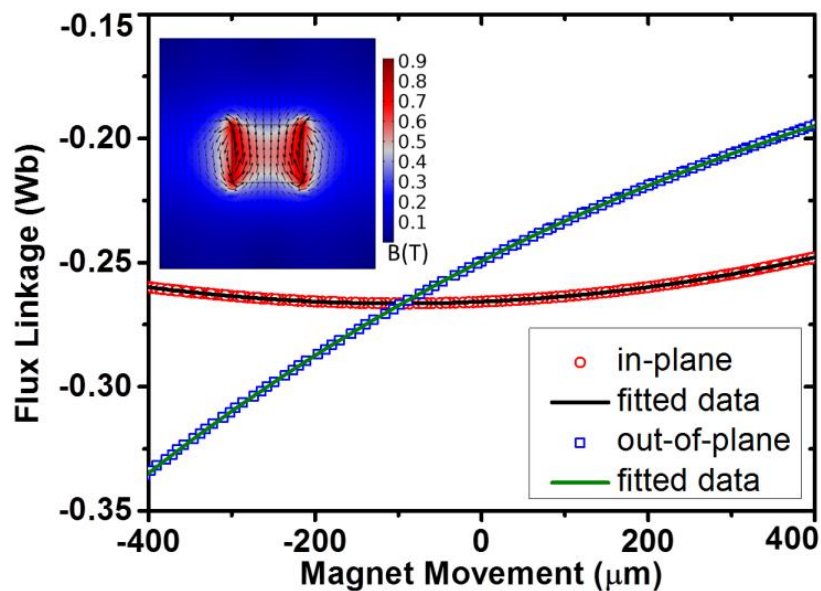
Fig. 5.17: Flux linkage variation for in-plane and out-of-plane motion of the magnet. The inset shows the static magnetic flux distribution of the magnet.

Flux Linkage Constants	In-plane motion	Out-of-plane motion
a_3 (Wb/m^3)	4668.1	31574.8
a_2 (Wb/m^2)	74.2	-96.7
a_1 (Wb/m)	1.4×10^{-2}	17×10^{-2}
a_0 (Wb)	-2.65×10^{-4}	-2.49×10^{-4}

Table 5.3: Flux linkage constants for in-plane and out-of-plane motion of the magnet

where a_3, a_2, a_1, a_0 are constants. The values of these constants for in-plane and out-of-plane movement of the magnet are given in Table 5.3. For a rectangular block magnet, the

magnetic flux density (B) at a distance z along the line passing through the center of the magnet is given as [231]

$$B = \frac{B_r}{\pi} \left[\sin^{-1}\left[\frac{M_W M_L}{4\left[\left(\frac{M_W^2}{4}+z^2\right)\left(\frac{M_L^2}{4}+z^2\right)\right]^{1/2}} \right] - \sin^{-1}\left[\frac{M_W M_L}{4\left[\left(\frac{M_W^2}{4}+(z+M_T)^2\right)\left(\frac{M_L^2}{4}+(z+M_T)^2\right)\right]^{1/2}} \right] \right]$$

(5.12)

where B_r is the remanent magnetic flux density, M_L, M_W and M_T are length, width and thickness of the magnet respectively. In our designs, NdFeB N52 magnets with residual magnetic flux density (B_r) of 1.4 T are used. The inset of Fig. 5.17 shows the static magnetic flux line distribution along the cross-section of the magnet using Maxwell Ansoft 2D software.

A Scanning Electron Microscope (SEM) image of the double mass spring structure is shown in Fig. 5.18 (a). The thin spring arms and bulk silicon masses are identified in the tilted image in Fig. 5.18 (b).
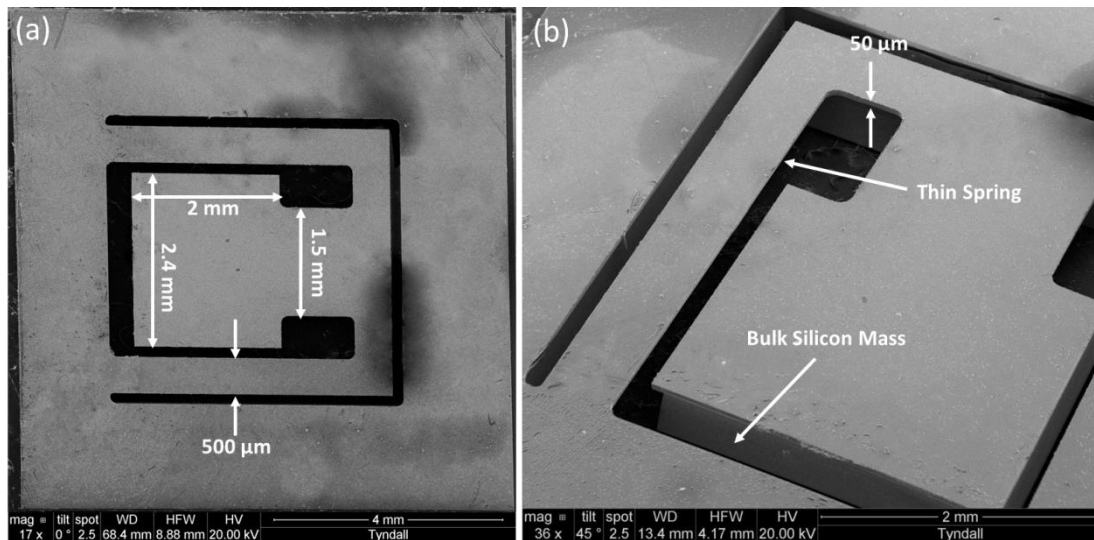
Fig. 5.18: SEM images of the (a) Double mass spring structure (b) Ttilted image to show the thin spring arm and bulk silicon paddle.

The image of the packaged double mass TDOF device is shown in Fig. 5.19, where the packaged device has a volume of 0.14 cm^3.
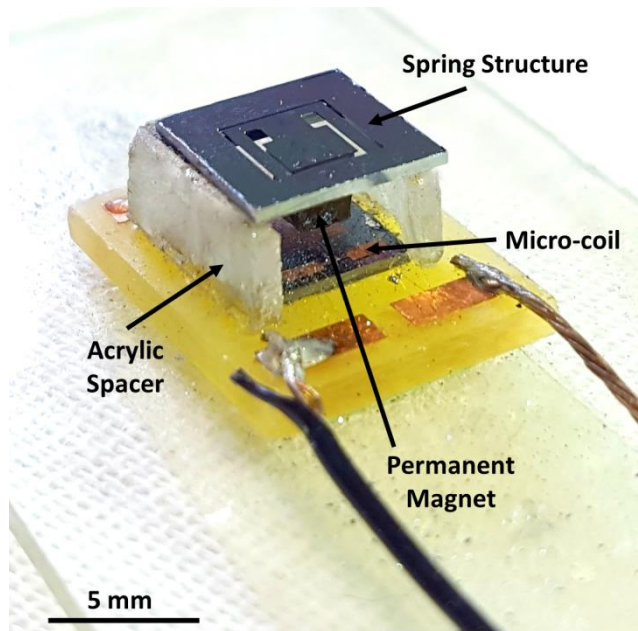
Fig. 5.19: Fabricated and fully packaged the TDOF MEMS harvester.
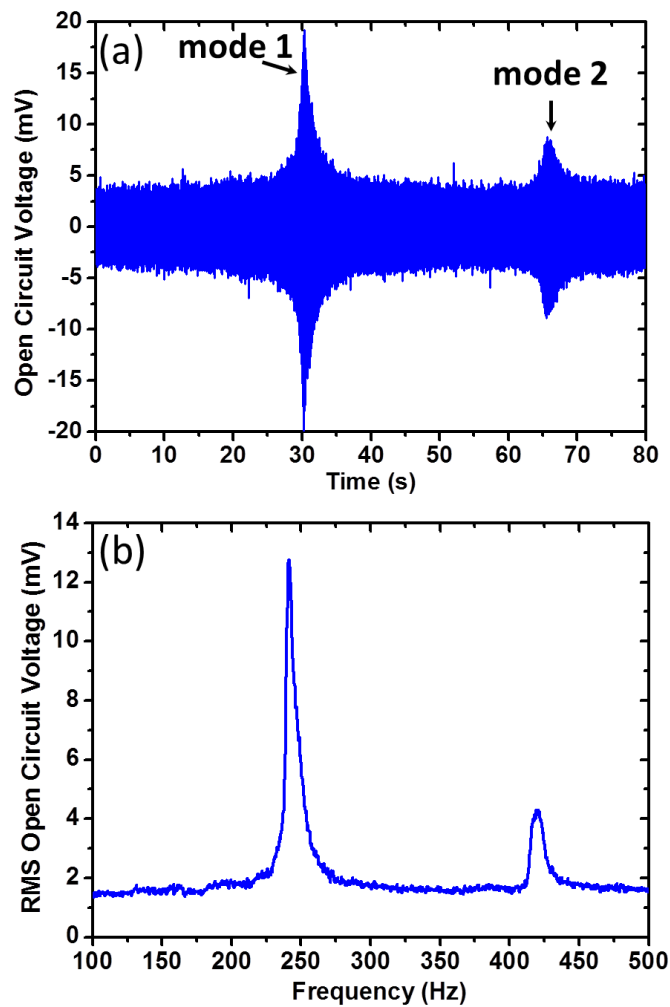

Fig. 5.20: (a) Time history for output open circuit voltage of the TDOF device as the input frequency is swept from 100 to 300 Hz at 0.5g. (b) The corresponding frequency response.

5.3.3. Results and Discussions: The time history of the DMD under no-load condition is depicted in Fig. 5.20 (a) as the input vibration frequency is varied from 100 to 500 Hz at a fixed acceleration of 0.5g at a rate of 1.67 Hz/sec. It is observed from the time trace that the large amplitude voltage peak is generated at the lower frequency which is due to the large amplitude motion of the magnet in the low frequency mode, creating higher electromagnetic flux linkage. The magnet covers a comparatively much lower motion range in the high frequency mode as observed from the modal analysis. Hence the generated voltage is much lower there. From the FFT plot in Fig. 5.20 (b), the two peaks are generated at 241.4 Hz and 419.6 Hz respectively. The obtained values are close to simulated modal frequencies of 227.2 Hz and 434.5 Hz. Similar to the single mass MEMS device, here also the reason for the discrepancy could be due to the mismatch between the designed and final fabricated geometric parameters. The calculated open circuit quality factors (Qoc) of the two modes are 46.28 and 39.33 respectively.

The load power variation of the two natural modes of the device for varying load resistance (R_L) is shown in Fig. 5.21 (a) at an acceleration of 0.5g for comparison with the single mass device. The matched load in this case is also equal to the internal load of the coil (R_C=191 Ω). In the first mode, the maximum electrical power that is transferred to the load is 0.22 μW. That value reduces to 0.02 μW in the second vibration mode due to the aforementioned reason. The maximum load power rises to 1.13 μW and 0.07 μW respectively at 1g acceleration, as shown in Fig. 5.21 (b).

Table 5.4 summarizes the output performances of the TDOF MEMS device in a nutshell.

Output Parameters	Experimental Results
Resonance Frequencies (Hz)	241.4 (mode I), 419.6 (mode II)
RMS Open Circuit Voltage at 0.5g (mV)	12.8 (mode I), 4.34 (mode II)
Matched Load (Ω)	190
Load Power at 0.5g (μW)	0.22 (mode I), 0.024 (mode II)
NPD (kg.s/m^3)	0.08 (mode I), 0.01 (mode II)

Table 5.4: Summary of experimental output performances of the DMD
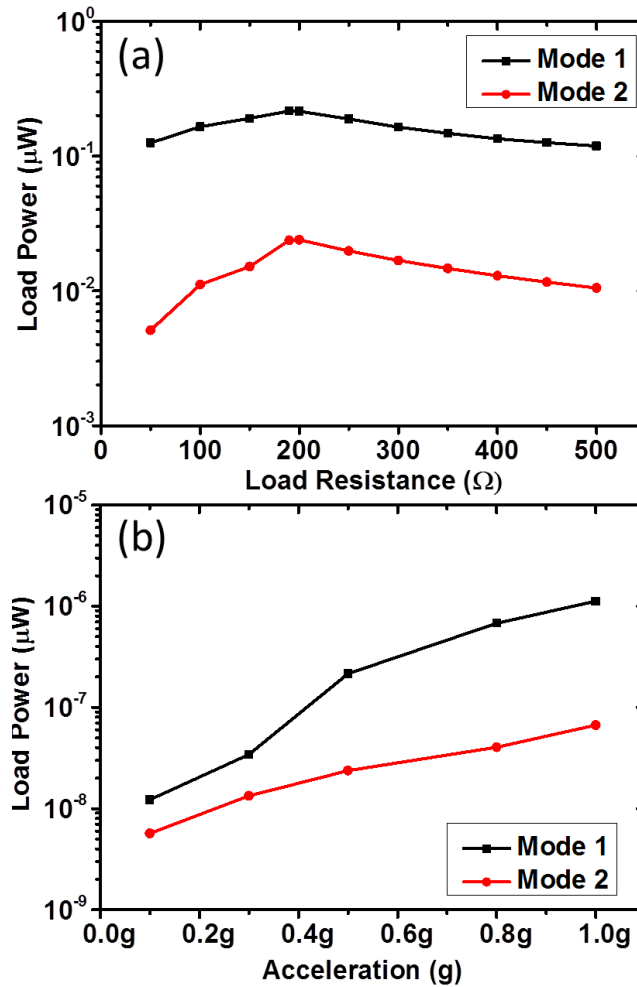
Fig. 5.21: (a) Variation of load power of the different modes of DMD with load resistance and (b) variation of load power with input acceleration.

5.4. Conclusions:

This chapter reports multi-frequency MEMS electromagnetic energy harvesters employing two different topologies. The first system is single mass, where different fundamental modes are obtained within a close range through spring design innovation, realization of the spring architectures and by using a large magnetic proof mass. The second system is dual mass, which inherently has two major vibration modes corresponding to the movement of each of the masses. The output power is improved in the design, in general, by using the bulk magnet as a proof mass compared to the reported MEMS scale EM generators and this high performance is benchmarked through the normalized power density parameter. The spring structures are developed using a Silicon-on-Insulator (SOI) substrate while voltage is induced in a double layer electroplated copper coils.

A single mass MEMS multi-frequency generator is designed to accommodate different fundamental frequency modes in close proximity, at the same time being in the low frequency range (<300 Hz). The MEMS generator is fabricated in two steps: the vibrating spring structure is fabricated using DRIE etching process whereas high efficiency, double layer copper coil is developed using electroplating technique. The first three fundamental frequencies of the generator are found to be 188, 255.1 and 287.9 Hz, respectively, where comparative output responses are obtained from each of the peaks, making it a suitable design for multi frequency input vibration applications. The device produces 0.6, 1.5 and 0.9 μW, respectively, at 1g input acceleration for a matched load of 190 Ω, which leads to Normalized Power Densities (NPDs) of 0.04, 0.11 and 0.06 kg.s/m^3 respectively, being one of the highest values for MEMS scale EM VEH devices.

For the dual mass, TDOF MEMS device, 3D finite element analysis shows that different modes are activated in the low frequency (< 500 Hz) region. The first two modes of the dual mass device are at 241.4 Hz and 419.6 Hz respectively. At 0.5g, the dual mass device generates 0.22 and 0.02 μW in modes I and II respectively against matched load. The experimental results are qualitatively explained using the simulation results and indicate a good potential in the development of multi-frequency energy harvesters for a number of practical applications.

Chapter 6

Nonlinear Energy Harvesters

6.1. Introduction:

The last two chapters deal with the single degree-of-freedom linear systems, their resonance frequency tuning and multi degree-of-freedom systems. Such approaches are applicable if the external vibration source spectrum has discrete peaks. But if the vibration varies continuously then wideband generators are essential. In chapter 2, recent developments in the field of wideband energy harvesting has been reviewed including the devices using nonlinear oscillation principles. It is observed that the majority of the nonlinear energy harvesting techniques are either bulky or require some extra components which make them not suitable for MEMS scale integration. The geometric nonlinearity arising due to the stretching strain based monostable systems are rather easy to implement as the source of nonlinear stiffness in such systems is from the special design of the spring arms.

In this chapter, the focus is on miniaturized, nonlinear monostable hardening structures where a beam with a fixed-guided configuration produces nonlinear stretching strain in addition to linear bending strain under large deflection. First, a proof-of-concept device is developed at meso-scale which is further optimized to get improved performance. Later, two MEMS electromagnetic energy harvesting systems are studied. The nonlinear spring architecture is varied in the two different spring structures to study the consequent effect on the wideband output response. Using suitable design choices of the spring architectures, different fundamental modes are obtained close to each other, while further widening the output response. The devices are characterized at a different level of MEMS integration to obtain a comparative result. However, before starting with the prototypes, it is worth to understand the behavior of a nonlinear oscillator as different parameters are varied. In the following section, the dynamical equations of a nonlinear oscillator are normalized for simplification and to investigate the change in output response of the

oscillator with parametric variation. A theoretical framework is also developed to gain insight into the source of nonlinearity in stretching strain based monostable nonlinear system.

6.2. Theoretical Framework:

6.2.1. Non-dimensionalization of Duffing Oscillator Equation: The dynamics of nonlinear energy harvesting systems are mainly governed by the Duffing potential as mentioned in equation (2.2). The equation of motion of a harmonically excited and viscously damped Duffing oscillator is given by:

$$\ddot{x} + \frac{c}{m}\dot{x} + \frac{k}{m}x + \frac{k_n}{m}x^3 = F sin(\omega t) \tag{6.1.}$$

where m is the mass, γ is the damping co-efficient, k is the linear stiffness parameter, k_n is nonlinear stiffness parameter, F is the amplitude of forcing and ω is the external excitation frequency.

To better understand the effect of different parameters like damping and external force on the output response of the nonlinear oscillator, non-dimensionalization of the parameters is a useful technique.

Let us consider the non-dimensionalized time $\tau = \omega t$ and $\omega = \sqrt{\frac{k}{m}}$. Then,

$$x' = \frac{dx}{d\tau} = \frac{dx}{dt} \cdot \frac{dt}{d\tau} = \dot{x}\sqrt{\frac{m}{k}};$$

$$x'' = \frac{m}{k}\ddot{x};$$

$$\omega t = \omega\tau\sqrt{\frac{m}{k}} = \omega'\tau \quad \text{Where, } \omega' = \omega\sqrt{\frac{m}{k}}$$

Using the above approximations, equation (6.1.) can be written as

$$\frac{k}{m}x'' + \frac{c}{m}\sqrt{\frac{k}{m}}x' + \frac{k}{m}x + \frac{k_n}{m}x^3 = F sin(\omega\sqrt{\frac{m}{k}}\tau)$$

or, $$x'' + \frac{\gamma}{\sqrt{mk}}x' + x + \frac{k_n}{k}x^3 = F\frac{m}{k}sin(\omega'\tau)$$

Let us now consider the non-dimensionalized amplitude $X = ax$. The value of a is taken in such a way that $a^2 = \frac{k_n}{k}$.

It can be written,

$$\frac{X''}{a} + \frac{c}{\sqrt{mk}}\frac{X'}{a} + \frac{X}{a} + \frac{k_3}{k}\frac{X^3}{a^3} = F\frac{m}{k}sin(\omega'\tau)$$

or,
$$X'' + \frac{c}{\sqrt{mk}}X' + X + \frac{k_3}{k}\frac{X^3}{a^2} = F.\frac{m}{k}.a.sin(\omega'\tau)$$

or,
$$X'' + \frac{c}{\sqrt{mk}}X' + X + X^3 = F.\frac{m}{k}.a.sin(\omega'\tau)$$

or,
$$X'' + dX' + X + X^3 = fsin(\omega'\tau) \qquad (6.2.)$$

where $d = \frac{c}{\sqrt{mk}}$ and $f = F.\frac{m}{k}.a$.
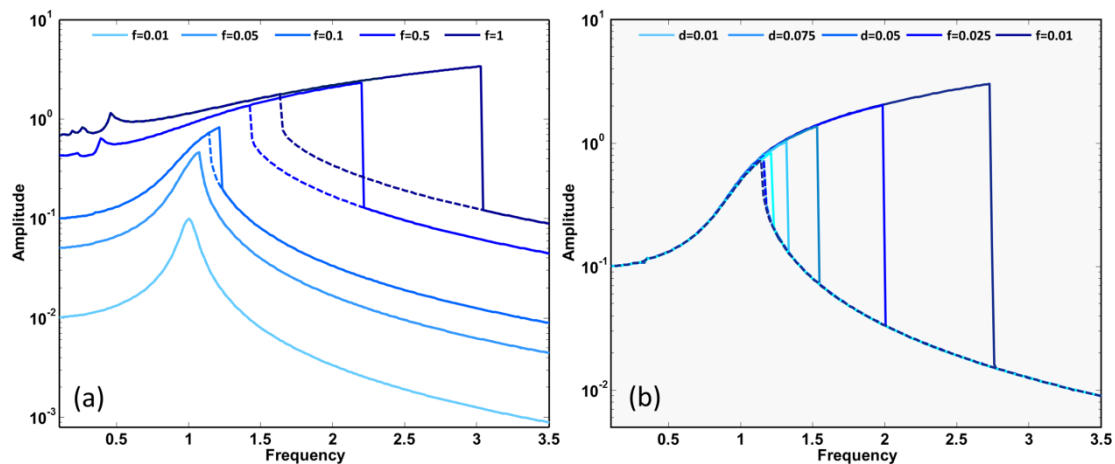
Fig. 6.1: Duffing oscillator response obtained from numerical solution of equation 6.2 for various (a) amplitude of external force (d=0.1) (b) damping co-efficients (f=1).

Equation (6.2) was solved numerically in MATLAB using the Runge-Kutta Integration method (Appendix IV). The solved responses for different values of the input force and damping co-efficient are shown in Fig. 6.1(a) and Fig. 6.1(b) respectively while the other parameter is kept fixed. The peak of the response is pulled further toward higher frequencies as the driving amplitude f is increased, as expected from a stiffening nonlinearity. A significant difference between the responses of the linear oscillator and that of the Duffing oscillator is that the response of the latter is multivalued; that is, for a fixed value of the driving frequency, there are two stable responses with different

amplitudes. Like the linear oscillator, the Q-factor of the nonlinear oscillator also reduces with increasing damping which detunes the output response further.

6.2.2. Nonlinear Effects in a Fixed-Guided Cantilever Beam Under Large Deformation: In this section, the components of spring force due to bending and stretching are obtained separately. For analytical modelling of the nonlinear spring force, a simplified model of the fixed-guided cantilever beam is used as shown in Fig. 6.2. It consists of a beam of length L, width W and thickness t. One end of the beam (x=0) is clamped and the other end (x=L) is guided. The tip deflection at the guided end is δ_g. In this model, the possibility of any twisting movement in other directions has been neglected.
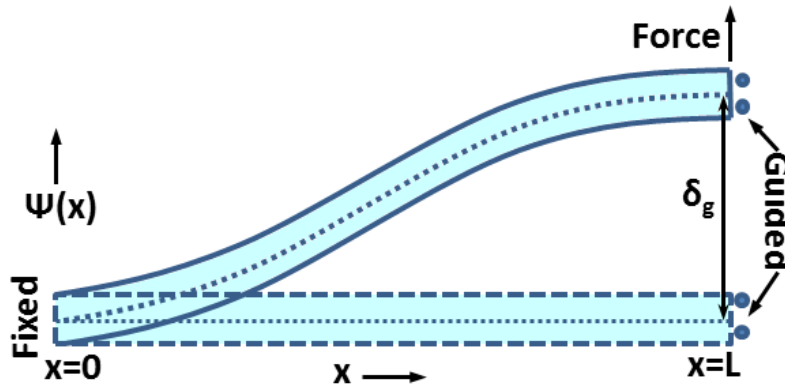
Fig. 6.2: Simplified model of a fixed-guided beam for calculation of force due to linear bending strain and nonlinear stretching strain. Thick dotted line beam represents the rest position whereas solid line beam shows the deformed shape.

- **Contribution due to bending:** The contribution due to bending of the beam can be approximated analytically by applying the Euler Bernoulli's beam equation. Fig. 6.3 shows the small section of a beam.

Strain energy per unit volume $\frac{E}{V} = \frac{1}{2} Y \sigma^2$, where σ is the strain.

From Fig. 6.4,

$$\Delta\varphi.r = l$$

or,
$$\Delta\varphi.\left(r - \frac{t}{2}\right) = l_s$$

Then,
$$\sigma = \frac{l_s - l}{l} = -\frac{t}{2}\frac{\Delta\varphi}{\Delta\varphi.r} = -\frac{t}{2}\frac{1}{r}$$
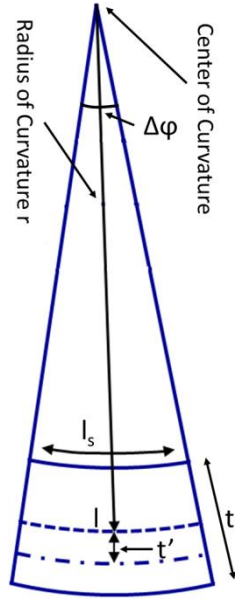
Fig 6.3: Slice view of a portion of the beam showing neutral axis and curvature.

For any line at a distance t' from the neutral axis, the strain σ is then, $\sigma = t'.\frac{1}{r}$

The strain energy over the entire beam is

$$E = \frac{1}{2}Y \int (\frac{t'}{r})^2 tt'. WL = \frac{1}{6}Y\frac{1}{r^2}[t'^3]_{-\frac{t}{2}}^{+\frac{t}{2}}. WL = \frac{1}{6}\frac{Y}{r^2}\frac{t^3}{4}WL$$

or,
$$E = \frac{1}{24}\frac{Y}{r^2}t^3 WL \tag{6.3.}$$

A function Ψ is assumed such that,

$$\frac{1}{r} = \frac{\partial^2 \Psi}{\partial x^2}$$

Hence,
$$E[\Psi] = \int_0^L (\frac{\partial^2 \Psi}{\partial x^2})^2 dx.\frac{Y}{24}.t^3.W \tag{6.4.}$$

In order to minimize the strain energy, the value of Ψ_0 which minimize E[Ψ] is to be found. Mathematically it can be said that,

$$E[\Psi_0 + \delta\Psi] \geq E[\Psi_0]$$

or,
$$E[\Psi_0 + \delta\Psi] = \int_0^L [\frac{\partial^2 (\Psi_0 + \delta\Psi)}{\partial x^2}]^2 dx$$

$$= \int_0^L [(\frac{\partial^2 \Psi_0}{\partial x^2})^2 + 2\frac{\partial^2 \Psi_0}{\partial x^2}.\frac{\partial^2 \delta\Psi}{\partial x^2} + (\frac{\partial^2 \delta\Psi}{\partial x^2})^2] dx$$

$$= E[\Psi_0] + \int_0^L 2\frac{\partial^2\Psi_0}{\partial x^2}\cdot\frac{\partial^2\delta\Psi}{\partial x^2}dx$$

Integrating by parts,

$$= E[\Psi_0] - 2\int_0^L \frac{\partial^3\Psi_0}{\partial x^3}\cdot\frac{\partial\delta\Psi}{\partial x}dx + [\frac{\partial^2\Psi_0}{\partial x^2}\frac{\partial\delta\Psi}{\partial x}]_0^L$$

or, $\qquad E[\Psi_0 + \delta\Psi] = E[\Psi_0] + 2\int_0^L \frac{\partial^4\Psi_0}{\partial x^4}\cdot\delta\Psi\cdot dx + [\frac{\partial^3\Psi_0}{\partial x^3}\cdot\delta\Psi]_0^L + [\frac{\partial^2\Psi_0}{\partial x^2}\cdot\frac{\partial\delta\Psi}{\partial x}]_0^L$

The above inequality is true when

$$\int \frac{\partial^4\Psi_0}{\partial x^4}\cdot\delta\Psi\cdot dx \geq 0$$

or, $\qquad\qquad\qquad\qquad \frac{\partial^4\Psi_0}{\partial x^4} = 0 \qquad\qquad\qquad\qquad (6.5.)$

For a simple bending of beam, $\Psi(x)$ can be defined with length of the beam,

The boundary conditions are:

$$\Psi(0) = 0, \quad \Psi'(0) = 0, \quad \Psi(L) = \delta_g, \quad \Psi'(L) = 0$$

Now as equation (5.5.) is a fourth order equation, let us define Ψ as,

$$\Psi = a_0 + a_1x + a_2x^2 + a_3x^3 \qquad\qquad\qquad (6.6.)$$

Then from the above boundary conditions, it follows that, $a_0=0$, $a_1=0$,

$$a_2L^2 + a_3L^3 = \delta_g,$$

$$2a_2L + 3a_3L^2 = 0$$

Solving the two equations gives, $a_2 = \frac{3\delta_g}{L^2}$ and $a_3 = -\frac{2\delta_g}{L^3}$

Hence, $\qquad\qquad\qquad \Psi(x) = \frac{3\delta_g}{L^2}x^2 - \frac{2\delta_g}{L^3}x^3$

Or, $\qquad\qquad\qquad \Psi(x) = \frac{\delta_g}{L^2}\left[3x^2 - \frac{2x^3}{L}\right]$

From equation (6.6), the deformation $\Psi(x)$ along the length x of the beam for any definite tip deflection (δ_g) is obtained. Hence,

$$\Psi(x, \delta_g) = \frac{\delta_g}{L^2}\left[3x^2 - \frac{2x^3}{L}\right] \qquad (6.7.)$$

From equation (6.4.),

$$E(\delta_g) = \int_0^L \left(\frac{\partial^2 \Psi}{\partial x^2}\right)^2 dx \cdot \frac{Y}{24} \cdot t^3 \cdot W$$

From equation (6.7),

$$\frac{\partial \Psi}{\partial x} = \frac{\delta_g}{L^2}\left[6(x - \frac{x^2}{L})\right]$$

$$\frac{\partial^2 \Psi}{\partial x^2} = 6\frac{\delta_g}{L^2}\left[1 - \frac{2x}{L}\right] = 12\frac{\delta_g}{L^3}\left[\frac{L}{2} - x\right] \qquad (6.8.)$$

For simplicity of calculation, let us introduce a new co-ordinate system as shown in Fig. 6.4, where the origin is at the middle of the beam and two end points are at –L/2 and L/2. This assumption is based on the fact that bending is symmetric in two ends of the beam.
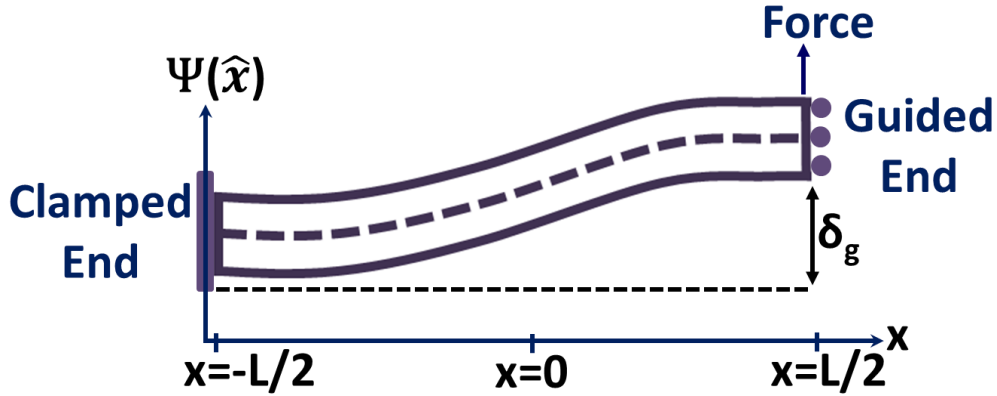
Fig. 6.4: New co-ordinate system where the origin is in the middle of the beam.

Now the relation between new and old co-ordinate is $\hat{x} = x - \frac{L}{2}$

Hence, from equation (6.8),

$$\frac{\partial^2 \Psi}{\partial x^2} = 12\frac{\delta_g}{L^3}\left[\frac{L}{2} - x\right] = -12\frac{\delta_g}{L^3}\hat{x}$$

Integrating over the length of the beam,

$$\int_{-\frac{L}{2}}^{\frac{L}{2}}(-12\frac{\delta_g}{L^3})^2\hat{x}^2 = \frac{1}{3}(-12\frac{\delta_g}{L^3})^2[\hat{x}^3]_{-\frac{L}{2}}^{\frac{L}{2}} = \frac{1}{3}(-12\frac{\delta_g}{L^3})^2\frac{L^3}{4} = 12\frac{\delta_g^2}{L^3}$$

Now regardless of the co-ordinate system, the above value should remain the same as it is a constant term. Hence,

$$\int_0^L (\frac{\partial^2 \Psi}{\partial x^2})^2 dx. = 12\frac{\delta_g^2}{L^3}$$

The component of energy due to bending as a function of deflection δ_g,

$$E_b(\delta_g) = \frac{Y}{24}.dt^3.W.\int_0^L (\frac{\partial^2 \Psi}{\partial x^2})^2 dx$$

or,

$$E_b(\delta_g) = \frac{1}{2}Y\frac{t^3 W}{L^3}\delta_g^2 \tag{6.9.}$$

The component of spring force (F_b) arising due to bending is derived as

$$F_b = -Y\frac{t^3}{L^3}W\delta_g \tag{6.10.}$$

- **Contribution from stretching:** Considering the stretching strain using the same model, the elongated length of the beam (ΔL) can be written as

$$L + \Delta L = \int_0^L \sqrt{1 + (\Psi'(x))^2}dx \tag{6.11.}$$

Hence, length of the stretched portion is given by

$$\Delta L = \int_0^L (\sqrt{1 + (\Psi'(x))^2} - 1)dx \approx \int_0^L \frac{(\Psi'(x))^2}{2}dx = \frac{3\delta_g^2}{5L} \tag{6.12.}$$

The stretching component of the strain is formulated as follows:

$$Strain(v) = \frac{\Delta L}{L} = \frac{3\delta_g^2}{5L^2} \tag{6.13.}$$

The energy stored due to this stretching component of strain can be written as:

$$E_S = \int(\frac{1}{2}YtWv^2)dL = \frac{1}{2}Y(\frac{3}{5}\frac{\delta_g^2}{L^2})^2 tWL = \frac{9}{50}Y\frac{dW}{L^3}\delta_g^4 \tag{6.14.}$$

Similarly, the component of spring reaction force (F_s) arising due to stretching can be expressed by following equation (6.14).

$$F_s = -\frac{\partial E_S}{\partial \delta_g} = -\frac{18}{25}Y\frac{t}{L^3}W\delta_g^3 \tag{6.15.}$$

Combining both bending and stretching components, the total spring reaction force is obtained analytically as

$$F = F_b + F_s = -\frac{Y}{L^3} W \left[t^3 \delta_g + \frac{18}{25} t \delta_g{}^3\right] = -\frac{Y}{L^3} W t^4 \left[\frac{\delta_g}{t} + \frac{18}{25} \left(\frac{\delta_g}{t}\right)^3\right] \quad (6.16.)$$

The restoring spring force (F) arising due to this combined effect of bending and stretching is a cubic nonlinearity and gives rise to a Duffing potential of the form $U = \frac{1}{2} k x^2 + \frac{1}{4} k_n x^4$. When the ratio $\frac{\delta_g}{t}$ is less than unity, the cubic nonlinearity is insignificant. When the tip deflection (δ_g) is only greater than the thickness of the arm (t), or in other words, $\frac{\delta_g}{t}$ is greater than unity, then only the effect of nonlinearity comes into play. From equation (6.16), the relation between linear stiffness constant ($k = \frac{YWt^3}{L^3}$) and nonlinear stiffness constant ($k_n = \frac{18YWt}{25L^3}$) is

$$\frac{k_n}{k} = \frac{18}{25} \frac{1}{t^2} \quad (6.17.)$$

Equation (6.17) provides an important implication for designing this kind of nonlinear systems. The nonlinearity arising due to stretching has inverse square dependence on thickness of the spring arm.

6.2.3. Dynamical Modelling of Nonlinear EM Generator: Recapitulating the governing equation for an electromechanical oscillator with restoring force $\frac{dU}{dx}$, external excitation $\ddot{Z}$, mechanical damping ratio c and including electromagnetic conversion mechanism is given by

$$m\ddot{x} + c\dot{x} + \frac{dU}{dx} + \gamma I = -m\ddot{y} \quad (6.18.)$$

Where m is the moving mass, γ is the electromagnetic coupling co-efficient and I is the current flowing due to EM transduction.

As discussed in the previous sub-section, the restoring force is of the form $F = -\frac{dU}{dx} = kx + k_n x^3$. So, substituting this in equation (6.18), the equation of motion of the oscillator is

$$m\ddot{x} + 2m\rho\omega_0\dot{x} + kx + k_n x^3 + \gamma I = -m\omega^2 Y_0 \sin\omega t \quad (6.19.)$$

Where, ρ is the mechanical damping co-efficient, $y = ZY_0 sin\omega t$ is the sinusoidal external perturbation, ω is the external frequency. Since EM transduction is considered, the external conversion circuit is modelled using the following equation

$$L\dot{I} + RI - \gamma\dot{x} = 0 \qquad (6.20.)$$

R is the total resistance which includes coil resistance R_C and load resistance R_L, L is the electromagnetic inductance. At low frequencies, the effect of L is neglected.

Since the equation (6.20) describes a second order non-autonomous system, it can be transformed into an autonomous form by considering the phase ωt as the third state-space variable. The system can now be represented in a three dimensional state space form

$$\begin{cases} \dot{x}_1 = x_2; \\ \dot{x}_2 = -\left(2\rho\omega_0 + \frac{\gamma^2}{mR}\right)x_2 - \frac{k}{m}x_1 - \frac{k_3}{m}x_1^3 + \omega^2 Z_0 \sin x_3; \\ \dot{x}_3 = \omega; \end{cases} \qquad (6.21.)$$

Equation (6.21) has been solved numerically using the 4th order Runge Kutta method. The power dissipated in the electrical domain for the electromechanical oscillator is given by $P(t) = \frac{\gamma^2}{R}\dot{x}^2$ and consequently the average power has been calculated as $P_{avg} = \frac{1}{T}\int_t^{t+T} P(t')dt'$. All numerical simulations are performed using the stiffness constants found from the COMSOL modelling and the results are compared with the experimental findings.

6.3. Wideband Nonlinear EM Generator on FR4 (Prototype I):

6.3.1. Design and Fabrication of the Energy Harvesting Prototype: The designed transducer utilizes nonlinear stretching strain to obtain a wideband response. The magnets are placed on the top of the central paddle (1 cm^2 square) of the vibrating resonator. Under the influence of external vibrations, the magnets move up and down and flux lines are cut by a coil assembled above it. As a result, voltage is induced into the coil. A schematic of the overall prototype is shown in Fig. 6.5(a). Like in the previous chapters, the spring structure in the meso-scale prototype is fabricated on FR4 using a laser micromachining process. The designed spring structure is shown in Fig. 6.5(b). The spring structure has been designed and optimized for macro scale EM harvesting in which the magnets act as the proof mass. The thin (150 μm) cantilever springs allow the

resonator to move in the out-of-plane direction. One end of each of the four cantilever arms is fixed, while the other ends of the cantilevers are connected pairwise. This gives a fixed-fixed cantilever configuration. As explained analytically in the previous section, nonlinear stretching arises due to this fixed-guided configuration of the cantilever. The overall outer dimension of the resonator including the frame is 1.72×1.72 cm^2. The COMSOL simulated eigen frequency modes for the spring structure are shown in the Fig. 6.6. It is observed from experiments that out-of-plane movement occurs in the first mode of vibration at 170 Hz whereas twisting movements are obtained at 384 Hz and 484 Hz respectively.
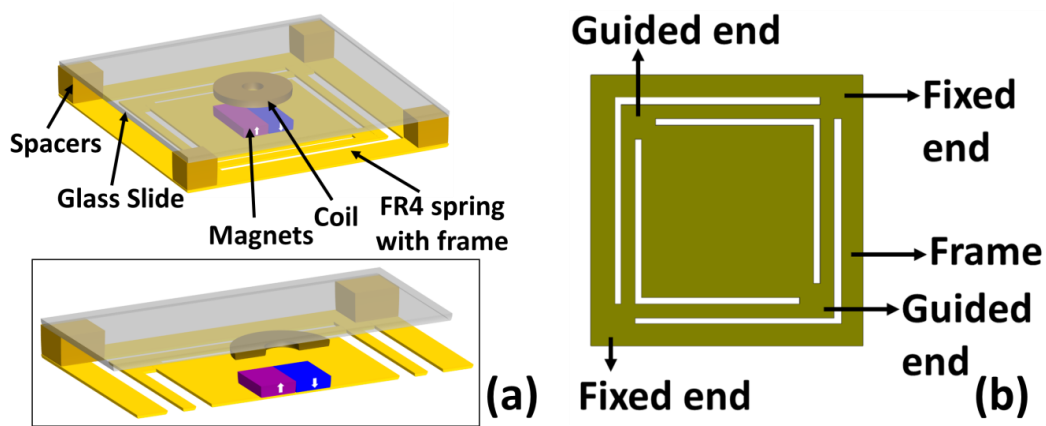
Fig. 6.5: (a) Schematic of the nonlinear electromagnetic energy harvester showing different components (inset figure shows the cross-section of the prototype). (b) Architecture of the designed resonator on FR4.

Two oppositely polarized Neodymium Iron Boron (NdFeB N42H) permanent magnets were epoxy bonded at the middle of the central paddle of the resonator. Each of the magnets has a dimension of 4 mm × 2 mm × 1 mm, 1 mm being in the poled direction. To provide a strong magnetic field, sintered NdFeB N42H magnets were used, which has a typical (BH)max of 40 MGOe. The field strength of this magnet arrangement was simulated using Ansoft Maxwell 2D v12. Fig. 6.7(a) shows the simulation result. It is found that at 0.5 mm above the magnets, the magnetic field strength is about 0.4 T. The orientations of the magnets are also shown in Fig. 6.7(a) by the arrow. An enamelled copper wire wound coil was epoxy bonded to a glass slide and placed at a gap of 1 mm from the top of the magnets. The gap was-
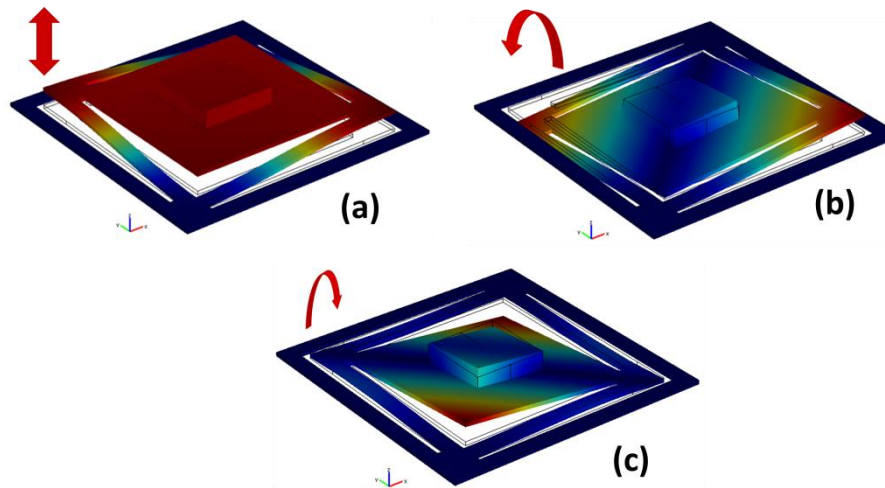
Fig. 6.6: Eigen modes of the designed resonator from COMSOL: (a) Vertically up and down movement at 170 Hz, (b) Twisting movement at 384 Hz, (c) Another twisting movement at 484 Hz.

created using the spacers. The coil has an outer diameter, inner diameter and thickness of 3 mm, 1.15 mm and 0.5 mm, respectively, and has about 450 turns. The copper wire has a diameter of 32 μm. The resistance of the coil was found to be 69 Ω upon measurement. Different parameters for the designed harvester, which are used in the modelling and experiment in following sections, are listed in the Table 6.1. The final assembled prototype is shown in Fig. 6.7(b). The overall volume of the prototype is 0.78 cm^3.
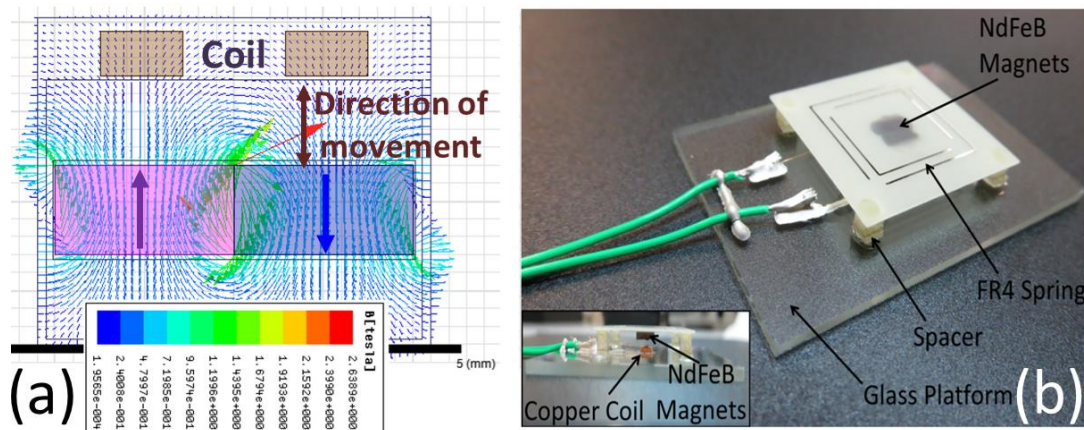
Fig. 6.7: (a) Simulation result for magnetic field. The orientations of the magnets are shown by the arrows. (b) Prototype harvester. The overall volume of the prototype is 0.78 cm^3. The Magnets act as the proof mass for the FR4 resonator.

The device was designed in such a way that it exploits this analytically derived conclusion of a cubic nonlinearity in equation (6.16). The corresponding variation of the spring force with deflection is shown in Fig. 6.8(a). The same result is validated by

Parameters	Value
Spring Arm Length (L)	9.2 mm
Spring Arm Width (W)	0.8 mm
Thickness of the resonator (d)	0.15 mm
Area of the central paddle	1 cm^2
Young's Modulus of FR4 (Y) (COMSOL)	21 GPa
Coil Outer Diameter	3 mm
Coil Inner Diameter	1.15 mm
Coil number of turns	450
Coil Resistance (R_C) (Measured)	69 Ohm
Magnets Dimension	$4 \times 2 \times 1$ mm^3
Linear Stiffness (k) (Calculated)	185.66 N/m
Nonlinear Stiffness (k_n) (Calculated)	3.56 x 10^9 N/m^3
Electromagnetic Coupling Co-efficient (γ) (Calculated)	0.035 Wb/m
Inertial Mass (m) (Measured)	16 X 10^{-5} Kg
Mechanical Damping Co-efficient (ρ) (Measured)	0.015

Table 6.1. Different parameter values for the designed prototype I that are used for modelling and experiments

finite element analysis using COMSOL. However, there is a difference between the COMSOL and analytical calculation of stiffness at large deflection. The analytical model is based on a simple fixed-guided beam and derivation shows that the spring force can be expressed in terms of a sum of a linear term and a cubic order term of the deflection of the spring arm. This is a simplified model of the designed system which did not consider any higher order terms in the calculation which also contribute to the spring force. COMSOL, on the other hand, considers the entire structure into finite size elements and numerically calculates the spring force considering all terms. The calculated values of linear stiffness (k) and nonlinear stiffness (k_n) from the analytical model and COMSOL are given in Table 6.2. However, the difference between the values of nonlinear stiffness (k_n) from analytical model and COMSOL is 262%. To investigate the root for this mismatch, we looked further into our COMSOL model. Under 0.2 N applied force, the deformation of the entire central platform of our structure is not uniform (Fig. 6.8(b)). The deflection at the middle point of the central platform is 378.2 μm, whereas that at the

two corners (connection points between the beams and the central platform) is 290.1 μm. This mismatch could arise from the softness of the spring material. In effect, the deflection of the guided ends of the beams is not as high as it should be and resulted in a negative effect on the 'large deflection' of the spring arms and thus resulted in the mismatch.

Stiffness	Analytical	COMSOL
Linear (k)	275.5 N/m	185.66 N/m
Nonlinear (k_n)	9.32×10^9 N/m^3	3.56×10^9 N/m^3

Table 6.2: Comparison of linear and nonlinear stiffness values obtained from Analytical calculation and COMSOL model.
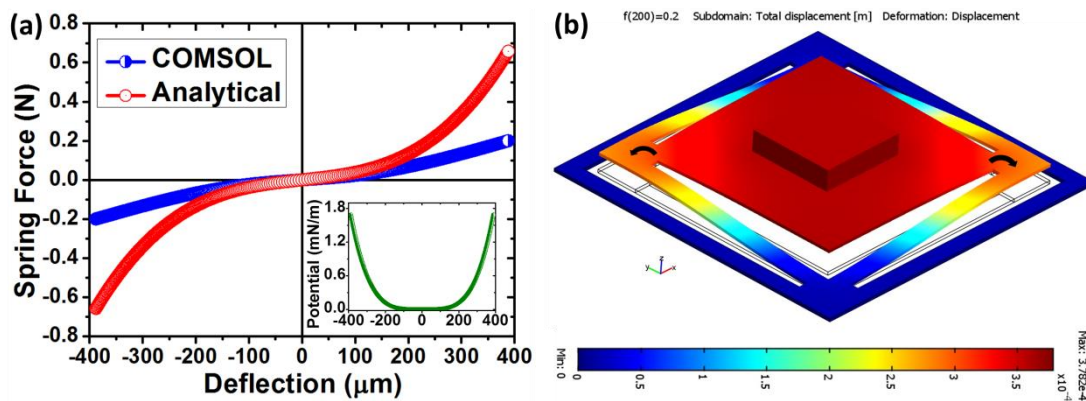
Fig. 6.8: (a) Variation of Spring Force as a function of deflection. Inset figure shows the potential energy function of the spring arm as it gets deformed. (b) Deformation of the designed structure under 0.2 N applied force. Inverse deflection of the corners is marked by the arrows. The deflection at the middle point of the central platform is 378.2 μm whereas that at the two corners is 290.1 μm.

For small deflections, the spring force is mainly dominated by the linear term and the nonlinear stretching based force become significant only as the deflection become large. Using the COMSOL stiffness values, for 50 μm, 150 μm and 300 μm deflections, the contributions due to the linear force term F_b are 0.0093 N, 0.028 N and 0.056 N whereas those due to nonlinear force term F_s are 0.0004 N, 0.012 N and 0.096 N. So for increasing deflection of the spring arm, the contributions of the nonlinear force term in the total force also increases significantly being 4.2% for 50 μm, 30% for 150 μm and 63.2% for 300 μm.

6.3.2. Results & Discussions:

- **Measurements at different acceleration levels:** The fabricated prototype was tested under different peak acceleration levels including 0.05g, 0.1g, 0.5g, 1g, 1.5g and 2g (1g=10 m/s^2). The optimum load resistance (at which maximum power is generated) is found to be 70 Ω (which is almost equal to the coil resistance of the device) at 244 Hz for 1g input acceleration level. The average load power is 0.35 μW, the RMS load voltage is 9.45 mV across the optimal load (R_L = 70 Ω) and the half-power bandwidth is 10 Hz at this acceleration level. The RMS load voltages and load powers for different input accelerations are shown in Fig. 6.9(a) and (b) respectively.
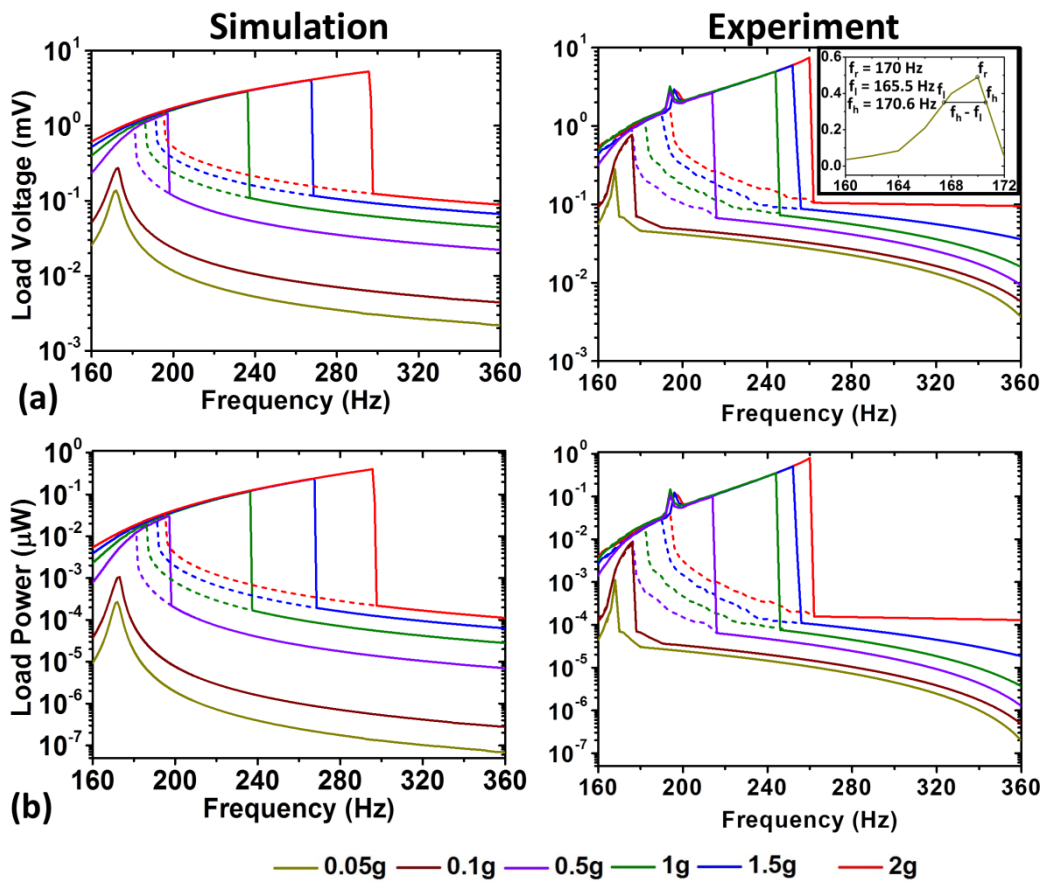
Fig. 6.9: (a) Load RMS Voltage, inset shows the calculation of Q factor around the linear resonant point and (b) Average Load Power. For all the plots, R_L was kept constant at 70Ω. The solid lines are for up-sweep and dotted lines are for down sweep.

For all these measurements, the driving frequency of the input sinusoidal signal was swept from 160 Hz to 360 Hz for 480 seconds both in up and down directions. The experimentally obtained data has been compared with the result obtained from numerical modelling of the system according to the theoretical framework, as discussed in the previous section. For very low input acceleration of 0.05g, the response is similar to that

of a linear resonant system. The linear resonant frequency is found to be 170 Hz, which matches well with the value obtained from the COMSOL model. As the response is near the linear regime for an input acceleration of 0.05g, a slow sweep of 8 minutes has been performed around the resonance point and the open circuit quality factor (Q_{OC}) is calculated from the resultant curve (inset of Fig. 6.7(a)) and it is found to be 33.33. The mechanical damping factor ($Q_{OC} = \frac{1}{2\rho}$) is calculated (ρ=0.015) using Q_{oc} and used subsequently for modelling purposes. With increasing input acceleration, the system response becomes more and more non-resonant in nature and a wideband operational region is obtained. However, this comes at the expense of a nonlinear hysteresis phenomenon where two stable states (one high energy state and the other low energy state) co-exist. A jump phenomenon is a characteristic feature of nonlinear oscillators. When the external frequency is slowly varied, the steady state amplitude of the output response changes discontinuously and drastically at one point. This frequency is known as the jump frequency or saddle node point. It is seen that for low amplitude of the input accelerations, the voltage and power spectra are quite well matched for experimental and modelled curves. However, for high amplitude of the input accelerations (1.5g, 2g), the experimental output responses differ from the modelled results. For 1.5g and 2g input accelerations, the jump point during up-sweep are at 259.6 Hz and 279 Hz respectively whereas those values in the experiment are at 254 Hz and 260 Hz.

- **Comparison of saddle node bifurcation between modelling and experiment:** The Saddle node bifurcation point or the jump point during the up-sweep of the frequency differs for the two sets of curves. The reason for this inconsistency can be two-fold. First, the nonlinearity arises due to the stretching strain of the spring arms. Certainly some energy is dissipated due to this and the effect of stretching and dissipation rises for large values of force (high levels of base excitation). However, the model does not include such complex dissipation terms. Additionally, for high base excitation levels, the effect of nonlinearity is quite high and as a result the system becomes very sensitive to any kind of small perturbation. Such small perturbations are always present within the real experimental system due to noise, whereas numerically a deterministic system is considered. As a result of this, the system losses increase much more quickly than expected for those values of the base accelerations and the saddle node point appears much earlier. Similar observations also have been made by Sebald et al [232] and Barton et al [233]. To understand further the influence of noise, basin of attractions for the

system are plotted for four different frequencies in Fig. 6.10 using the numerical model. The basin of attraction shows that starting from different set of initial conditions at vanishing driving force, the solution leads to different branches, where the high energy state is shown by red and the low energy state is shown by blue. The fixed points of the high energy and low energy states are also marked as FP_H and FP_L in the plots. If noise is added to the system, it can be easily perturbed from FP_H in the red region into the blue region and end up in FP_L. At 190 Hz (Fig. 6.10 (a)), i.e., at the start of the hysteresis loop, the probability of staying in the high energy state is much higher. This probability, however, reduces as the external frequency is increased as shown in Fig. 6.10 (b) for 205 Hz and Fig. 6.10 (c) for 215 Hz. At 225 Hz (Fig. 6.10 (d)), just before the jump occurs, there is very little probability of staying in the high energy branch of the response.
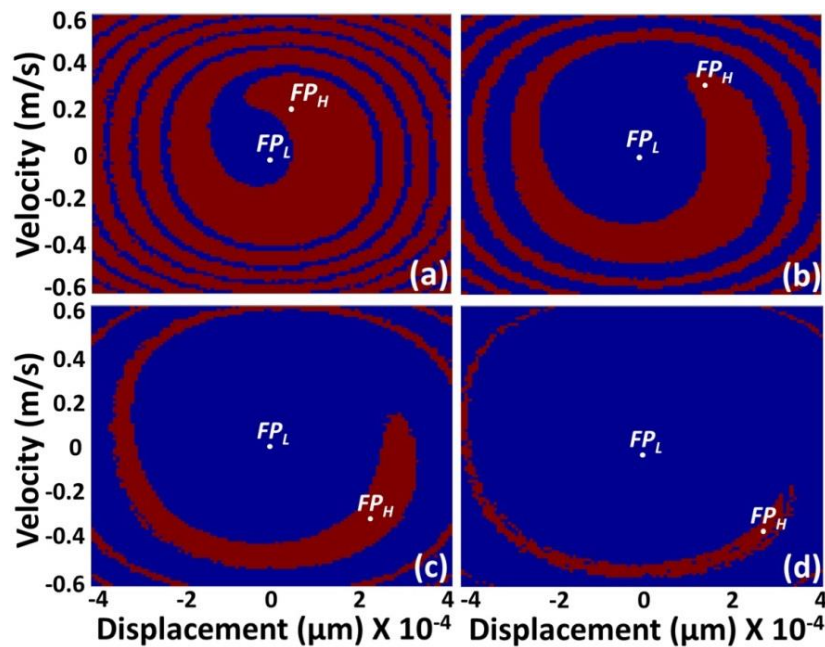
Fig. 6.10: Basin of attraction plots from the numerical model at (a) 190 Hz, (b) 205 Hz, (c) 215 Hz, and (d) 225 Hz. The basin of attraction for the low energy state is shown in blue and that in high energy state is shown in red. FP_L and FP_H are fixed points for low energy and high energy attractors respectively.

However to justify the claim, an Additive Gaussian White Noise (AGWN) is included along with the harmonic excitation in the numerical model and a qualitative discussion is performed using the numerical simulations to exhibit the effect of dynamical noise that becomes prominent in the experimental system during high acceleration inputs. The modified model is solved numerically by using the Euler-Maruyama method where the modified equation of motion can be written as

$$m\ddot{x} + 2m\rho\omega_0\dot{x} + kx + k_nx^3 + \gamma I = -m\omega^2 Z_0\sin\omega t + \sqrt{D}\xi \qquad (6.22.)$$

where D is the noise parameter and ξ is the noise function with zero expected value and auto-correlation equals to the delta function. The above equation is solved numerically for various noise parameter values at 2g input acceleration. Fig. 6.11 shows that the jump point in the up-sweep is sensitive to the noise and it becomes smaller as the noise parameter value is increased. For zero noise, the jump point is 279 Hz whereas it becomes 264.6 Hz, 226.6 Hz and 211.5 Hz for D=1×10^{-8} m^2/s^3, 2.25×10^{-8} m^2/s^3 and 4×10^{-8} m^2/s^3 respectively. These noise levels are very small compared to other reported noise levels that are used to harvest energy [146]. Thus, the mismatch between saddle node bifurcation points between experiment and simulation could be due to the dynamical noise that is present in experimental systems, possibly due to the excitation of any other degrees of freedom.
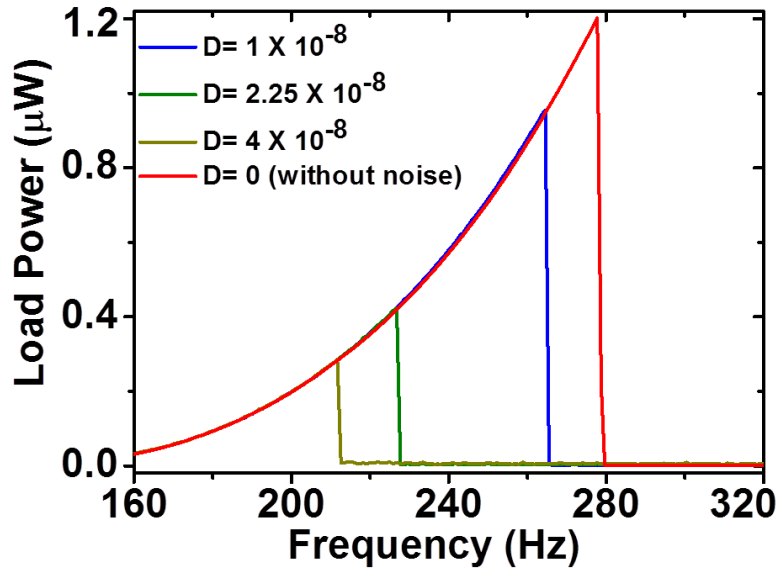
Fig. 6.11: Numerical simulation on effect of noise in jump point at 2g acceleration level. With increase in noise, the saddle node bifurcation point during up-sweep becomes lower.

For 2g acceleration level, the peak power that is generated at the jump-point is 0.78 μW whereas that value from the simulation is 1.22 μW. However the trend of power variation with frequency is similar to the experimentally observed curves. It is also to be noted that in the experiment jump-point comes earlier at 260 Hz as compared to the 279 Hz of the model and the generated power is 0.86 μW at 260 Hz from the model which is close to the experimental value. The presence of noise cuts off the generated power at a lower value than what could have been achieved in a noise free environment. The above mentioned values for 1g acceleration level are 0.35 μW and 0.38 μW respectively.
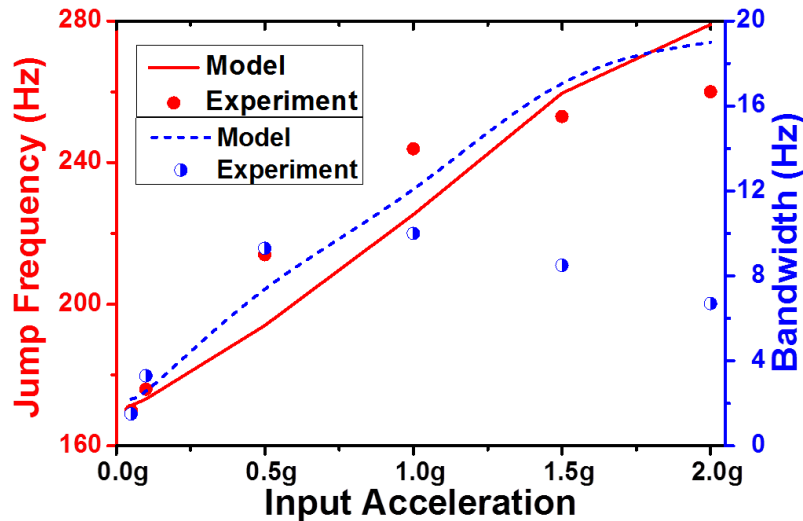
Fig. 6.12: Variation of Jump Frequency on up-sweep and half power bandwidth with input acceleration.

Two important observations in this analysis are the saddle node point (or jump point) during up sweep of the frequency as maximum power is normally generated at this point and the half power bandwidth. It is seen from the Fig. 6.12 that for higher values of accelerations, the half power bandwidth also deviates from the modelled values due to the above mentioned reasons.

- **Non-characteristic secondary peaks:** Additionally, a non-characteristic secondary peak was observed experimentally at around 196 Hz. To check the possibility of an additional eigen-mode due to unbalance of mass due to misalignment of the magnets on the resonator, the location of the magnets is shifted relatively by 0.5 mm/1 mm/2 mm in either direction in the COMSOL model and simulated. The change in configuration of the magnets made a small change in the frequency but no additional eigen-mode is obtained from simulation and hence this possibility is ruled out. To investigate further, the time domain data of the open circuit voltage are recorded at different frequencies for a constant input acceleration level of 1g. Fig. 6.13 (a) shows the open circuit voltage up to 800 Hz frequency sweep. Two small linear resonant peaks appear at 384 and 484 Hz respectively. The time responses is recorded both during the up (Fig. 6.13 (b)) and the down sweep (Fig. 6.13 (c)) of the frequency around the hysteresis region. The frequency is swept at a very slow rate (for 16 minutes in each sweep direction) and the oscilloscope is paused to record the signal when the required frequency was reached.
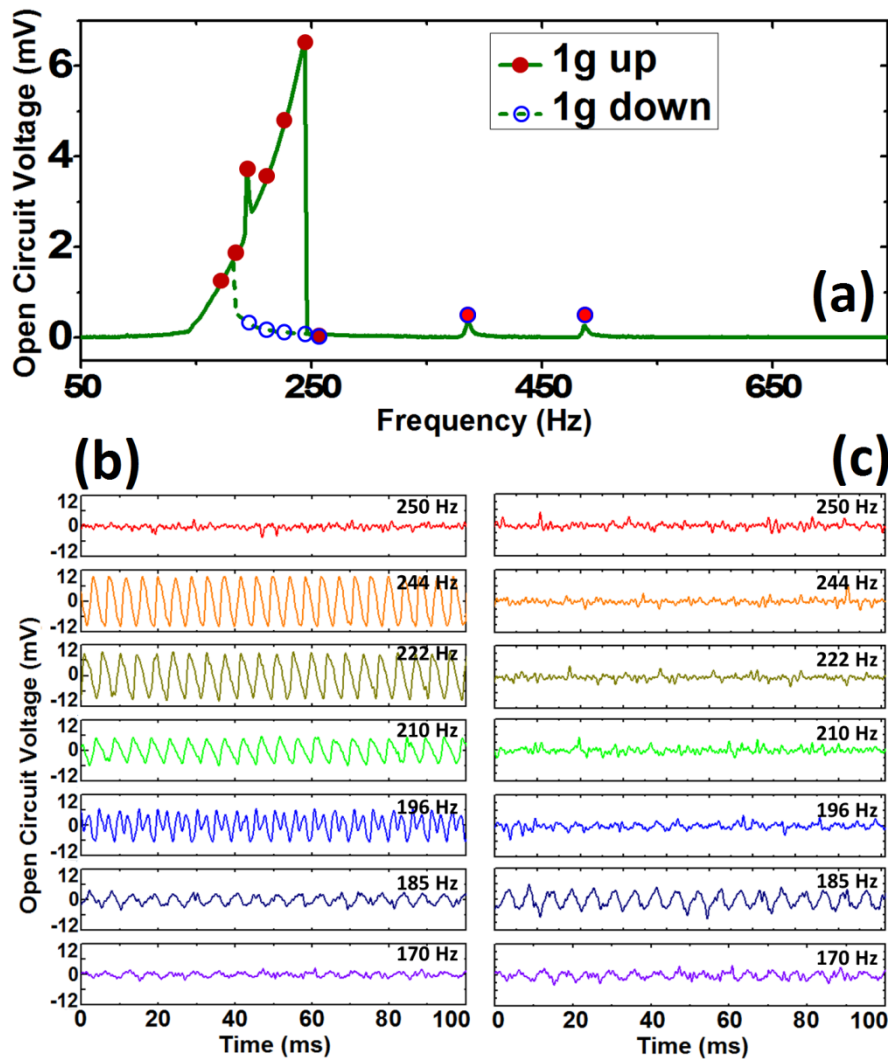
Fig. 6.13: (a) Frequency response of the Open Circuit Voltage for extended frequency range is shown for input acceleration of 1g. Solid rounds and hollow rounds are open circuit voltages during up- and down-sweep respectively. Time trajectories of open circuit voltage at 170 Hz, 185 Hz, 196 Hz, 210 Hz, 222 Hz, 244 Hz and 250 Hz during (b) up- and (c) down-sweep are shown.

At 196 Hz, it is observed that the time trajectory loses its symmetry around the origin i.e., all the other time trajectories remain symmetric if they are flipped with respect to the zero line on the voltage axis but the trajectory at 196 Hz does not remain so. Similar dynamic symmetry breaking phenomena have been observed theoretically for the Duffing oscillator by a number of researchers like Parlitz et. al. [234] and Olson et. al. [235]. As the frequency is increased (from 210 to 244 Hz), the peak to peak value of the large amplitude oscillation increases until 250 Hz, and then the amplitude drops to the low energy branch. From the steady state time traces during the up and down sweep of the frequency, co-existence of two stable states (high energy and low energy) can be easily seen. In Fig. 6.14, a close examination on this symmetry broken state is performed for a

further qualitative analysis. Open circuit voltage trajectories show the evolution of the symmetry broken state from its inception at 192 Hz to its disappearance at 200 Hz in detail. It is remarkable that a transition to a dynamically symmetry broken state occurs in the monostable (single valley potential well) device, which according to the best of author's knowledge, so far has not been reported in the experimental literature before.
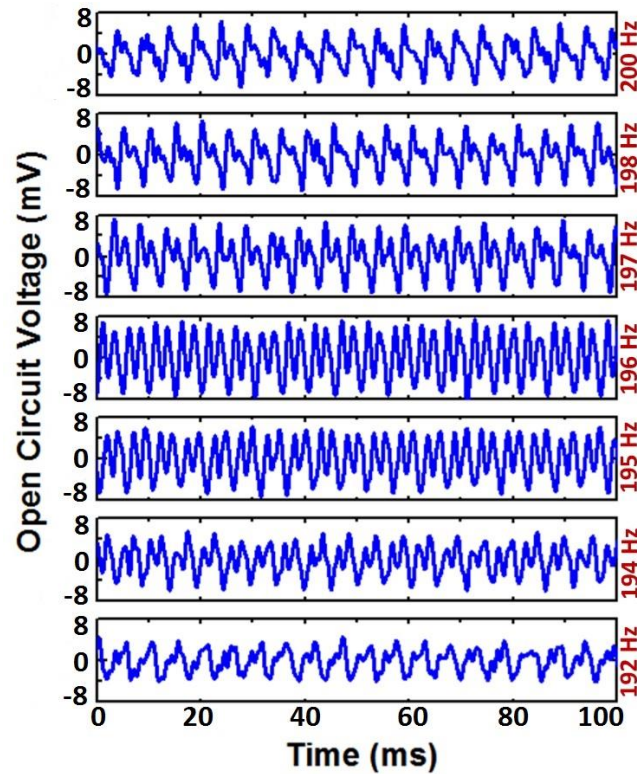
Fig. 6.14: Chronological evolution of the symmetry breaking observed near 196 Hz. Time trajectories of open circuit voltage from 192 Hz to 200 Hz is shown here.

However, a one degree-of-freedom dimensional model of the Duffing oscillator did not produce this kind of symmetry broken behaviour. To investigate it further, the non-dimensionalized model for the Duffing oscillator is used which is described in the first section of this chapter. Non-dimensionalized equation (6.2) is solved numerically and the non-dimensional velocities, which are proportional to the induced voltage, are plotted in Fig. 6.15 (a) against non-dimensional frequency ($\omega_1 = 1$ stands for the natural frequency of the system $\omega_0 = 170$ Hz) for various input accelerations from f=0.0019 (=0.05g) to f=0.0755 (=2g). The non-dimensional damping is found to be d=0.031 for open circuit case. However, further study is performed to gain deeper understanding of the observed symmetry breaking. For higher order force and damping (f=3, d=0.2), the non-dimensional model shows the presence of a dynamic symmetry breaking bifurcation

(SBB) along with other secondary resonances (Fig. 6.15 (b)). In that case the dynamic symmetry breaking appears around ω=1.
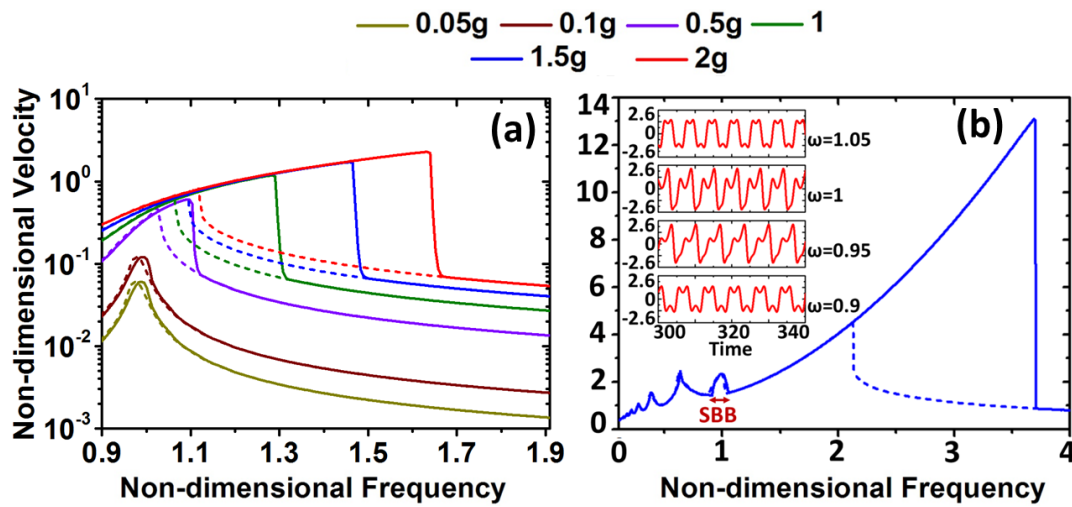
Fig. 6.15: (a) Non-dimensional velocity at different input acceleration levels. (b) Frequency response from the Non-dimensional model for F=3, d=0.2. In this case Symmetry Breaking Bifurcation (SBB) appears around ω=1. The evolution of the symmetry broken states are shown on the inset for ω=0.90, 0.95, 1.00 and 1.05 respectively for a qualitative comparison with our experimental observation.

The chronological evolution of the symmetry breaking phenomena is shown in the inset of Fig. 6.15 (b) from ω=0.9 to 1.05. There is a qualitative difference between the way in which symmetry breaking appears in this numerical model and the time histories obtained experimentally in Fig. 6.14; in particular, the relative heights of maxima and minima in the numerical and experimental time traces do not fully agree. However, the symmetry broken state at ω=1 is of a similar nature to that found experimentally at 194 Hz. The developed system does not predict the existence of any additional secondary peak from this one degree-of-freedom non-dimensional model and it is seen that the underlying trajectories of the symmetry broken states differ from those of dynamical symmetry breaking. It is further noticed that the additional peak is seen only during frequency up-sweep and disappears during down-sweep. It is also observed experimentally that higher order linear modes in the output voltage occur at 384 Hz and 484 Hz (Fig. 6.13 (a)), which could be due to the different twisting modes of the device in agreement with the eigen frequency modes in COMSOL (Fig. 6.6 (b) & (c)). These higher order resonances could also explain the peak observed at 196 Hz due to the coupled interaction with the first nonlinear resonance. However, in that case the peak would have shown up both in the up and down sweep directions. The assembled prototype has an in-built asymmetry in its structure, as shown in Fig. 6.5 (a). Magnets are placed on one side of the resonator and

inductive transduction is carried out from that side. So damping is much more complex on this side of the resonator compared to the opposite side. This inherent asymmetry could also have led to the symmetry broken states.

- **Advantage of the secondary peaks:** It is a unique advantage of using a nonlinear dynamical system that can produce large-amplitude oscillation at low frequencies other than having its inherent wideband frequency response and normally it is perceived that triggering the symmetry breaking peaks for monostable systems is not easy, even for moderately high acceleration levels [236]. However, such peaks are observed in the developed system in the vicinity of the nonlinear peaks due to the first fundamental mode, and hence, sudden large amounts of power could be obtained around those peaks. The heights and positions of these secondary peaks on the frequency scale remain the same for increasing input acceleration levels, bringing them closer to the nonlinear peaks for lower acceleration levels, while increasing the effective output power. It is seen that 15.8%, 24%, 40.6% and 110% of the peak power can be obtained at the secondary peak for 2g, 1.5g, 1g and 0.5g accelerations respectively. So, for example, at 0.5g acceleration, 0.1 µW is generated at 214 Hz (nonlinear peak) whereas 0.11 µW is obtained at 196 Hz (secondary peak) which are only 18 Hz apart. Also, symmetry breaking states are useful in generating significantly large power compared to symmetric states. It can be observed that just before or after the secondary peak, where time traces are symmetric, only a small power is obtained compared to the symmetry broken peak point. For 1g acceleration, 0.14 µW is recorded at the secondary peak (194 Hz) which would have been ~3 times higher than the extrapolated symmetric state at that point from the frequency response. So with further optimization, the symmetry breaking phenomenon has the potential for exploitation to achieve enhanced performance of energy harvesting devices by increasing the output power compared to symmetric states.

- **Comparative Study with a comparable linear generator:** To establish the bandwidth enhancement ability of the specially designed energy harvester with fixed-guided spring arms, a linear EM energy harvester is designed and fabricated (Fig. 6.16), with exactly of the same volume (0.78 cm^3) as the nonlinear counterpart. The linear resonator consists of four fixed-free configuration cantilever arms (as shown in Fig. 6.16 (a)). Compared to the specially designed fixed-guided cantilever, the restoring force ($F = kx$) in this case consists of only a linear term. Similarly oriented magnets with exactly similar sizes are used as the proof masses whereas an identical coil is used to

transduce electrical power. A comparison between the frequency responses of the open circuit voltage at 1g acceleration for both the linear and nonlinear prototypes is plotted in Fig. 6.16 (c). By using a nonlinear stretching based EM energy harvester of exactly the same size, a five times wider half power bandwidth is obtained.
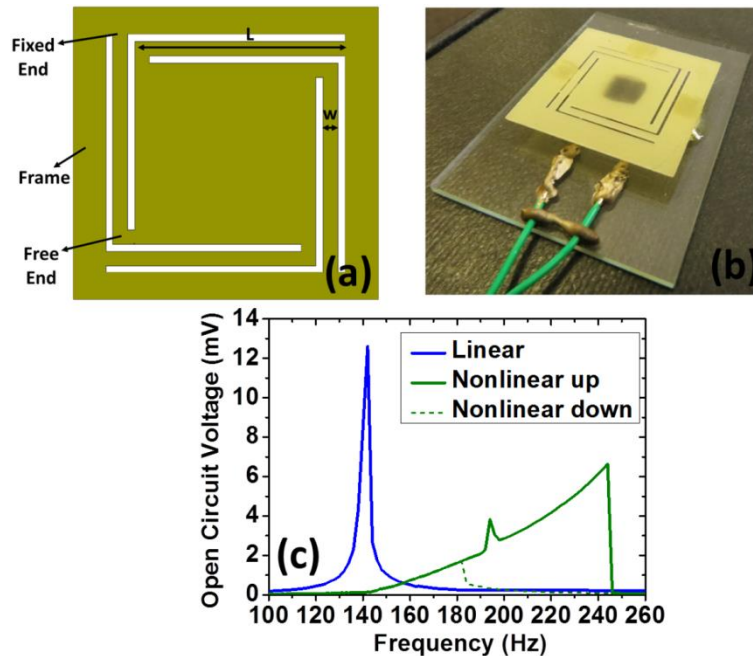
Fig. 6.16: (a) Spring configuration of the linear prototype on FR4. (b) Assembled prototype for testing. (c) Comparison of Open Circuit Voltage response for the Linear and Nonlinear prototypes under 1g input acceleration.

6.4. High Performance Meso-scale Nonlinear EM Generator (Prototype II):

Though the theoretical model of the nonlinear oscillator is successfully validated through the prototype I and the wideband output response is also obtained, the power output from the reported proof-of-concept device is relatively small, particularly due to the ineffective magnet coil assembly. Also, the design goal of the energy harvesting devices is to maximize the power output in an environment where vibration frequencies and amplitudes are varying in time, neither the maximum power nor the bandwidth is a suitable performance metric because large bandwidth occurs at high (or infinite) load resistance but at the cost of small (or zero) power output and vice versa. In this section, the performance of the reported generator is improved with a few design modification and utilizing a high efficiency magnet-coil configuration to increase the electromagnetic coupling which, as a consequence, not only improves the output power but also enables one to modify the bandwidth by changing the load resistance only. Using the insight

obtained by combining experimental and theoretical results, the general design parameters are identified for improving the bandwidth along with the power and define a more appropriate figure of merit in vibration based nonlinear energy harvesters.
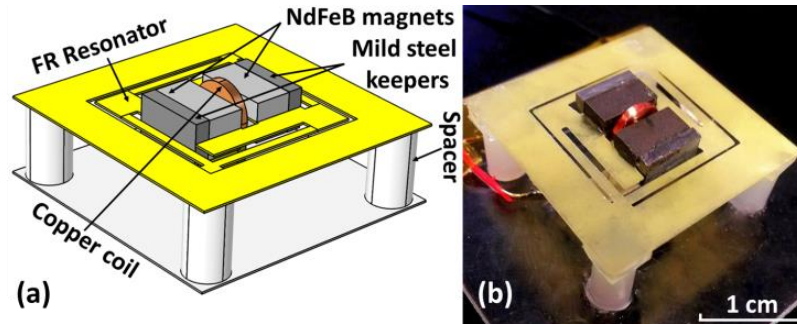
Fig. 6.17: (a) Schematic of the nonlinear stretching induced electromagnetic energy harvester. (b) Built energy harvester prototype on FR4.
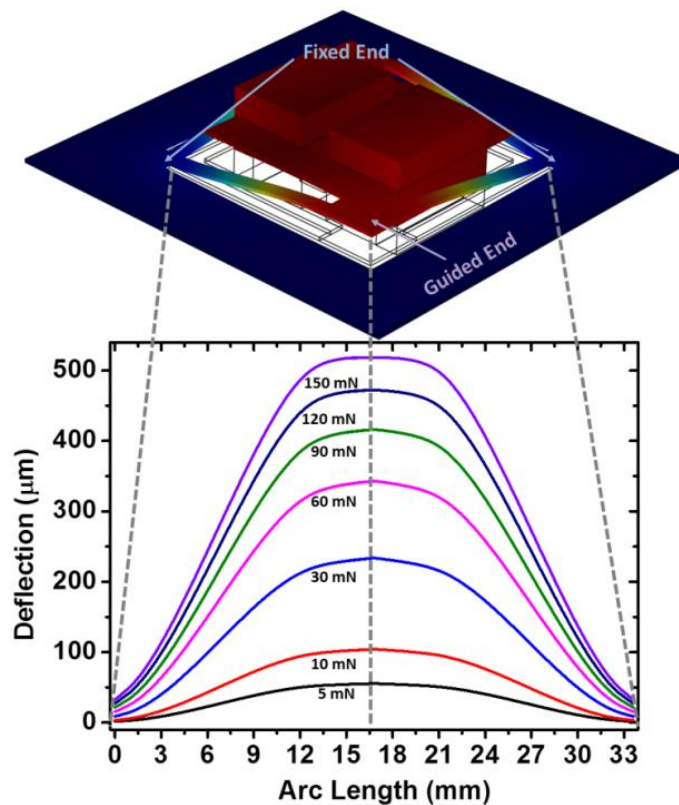
Fig. 6.18: The top figure depicts the first fundamental mode for fixed applied force calculated using COMSOL. The bottom figure shows the deflection along the fixed-guided beam for different applied forces.

6.4.1. Device Design & Modelling: The spring structure is architecturally the same as that of prototype I. However, in this case a slot is created in the middle of the central paddle to align the coil vertically with respect to the moving magnets. A schematic of prototype II is shown in Fig. 6.17 (a) and the fabricated prototype is depicted in Fig. 6.17 (b). The spring structure is fabricated using Laser micromachining technology on 0.24

mm thick FR4 substrate. The length and width of each of the spring arms are 12.2 mm and 1 mm respectively. The magnet coil configuration in this case is similar to the one reported for linear prototypes P1 and P2 in chapter 4. An arrangement of two pairs of oppositely polarized sintered NdFeB N50 magnet with soft magnetic blocks at the ends provides a closed magnetic flux path to maximize the flux density. The dimensions of each of the NdFeB magnets are $8\times4\times2$ mm^3 whereas those of the mild steel blocks are $8\times4.2\times1.6$ mm^3. The magnetic arrangement constitutes of an inertial mass of 3×10^{-3} Kg. An enamelled copper wire wound coil having 6.5 mm outer diameter, 1.15 mm inner diameter, 1 mm thickness and 2500 turns with measured coil resistance of 714 Ω was used to generate the electrical voltage. As illustrated in Fig. 6.18, the effect of the stretching becomes more and more prominent with large applied force. The deformation of the structure consists of bending dominantly when the deflection is smaller or comparable to the thickness of the spring arms (0.24 mm) and this is when the stiffness is almost in the linear region. Under the large deflection of the spring arms, the stretching effect comes into play and the stiffness enters in the nonlinear regime. From FEM analysis, the linear stiffness constant (k) is calculated to be 384.1 N/m and the nonlinear stiffness constant (k_n) is found to be 1.51×10^9 N/m^3. As discussed already, the system behaviour is dominated by the nonlinear force under large deformation of the spring arms only. For example, when the deflection (x) is 50 μm, the contribution due to the linear bending force (kx) is 19.2 mN whereas that due to the nonlinear stretching force ($k_n x^3$) is only 0.19 mN and the system response is in the linear region. However, under a large deflection (600 μm), the contribution due to the nonlinear force (326.1 mN) dominates over that due to the linear force (230 mN). Hence the system is dominated by the nonlinear effects under large deflection conditions only when the external excitation is large.

Consequently, the output response of the device (Fig. 6.19) is resonant (resonance frequency = 57 Hz) at low acceleration and become gradually wideband with increasing input vibration. In addition to the nonlinear wideband output response, secondary resonance peaks are also observed at 28.5 Hz and 19 Hz, respectively, and these peaks are prominent at higher acceleration levels when the nonlinearity is stronger. The observation of these large voltages at lower frequencies, occurring near a half and one-third of the fundamental frequency of the harvester, can be attributed to the activation of the super harmonic resonances [236-237] and such resonant peaks are characteristic features of

nonlinear systems. The super harmonics are observed during both the up- and down-sweep of the frequency, unlike the nonlinear jump phenomena which create hysteresis in the frequency sweeps. At an excitation frequency of 28.5 Hz for 0.5g, the asymmetric oscillations are observed (Fig. 6.19) at twice the excitation frequency which is a characteristic of the super harmonic resonance. This feature generates an unique opportunity of harnessing almost 1.8 times higher output voltage at the super harmonic peak compared to its vicinity. Before the start of the nonlinear hysteresis, the vibration consists of principally the bending component and the output voltage is still small while, with a further increase in oscillation amplitude, the stretching nonlinearity becomes significant, enabling the large amplitude output.
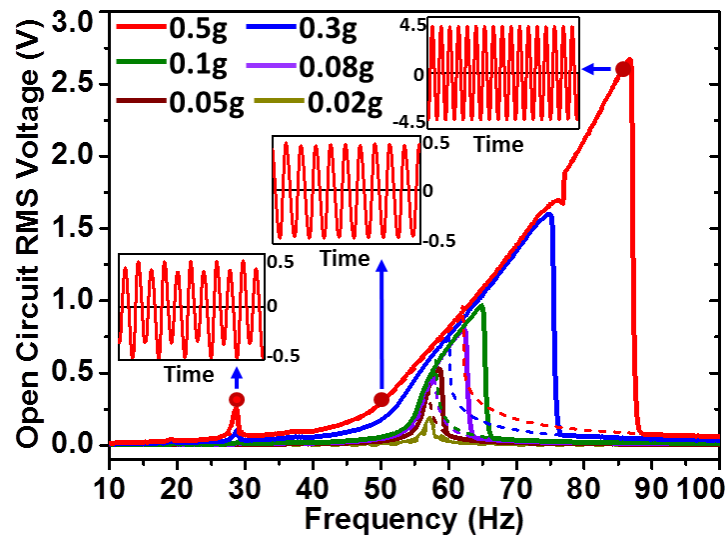
Fig. 6.19: Open circuit voltage up-sweeps (solid) and down-sweeps (dashed) at different input accelerations. Open Circuit Voltage time traces zoomed in at: 28.5 Hz, 50 Hz and 86 Hz respectively (Inset).

6.4.2. Interplay Between Mechanical and Electrical Parameters: An electrical resistive load is connected to the harvester to extract electrical power which adds additional damping to the mechanical oscillator. The maximum generated power across the resistive load and the half-power bandwidth can be modulated by changing the input acceleration level, as shown in Fig. 6.20 (a). At 0.05g, a maximum power of 14.1 μW is generated across R_L of 4000 Ω and the half-power bandwidth is 1.6 Hz. As the input acceleration is increased to 0.1g, the corresponding maximum power becomes 56.8 μW and the bandwidth is 2.65 Hz. With a further increase in the input acceleration, at 0.5g, the maximum generated power increases to 488.47 μW and the bandwidth also widens to 9.55 Hz. Since the noise term is enhanced with increasing acceleration, a small value of D is assumed in all simulations, being equal to 1×10^{-8} m^2/s^3 for 0.1g, 4×10^{-8} m^2/s^3 for 0.3g

and 9×10^{-8} m^2/s^3 for 0.5g respectively. With these chosen values of noise levels, the jump down frequencies matches well with the experiment (Fig. 6.20 (b)).
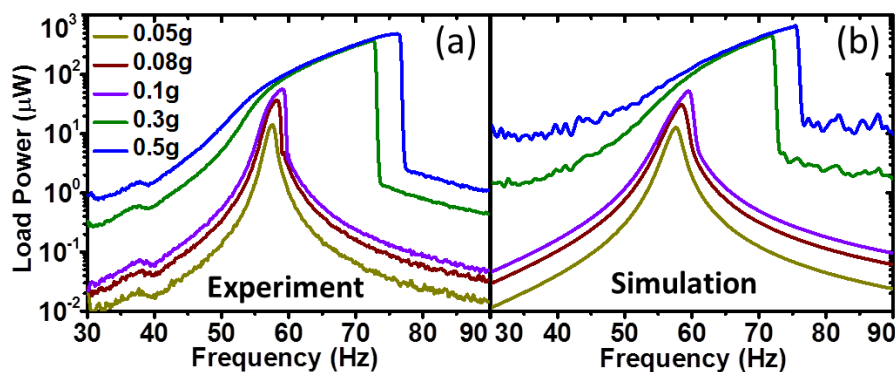
Fig. 6.20: Variation load power with input frequency for different acceleration levels (a) Experiment, (b) Simulation. R$_L$=4000Ω.

The electromagnetic inductance (L) of the coil is 1.81 mH. Thus the impedance offered by the inductive component (ωL = 0.103 Ω) is very low compared to the resistive components (R$_C$ = 714 Ω and R$_L$ = 4000 Ω) at the intended low frequency of operation and so the effect of L is neglected. Thus under the approximation $\omega L \ll (R_C + R_L)$, the electrical damping co-efficient (c$_{EM}$) of the electromagnetic energy harvester is given as

$$c_{EM} = \frac{\gamma^2}{(R_C+R_L)}$$

(6.23.)

Since c$_{EM}$ is a function of R$_L$, thus damping can be changed by also changing the load resistance. The effect of changing the load resistance is studied by recording the frequency sweep data at 0.1g acceleration for various R$_L$ values. Maximum power is generated at the jump-down frequency during up frequency scan. However, it is observed that the maximum achievable load power does not increase continuously with the load resistance. The variation of load power with frequency is shown in Fig. 6.21 (a) experimentally and using numerical simulations in Fig. 6.21 (b) for different load resistances, maintaining a good agreement between the two. For a very small load value (R$_L$ = 500Ω), the electrical damping is quite high and thus the response is approximately like a resonant spectrum. Moreover, a noise parameter of 1×10^{-8} m^2/s^3 is considered for 0.1g for all simulations. For very low load resistance, the damping is very high (low Q-factor) and the effect of dynamical noise might be negligible and additional input noise results in a wide spectrum with a lower height in simulation. However in order to maintain consistency within the analysis, a white noise with a noise parameter of 1×10^{-8} m^2/s^3 for 0.1g is incorporated in all simulations.
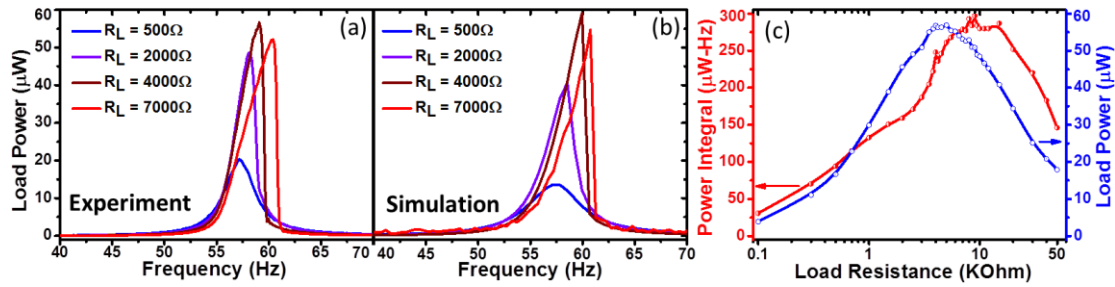
Fig. 6.21: Load power with frequency sweep for various load resistance values are shown in (a) experimentally and (b) using simulations (D=1×10^{-8} m^2/s^3). (c) Load power and power integral variation with load resistance. All plots are obtained at 0.1g acceleration.

The bandwidth increases continuously with the load resistance, whereas the maximum power is generated for 4000Ω load resistance. Since the nonlinear jump point and bandwidth depend on damping, they could also be changed just by altering the resistive load. With an increase in R_L, the electrical damping eventually becomes smaller and, as a result, the jump-down frequency shifts further away from the resonance frequency, resulting in the widening of the bandwidth. This is advantageous compared to linear EM energy harvesters whereas complex load topologies are used to modify the resonance frequency [125, 238]. For devices with low magnetic flux gradient, the electrical damping is low compared to mechanical parasitic damping and, as a result, load resistance has no effect on jump frequency or bandwidth. Thus, the highly efficient magnetic circuit not only maximizes the generated power due to a large flux gradient but also modifies significantly the nonlinear down jump frequency and bandwidth. The lower limit of the tuned frequency is the resonant frequency of the device in the case of the hardening type monostable system as the amplitude-frequency curve tends to bend in the higher frequency direction for such a system whereas the upper limit is the open circuit condition. The envelope of the maximum generated power with the variation of the load resistance under 0.1 g acceleration is shown in Fig. 6.21 (c). The maximum load power of 56.8 μW is generated at R_L = 4000 Ω and, with a further increase in R_L, the maximum load power reduces.

6.4.3. Power Integral – Figure of Merit: The main motivation behind using nonlinear energy harvesters is to transduce electrical power from a wideband vibrational source where the available energy is distributed over a broadband of frequencies as opposed to linear devices which are suitable for transducing power from vibrations with discrete frequency peaks. So far, the state-of-the-art figure of merits for energy harvesters considers peak power generated at a particular frequency as described by Beeby et. al.

[62] which is suitable for linear generators only as they have narrow bandwidths. On the other hand, Sebald et al [232] proposed a figure of merit for nonlinear energy harvesters where they have considered generated power over a half-power bandwidth. As nonlinear energy harvesters are aimed to improve the off-resonance performance over a wide bandwidth and could have unusual peaks generating significant power at different frequencies outside the so called half power bandwidth, no existing figure of merit is useful for such systems which consider output power at a particular frequency or only over a certain frequency range only. For example, the power-frequency response depicted in [239] for a 35V bias has a narrow bandwidth where maximum power is generated but a significant wideband region is obtained outside that narrow bandwidth. Thus, a more generalized figure of merit is necessary for comparing different nonlinear energy harvesters. Here, a useful figure of merit for nonlinear energy harvesters is introduced, called the power integral, which is the area under the power frequency curve at a fixed acceleration level and is defined as $P_f = \int P_L . df$, where P_L is the load power and f is the frequency. As the bandwidth increases continuously with load but the maximum power does not, to address this trade-off between load power and bandwidth, power integral optimizes the load resistance for which the integral of the load power over frequency is maximized, i.e. the value of load resistance is obtained for which maximum bandwidth is obtained with a minimum loss of power from the peak point. Thus for optimum performance of nonlinear energy harvesters, they must be operated with an electrical load which is optimized with respect to the Power Integral value instead of load which is optimized with respect to the load power. In this case, the maximum value of power integral is 297 μW-Hz and is obtained at R_L=9000Ω, which is different from the value of R_L (=4000Ω) at which maximum peak power is recorded. To justify the significance of P_f, load power-frequency responses for three different load values are plotted in Fig. 6.22. It is observed from Fig. 6.21 (c) that the maximum output power is generated at R_L = 4000 Ω when electrical damping is nearly equal to mechanical damping, whereas P_f is maximum for R_L = 9000 Ω. The load power frequency responses for these two load conditions, and for R_L = 50000 Ω, are shown in Fig. 6.22. For a load of 4000 Ω, the maximum generated power is 56.8 μW, with a bandwidth of 2.9 Hz. For a very large load (50000 Ω), the system comes close to the open circuit condition and the maximum power falls to 17.9 μW while the bandwidth increases to 5.9 Hz. By optimizing the load to 9000 Ω using the Power Integral, the maximum power of 50.5 μW is achieved with an

operational bandwidth of 4.5 Hz at 0.1g. Thus, using the Power Integal optimization, 76.3% of the maximum achievable bandwidth is obtained with only 11.1% loss from the maximum load power.
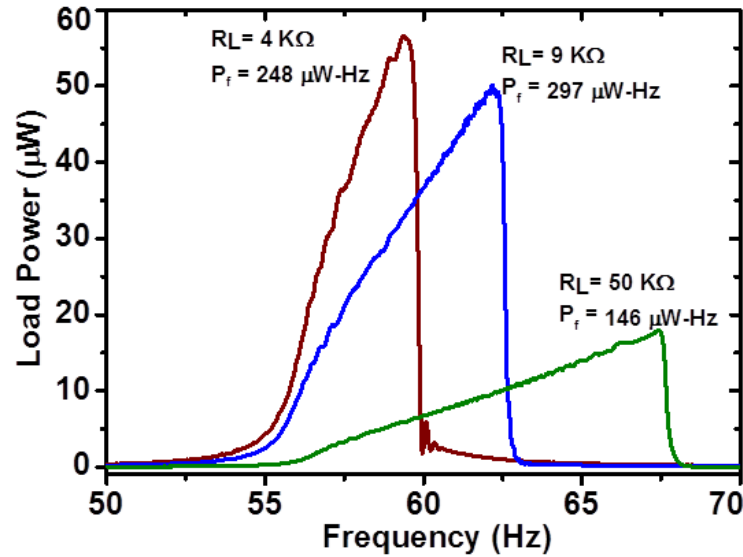
Fig. 6.22: Load power frequency responses at 0.1g to demonstrate the Power Integral optimization. Optimum load of 9 KΩ is used to balance between maximum load power and maximum achievable bandwidth.

6.4.4. Effect of Load Resistance on Bandwidth: The modulation of bandwidth using the interplay between electrical load and mechanical input could be explained by Fig. 6.23 which shows the down- and up-jump frequencies as a function of R_L for various input accelerations. For 0.1g, the behavior is resonant for values of R_L up to 1200 Ω due to large electrical damping and thus both the jump points merge into one.

With an increase in R_L, electrical damping decreases drastically, the jump points separate out, and the gap between them rises. The shaded portions of the plots depict the nonlinear hysteresis regions and they widen for higher load resistances. However, with an increase of the input acceleration, the hysteresis regime begins at a lower load resistance and there is already a loop width of 3.6 Hz at 0.5g for load of only 100 Ω. It is to be noted from equation (6.23) that the electrical damping is independent of the driving force. But even if c_{EM} is large for smaller load values, the nonlinear effect becomes prominent with growing input acceleration levels. The nonlinear jump down frequency does not increase indefinitely with a increase of electrical load resistance but saturates at one point and that threshold saturation point shifts to a lower value of load with an increase of the input acceleration. Since the jump down frequency defines the bandwidth, the operational bandwidth also gets saturated at a certain load resistance and does not increase with any

further increment of the load. On the other hand, the jump up frequency remains almost constant for all values of the load. The points of maximum P_f are also marked in Fig. 6.23 for various acceleration levels and they occur near the load where the threshold saturation for the jump-down frequency occurs. It is to be noted that the P_f values are calculated by considering the high energy branch solutions as the maximum power is generated at the jump-down frequency during the up-sweep. However, system response may result in either of the high or low energy branch for a frequency varying, excitation which is a classical problem for Duffing oscillator based nonlinear systems. The value of maximum P_f changes drastically from 297 μW-Hz at 0.1g to to 7560 μW-Hz at 0.5g as both the output power and bandwidth increase significantly with the same change in acceleration level.
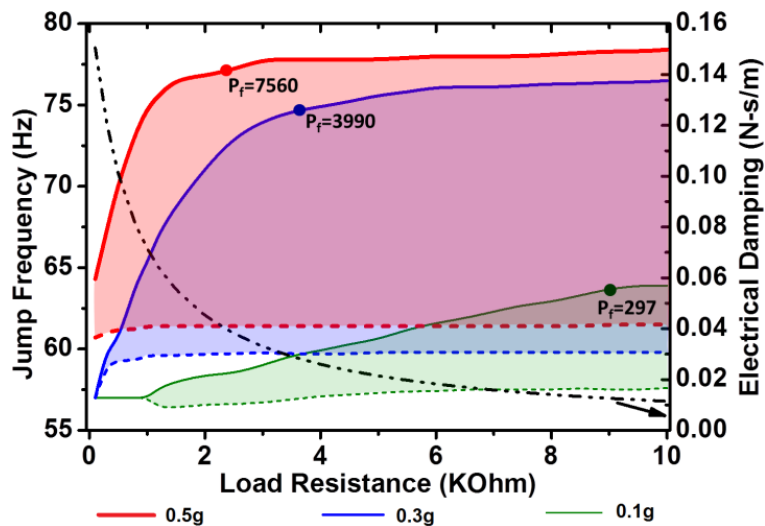
Fig. 6.23: Down-(solid) and up-(dashed) jump frequencies as a function of load resistance for different input accelerations. The shaded regions show the nonlinear hysteresis region for respective acceleration levels. Maximum P_f are marked at the corresponding load values. Electrical damping is also shown as a function of R_L.

6.5. MEMS based Nonlinear EM Energy Harvesters:

In this section, two MEMS electromagnetic energy harvesting systems are studied. The nonlinear spring architecture is varied in the two different spring structures to study the consequent effect on the wideband output response. Using suitable design choices of the spring architectures, different fundamental modes are obtained close to each other, while further widening the output response. The devices are characterized at different level of MEMS integration to obtain comparable results.
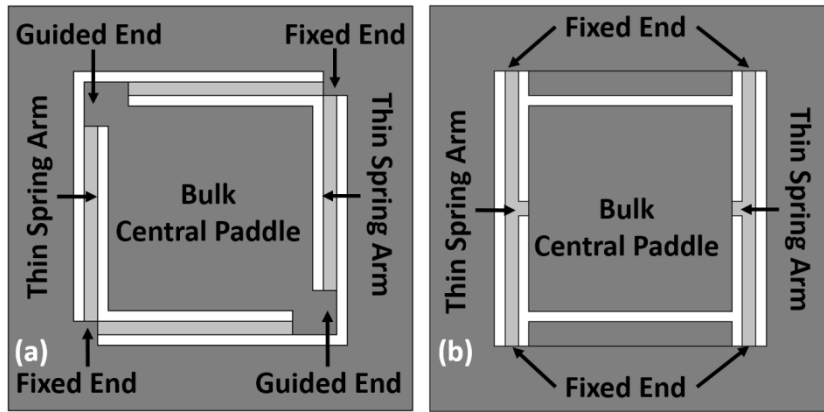
Fig. 6.24: Schematic of the nonlinear spring architectures (a) Nonlinear Acrchitecture 1 (A1) and (b) Nonlinear Architecture 2 (A2). The light grey represents the thin silicon spring arms whereas the dark grey denotes the bulk silicon-on-insulator.

Parameters	Nonlinear Architecture 1 (A1)	Nonlinear Architecture 2 (A2)
Length of a beam from a fixed to guided end (mm)	2.85	1.9
Angle between fixed-fixed ends (degree)	90	0
Width of the beams (mm)	0.2	0.2
Thickness of the beams (μm)	50	50
Dimension of movable paddle (mm^3)	3×3×0.5	3×3×0.5
Mass attached (magnet) (kg)	9.83×10^{-5}	9.83×10^{-5}

Table 6.3: Different design parameters of the two nonlinear spring architectures

6.5.1. Device Configurations: Schematic drawing of the nonlinear MEMS spring structures are shown in Fig. 6.24. The first nonlinear architecture, A1 (Fig. 6.24 (a)), consists of a large movable mass suspended by four fixed-guided beam arms. The arms are fixed in two opposite corners of the frame and attached pairwise to two other opposite corners of the movable paddle. The second nonlinear spring architecture A2 (Fig. 6.24 (b)) consists of a pair of fixed-fixed beams which form an H-shaped configuration. The large movable mass along with the thin beam joints act as the middle bar of the 'H' in this case. For both the spring architectures, the thickness and width of the beam arms are 50 μm and 200 μm, respectively, whereas the movable paddles have dimension of 3×3×0.5 mm respectively. Detailed dimensions of the two nonlinear spring designs are provided in Table 6.3. The movable spring structures are fabricated using MEMS fabrication techniques. Double layer electroplated copper coils are fabricated on a separate Silicon substrate, which consist of two layers of copper coils with the coil track width, the inter-track gap and the height of each of the coil being 10 μm each. The square shaped coil has

an outer dimension of 2.8×2.8 mm². Each of the microfabricated double layer coils has 144 turns with the coil resistance of 192 Ω. The MEMS spring structure and coil are packaged together to form the nonlinear microelectromagnetic energy harvesting devices. A small NdFeB block magnet (2.5×2.5×2 mm³) is epoxy bonded onto the movable paddle which provides mass (9.83×10⁻⁵ Kg) to the vibrating oscillator.
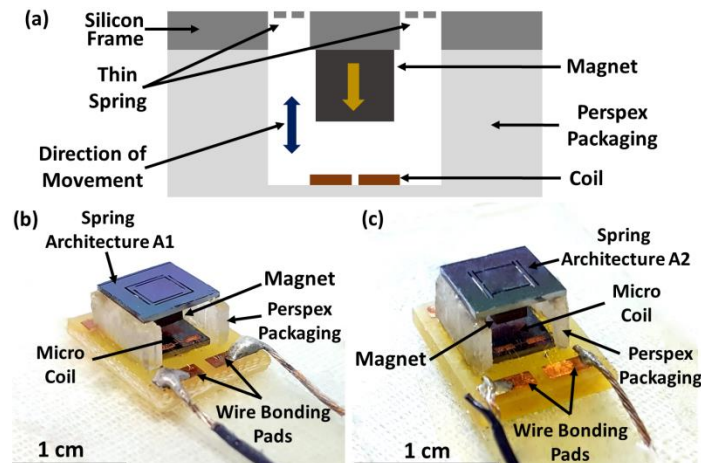
Fig. 6.25: (a) Cross-sectional view of the packaged devices. Packaged nonlinear MEMS electromagnetic energy harvesting devices (b) device with A1 architecture and (c) device with A2 architecture.
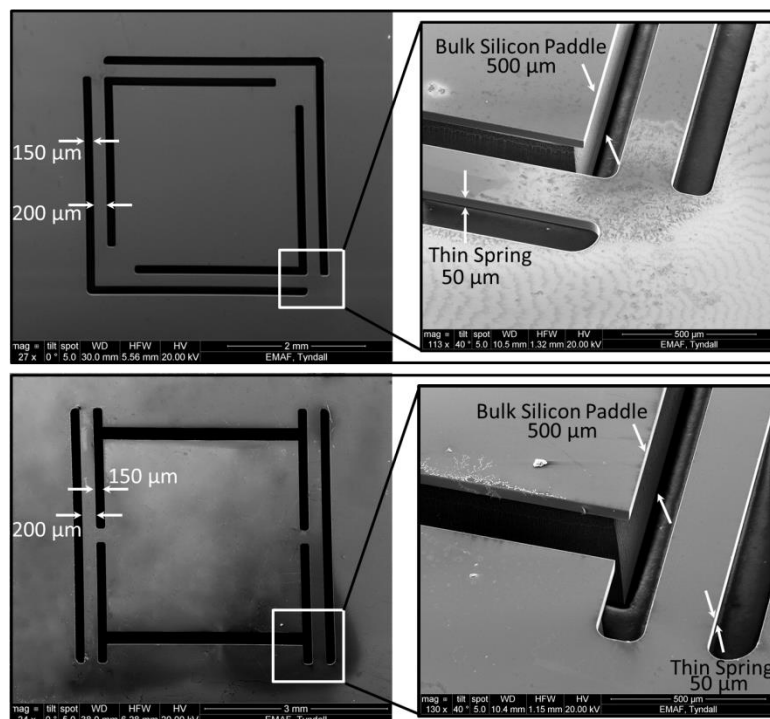
Fig. 6.26: SEM images of the (a) nonlinear architecture 1 (A1) and (b) nonlinear architecture 2 (A2). Inset figures show the tilted view of the fabricated spring structures identifying the thin spring arms and the bulk movable paddles.

Initially, the batch fabricated and diced nonlinear spring structures are packaged with commercially available wire wound copper coils having comparable dimensions to those of the micro-fabricated copper coils. The circular wire wound coil with 3mm outer diameter, 0.5 mm thickness and 25 μm wire diameter, has 560 turns and a coil resistance of 140 Ω. The cross-sectional schematic of the packaged MEMS devices is shown in Fig. 6.25 (a). An acrylic spacer is used to create a gap of 1 mm between the moving magnet and the fixed coil of the device to allow relative motion between the two. Two experimental prototypes with each of the MEMS spring architectures are shown in Fig. 6.25 (b) and Fig. 6.25 (c) respectively, where each device has a volume of 0.14 cm^3.

The spring structures are fabricated using the same steps as described in chapter 5. Scanning Electron Microscope (SEM) images of the two spring configurations are shown in Fig. 6.26 (a) and (b) respectively. The thin spring arms and bulk central paddles are identified in the tilted images in the inset figures. Similarly the micro-coil fabrication steps are also outlined. The micro-coil used in this case is same as the one used in chapter 5. A comparison between the micro-fabricated coil and the wire wound coil of similar dimension is provided in Table 6.4.

Coil	No. of turns	Area (cm^2)	Thickness (mm)	Resistance (Ω)
Wire Wound	560	0.08	0.5	140
Micro-fabricated	144	0.09	0.03	192

Table 6.4: Comparison between micro-fabricated and wire-wound copper coils

6.5.2. Electro-mechanical Model: It is well understood already that the thickness of the spring arms is an important parameter for designing this kind of stretching induced nonlinear architectures i.e., the smaller the thickness of the spring arms, greater will be the nonlinearity. Thus this method of introducing nonlinearity into the system is one of the most convenient technique for micro-fabricated energy harvesting devices as it is comparatively easy to manufacture very thin beam structures on SOI using standard MEMS processing technologies, even though such thinning of the spring arms is also restricted by process technologies such as clamping issues during dry etching of the bulk silicon etc. In the reported devices, the thickness of the spring arms is chosen to be 50 μm.
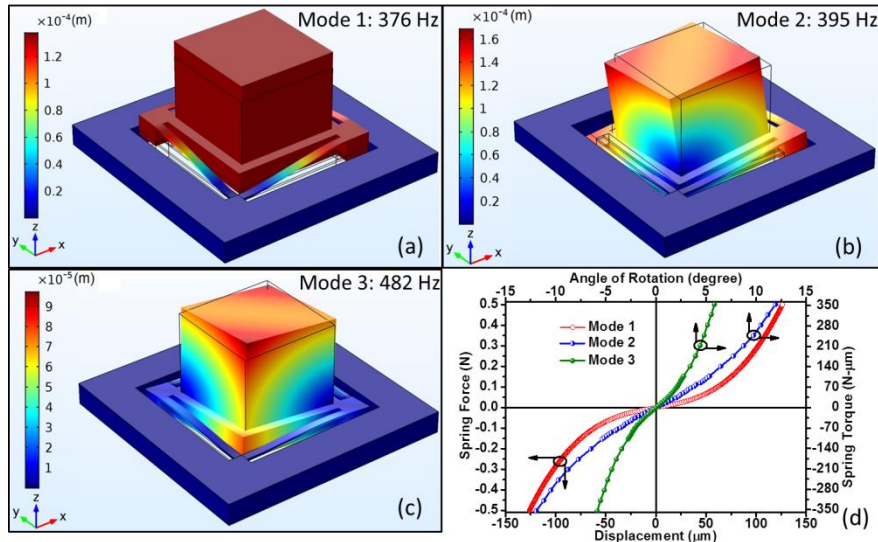
Fig. 6.27: First three fundamental modes of A1 from COMSOL: (a) Vertically up and down movement at 376 Hz, (b) Torsional motion at 395 Hz, (c) Another torsion at 482 Hz. (d) Variation of spring force vs. deflection for mode 1 and spring torque vs. angular rotation for other modes of vibration respectively.

As shown in Fig. 6.27 (a-c), the first three vibrating modes of A1 are at 376 Hz, 395 Hz and 482 Hz respectively, where the device undergoes vertical deflection and torsion along different directions. The closely spaced fundamental modes help to improve the wideband characteristic of the nonlinear springs. In linear resonator based systems, multi modal design is a common approach to harness energy from different vibration frequency peaks; whereas the nonlinear effect associated with different vibration modes and their potential interactions producing an even enhanced wideband response is unreported and hence not analyzed properly. The nonlinear behavior of the different modes of A1 can be understood from Fig. 6.27 (d). The spring force variation in the case of the first mode is shown as a function of the displacement whereas the variation of the produced spring torque as a function of the angular rotations of modes 2 and 3 are shown using FEM analysis in COMSOL Multiphysics. Using small angle approximation, the angular rotations are calculated from the deflection values in COMSOL for different applied torques. The nonlinearity produced at the large deflections can easily be observed from the plots. For mode 1, the spring force variation is almost in the linear regime till 50 μm. Beyond this point the spring force enters the nonlinear regime as the stretching strain becomes significant.
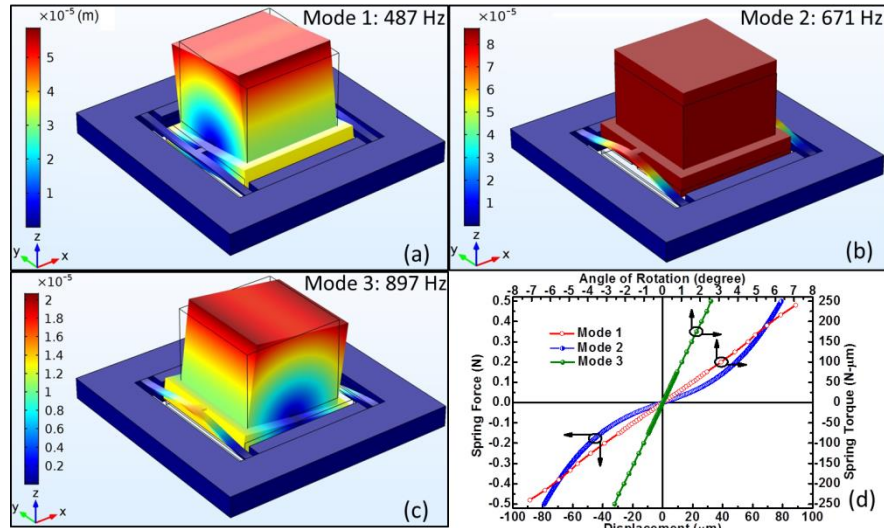
Fig. 6.28: First three fundamental modes of A2 from COMSOL: (a) Torsional movement at 487 Hz, (b) Vertically up and down movement at 671 Hz, (c) Twisting movement at 897 Hz. (d) Variation of spring force vs. deflection for mode 2 and spring torque vs. angular rotation for vibrational modes 1 and 3 respectively.

The first three fundamental modes of A2 are at 487 Hz, 671 Hz and 897 Hz respectively, as shown in Fig. 6.28 (a-c). These modes correspond to torsional, vertical and twisting motions. Ideally one would like to have the vertical up-down motion as the first mode as that should be the most dominant mode of the spring architecture as that would maximize the magnetic flux linkage. But in this case torsional motion is obtained at lower frequency due to the presence of the thin beam joints, as indicated in Fig. 6.24 (b), which makes the torsion easier compared to A1 where the beam joints are bulk (Fig. 6.24 (a)). In A2, the gap between different modes is quite wide compared to that in A1. Also, it is observed from Fig. 6.28 (d) that except for the vertically moving mode 2, other modes do not incorporate any nonlinear effect. Hence, the influence of the interaction between different degrees-of-freedoms is expected to be lower. It is observed that both linear and nonlinear stiffness for the vertical mode A2 are higher compared to those of A1. Thus, much higher force is required to produce the same deflection in A2. However as the nonlinear stiffness is higher for A2, the frequency widening effect due to nonlinear stretching of a single vibration mode is also expected to be higher. This higher stiffness leads to higher operating frequency as well. The derived linear and nonlinear stiffness constants of A1 and A2 spring architectures are given in Table 6.5.

Theoretically, the upper bound on the maximum obtainable power from nonlinear energy harvesting device was calculated by Ramlan et al. [139] and is given as

$$P_n = \frac{2m\omega^3 Z X_{max}}{\pi} \tag{6.24.}$$

where ω and Z are the angular frequency and amplitude of the input harmonic vibration and X_{max} is the maximum displacement of the oscillator under any circumstances. Since the essential features like proof mass and maximum allowable displacements of the different nonlinear energy harvesting devices are same, the theoretical maximum average output power is plotted in Fig. 6.29 as a reference over a frequency range of $0 - 1000$ Hz under different input accelerations from 0.1g to 1g (1g=10 m/s^2). From equation (6.24), it is clear that proof mass plays an important role in increasing the output power. The effect of changing the mass on output power at a fixed frequency (500 Hz) is shown on the inset of Fig. 6.29, while keeping the other parameters unchanged. However, the actual performance of the reported devices is limited by a number of factors such as parasitic damping, the stiffness of the springs etc.

Stiffness Constant	Nonlinear Architecture 1 (A1)	Nonlinear Architecture 2 (A2)
Linear Stiffness (k) (N/m)	917.2	2665.7
Nonlinear Stiffness (k_n) (N/m^3)	1.93×10^{11}	5.62×10^{11}

Table 6.5: Comparison between stiffness parameters of the two nonlinear architectures
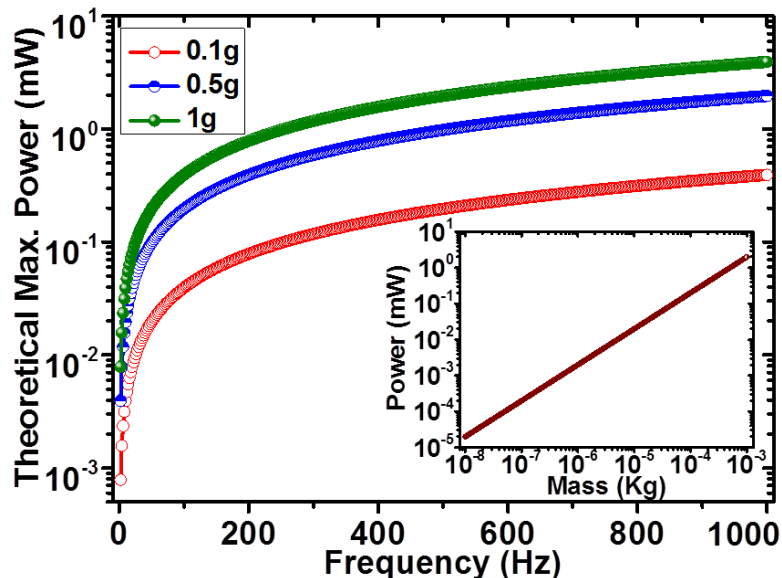
Fig. 6.29: Theoretical maximum average power from the devices is plotted for different input accelerations as a reference of the actual performance. The dependence of proof mass on output power at a particular frequency (500 Hz) is shown as an inset.
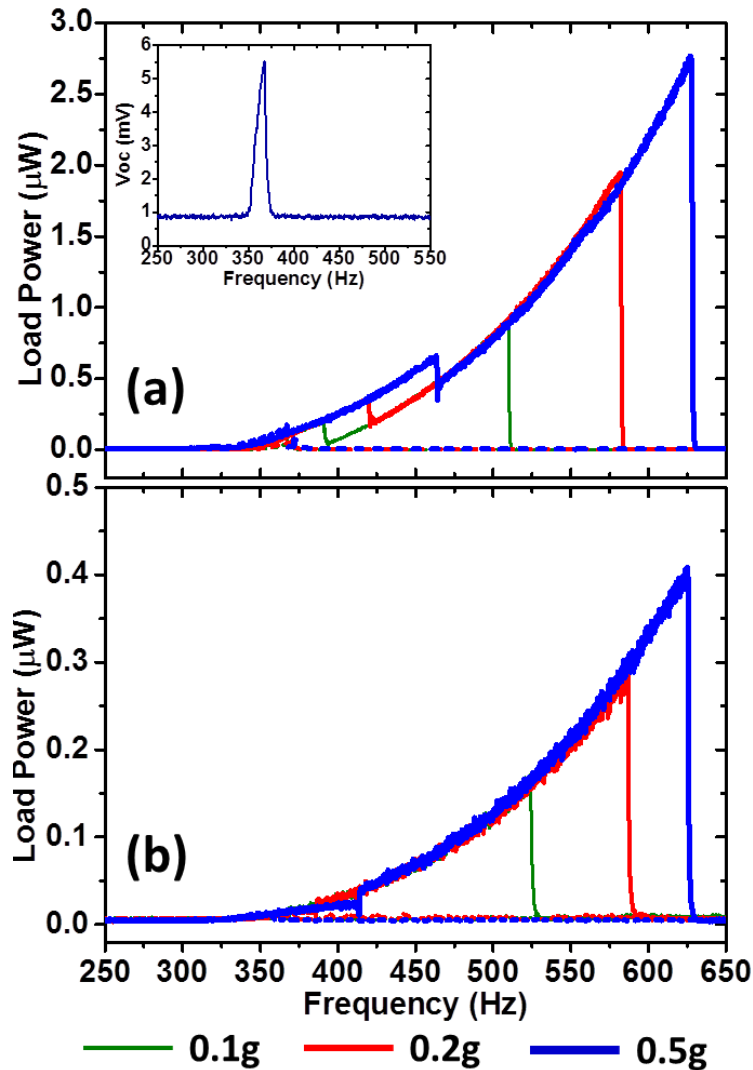
Fig. 6.30: Measured load power response of (a) A1WC and (b) A1MC as a function of input frequency for various accelerations for both up- and down-sweep of the frequency. The inset in (a) shows the open circuit voltage response of A1 at an acceleration of 0.02g.

6.5.3. Experimental Characterization: The two MEMS nonlinear spring architectures are characterized by two different coils, wire wound and micro-fabricated, respectively. For ease of understanding, the following terminologies have been used.

A1WC – nonlinear architecture A1 assembled with the wire wound coil.

A1MC – nonlinear architecture A1 assembled with the micro-fabricated coil.

A2WC – nonlinear architecture A2 assembled with the wire wound coil.

A2MC – nonlinear architecture A2 assembled with the micro-fabricated coil.

In all of these cases, the NdFeB magnet (epoxy bonded onto the central paddle of the springs) acts as the proof mass, which increases the energy transduction efficiency due to

the large mass of the magnet compared to the conventional MEMS based approaches where a coil proof mass is used. The spring architectures A1 and A2 are characterized at different acceleration levels to obtain comparable outputs. As already explained, A2 is much stiffer than A1. Therefore, a much stronger force is required to enter the nonlinear regime for A2 spring architecture. As a consequence, high acceleration values are used to obtain significantly wider bandwidth and power output from the devices with the A2 spring architecture. However, 0.5g is used as a common acceleration value to compare the performance of the two different spring designs.

- **Characterization of Nonlinear Architecture 1 (A1):** The load power response of the devices A1WC and A1MC as a function of the input excitation frequency for both up- and down-sweeps are shown in Fig. 6.30 (a) and Fig. 6.30 (b), respectively, under different acceleration levels. As mentioned before, the first three fundamental modes of nonlinear design A1 are relatively closely spaced at 376 Hz, 395 Hz and 482 Hz. The large deflection, stretching strain nonlinearity results for the out-of-plane and different tilting vibration modes of the spring architecture, which leads to nonlinear output responses at each mode. The first mode (376 Hz), which corresponds to the vertical up-down movement, is most dominant as the external excitation is also aligned along that direction. Also, the nonlinear contribution due to this mode is quite large, as seen from Fig. 6.27 (d). With an increase of input excitation frequency, the nonlinear contribution due to the following modes compliance with the first mode and that adds up to the overall nonlinear output response of the device. As a result, ultra-wide output response is achieved and the corresponding wideband nature escalates with the increase of input acceleration. A similar frequency response is observed for both A1WC and A1MC as the same nonlinear spring architecture is used for both. The inset in Fig. 6.30 (a) shows the open circuit voltage response of A1WC at a low acceleration of 0.02g where only the vertically moving first mode is significant whereas other modes are not recognizable. The peak is obtained at 367 Hz which agrees fairly well with the FEM analysis (376 Hz). As seen from the experiments, the maximum load power is generated for both the prototypes when the internal coil resistance is equal to the external load resistance. This condition holds when the parasitic damping is higher compared to the electrical damping. In MEMS based electromagnetic generators, the electrical damping is expected to be low as the small dimension magnet and coil assembly produces relatively lower electromagnetic coupling and there is little scope to form efficient magnetic arrangements, which also

affects the output power. Thus, the optimized loads for both the devices are equal to the respective coil resistances i.e., for A1WC it is 140 Ω and for A1MC the same is 190 Ω respectively. At 0.5g, the maximum average load power of 2.87 µW is obtained at the jump-down frequency of 629 Hz with a half power bandwidth of 82 Hz. A peak load power of 0.41 µW is generated at 627Hz for A1MC along with a bandwidth of 80 Hz at 0.5g input acceleration. The significant fall in the output power for A1MC compared to that of A1WC is due to the low electrical damping produced by the microfabricated coil with fewer coil turns than the wire wound coil, whereas the output bandwidth remains almost the same due to the identical mechanical structures.

- **Characterization of Nonlinear Architecture 2 (A2):** Load power variations of the devices A2WC and A2MC with up- and down-sweeps of the input frequency are shown in Fig. 6.31 (a) and Fig. 6.31 (b) under three different acceleration levels such as 0.5g, 0.8g and 1g. It is observed from FEM analysis in the previous section that the first vibration mode (487 Hz) of this spring structure is a torsional mode which is relatively linear, whereas the second vertically moving mode at 671 Hz is nonlinear in nature. Thus, for devices with the A2 architecture, no overlap between the wideband responses occurs. A linear peak is obtained near 587 Hz, generating 0.023 µW at the peak for A2WC and 0.0054 µW for A2MC. However, such a resonant response is followed by the wideband output frequency response due to the strong nonlinearity of the second vibrational mode. Like the previous case, the output response also widens with the increase of the amplitude of the input acceleration. The jump-down frequency for this strong nonlinear response increases significantly from 700 Hz at 0.5g to 704 Hz at 0.8g and 829 Hz at 1g. This can be explained from the spring force variation with displacement of the corresponding mode shown in Fig. 6.28 (d). As compared to A1, much higher force is needed for A2 to enter into the sufficiently nonlinear regime. Thus, larger input accelerations are needed to achieve the desired wideband output. At 1g acceleration, a maximum load power of 1.05 µW is generated for A2WC at 829 Hz. The corresponding half power bandwidth of the device is 60 Hz. On the other hand, a maximum load power of 0.22 µW is produced for the device A2MC under similar excitation condition at 830 Hz which corresponds to a half power bandwidth of 61 Hz. In this case also the load resistances of both prototypes are adjusted to match the respective coil resistances for optimal power generation. It is to be noted that both the load power and the half power bandwidth of the prototypes with the A2 nonlinear structures are comparatively smaller than those of the prototypes with the

A1 variant. This can be attributed to the fact that A2 is much stiffer compared to A1, which imposes higher structural damping [240] as well and reduces the output power in spite of the nonlinear contribution from other modes as in the case of A1WC and A1MC.
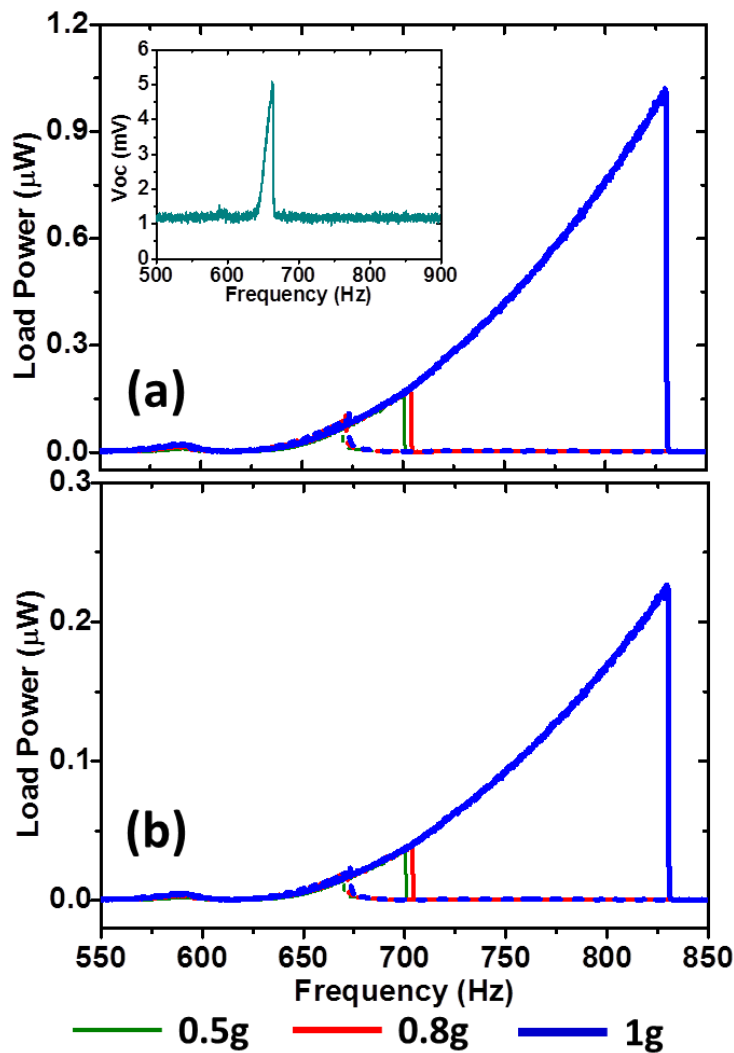
Fig. 6.31: Measured load power response of (a) A2WC and (b) A2MC as a function of input frequency for various accelerations for both up- and down-sweep of the frequency. The inset in (a) shows the open circuit voltage response of A2 at low acceleration of 0.1g.

6.6. Conclusions:

In this chapter, we have discussed the design, modelling and experimental validation of stretching strain based nonlinear monostable EM Energy Harvesters. An analytical formulation of large deformation of the spring arms shows that a cubic nonlinearity results from the contributions of stretching in addition to bending. This nonlinearity increases the operational bandwidth of the VEH significantly. Further, numerical investigation of a deterministic model based on a monostable Duffing oscillator supports this increase in bandwidth. A qualitative discussion based on the numerical model shows

that the presence of dynamical noise in the experimental system reduces the expected bandwidth. Using FR4 as the spring material, an initial device (prototype I) shows up to 10 Hz bandwidth at 1g acceleration. In this prototype, a non-characteristic secondary peak (at 196 Hz) was observed experimentally, where 110% of the peak power at the nonlinear jump point can be achieved at 0.5g acceleration. Almost three times more power is generated at this symmetry broken peak compared to the nearby symmetric states, showing high potential of dynamical symmetry breaking in generating more power compared to the symmetric states and this can be utilized by further optimization. A detailed examination of this secondary peak shows the symmetry breaking bifurcation at that particular position. However, an elementary dimensional and non-dimensional one degree-of-freedom model could not justify the presence of any such additional peak. It is inferred that the symmetry broken secondary resonance may appear due to the dynamic symmetry breaking of the oscillator or due to the inherent asymmetry of the built prototype. The work also shows the potential of FR4 based a small footprint, wide bandwidth, nonlinear EM harvester generating a useful amount of power, which can be increased significantly by further optimization of the magnet coil assembly. The same is demonstrated in an improved prototype II. A reasonably good bandwidth of 9.55 Hz is obtained with prototype II among the reported macro prototypes whereas the load power of 488.47 μW generated across a resistive load of 4000 Ω under 0.5g input acceleration at 77 Hz, which is also useful for practical applications.

Further, a generalized bandwidth widening scheme with respect to a nonlinear vibration energy harvester is proposed. It is shown that bandwidth and the maximum power point (or jump-down frequency) can be modulated by changing either the input acceleration or the resistive load as opposed to a linear device, showing the inter-dependence among different physical parameters of nonlinear generator. By exploiting the interaction between the electrical circuitry and the mechanical motion of the device, the power output is improved over a large frequency range. This improvement is quantified using a new figure of merit based on a suitably defined 'power integral (P_f)' for nonlinear vibrational energy harvesters.

Following a successful demonstration in meso-scale, the concept is utilized at MEMS scale with further innovations. Two different topologies are studied there. In the first nonlinear architecture (A1), the fixed ends are orthogonal to each other with the beam joined in the middle, whereas the second nonlinear architecture (A2) is H-shaped. The

realization of the spring architectures on the thin Silicon-on-Insulator substrate using MEMS processing technology activates different fundamental modes of the devices which further widens the output response. The devices are characterized at different levels of MEMS integration to report a comparative result. Experimental results show that around 80 Hz of the half power bandwidth is obtained for devices with A1 architectures due to nonlinear contributions from closely spaced vibration modes. On the other hand, devices with A2 spring structures have 60 Hz half power band width due to strong nonlinear stiffness of the beams.

However, all of the devices suffer from problem of hysteresis which might restrict their operation in practical applications. This issue is addressed in the following chapter.

Chapter 7

Electrical Switching in Nonlinear Energy Harvesters

7.1. Introduction:

Nonlinear oscillator based energy harvesters have improved the off-resonance performance significantly due to their inherent wideband frequency response when compared with linear resonators. Various nonlinear energy harvesters with different types of potential energy functions, e.g. single-well [142–147], double-well [150-151, 154-155, 241-242] and triple-well [243-245] systems have been explored comprehensively to achieve energy transduction over a wide frequency range as has been already mentioned in chapter 2. However as it has been mentioned in the concluding section of the previous chapter that the branching of the frequency response introduces the phenomena of multistability and hysteresis in the dynamics of the devices, which means that a number of stable steady states with different energy output may coexist. The device selects a stationary state depending upon the frequency schedule of the external excitation and the initial conditions [127, 149].

In this chapter, it is demonstrated that a suitable electrical control signal switches the state of a nonlinear VEH from the Low Energy Branches (LEBs) to the High Energy Branch (HEB). The VEHs have an inherent connection between their mechanical and electrical degrees of freedom. This interplay is exploited in an innovative way to supply a periodic electrical signal over a short period of time to the system to initiate the large amplitude mechanical motion when the system response is on the LEB. The dynamical characteristics of the proposed methods are theoretically reproduced and explained by a modified Duffing oscillator model. This elegant approach can be generalized to systems of any scale (MEMS or nanoscale devices) and with different transduction mechanisms where the manipulation of mechanical parameters may not be easy to implement.

Experimentally the proposed scheme is demonstrated using the stretching strain induced nonlinear EM energy harvester (prototype II) which is discussed thoroughly in the previous chapter.

7.2. Precedent Works in Switching of States:

In general, this phenomenon of hysteresis is not only restricted within the energy harvesting field but many dissipative nonlinear dynamical systems exhibit the coexistence of several stable states for a given set of parameters and can be found in various disciplines of science, including electronics [246], optics [247], mechanics [248], and biology [249]. In such systems, the control of the coexisting states is critical, because the corresponding attractors are extremely sensitive to any sort of perturbation. A number of control mechanisms [250] have been reported by researchers to achieve the desired state in a multistable system such as feedback control [251], using chaotic [252] or noise [253] signals or by creating a crisis of the undesired state [254].
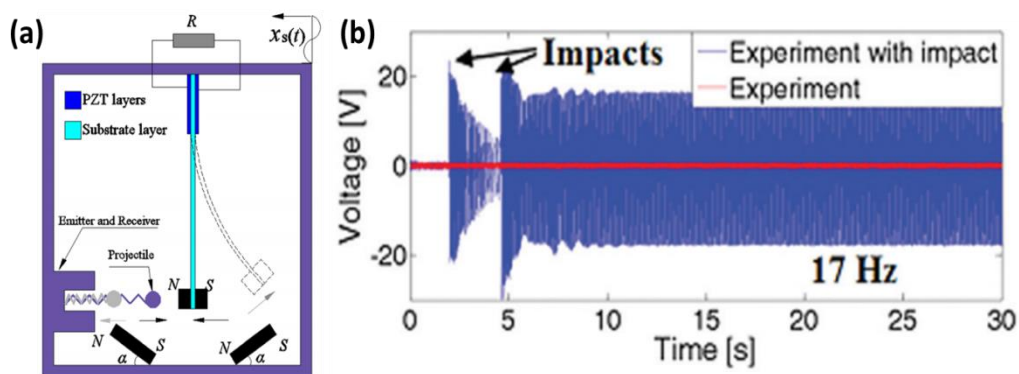
Fig 7.1: Schematic of the mechanical impact mechanism proposed by Zhou et al [256]. (b) Typical time histories showing the effectiveness of the impact method in realizing high amplitude output.

The vibrational energy harvesting application, which is a crossover between mechanical and electrical domains, serves as the proving ground for many nonlinear dynamical phenomena. In principle, it is desirable to surf the state with the largest possible energy output. However in a real-world environment there is little control available over the frequency and amplitude of the driving vibration and therefore a large energy output is not guaranteed. Thus, efficient and convenient control mechanisms are required to perturb the system from a LEB to a HEB to facilitate the maximum energy conversion within the region of multistability. Previously this pertinent problem was addressed by Cammarano et. al. [255], who proposed the concept of altering the natural frequency of the oscillator

to a higher value where only a single solution exists for the given excitation frequency and then reducing the natural frequency as the oscillator response stays on the HEB. This concept is similar to the formation of a crisis, but the destruction of coexisting states can be difficult for some nonlinear systems as small perturbations of the system parameters can give rise to new complex multistabilities. Zhou et. al. [256] used mechanical impact to provide additional kinetic energy to the oscillator to reach the HEB. Their proposed method is shown in Fig. 7.1. However, both of these mechanisms involve mechanical modifications which are practically not very convenient. Recently, Masuda and Sato [257] introduced an electrical method to destabilize the lower output branch by developing a switching circuit of the load resistance between positive and negative values depending on the response amplitude of the oscillator. This switching of the effective damping is difficult to implement and changes the dynamics of the oscillator which is not desirable.

7.3. Electrical Switching Scheme:

7.3.1. Modelling of the Switching Mechanism: The proposed electrical switching method is shown in a circuital form in Fig. 7.2. The voltage induced in the coil due to the relative movement of the magnet and coil is modeled as a voltage source with a series resistance. Hence, it is supposed that a voltage $\gamma\dot{x}$ is induced in the coil of the EM harvester which has an internal resistance R_C, where γ is the electromagnetic coupling co-efficient and $\dot{x}$ is the velocity of the mechanical oscillator. The electrical power is extracted through the load resistance R_L which is connected in series with the coil. Additionally, a voltage source V_A (with internal resistance R_A) is connected across the coil which generates electrical voltage over a short period of time to supply enough energy to the system to switch the state. The generated voltage V_A is given as

$$V_A(t) = \begin{cases} V_{OA}\sin(2\pi f_A t) & for\ t_i \leq t \leq t_f \\ 0 & Otherwise \end{cases} \tag{7.1.}$$

where V_{OA} and f_A are the amplitude and frequency of the signal within the switching period, and t_i and t_f are the starting and ending times of the switching period, respectively. V_A drives a large current (I_A) through the coil which in turn produces a magnetic field that forces the outer magnetic assembly, along with the resonating spring of the EM energy harvester to vibrate with a large amplitude and make a transition into the high energy branch. Kirchhoff's laws for the loops in Fig. 7.2 provide,

$$(R_A + R_C)I_A - R_C I_L + \gamma \dot{x} = V_A$$
$$(R_C + R_L)I_L - R_C I_A = \gamma \dot{x} \tag{7.2.}$$
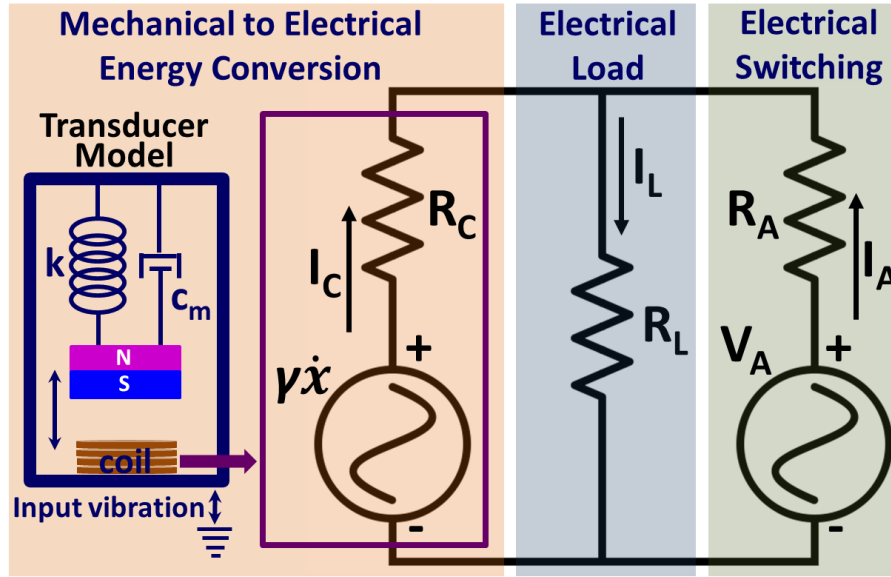
Fig. 7.2: Proposed circuit to model the electrical switching method.

Solving the above equations, the current I_L through the electrical load R_L is

$$I_L(\dot{x}, t) = \frac{V_A(t)R_C + \gamma \dot{x} R_A}{R_C R_A + R_A R_L + R_L R_C} \tag{7.3.}$$

From Fig. 7.2, the net current I_C through the coil is given as

$$I_C(\dot{x}, t) = I_L - I_A \tag{7.4.}$$

Dividing both sides of second equation of (7.3) by R_C,

$$\left(1 + \frac{R_L}{R_C}\right)I_L - I_A = \frac{\gamma \dot{x}}{R_C} \tag{7.5.}$$

Or,
$$I_L - I_A = \frac{\gamma \dot{x}}{R_C} - \frac{R_L}{R_C}I_L \tag{7.6.}$$

Substituting the value of I_L from equation (7.3),

$$I_C(\dot{x}, t) = I_L - I_A = \frac{\gamma \dot{x}}{R_C} - \frac{R_L}{R_C} \cdot \frac{V_A(t)R_C + \gamma \dot{x} R_A}{R_C R_A + R_A R_L + R_L R_C} \tag{7.7.}$$

Taking into account the effect of the additional voltage signal, the coupled electromechanical equation of motion of the oscillator is given as

$$m\ddot{x} + 2m\rho \omega_n \dot{x} + kx + k_n x^3 + \gamma I_C = -m\ddot{z} \tag{7.8.}$$

where m, ρ, ω_n, k, k_n and z are the mass, mechanical damping ratio, natural frequency, linear stiffness, nonlinear stiffness of the oscillator and the external excitation amplitude respectively. Equation (7.8) has been solved numerically using the Runge-Kutta method and compared with the experimental results.
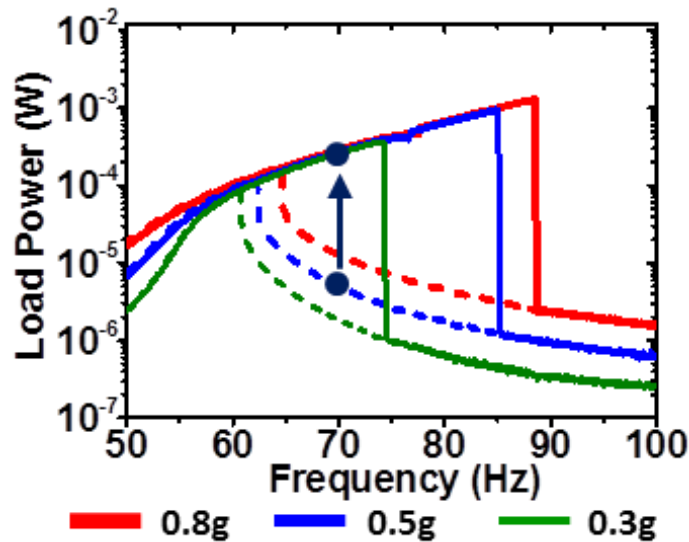
Fig. 7.3: Load power vs. frequency response of the nonlinear VEH device at various accelerations. The target switching action is indicated by the arrow.

Parameters	Values
Mass (m)	3×10^{-3} kg
Mechanical damping co-efficient (c_m)	0.018 kg/s
Natural frequency (ω_n)	114π rad/sec
Linear stiffness (k)	384.4 N/m
Nonlinear stiffness (k_n)	1.5×10^9 N/m^3

Table 7.1: Physical parameter values for the nonlinear generator which is used in the electrical switching experiment.

7.3.2. Experimental Validation of the Switching Mechanism: Experimentally the proposed scheme is demonstrated using the stretching strain induced nonlinear prototype II (chapter 6). To recapitulate, the vibrating spring structure is fabricated on FR4 substrate using Laser micromachining technology. Two pairs of oppositely polarized sintered NdFeB N50 magnets with soft magnetic iron blocks at the outer ends constitute a magnetic arrangement to maximize the flux density around an enameled copper wire coil (coil resistance, R_C = 0.71 kΩ) which is used to induce electrical voltage. A load resistance R_L = 5 kΩ is used throughout the study in order to record the load voltage. The fabricated device is tested in a LDS V455 shaker using harmonic excitation at different

acceleration levels (0.3g, 0.5g and 0.8g; g = 9.8 m/s^2). The LDS comet USB control system is used to maintain constant acceleration amplitude during the frequency sweep. Different system parameters are listed in the Table 7.1.
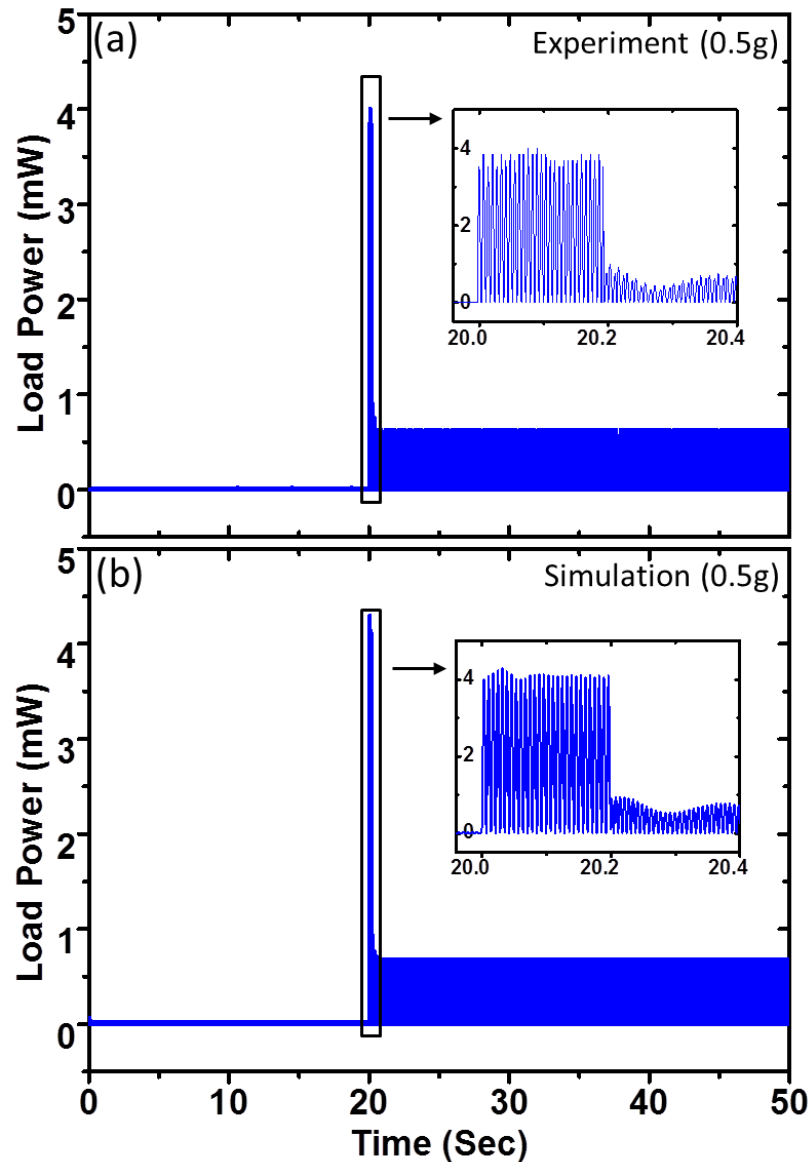
Fig 7.4: Transition from LEB to HEB at 0.5g and $f_m = 70$ Hz while using an electrical switching signal of 5v at $f_A = 70$ Hz: (a) Experimental result. (b) Numerical result.

The frequency response of the experimental nonlinear generator is also reiterated in the Fig. 7.3 which shows that the frequency response widens with increasing accelerations as the jump down frequency during the up-sweep gradually increases. During the down sweep, the VEH follows the LEB of the hysteresis, resulting in a very small output power. In Fig. 7.4(a), the switch from LEB to HEB is demonstrated for a mechanical driving frequency, $f_m = 70$ Hz, at an acceleration of 0.5g. A periodic sinusoidal electrical signal of

frequency f_A = 70 Hz and 5V amplitude is supplied within the time interval from 20 to 20.2 seconds, which is approximately 15 cycles. As a consequence, the peak output power changes dramatically by a factor of more than 35, from the LEB steady state value of 16µW before the switching period to the HEB steady state value of 563µW after the switching period. This large power is maintained even without any further supply of electrical energy. This transition from the LEB to the HEB is indicated by the arrow shown in the frequency response of Fig. 7.3. The experimental result is validated using numerical simulations based on a modified Duffing oscillator [Fig. 7.4(b)] as described in equation 7.8.
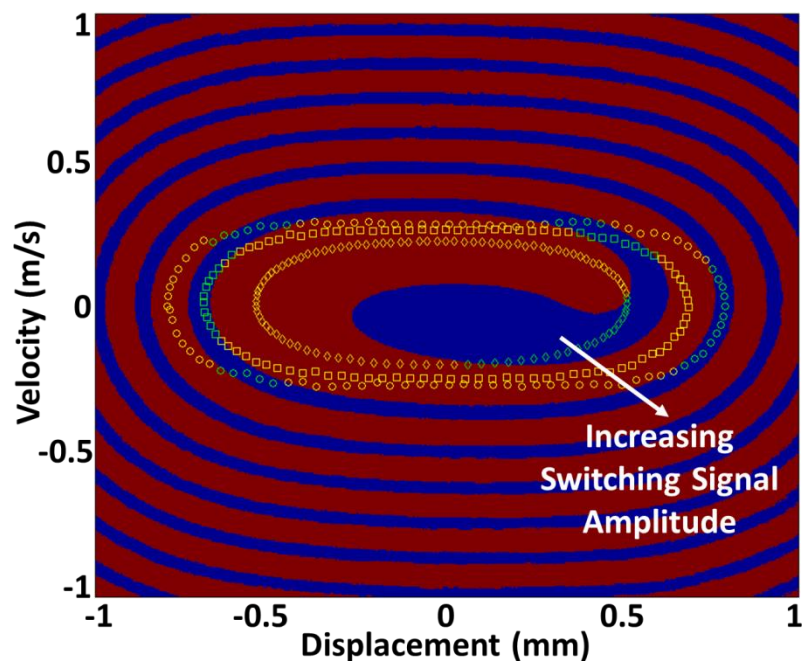
Fig. 7.5: The basin of attraction of the nonlinear oscillator. High and low energy attractors are denoted by red and blue regions respectively. Successful (yellow) and unsuccessful (green) switching are mapped for varying the phase of the switching signal at fixed amplitudes (diamonds - 5V, squares - 15V, circles - 25V).

The switching action attributes to the basin of attraction of the oscillator as indicated in the Fig. 7.5. The basin of attraction shows that starting from different initial conditions at vanishing driving force, the solution approaches either the LEB (blue) or the HEB (red). The state of the Duffing oscillator can be switched easily under external perturbation due to the intermingled nature of the basin of attraction, as the system can be driven from the current to the other attractor using a small amount of energy. This feature of the Duffing oscillator is used to intentionally perturb the system to the HEB. Previously, it has been demonstrated using basin of attraction plots that the steady states are largely dependent on

the initial conditions; the phase space volume associated with the HEB shrinks as the system comes close to the jump-down frequency [149, 233]. Close to the jump up frequency, the phase-space of the HEB is large and a comparatively small perturbation is sufficient to switch the state and vice versa. However, the phase φ of the switching signal relative to the mechanical driving force plays an important role in the switching action, as illustrated by the yellow and green symbols in the basin of attraction plot Fig. 7.5. By varying $\varphi \in [0\ 2\pi]$ for fixed switching signal amplitudes, it is observed that even very large switching amplitudes cannot guarantee a successful switching. For a particular switching amplitude, the successful switching occurs for those phase values for which the oscillator lands in the high energy attractor just after the electrical signal is switched off and vice versa for the unsuccessful cases. In mathematical terms, the LEB and HEB correspond to stable fixed points in the Poincaré map of equation (7.8) with respect to constant phase of the external driving force. The separatrix (i.e. the boundary) which divides the two basins of attraction is given by the stable manifold of the saddle of this Poincaré map.
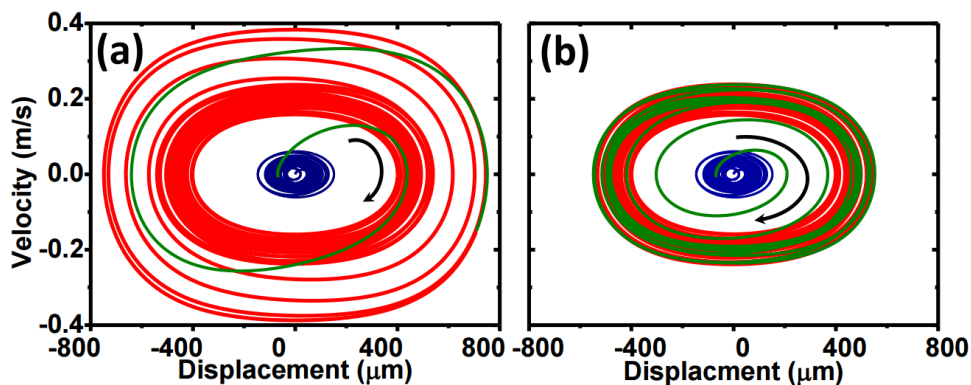
Fig. 7.6: Phase portrait of the system are depicted when the electrical excitation used is (a) large amplitude (10 V), short duration (0.02 sec) and (b) small amplitude (3.5 V), long duration (0.2 sec). The blue and red spirals are the LEB and HEB respectively whereas the green lines denote the electrical perturbation period.

However, even if the desired attractor cannot be obtained using a very large switching signal and at the same time can be obtained using a relatively smaller switching signal, it is important to understand the dynamics behind every successful switching action. In Fig. 7.6, the oscillator phase portrait is demonstrated for large and small amplitudes of the switching signal. For a large amplitude, shorter duration electrical input, the low amplitude limit cycles in the phase portrait of the system diverge out to very large orbits due to a sudden gain of kinetic energy before finally spiralling into the HEB limit cycles

as the electrical input is turned off, which is demonstrated in Fig. 7.6 (a). On the other hand, using a small amplitude, longer duration periodic signal, the low amplitude orbits are gradually driven to the desired orbit (Fig. 7.6 (b)).

7.4. Results & Discussions:

7.4.1. Probabilistic Study on Energy Requirement: To obtain further insight into the switching mechanism, the successful and unsuccessful switching is mapped in Fig. 7.7(a) for varying phase and amplitude of the electrical switching signals.
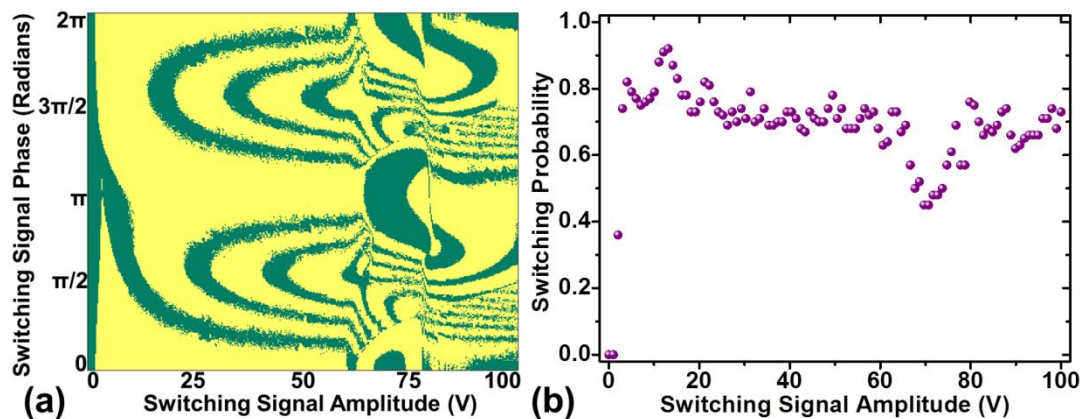
Fig. 7.7: Probabilistic study on the switching mechanism: (a) Mapping of successful (yellow) and unsuccessful (green) switching for varying the phase of the electrical switching signal with its amplitude. (b) Probability of successful switching as a function of the switching signal amplitude.

For very small amplitudes, there is no switching as expected due to the lack of injected energy to facilitate a switch. For moderately high amplitudes, the probability of successful switching increases due to the presence of the high energy attractor near the origin. Thus, suitably injected electrical energy can relatively easily drive the oscillator from the low to the high energy attractor. Very high amplitude signals, on the other hand, can oscillate the system into concentric and shallow elliptical rings of high and low energy attractors. Therefore, the probability of switching decreases relatively as the unsuccessful switching are obtained for many phase values. The corresponding variation of the probability of switching is shown in Fig. 7.7(b). The optimization of the energy required for optimal control of coexisting states is a topic of further research. The practical implication of this phase dependence of the switching method is to simply repeat the process if success is not obtained in the first attempt. A calculation is given below in order to estimate the total energy that might be needed to facilitate a switching.

Let E_0 be the energy required to apply switching signal once and P_S be the probability of successful switching in one attempt. The total energy (E_T) that would be spent in order to switch the state is calculated as

$$E_T = P_s E_0 \sum_{k=1}^{\infty} k(1 - P_S)^{k-1}$$

$$= P_s E_0 + (1 - P_S)P_S 2E_0 + (1 - P_S)^2 P_S 3E_0 + \cdots$$

$$= P_s E_0 [1 + 2(1 - P_S) + 3(1 - P_S)^2 + \cdots]$$

$$= P_s E_0 \frac{\partial}{\partial q} [q + q^2 + q^3 + \cdots]$$

$$= P_s E_0 \frac{\partial}{\partial q} \frac{q}{(1-q)}$$

$$= P_s E_0 \frac{1}{(1-q)^2}$$

$$= \frac{E_0}{P_S} \tag{7.9.}$$

where $q = (1 - P_S)$.

Since P_S is not too small, the total energy required is not very large under practical conditions even if successful switching into the HEB is not obtained in a single trial.

One of the most significant concerns about the proposed approach is that a certain amount of energy needs to be supplied in order to facilitate the switching. However this invested energy is quickly recovered through increased power conversion in the HEB. This is demonstrated in Fig. 7.8, where the numerically calculated net electrical energy evolution of the system is shown. The net energy increases very slowly as long as the system remains in the LEB as only little power is generated. The energy is supplied electrically for 0.2 seconds and this results in a negative slope of the energy curve. Once the system reaches the HEB, the slope of the energy curve becomes steep as large power is generated. With a decreasing acceleration amplitude, both the required switching energy and the energy recovery time become larger. If the switching is successful at the first attempt, the externally supplied energy is recovered within 2 seconds at 0.3g, which shortens to 0.4 seconds at 0.8g. Similarly to E_T in equation (7.9), the expectation times for energy recovery increase by a factor $1/P_S$ if multiple switching attempts are required.
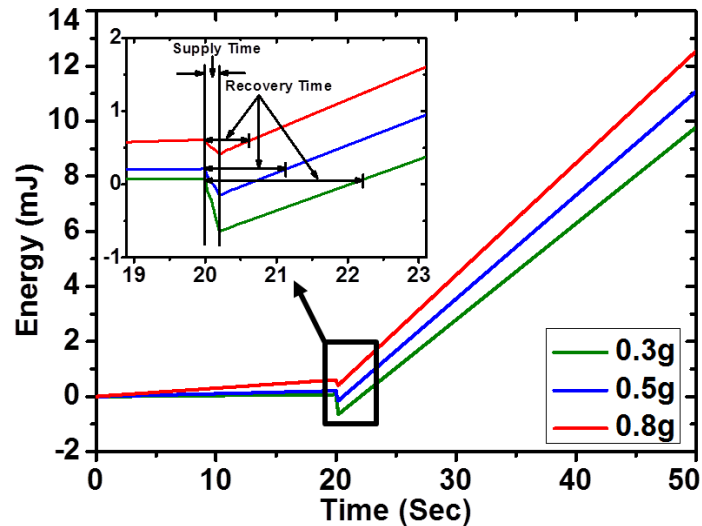
Fig. 7.8: The evolution of the net electrical energy under different acceleration levels. The negative slope from 20 to 20.2 seconds indicates that energy is supplied over that period of time.

7.4.2. Demonstration under amplitude-frequency varying input: In general, there is no control over the amplitude and frequency of the ambient sources and the convertible energy is distributed over broad ranges of these parameters, making nonlinear energy harvesters an attractive solution. However, as mentioned already, the selection of the desirable branches in a nonlinear harvester is strongly dependent on knowledge of the input amplitude and frequency. Thus its application is limited due to this fundamental effect without much effort to exploit it. Using the proposed method, the oscillation can be sustained in the desired branch within the multi-stable regime. To demonstrate this improvement, two such input trajectories (R → R′ and S → S′) are mapped in Fig. 7.9 as both the above mentioned parameters are varied simultaneously. The jump-up and jump-down lines correspond to saddle-node bifurcation lines of the Poincaré map and are plotted to define the multistate regime of the oscillation using AUTO-07P [258]. Below 0.15g, the two jump frequencies merge into a co-dimension two cusp point at 57 Hz which is close to the linear resonance frequency of the device. The R to R′ input variation is confined within the LEBs, defined by the area above jump down frequency line, and the hysteresis of the oscillation. By contrast the input path S to S′ crosses the threshold of the HEB regime, defined by the jump up frequency line, before traversing back in the hysteresis again. The output response always remains in the LEB and HEB for input parameter values which are above the jump down frequency line and below the jump up frequency curves respectively.
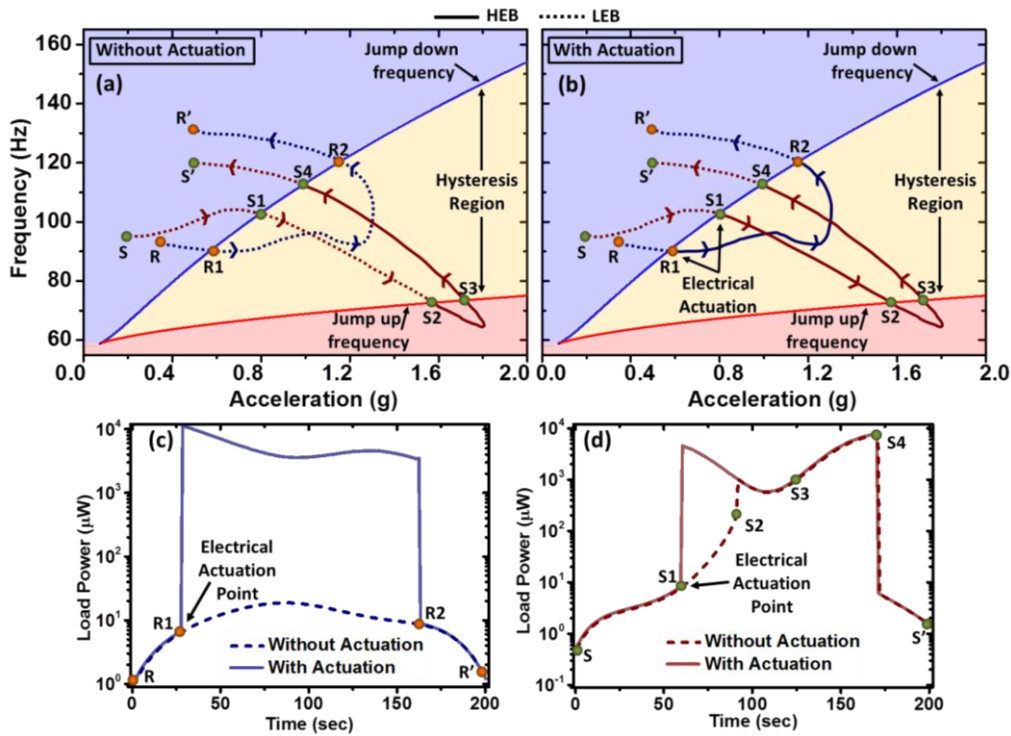
Fig. 7.9: Electrical switching under frequency-amplitude varying input vibration: Two input vibration trajectories (R → R′ and S → S′) are defined. Jump up- and down-frequencies are plotted in (a) and (b) as a function of input acceleration. Output states: (a) Without the electrical actuation, (b) With the electrical actuation. Numerical results show the improvement in load power due to electrical actuation for input trajectories (c) R → R′ and (d) S → S′.

In the absence of electrical actuation (Fig. 7.9 (a)), the low amplitude oscillation is maintained as the oscillator enters the hysteresis region crossing the jump down frequency line for both the input variation paths (R1 → R2 and S1 → S2). For the S to S′ trajectory, the oscillator is pushed to the HEB automatically when it crosses the jump up frequency from the hysteresis region at S2 and remains there till S3 as that is the only available state. This high amplitude oscillation continues even when the oscillator returns to the hysteresis from the HEB region through S3 and maintains the corresponding state until S4, as there are no other perturbations. By applying the short duration electrical actuation at the inception of the hysteresis, the system can be driven onto the HEB, which persists during the entire multistate regime (Fig. 7.9 (b)) for both the input vibrations. These result in substantial improvements in the harvesting efficiency over the entire trajectories (being more than 300 times for R → R′) and the improvements are shown in Fig. 7.9 (c) and Fig. 7.9 (d) respectively for the two input trajectories. The proposed method is significant for input excitations as R to R′, where the device oscillates mostly within the multi-stable region.
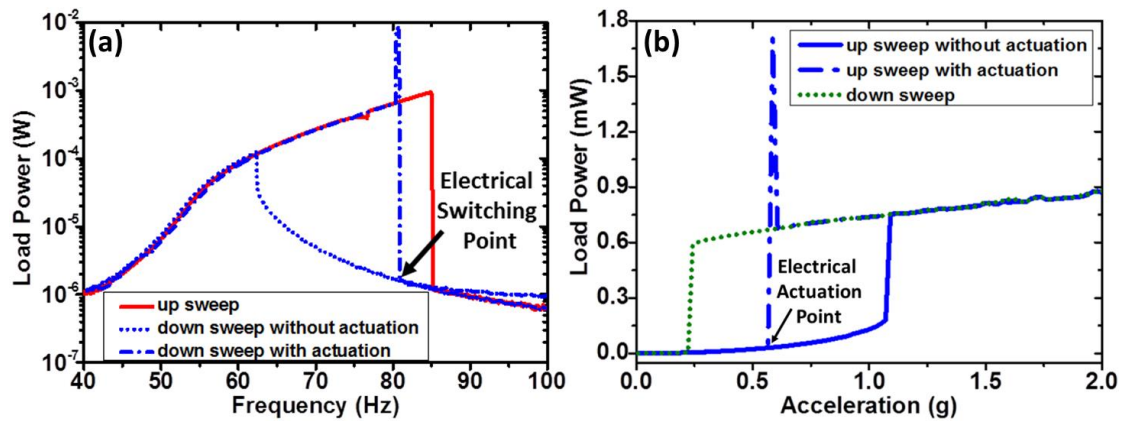
Fig. 7.10: The up-sweep is indicated by the solid line and the down-seep by the dotted line. Load power variation: (a) with frequency for the harvester under 0.5g input acceleration with switching signal applied during down sweep to switch into the HEB and (b) with input acceleration for a fixed input frequency of 70 Hz. The output remains in the LEB during up sweep unless the switching signal is applied.

It is a classical approach in VEH applications to sweep either the frequency or acceleration of the input vibration which corresponds to straight lines parallel to either axis of Fig. 7.9(a) or 7.9(b). In such cases, the switching technique can be employed to surf the HEB during down sweep (for frequency variation) or up sweep (for acceleration variation). In Fig. 7.10 (a), the switching action is successfully implemented at $f_m = 81$ Hz during the down sweep of the frequency while the excitation is kept fixed at 0.5g. Both the down sweep results without and with switching action are shown to demonstrate the improvement in output power. After the switching, the harvester follows the HEB till the end of the hysteresis region, which results in a large power output over a wide frequency range. Similarly, the application of switching to improve the harvesting efficiency is shown in Fig. 7.10(b) for input acceleration variation while keeping the input frequency fixed at 70 Hz. Without switching, the output remains in the HEB during the down-sweep as the input is slowly reduced from a very high acceleration where the oscillator already has a high amplitude oscillation. During the up-sweep, the oscillation remains in the LEB but the switching method is applied at 0.55g to transit into the HEB.

So far, a single frequency sinusoidal input vibration ($Zsin\omega t$, Z is the amplitude) is used in equation (7.8) in order to study the proposed electrical switching method. However, the same mechanism will work even if the input is multi frequency. In order to demonstrate this, a multi frequency input of the form $Z[sin(\omega t) + sin(1.2\omega t)]$ is considered and the frequency sweep is performed. It is observed that in absence of any electrical switching, a hysteresis region is generated similar to the case of a single frequency input (Fig. 7.11)

becaue the output response follows the HEB during the up-sweep and the LEB during the down-sweep. But the electrical perturbation during the down sweep is shown to switch the oscillation into the HEB. In principle, this mechanism will work for any multi frequency or broadband input vibration to switch the state.
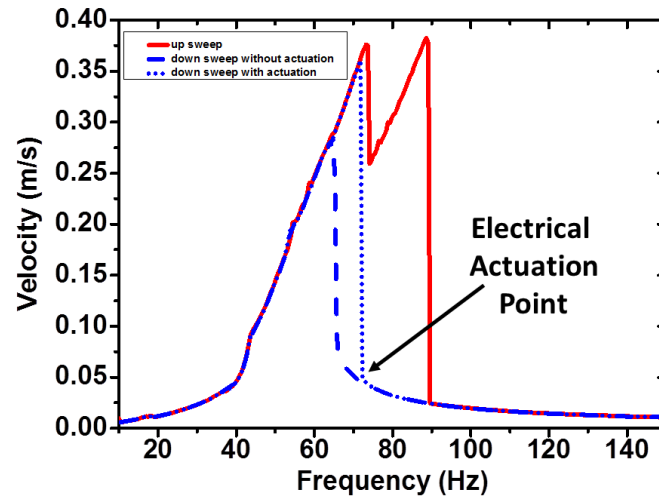
Fig. 7.11: Demonstration of electrical switching mechanism under multi frequency input. Velocity variation with frequency for the harvester under 0.5g input acceleration with switching signal applied during down sweep to switch into the LEB. The up-sweep is indicated by the solid line and the down-seep by the dotted line.

7.5. Electrical Switching in Nonlinear MEMS Device:

As described in the introduction, the electrical switching mechanism is generic and can be extended to devices of any scale. To prove the point, the electrical switching method is applied to the nonlinear MEMS VEH device with the A1 spring architecture which is already described in the previous chapter. Different physical parameters for the device are given in Table 7.2. The frequency response of the device at 0.5g is shown in Fig. 7.12 (a) using numerical simulation. It is to be noted here that the effects of different modes are not considered in the single degrees-of-freedom numerical model and it is solved by considering the first vibration mode (376 Hz) and the corresponding nonlinearity only. Hence the simulated frequency response is significantly different from the one experimentally obtained in Fig. 6.30 (b) particularly in terms of the jump-down frequency. However, the load power (1.03 µW) at the simulated jump down frequency (555.7 Hz) is quite close to the experimentally obtained load power at the corresponding frequency which highlights the accuracy of the single degree-of-freedom numerical model. The switching from the low to the high energy branch by application of the electrical signal is shown in Fig. 7.12 (b). For a mechanical driving frequency, $f_m = 475$

Hz at an acceleration of 0.5g, a periodic sinusoidal electrical signal of frequency $f_A = 475$ Hz and 10V amplitude within the time interval from 2 to 2.2 seconds shifts the output power by three orders of magnitude in the HEB.

Parameters	Values
Mass (m)	9.83×10^{-5} kg
Mechanical damping co-efficient (c_m)	0.00093 kg/s
Natural frequency (ω_n)	752π rad/sec
Linear stiffness (k)	548.6 N/m
Nonlinear stiffness (k_n)	1.93×10^{11} N/m^3

Table 7.2: Physical parameter values for the nonlinear MEMS generator which used in the electrical switching numerical modelling.

The difference in total energy (kinetic plus potential) between the HEB and LEB indicated in Fig. 7.12 (a) is 0.018 mJ, whereas the same difference between the HEB and LEB for the meso-scale prototype indicated in Fig. 7.3 is 0.1 mJ. Hence, it can be expected that the amount of energy that needs to be input through electrical excitation for the MEMS device should be much lower than the energy needed for the meso-scale prototype. However, the electromagnetic coupling factor (γ) for the MEMS device (0.17 Wb/m) is also quite low compared to that of the meso-scale device (11.069 Wb/m), as calculated through finite element analysis. Hence it can be concluded that, as the energy is transferred in this method from the electrical to the mechanical domain, the efficiency depends largely on the coupling between the two domains also. However, the proposed method is demonstrated here as a proof-of-concept just using a periodic signal generator, which can be further optimized through advanced design of the switching element. Also, to work in practical circumstances, a feedback circuit must be designed which can determine in-situ if the response is in the HEB or not and can initiate the electrical switching mechanism. The circuit may constitute of a voltage comparator to decide if the system is on the low energy branch, an energy storage element to store the energy from the harvester itself, a triggering circuit and a voltage amplifier to generate a large amplitude signal. This is however out of the scope of the current study and could be attributed as the future work.
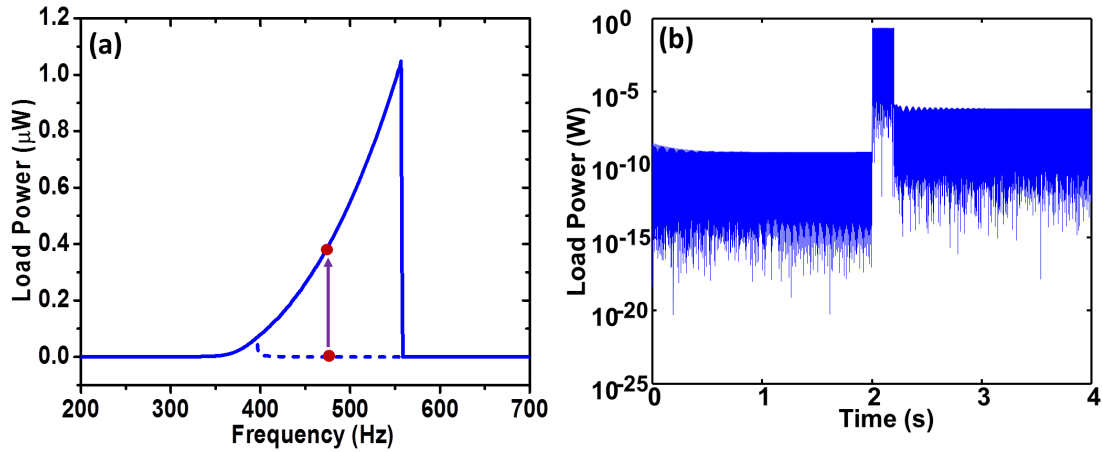
Fig 7.12: (a) Numerically simulated frequency response of the MEMS nonlinear VEH at 0.5g. (b) Transition from LEB to HEB at 0.5g and $f_m = 475$ Hz while using an electrical switching signal of 10V at $f_A = 475$ Hz.

7.6. Conclusions:

In summary, the reported work has demonstrated the potential of the electrical control mechanism to switch into the HEB of a nonlinear energy harvester within the region of hysteresis. In principle, the control method can be applied to any device with nonlinear hysteresis, having different sizes and transduction methods, through required modifications. The presented physics is generally applicable for other means of switching mechanism to control the coexisting states of the nonlinear oscillators which may find many applications in different branches of science and engineering.

Chapter 8

Development and Integration of Nano-structured CoPtP Permanent Magnets

8.1. Introduction:

Previous chapters describe the design, simulation, micro-fabrication and testing of EM VEH devices using NdFeB bulk magnets and integrated or wire wound coil. As mentioned in chapter 2, it is a major challenge in this field and in general in many applications of magnetic MEMS to develop high performance micro-magnets using MEMS or CMOS compatible processes. However, in spite of the various application needs of having permanent magnets at micro-scale, unfavourable volume dependent scaling laws for magnetic forces limit their applications like actuation and transduction. This is due to the fact that magnetic fields from a current carrying electromagnet (where the source of magnetic field is the current) scale down unfavourably with size, whereas the fields from a permanent magnet (where the source of the magnetic field is residual magnetization due to atomic scale phenomena) are scale invariant up to the atomic scale. This scaling is fairly constant down to the size scale of a single domain (usually < 100 nm), below which thermal energy can dominate, and the magnet may exhibit a super-paramagnetic behaviour with no residual magnetization [259]. Hence, above this atomic limit, permanent micro-magnets provide an effective way of realizing strong static magnetic fields. Rare earth based permanent magnets are mostly used in motors, actuators or energy generation applications. Sintering or melt spinning are a few of the industrial deposition processes for NdFeB, SmCo and other rare earth magnets, but these processes usually require very high temperatures and are incompatible with MEMS fabrication [260]. Moreover, miniaturization and patterning for batch fabrication of these sintered or melt spun rare earth based magnets is an extremely difficult task to achieve. As mentioned earlier, in order to achieve full integration of EM VEH devices, the bulk

magnets have to be replaced by hard magnetic materials which can be developed using MEMS compatible processes. Also it is important to develop relatively thick magnetic material to achieve high flux density without compromising the magnetic properties using such processes so that they can be employed in aforementioned applications replacing the bulk magnets.

This chapter starts by providing a brief introduction to basic theories of magnetic materials and reviewing the state-of-the-art of hard magnetic materials.
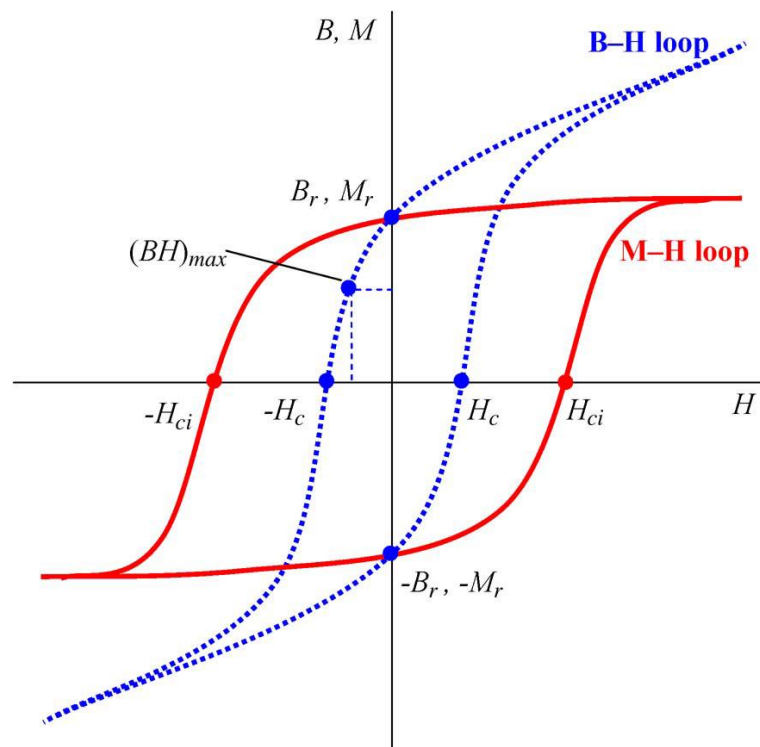
Fig. 8.1: Illustration of the B-H and M-H hysteresis loops [259].

8.2. State-of-the-Art of Hard Magnetic Material:

8.2.1. Hard Magnetic Materials: Both ferromagnetic and ferrimagnetic materials can be classified as either soft or hard on the basis of their hysteresis characteristics. Permanent, or hard, magnets deliver high magnetic flux combined with high stability against demagnetization. In the absence of an external magnetic field, these materials exhibit strong magnetization. Also, they can act as a source of magnetic fields when magnetized, without requiring any external power. Soft magnetic materials, on the other hand, only become magnetized in the presence of an external magnetic field from either a current-carrying conductor or a permanent magnet. Soft magnetic materials are normally used in devices that are subjected to alternating magnetic fields and in which energy losses must

be low. Soft magnetic materials are popular for their applications in transformer and inductor cores [261-262]. Hard magnetic materials are widely used in magnetic storage media, motors and energy generators [259, 263-264]. To better understand the behaviour of hard magnetic materials and to differentiate them from soft ones, a brief review of magnetic hysteresis and other important parameters is given below.

Below the **Curie temperature**, any ferromagnetic or ferrimagnetic material contains small-volume regions in which there is a mutual alignment in the same direction of all magnetic dipole moments. Such regions are called **magnetic domains**. One domain is separated from the adjacent domains by **domain walls** or boundaries, across which the direction of magnetization gradually changes. Normally, domains are nano-sized, and in a macroscopic piece of material, there are large numbers of domains, where all of them may have different magnetization orientations. The magnetization for the entire solid is the vector sum of the magnetizations of all the domains, each domain contribution being weighted by its volume fraction. For an unmagnetized specimen, the appropriately weighted vector sum of the magnetizations of all the domains is zero. The macroscopic magnetic behaviour of any ferromagnetic material is most commonly represented by its **magnetic hysteresis loop**, which is shown in Fig. 8.1. Flux density (B) or magnetization (M) and field intensity (H) of ferromagnetic materials are not linearly proportional. If the material is initially not magnetized, then B varies as a function of H, as shown in Fig. 8.1, which is known as the hysteresis curve. The curve begins at the origin, and the B field begins to increase slowly as external field intensity H is increased. B then increases more rapidly with H, and finally settles and becomes independent of H. With the applied field, the magnetic domains change shape and size by the movement of domain walls. The domains that are oriented with the applied field grow at the expense of those that are unfavourably oriented. This process continues with increasing field strength until the macroscopic material becomes a single domain, which is nearly aligned with the field. When this domain becomes fully oriented with the applied field, saturation occurs. The maximum value of B is the **saturation flux density (B_s)** and the corresponding magnetization is the **saturation magnetization (M_s)**. From the saturation point, as the H field is reduced by reversal of the field direction, the curve does not retrace its original path. A hysteresis effect is produced in which the B (or M) field lags behind the applied H field, or decreases at a lower rate. The residual magnetic field that exists at zero H field, is called the **magnetic remanence (M_r), or remanent flux density (B_r)**. The process by

which the domain structure changes due to the inversion of the field direction from the saturation point is completely opposite to what was described earlier. The single domain rotates with the reversed field and domains having magnetic moments aligned with the new field form and grows at the expense of the former domains. The resistance to movement of the domain walls that occurs in response to the increase of the magnetic field in the opposite direction accounts for the magnetic remanence. To reduce the magnetic flux density or magnetization of the material to zero, the H field which needs to be applied in the opposite direction to the original field, is called the **coercivity (H_c)** of that magnetic material. As the applied field is increased in this opposite direction, reverse saturation is obtained. Now as the H field is increased in the first direction up to the point of first saturation, a symmetrical hysteresis loop is obtained, yielding a negative remanence and a positive coercivity.

The area within a hysteresis loop represents the magnetic energy loss per unit volume of the material per magnetization-demagnetization cycle. Soft magnetic materials normally have low loss hysteresis loops which are thin and small and therefore are used for energy storage applications. Consequently, a soft magnetic material must have a high initial permeability and a low H_c. These materials may reach their saturation magnetization at a relatively low applied field, i.e., they can be easily magnetized and demagnetized. Hard magnetic materials, on the other hand, have a high remanence, coercivity, and saturation flux density, as well as a low initial permeability and high hysteresis energy losses. Such materials possess broad and thick hysteresis. The two most important characteristics relative to applications for hard magnetic materials are the coercivity and the 'energy product' designated as $(BH)_{max}$. This corresponds to the area of the largest *B-H* rectangle that can be constructed within the second quadrant of the hysteresis curve and has the unit of kJ/m^3 or MGOe.

8.2.2. Literature Review: This section reviews the different conventional deposition techniques which include physical vapour deposition - sputtering, evaporation and pulsed-laser deposition (PLD), and electrochemical deposition route (electroplating). These wafer-level batch fabrication processes are suitable for MEMS integration and are used widely for studying hard micro-magnets.
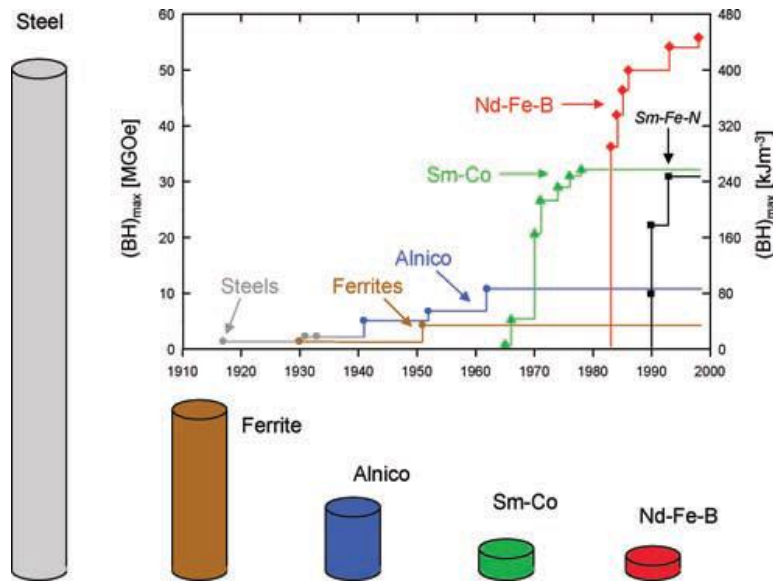
Fig. 8.2: Development in the energy density $(BH)_{max}$ at room temperature of hard magnetic materials in the 20th century and presentation of different types of materials with comparable energy density (each magnet is designed so that at a reference point 5 mm from the surface of the pole, a field of 100 mT is produced) [265].

There has been tremendous progress in the development of hard magnetic materials in the twentieth century. Fig. 8.2 shows the development of $(BH)_{max}$ of hard magnetic materials over the last 100 years. A peak energy product of ~ 450 kJ/m^3 has been achieved for sintered NdFeB (based on the Nd2Fe14B phase) rare-earth permanent magnets with very large intrinsic coercivity of 880-3260 kA/m. They are low cost and available in different sizes for various applications. But they have low corrosion resistance and very low maximum operational temperature (125-150ºC). Though sputtered NdFeB are the best performing micro magnets yet known, the requirements for specialized deposition system and high annealing temperatures have made them unsuitable for MEMS oriented devices.

Metallic alloy based hard magnets have been the researched extensively for potential integration in MEMS, mainly due to their favourable cost and relatively simple deposition processes. The earliest efforts at integrating permanent magnetic materials for MEMS focused on different cobalt based alloys with the presence of a small amount of non-magnetic elements. The general form of such materials can be expressed as CoNiX, where X is phosphorous (P) or tungsten (W). During deposition, these non-magnetic elements tend to segregate at grain boundaries, forming defects that inhibit domain walls from moving, hence increasing the coercivity. This alloy offers strong magnetic properties in the as-deposited state, i.e., without any high-temperature annealing. The final magnetic properties are, limited, however, because the intrinsic coercivities range

between 20-200 kA/m and the energy products are usually less than 10 kJ/m^3 [266-269]. However, these materials can easily be deposited and integrated in MEMS structures using the electrodeposition technique which makes them useful in a number of applications despite their modest performance.

After the successful application in the magnetic recording area, CoPt and FePt emerged as promising hard magnetic thin film materials due to their high magnetocrystalline anisotropy and magnetic saturation [270-271]. Particularly, the tetragonal L$_{10}$ ordered phase in equiatomic CoPt and FePt show very high coercivities (>800 kA/m) [272-282]. L1$_0$ refers to tetragonal distortion of a face centred cubic (fcc) structure, where atomic layers of Pt are sandwiched between Co (or Fe) layers. Weller et. al. [272], reviewed and compared the properties of various hard magnetic materials for ultra-high density magnetic recording applications. They reported that FePt and CoPt equiatomic face centered tetragonal (fct) hard magnetic films have a higher anisotropy field due to their large grain sizes compared to CoPt hexagonal (hcp) films, while the CoPt hcp phase has a higher saturation magnetization and remanence compared to the equiatomic fct phase. They suggest the use of CoPt and FePt equiatomic fct thin film magnets for developing smaller, thermally stable recording media. However, this ordered phase is normally not obtained in the as-deposited state but high temperature annealing (500 - 700°C) is required to induce the ordered L$_{10}$ structure. Films of equiatomic Co/Fe, Pt with varying thicknesses have been deposited by electroplating [273-277], sputtering [279-281] and PLD [282] techniques. Intrinsic coercivities of up to 1440 kA/m [284] and energy products of up to 124 kJ/m^3 [285] have been achieved after annealing. Shima et. al. [279] reported the microstructure and magnetization processes of highly ordered FePt (001) films with large perpendicular magnetic anisotropy. The FePt films were prepared by co-sputtering of Fe and Pt targets directly onto heated, single crystalline MgO (001) using high vacuum dc-sputtering system. They managed to control the film morphologies from assemblies of single-domain nanoparticles to multi-domain islands by varying the nominal thickness of the FePt films. They report coercivity values as high as 5570 and 8360 kA/m in the film with single-domain particles at room temperature and 4.5K. Yamane et. al. [22], have reported the development of CoPt/Ag nanocomposites and investigated the structural and magnetic properties of the deposited film. They report an as-deposited CoPt film having a soft magnetic fcc phase, which on annealing transformed to a hard magnetic fct phase, with large values of coercivity from 80-1350 kA/m and

remanence of 0.75 T for a 610 nm thick film with grain sizes varying from 7-100 nm. An et. al. [23] reported the magnetic properties and internal stresses of AlN(20 nm)/[CoPt(2 nm)/AlN(20 nm)] 5 multilayer structure deposited at different substrate temperatures by dc magnetron sputtering. It is observed that the film deposited at room temperature has in-plane magnetic anisotropy and weak remanence, which indicates the poor crystallinity. When deposited at a substrate temperature of 573K, the film shows in-plane magnetic anisotropy and the corresponding anisotropy field is smaller. But when deposited at a substrate temperature of 673K, the perpendicular magnetization becomes as strong as the in-plane magnetization. The authors pointed out that the internal compressive stress favours in-plane anisotropy while the tensile stress favours perpendicular anisotropy. Recently, Varghese et. al. [282] also sputtered a very thin layer of equi-atomic CoPt at 623K with perpendicular anisotropy for magnetic recording media applications where they achieved 520 kA/m coercivity in a 8 nm thick film.

Equi-atomic CoPt and FePt materials can also be deposited using low cost electrodeposition methods. Huang et. al. [273], fabricated CoPt and FePt nanowires in an anodized alumina (AAO) template using electrodeposition. They observed a strong perpendicular anisotropy when annealed at 973K, with a coercivity varying between 240-480 kA/m. Rhen et. al. [274], were the first to report on the preparation of continuous FePt films by electrodeposition from a novel bath and on copper substrates. About 450 nm of FePt films were deposited and annealed at 673K to generate $L1_0$ fct phase with coercivity up to 240 kA/m. Rhen and Coey [275] also developed thick films of nearly equiatomic CoPt by electrodeposition into nanoporous membranes which exhibit an isotropic magnetic phase with square hysteresis loops ($M_r/M_s = 0.95$) and coercivity of up to 1040 kA/m. Recently Oniku et. al. [276] reported the fabrication and magnetic characterization of 15 μm thick electroplated $L1_0$ CoPt hard magnets. Experimental study of the dependence of the magnets' properties on annealing temperature reveals that an intrinsic coercivity of 800 kA/m, squareness > 0.8, and energy product > 150 kJ/m^3 are obtained for photolithographically patterned structures (250 μm × 2 mm stripes; 15 μm thickness) electroplated on silicon substrates and annealed in hydrogen forming gas at 973K.

Another class of hard magnetic material that is explored a lot is Co rich CoPtP [286-289], where the percentage of Co is approximately 80. This material also shows strong

magnetic properties in the as-deposited state and strong out-of-plane magnetic anisotropy can be achieved by aligning the c-axis of the Co crystalline perpendicular to the substrate with phosphorous-segregated grain boundaries. The properties of $Co_{80}Pt_{20}$ and $Co_{80}Pt_{20}P$ were compared by Callegaro et al [286], where it is found that the addition of Phosphorus to the electrolyte for CoPt deposition induces P co-deposition and improves film hard magnetic properties. The addition of P improved the coercivity of CoPt films from 220 kA/m to 440 kA/m, along with an increased squareness of 0.7. Vieux-Rochaz et. al. [287] reported in-plane magnetization with coercivities as high as 220 kA/m can be reached for patterned layers of CoPtP electrodeposited using an acidic bath for micro magnetic sensor applications. Ramulu et. al. [288] recently reported the three-electrode potentiostatic electrochemical synthesis and characterization of one dimensional hard magnetic CoPtP nanowires. They deposited nanowires into a nano-porous track-etched polycarbonate membrane with a nominal pore diameter 50 nm and thickness around 6–9 μm. The coercive fields were measured to be 140 kA/m and 100 kA/m for parallel and perpendicular to the nanowire axis, respectively. The phosphorous segregation in the grain boundaries is enhanced by Wang et. al. [289] using textured seed layers, e.g., Cu (111) on Si (110), that provide a template lattice for the desired crystalline structure. They demonstrated 8-μm-thick patterned films with an energy product of 69 kJ/m^3.

Apart from FePt/CoPt/CoPtP, CoMnNiP hard magnetic material has also been investigated and used for magnetic MEMS applications. Liakopoulos et. al. [290] reported the development of CoNiMnP based permanent magnet arrays for MEMS applications. The deposition of 1500 magnets of 40 μm × 40 μm × 50 μm in a square shape silicon substrate of 2.5 mm × 2.5 mm area was reported. The magnets showed strong perpendicular anisotropy with a coercivity of 60-100 kA/m and remanence of 0.2 T - 0.3 T and a maximum energy product of 14 kJ/m^3. Guan et. al. [266], reported that addition of $Ce_2(SO_4)_3$ and $Nd_2(SO_4)_3$ to the plating solution, resulting in the reduction of stress in the thin plated CoNiMnP films and hence improving their magnetic properties. They claim that the stoichiometric addition of the above two salts improves coercivity to 175 kA/m and the remanence to 0.1 T. Sun et. al. [291] reported an improvement in the properties of CoNiMnP-based magnet arrays by electrodepositing in the presence of a magnetic field. They developed arrays containing cylinder magnets with various radii as well as cubic magnets with different aspect ratios. A high coercivity of 60 kA/m, a retentivity up to 0.88 T and an energy density of 17.4 kJ/m^3 were successfully obtained in

cubic arrays. They showed that by modifying the geometry of the arrays, the retentivity and the energy density can be improved up to 115% and 129%, respectively.
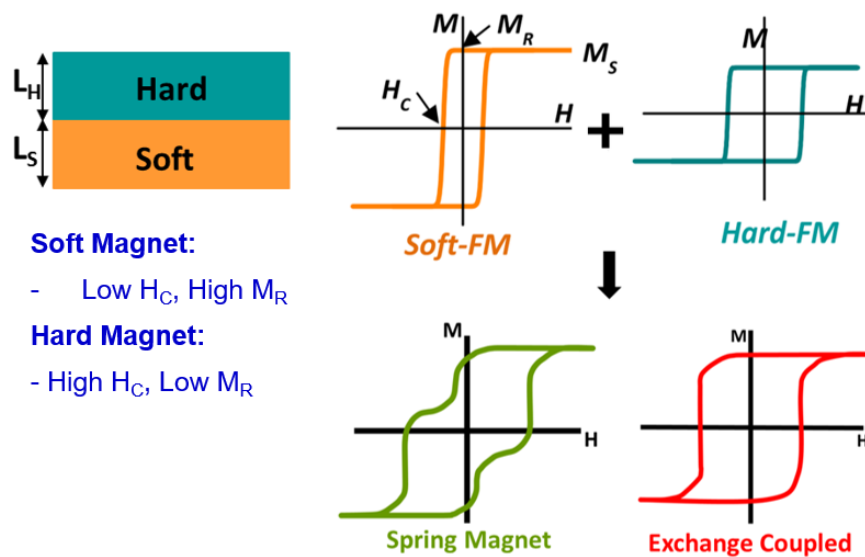
Fig. 8.3: Schematic representation of the hard/soft bilayer structure (top-left). Simple graphic representation of the hysteresis loops for soft and hard ferromagnets (FM) and their possible combinations: exchange coupled and exchange-spring magnet. The saturation magnetization, M_S, the remanent magnetization, M_R and the coercivity H_C, are indicated in the soft-FM loop.

In spite of the extensive efforts to develop metal-alloy magnets, their properties are fairly limited and there is no foreseeable indication to date which can show that any dramatic improvement in the performance can be made. As a result, interest has steadily grown in rare-earth magnetic materials. Rare earth magnets cannot be electroplated from aqueous baths. Hence, most efforts have employed sputtering or PLD to develop very thin (< 0.5 µm) rare earth based magnets which are comparable in performance to bulk magnets but not much use in MEMS applications. Some of the technical challenges like controlling the stoichiometry, the crystal structure, the microstructure and reduction of oxidation and corrosion are addressed on very thin films whereas issues that could help the MEMS applications like bath fabrication, faster deposition rate and patterning are relatively ignored. Among rare earth based magnets, both SmCo [292-293] and NdFeB [294-295] are deposited using both sputtering and PLD techniques. Both require post-deposition annealing at a very high temperature (450-750°C) in order to obtain the desired magnetic properties. Compared to SmCo, NdFeB alloys are more susceptible to oxidation, so additional coatings and protection layers are crucial. In some cases, though a very thick (120 µm) magnetic film is deposited, large area and fast deposition challenges are still

open. A comparison of different conventionally micro-fabricated hard magnetic materials is given in Table 8.1.

Alloy	Deposition Method	Coercivity (H_C) kA/m	Remanence (B_r) T	Energy Product $(BH)_{max}$ kJ/m^3
CoNiP [267]	Electrodeposition	104	0.1	1.8
CoNiP [310]	Electrodeposition	168	-	-
CoNiReWP [268]	Electrodeposition	190	0.51	-
CoNiMnP [266]	Electrodeposition	180	0.1	2.6
CoNiMnP [291]	Electrodeposition	60	0.88	17.4
CoNiMnP [311]	Electrodeposition – 0.2T magnetic field	210	0.2	10
CoPt [275]	Electrodeposition - 700ºC post deposition annealing	1045	-	-
CoPt [276]	Electrodeposition - 700ºC post deposition annealing	795	-	150
CoPt [316]	Electrodeposition - 700ºC post deposition annealing	795	0.37	
CoPt [282]	Sputtering- 700ºC post deposition annealing	517	-	-
FePt [274]	Electrodeposition - 400ºC post deposition annealing	239	-	-
FePt [307]	Electrodeposition - 600ºC post deposition annealing	446	-	124
FePt [308]	Electrodeposition - 800ºC post deposition annealing	1432	-	-

FePt [313]	Electrodeposition - 600°C post deposition annealing	875	-	-
FePt [279]	Sputtering - heated MgO (001) substrate	8355	-	-
FePt [314]	PLD	596	1.4	105
CoPtP [315]	Electrodeposition	366	0.6	52
CoPtP [316]	Electrodeposition	215	0.3	-
CoPtP [287]	Electrodeposition – 1.2T magnetic field	223	-	-
CoPtP [300]	Pulse Reverse Electrodeposition	120	-	-
CoPtP [289]	Electrodeposition	326	1	69
CoPtP [288]	Electrodeposition - nanowires	143	-	-
SmCo [317]	Sputtering - 550°C post deposition annealing	2077	-	-
SmCo [318]	Sputtering - at 450°C, 550°C post deposition annealing	2100	-	-
SmCo [319]	PLD - at 435°C, 550°C post deposition annealing	1200	-	-
NdFeB [320]	Sputtering - at 450°C	795	1	53
NdFeB [321]	Sputtering - at 470°C	795	1.5	150
NdFeB [322]	Sputtering - at 500°C, 750°C post deposition annealing	1273	1.4	400
NdFeB [323]	PLD - 550°C post deposition annealing	994	0.55	77

Table 8.1: Comparison of conventionally micro-fabricated permanent magnets.

The development of more advanced magnetic nanoparticles comprising two (or more) materials such as bi-magnetic core/shell particles [296] or multilayer structures [297] is currently being pursued extensively in order to gain fundamental understanding and for

useful applications. In these systems, the exchange interaction between both constituents introduces an extra degree of freedom to tailor the overall properties. The behaviour of these systems can be understood as a combination of the intrinsic parameters of the hard and soft phases. Usually, soft materials possess low anisotropy K, which results in a small coercivity (H_C) with a large saturation magnetization (M_S). On the other hand, a hard material usually has a large K and moderate M_S values. In exchange-coupled hard-soft thin film systems, the magnetization switching behaviour and consequently the M(H) loop, depend strongly on the dimensions of the soft phase (in thin films, the thickness of the soft layer, t_{soft}). For a thin t_{soft} there is a critical thickness below which the soft phase is rigidly coupled to the hard phase, and the two phases reverse at the same demagnetization field, H_N, resulting in a rectangular hysteresis loop. Such systems are considered as completely **exchange coupled**. By contrast, for thicker soft layers, the soft phase demagnetizes at significantly lower fields and the switching is characterized by an inhomogeneous reversal, and the system is usually called an **exchange-spring magnet**. Both cases are shown in Fig. 8.3. The value of H_N depends on the material parameters of both the hard and soft phases. The critical t_{soft} is found to be roughly twice the width of a domain wall, δH, in the hard phase: $\delta H = \pi (A_{hard}/K_{hard})^{1/2}$, where A_{hard} and K_{hard} are the exchange stiffness and anisotropy constants, respectively, of the hard phase. Among different exchange coupled systems, Co/CoO [296], SmCo/Fe [298], NdFeB/Fe [299] are popular.

In summary, all of the integratable approaches to develop permanent magnets have both pros and cons. Co-Ni based magnets can easily be integrated but they are limited in performance. On the other hand, the $L1_0$ fct phase of Co/Fe-Pt and rare earth based magnets are magnetically superior but require high temperature annealing to reach the expected properties, limiting their applications. Rare earth magnets are prone to oxidation and corrosion and it is difficult to pattern or batch fabricate them. The middle ground in terms of performance is occupied by the Co-rich Co–Pt alloys, which exhibit good performance in the as-deposited state and can be developed at room temperature using an electrodeposition process. Most of the better performing sputtered or electroplated films are limited to a few μm in thickness due to the intrinsic stresses that develop during deposition and/or thermal mismatch stresses that arise during annealing steps. Also, the magnetic properties degrade with thickness as the grain size and shape varies. To overcome this problem, alternative layers of ferro-magnet and non-magnet like Cu are

alternately electrodeposited to maintain the performance level. Hence, the development of stress free, multi micron thick good performance permanent magnets is an immediate need for the field of magnetic MEMS to flourish.

In terms of process technologies, sputtering is a simple process with the advantages of uniform deposition, good adhesion and reproducibility. But it is an expensive process and is not suitable for depositing thicker films. Hence, it is not an ideal process for depositing the thick hard magnetic materials needed in EM VEH devices. Electrodeposition, on the other hand, is an attractive technique for depositing hard magnetic materials from the submicron to hundreds of micron range, which is ideal for many MEMS applications. Also, electrodeposition has an advantage of a faster deposition rate, no requirement for a vacuum system, low cost, control over film composition and is compatible with standard CMOS fabrication processes.

In the following section, the electrochemical deposition, characterization and application of hard magnetic CoPtP is discussed.

8.3. Electrochemical Deposition of CoPtP Hard Magnets:

Co-rich CoPtP films are electrochemically deposited using a bath consisting of 0.1M Cobalt Sulfamate, 0.01M Diammine-Dinitro-Platinum, 0.1M Sodium Hypophosphite, 0.1M Dibasic Ammonium Citrate, 0.1M Glycine and 0.25M Saccharin (Table 8.2). The bath is modified compared to the earlier reported electrolytic bath by Kulkarni et. al. [300].

Bath Components	Composition
Cobalt Sulfamate	0.1M
Diammine-Dinitro-Platinum	0.01M
Sodium Hypophosphite	0.1M
Dibasic Ammonium Citrate	0.1M
Glycine	0.1M
Saccharin	0.25M
Sulfamic Acid	0.1M

Table 8.2: Electrolytic bath composition for deposition of CoPtP.
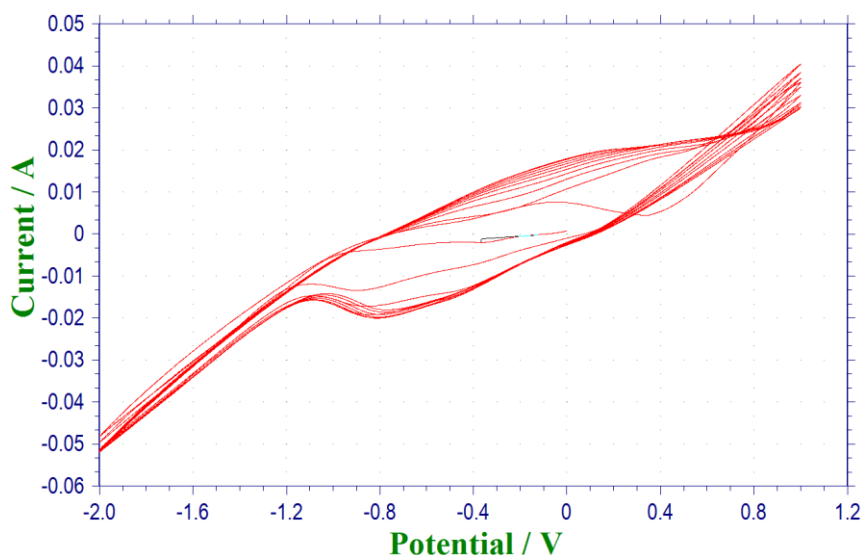
Fig. 8.4: Three electrode Cyclic Voltammetry analysis using Ag/AgCl as reference electrode.

Among the chemicals used in the bath, Cobalt Sulfamate, Diammine-Dinitro-Platinum and Sodium Hypophosphite act as the source of cobalt, platinum and phosphorous impurity ions. Dibasic Ammonium Citrate acts as the complexing agent to bring the reduction potentials of cobalt and platinum close together. Because of the presence of the NO_2^- ligand in the platinum salt, the current efficiency is reduced and precipitation is formed (especially after a few days of preparing the bath). This reduces the reproducibility of the electrolytic bath. To prevent this, Sulfamic acid is added which stabilizes the platinum compound. Glycine and Saccharin reduce the surface tension between the electrolyte and the working electrode whereas saccharin is added in the electrochemical bath as a stress-relieving additive. The pH of the solution was adjusted to 8. Cobalt pieces were used as anode and silicon pieces (1 cm^2 area) with a sputtered (200/20 nm) Cu/Ti seed layer were used as the cathode; deposition is carried out at room temperature. The optimized thickness of the seed layers are previously reported by Kulkarni et. al [300]. The microstructure and elemental characterization of the deposited materials are performed using Quanta FEI 450 Scanning Electron Microscope - Energy Dispersive X-ray spectroscopy (SEM-EDX) analysis. The X-Ray diffraction (XRD) analysis is performed in Panalytical X'Pert Pro MRD with Cu Kα radiation (40 kV, 50 mA) at a wavelength of 1.54 nm for phase analysis. The magnetic measurements of the deposited films are carried out in Quantum Design SQUID magnetometer (MPMS-XL5) for an applied field up to 5 Tesla.
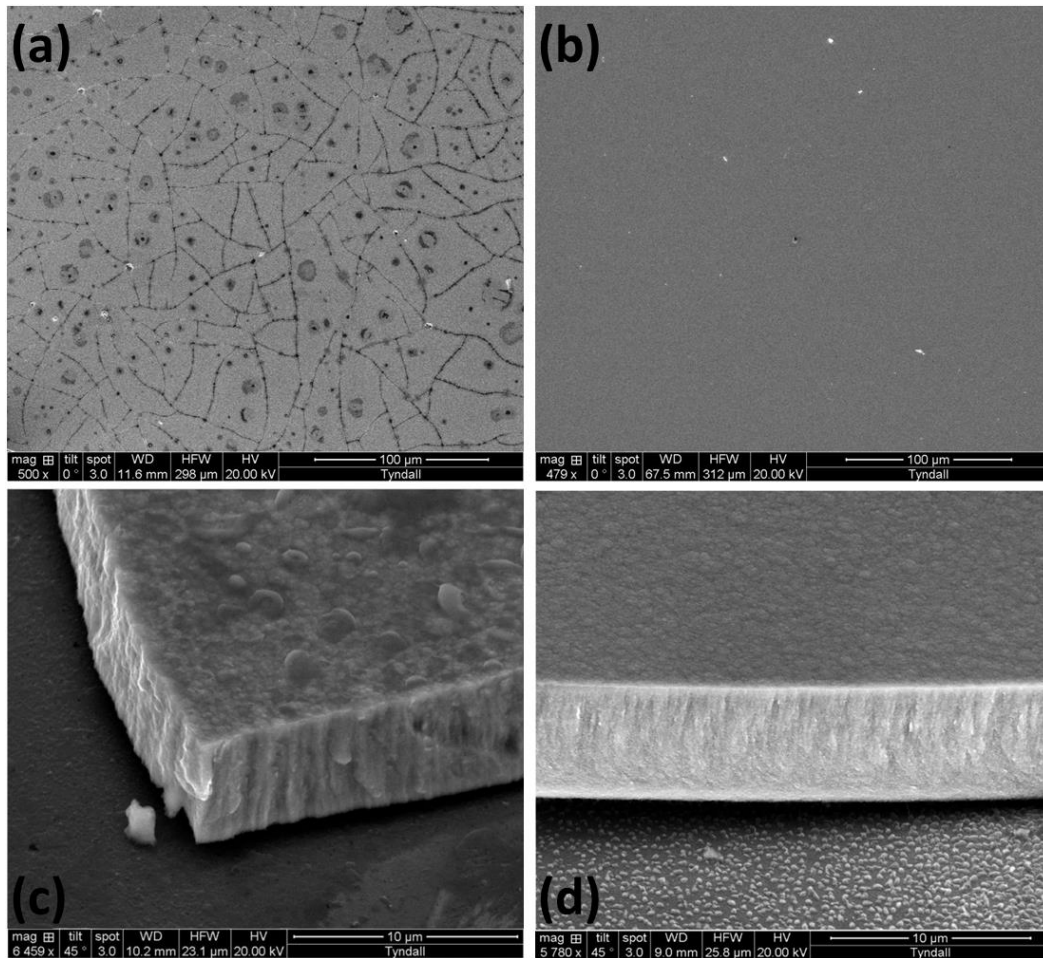
Fig. 8.5: Surface morphology of the films deposited at 20 mA/cm^2 density (a) DC (b) PRP. The cross-section image of the films deposited at 100 mA/cm^2 density (c) DC (d) PRP.

Three electrode cyclic voltammetry (CV) analysis is performed initially using a CH Instrument CHI660C electrochemical station in order to determine the deposition current density by a three electrode configuration with a cobalt piece and Ag/AgCl as the counter and reference electrodes, respectively. The current vs voltage plot from the CV analysis is shown in Fig. 8.4. The negative potential refers to the deposition region while the positive potential refers to the etching region from CV analysis. The deposition current is chosen as 20 mA/cm^2 from the CV analysis. Following the CV analysis, the first film is deposited using a conventional DC plating technique at a current density of 20 mA/cm^2. The surface morphology of the deposited film is shown in Fig. 8.5 (a). The DC plated film is full of micro-cracks even though a stress relieving agent, sacharin, is added to the bath. It is to be noted that even a highly polished silicon wafer has nano-scale surface roughness, creating an uneven Nernst diffusion layer. As a result, a smaller diffusion length from the peak and a larger diffusion length from the valley are obtained for the uneven surface for

Chapter 8: Development and Integration of Nano-structured CoPtP Permanent Magnets

depositing ions. This gives rise to a relatively higher metal ion concentration, and hence greater deposition rate, at the peaks than the valleys. This preferential growth of the metal alloy leads to the non-uniformity of the entire film and, as a result, it is stressed.
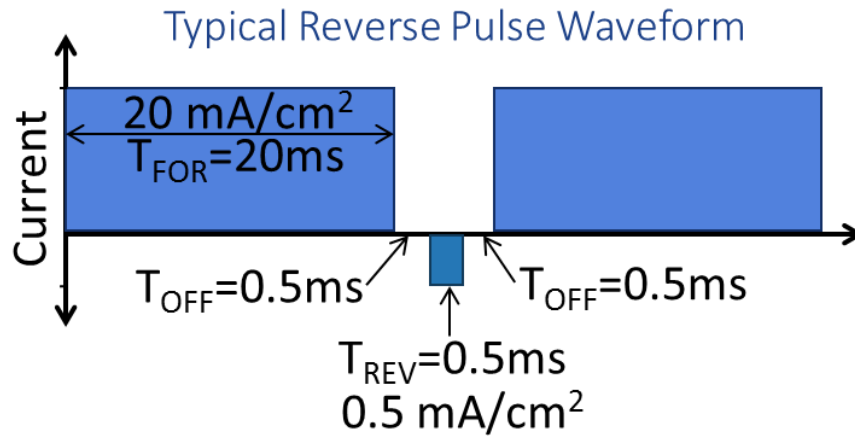
Fig. 8.6: Current waveform for Pulse Reverse Plating (PRP) deposition of CoPtP.

To avoid this effect, a second film is electroplated using the Pulse Reverse Plating (PRP) technique with a current waveform, as shown in Fig. 8.6. This consists of forward and reverse current densities of 20 mA/cm^2 (20 ms) and 10 mA/cm^2 (0.5 ms) respectively, with intermediate off times of 0.5 ms. The cycle is repeated for the entire deposition duration. The forward duty cycle (D$_f$) for the forward current and the reverse duty cycle (D$_r$) for the reverse current are given by

$$D_f = \frac{t_f}{T} \text{ and } D_f = \frac{t_r}{T} \tag{8.1}$$

where $T = t_f + t_r + 2t_o$ is the length of the entire one cycle, within which t$_f$ is the forward cycle time, t$_r$ is the reverse cycle time, and t$_o$ is the off time. The nano-scale roughness from the surface of the deposited film is etched away during each cycle due to the reverse current of the PRP process, which results in a smooth film with a uniform composition [Fig 8.5 (b)]. The cross-section images of the electrodeposited films at a higher current density of 100 mA/cm^2 are shown in Fig. 8.5 (c) and Fig. 8.5 (d). The uniform columnar growth of the film in the case of the PRP technique can be easily observed, even at a high current density, whereas the DC plated film becomes more and more non-uniform and the grain size increases significantly with the deposition current.
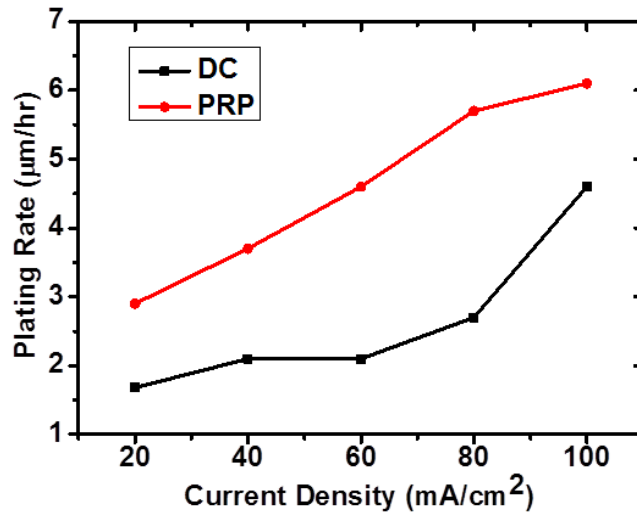
Fig. 8.7: Variation of plating rate with the current density for DC and PRP plating.
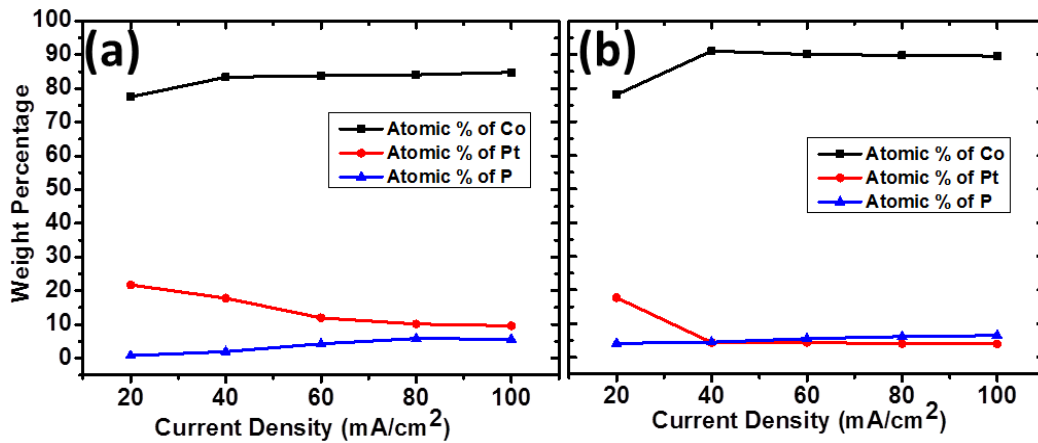
Fig. 8.8: Effect of deposition current density on the alloy composition: (a) DC plated film (b) PRP plated film.

The samples are electroplated for one hour each. The deposition rate for DC plated film is 1.7 μm/hr whereas that for the PR plated film is 2.9 μm/hr. The deposition current density is varied for both the electrodeposition techniques in order to observe the consequences on the developed films. In the case of the PRP technique, the reverse current density is always maintained at half of the forward current values with the previously mentioned durations as that is the optimized ratio to obtain high performance magnetic film [300]. The variation of the plating rates with current density is shown in the Fig. 8.7. With an increasing current density, the plating rate for both DC and PRP processes increases due to the enhanced charge movement. As shown in Fig. 8.8, the Co percentage increases significantly (over 90%) along with a further increase of current in both the deposition processes. As Co is soft magnetic in nature, the resulting films also lose their hard magnetic nature. Therefore, the above mentioned parameters are identified as optimized deposition conditions.
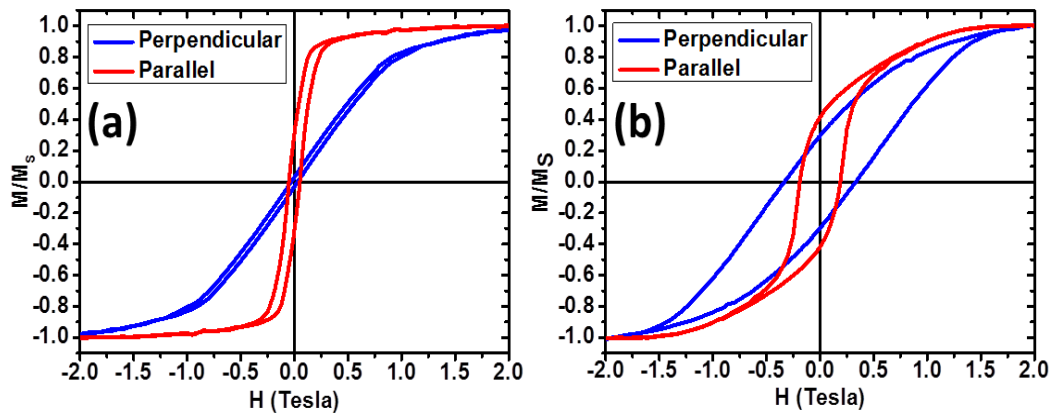
Fig. 8.9: Magnetic hysteresis loop measurement of the deposited films at room temperature: (a) DC plated film (b) PRP plated film.

The PRP method also improves the magnetic properties significantly as shown in Fig 8.9. The perpendicular and parallel coercivities of the DC plated film are 515 Oe and 300 Oe, respectively, whereas the same values for the PRP deposited film are 3345 Oe and 1904 Oe. This huge improvement in the magnetic property can be attributed to the structural uniformity of the PRP deposited film. The squareness factor ($S=M_R/M_S$) of the PRP deposited film in the perpendicular and parallel directions are 0.3 and 0.42 respectively. Corresponding values for the DC plated films are significantly low too. However, further improvements in the squareness and remanence properties of the developed films will be needed to increase the energy product, which is essential for hard magnetic applications.

8.4. Variation of Thickness of Electrodeposited CoPtP:

In the previous sections, the use of pulse reverse plating for deposition of stress-free hard magnetic material was described, including the optimization of the plating conditions to produce Co-rich CoPtP films with high coercivity. In this section, the above mentioned optimization conditions are used to electroplate Co-rich CoPtP micro-magnets with variable thicknesses. The surface morphology, crystalline structure and magnetic properties of CoPtP micro-magnets are compared for different thicknesses. For MEMS applications such as energy harvesting, it is particularly important to develop thick micro-magnets while retaining their magnetic properties.
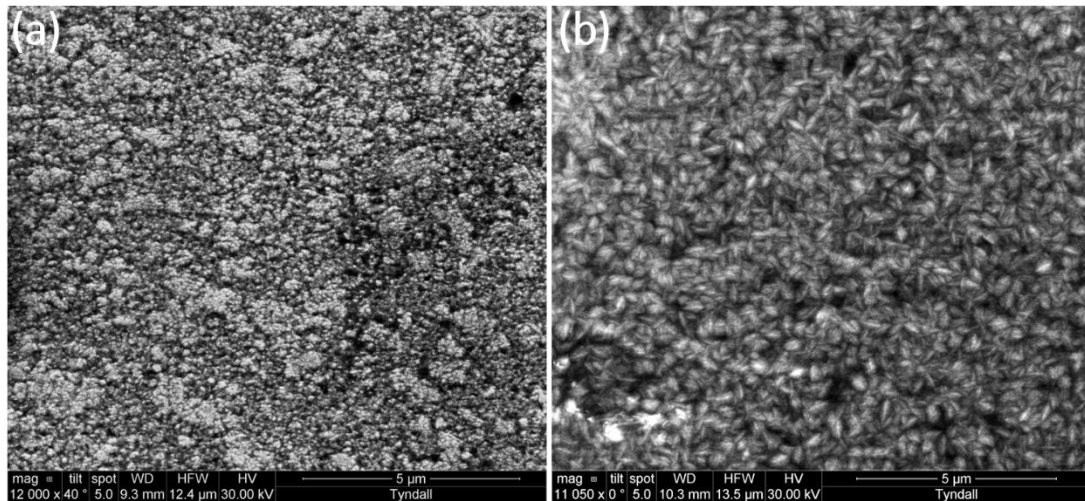
Fig. 8.10: Surface morphology of the (a) 0.9 μm thick and (b) 26 μm thick CoPtP films.

Using the above mentioned plating parameters CoPtP films are plated for up to 10 hours in order to deposit 26 μm thick films. During deposition, it is observed that the plated films retain their composition for a long deposition time, without any need to refresh the plating bath, which has been an issue in previously reported work [300]. This improvement is achieved due to the addition of the stabilizing agent in the plating bath which restrains the bath from precipitating over long time. However, the pH of the bath is constantly monitored during electrodeposition. Also there is a slight drop in the plating rate for a long duration of electrodeposition. Initially the plating starts on the Cu/Ti seed layered substrate but, as the plating process progresses, the film keeps depositing on already grown CoPtP film. This causes the loss of conductivity on the substrate and, as a result, the plating rate falls. The characterization and magnetic measurements of the plated films are performed similarly as described before. Co-rich CoPtP films with thicknesses of 0.9 μm, 2.9 μm, 6.1 μm, 12.5 μm, 20.2 μm and 26 μm are electrodeposited using the PRP technique. The plated films are visually smooth, shiny and showed good adherence to the substrate. All the films show a columnar structure in the perpendicular direction. Also the films remain crack-free and stress relieved up to their respective thicknesses. Fig. 8.10 (a) and (b) compares the surface morphology of 0.9 μm thick film with that of 26 μm thick film.
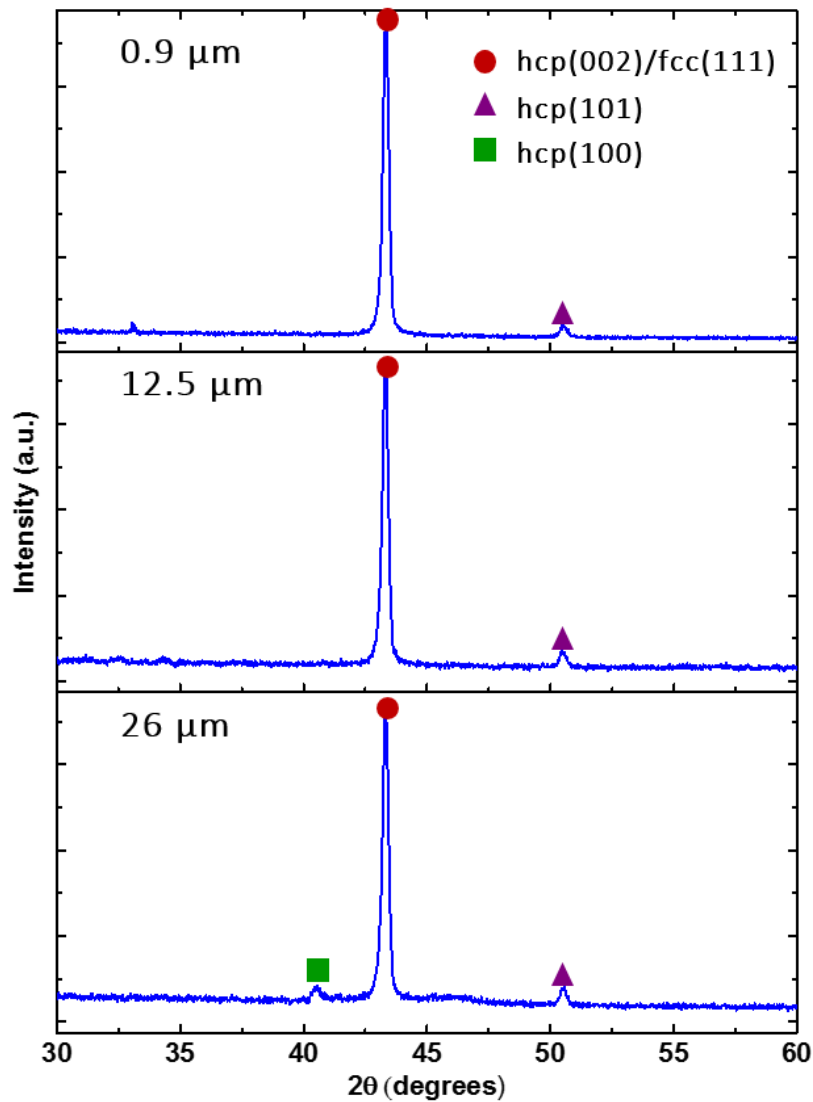
Fig. 8.11: X-Ray Diffraction (XRD) analysis of the deposited CoPtP films for various thickness of 0.9, 12.5 and 26 μm respectively.

The effect of thickness of Co-rich CoPtP films on hard magnetic properties such as coercivity, remanence and energy product can be analyzed using magnetic measurements along with XRD plots and micro-structure analysis. Fig. 8.11 compares the XRD measurements of the plated films with various thicknesses whereas the corresponding in-plane and out-of plane hystersis loops are shown in Fig. 8.12. Table 8.3 summarizes the different structural and magnetic properties of the CoPtP films with various thicknesses. The grain size of the films is determined using the Scherrer equation

$$\tau = \frac{K\lambda}{\beta cos\theta} \qquad (8.2)$$

where τ is the mean grain size, K is a dimensionless shape factor with a value close to unity, λ is the X-ray wavelength (1.54 Å), β is the line broadening at half the maximum intensity (FWHM), and θ is the Bragg angle (in degrees).

Thickness (μm)	Atomic Composition (%)	XRD Peak Position/ Phase	Grain Size (nm)	In-Plane Coercivity (kA/m)	Energy Product (kJ/m^3)
0.9	Co – 79.4 Pt – 19.5 P – 1.1	43.35°, Co hcp(002)/fcc(111)	6.36	173	45.9
2.9	Co – 79.6 Pt – 19.2 P – 1.2	43.26°, Co hcp(002)/fcc(111)	6.58	174	42.2
6.1	Co – 80.3 Pt – 18.5 P – 1.2	43.30°, Co hcp(002)/fcc(111)	7.08	167	41.3
12.5	Co – 83 Pt – 15.4 P – 1.6	43.26°, Co hcp(002)/fcc(111)	10.96	162	34.5
20.2	Co – 85.3 Pt – 12.9 P – 1.8	43.28°, Co hcp(002)/fcc(111)	15.03	156	30
26	Co – 85.9 Pt – 12 P – 2.1	43.32°, Co hcp(002)/fcc(111)	22.5	144	27.1

Table 8.3: Comparison of structural and magnetic properties for various thicknesses of electrodeposited CoPtP films.

The variation of the in-plane and out-of plane coercivities and squareness with thickness of the plated CoPtP films are shown in Fig. 8.13 (a) and (b), respectively. It is observed that both coercivity and squareness decrease with thickness. Coercivity has a strong dependence on the grain size. If the grain size exceeds the size of a single domain, domains can be formed within the grains, making them a multi-domain grain. It is found that as the size of multi-domain grains is increased, the coercivity decreases. The size dependence of the coercivity is experimentally found to be given by [301]

$$H_C = a + \frac{b}{D} \tag{8.3}$$

where a and b are constants and D is the particle diameter. From equation (8.3), it is clear that increase in the grain size (D) leads to a drop in coercivity. With the increase in the thickness of the films, the grain size increases, as observed from Table 8.2, also leading to

a loss of coercivity. However, the same is not apparent from the surface morphology of the films shown in Fig. 8.10. The particle size appears much bigger for 26 μm thick film. However, there could be smaller particles embedded in each of those big particles, which could be confirmed by Tunneling Electron Microscopy (TEM) analysis.
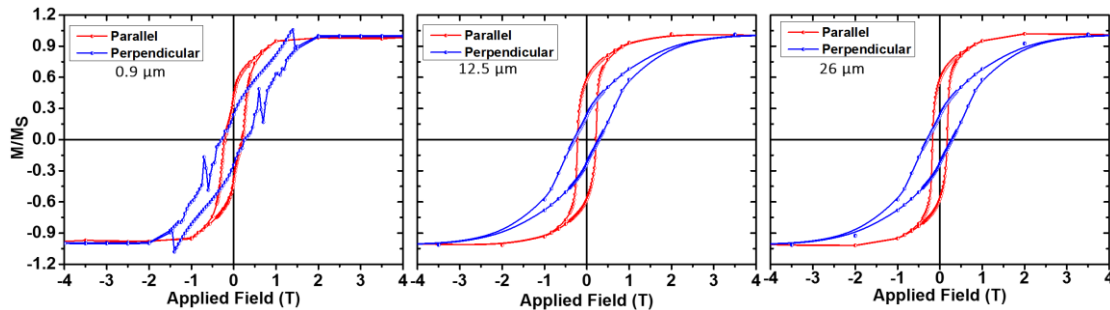
Fig. 8.12: In-plane (parallel) and out-of-plane (perpendicular) magnetic hysteresis loops of CoPtP films with various thickness values.
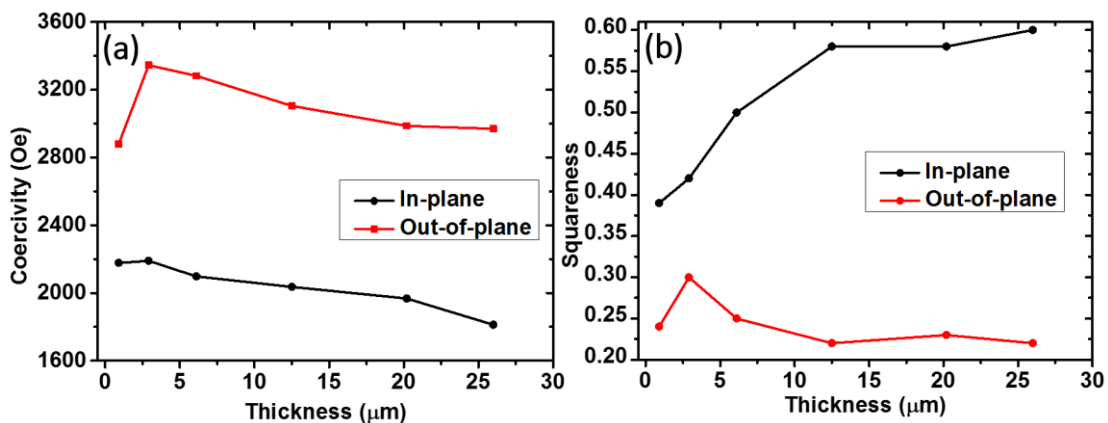
Fig. 8.13: Variation of the in-plane and out-of plane (a) coercivities and (b) squareness with thickness of the plated CoPtP films.

From the XRD analysis in Fig. 8.11, it is observed that a high intensity peak is obtained at 43.4° for all thickness values of the film, which indicates the coexistence of both Co-fcc (111) and Co-hcp (002) phases. A small diffraction peak of Co-hcp (101) is observed at 50.5° which strengthen the hcp phase. For thin to moderately thick films of CoPtP, the absence of hcp (100) reveals the possibility of an fcc phase. Co-hcp (100) peak is observed at 40.5° for a thick 26 μm film, which indicates strong c-axis orientation of the columnar crystal structure normal to the surface plane. The drop in coercivity can be explained by considering the Co-hcp hard magnetic phase. Pure Co-hcp is a soft magnetic phase [309] where the addition of Pt atoms leads to replacement of a few Co atoms in the Co-hcp unit cell. This results in an increased anisotropy of the Co-hcp phase, hence making it a hard magnetic phase. Additionally, as mentioned before, the P atoms tend to settle at the grain boundaries and act as pinning sites preventing domain wall movement

and as grain growth inhibitor. Now it is observed from Table 8.2 that the atomic percentage of Co increases with an increase of thickness, leading to the drop of Pt and less P acting as a pinning site and consequences in loss of coercivity.
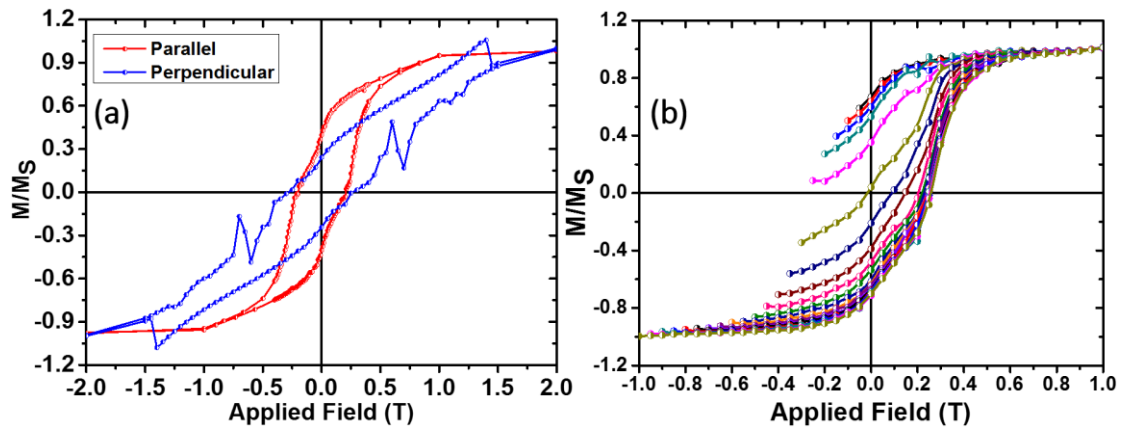
Fig. 8.14: (a) Magnetic hysteresis loop of 0.9 μm thick CoPtP. (b) FORC measurement plots for the sample from -0.5 kOe to -10 kOe as the field is swept again at a step of 0.5 kOe.

An interesting magnetic property is observed for thin 0.9 μm thick film in Fig. 8.12 (a) which has been zoomed and shown in Fig. 8.14 (a). A clear shoulder or kink is observed in the in-plane hysteresis loop which could arise due to deficient exchange coupling between the soft and hard phases. These phases could be the Pt and P induced Co-hcp (002) hard magnetic phase and Co-fcc (111) soft magnetic phase which is anticipated from the XRD analysis. As described earlier, the soft and hard phases reverse at different nucleation field, which results in the observed kink. Kinks are considered to be a sign that a soft phase is not fully coupled with a hard magnetic phase, and some free moments appear in the soft magnetic phase. Also, no such kink is observed for out-of-plane measurement. It has been observed previously [302] that the threshold condition for exchange coupling for in-plane and out-of-plane directions are significantly different. However, a symmetric pulse like behavior is observed in the out-of-plane hysteresis loop. From positive saturation, the soft phase and hard phase domains start to rotate as the reverse field is increased. But they do not do so at the same rate. As a consequence, they become repulsively oriented at one point. This is energetically unfavorable and the soft phase domains try to switch their directions, which might result in the pulse like behaviour. An interesting observation here is that the pulse like behavior is obtained at the same applied field for which the kink is obtained in the in-plane hysteresis loop.

For further understanding of the complicated magnetic property, First Order Reversal Curve (FORC) measurement [303-304] is conducted for the in-plane direction of the film. First-order-reversal-curve (FORC) measurements can provide insight into the relative proportions and irreversible components of the magnetization of various materials. For exchange-coupled nano-composite permanent magnet materials, FORC measurement enables differentiation of the magnetically hard and soft phases. A FORC is measured by saturating a sample in a field H_S, decreasing the field to a reversal field H_A, then sweeping the field back to H_S in a series of regular field steps H_B. This process is repeated for many values of H_A, yielding a series of FORCs. The measured magnetization at each step as a function of H_A and H_B gives $M(H_A, H_B)$, which is then plotted as a function of H_A and H_B in field space. The FORC distribution $\rho(H_A, H_B)$ is the mixed second derivative, i.e., $\rho(H_A, H_B) = \left.\frac{\partial^2 M(H_A, H_B)}{\partial H_A \partial H_B}\right.$, and a FORC diagram is a contour plot of $\rho(H_A, H_B)$ with the axis rotated by changing coordinates from (H_A, H_B) to $H_C = (H_B - H_A)/2$ and $Hu = (H_B + H_A)/2$, where Hu represents the distribution of interaction fields, and H_C represents the distribution of switching fields. Fig. 8.14 (b) shows a series of FORCs for the sample from -0.5 kOe to -10 kOe as the field is swept again at a step of 0.5 kOe. A full analysis of the FORC measurement can lead to the further understanding about the two phase material which is, however, attributed to future work.

8.5. Patterned CoPtP Micro-magnet Development for EMEH Applications:

8.5.1. Theoretical Background: The state of a magnet is defined by three vector fields: the magnetic flux density (B), the magnetic field (H) and the magnetization (M). At any given point, these field quantities are related by the constitutive equation, $B = \mu_0(H + M)$ where $\mu_0 = 4\pi \times 10^{-7}$ H/m is the permeability of free space.

The internal field H acting in a sample is the sum of the external field H_1 and the demagnetization field H_d produced by the magnetization distribution of the sample itself

$$H = H_1 + H_d \tag{8.4}$$
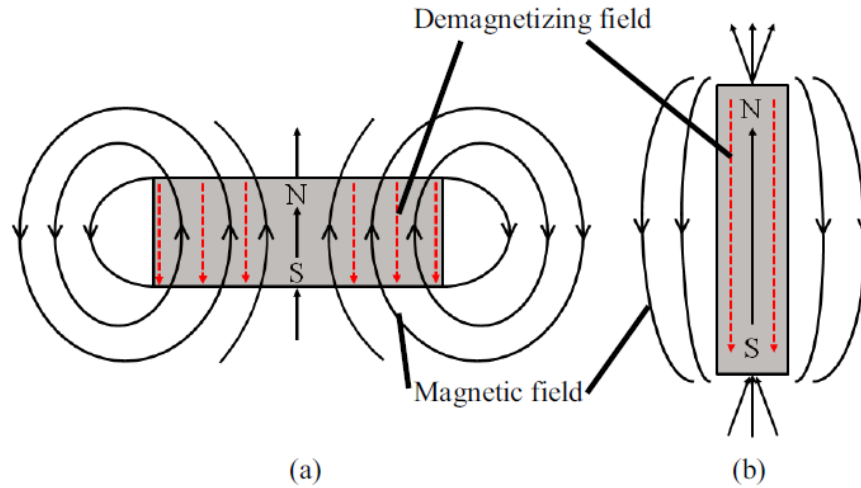
Fig. 8.15: Schematic diagram of the demagnetizing field of two types of magnets. (a) Low aspect ratio magnet shows large demagnetizing field. (b)High aspect ratio magnet shows small demagnetizing field [305].

In a magnet of finite length, a demagnetizing field arises because of the free magnetic poles at the terminating ends of the magnet. This strength of the demagnetization field is dependent on the magnetization and the physical magnet shape. The demagnetization field acts to demagnetize the magnet in a direction which is opposite to the direction of the magnetization. Hence, the magnetic flux density also diminishes due to the demagnetizing field [305], as shown in Fig. 8.15. The magnetic field and the demagnetizing field are expressed as solid and dashed line vectors. A commonly-used approximation is to assume that the demagnetizing field H_d is uniform and opposite in direction to the magnetization,

$$H_d = -DM \tag{8.5}$$

where, D is the demagnetization factor, which has a value between 0 and 1 depending on shape of the magnet. The significance of the demagnetizing field is that when a permanent magnet is used as a source of magnetic flux, its operating point is somewhere in the second quadrant of the hysteresis loop. The internal magnetic field H is in the opposite direction to the magnetic flux density B and magnetization M. This demagnetization curve (the second-quadrant portion of the hysteresis loop), provides the crucial information for magnetic design in terms of magnetostatic energy. The entire magnetostatic energy of a magnet can be derived by considering the identity [306]

$$\frac{1}{2}\int B.H dv = 0 \tag{8.6}$$

where the integration extends over all space. This integral can be divided into two parts constituting contributions from inside the magnet (index I) and from outside the magnet, where B=μ_0H (index A). The external magnetostatic energy then can be derived as

$$E_A = \frac{1}{2}\int \mu_0 H^2 dv_A = -\frac{1}{2}\int B.H dv_I \qquad (8.7)$$

This equation can be interpreted as $(BH) = \frac{2E_A}{V}$ where the energy product $(BH) =$ $V^{-1}\int B.H dv_I$ is twice the energy stored in the stray field of a magnet. Using the constitutive relation $B = \mu_0(H + M)$ and assuming that there is no external field in equation (8.4), and replacing H$_d$ as in equation (8.5),

$$(BH) = \mu_0 D(1-D)M_S^{\ 2} \qquad (8.6)$$

where it is assumed that M = M$_S$. This equation shows clearly that the energy product is a shape-dependent property of a magnet. Thin films with perpendicular and parallel magnetization have D≈1 and D≈0, respectively, and both correspond to vanishing energy products. Hence, uniformly magnetized thin films produce no stray field outside the magnet, except at the edges, and most of the magnetic material is wasted. The energy product can be maximized w.r.t. the shape of the magnet by putting $\frac{\partial(BH)}{\partial D} = 0$. It has been found that (BH)$_{\text{max}}$ is obtained for D=0.5 which occurs for a magnet with a height approximately equal to the radius [306], which yields $(BH)_{max} = \frac{1}{4}\mu_0 M_S^{\ 2}$, the maximum possible energy product that can be achievedfrom a perfectly rectangular M(H) loop.

8.5.2. FEM Simulation and Device Modelling: In a number of integrated magnetic MEMS applications, a film of permanent magnet is used as source of magnetic field. However, if the stray magnetic field appears only from the edge of the magnet then a large part of the material is wasted and the magnetic flux intensity is greatly reduced. This, however, can affect the performance of an integrated EM VEH device as the rate of change of magnetic flux will be greatly diminished. It is therefore proposed to replace a film or a block of permanent magnet by an array of magnets. In that case, the magnetic flux density can be intensified over a small space due to the increase of the magnetic element edges. FEM analysis in COMSOL is conducted to compare the magnetic field distribution between a block of magnet and different arrays (strip arrays, square arrays,

circular arrays and rectangular arrays). The simulation result is shown in Fig. 8.16. In the simulation, the total volumes of the whole block and magnet array (including the interspace) are kept the same. For the block, a 5×5 mm^2 structure is assumed, while the thickness is kept fixed at 30 μm for all of the patterns. The detailed dimensions of the simulated patterns are shown in Table 8.4. The magnetization direction is assumed to be along the perpendicular to the plane of the magnet. The coercivity (H_C) and magnetic remanence (B_r) values used in the simulation are obtained from the measured results of 26 μm thick CoPtP in the previous section. For all of the simulations, the only stray field that appears is from the edge of the magnets, which validates the aforementioned described theory. For all of the permanent magnets, the largest magnetic flux density appears at the edge region, which is about 0.01 T. In other regions, the value of magnetic flux density is reduced almost to zero. In the case of a circular array, it is observed that the directions of the magnetic field are radially outward; this could be due to shape anisotropy of circular structure. Hence, the magnetic flux density is greatly increased from block to strips to square patterns.
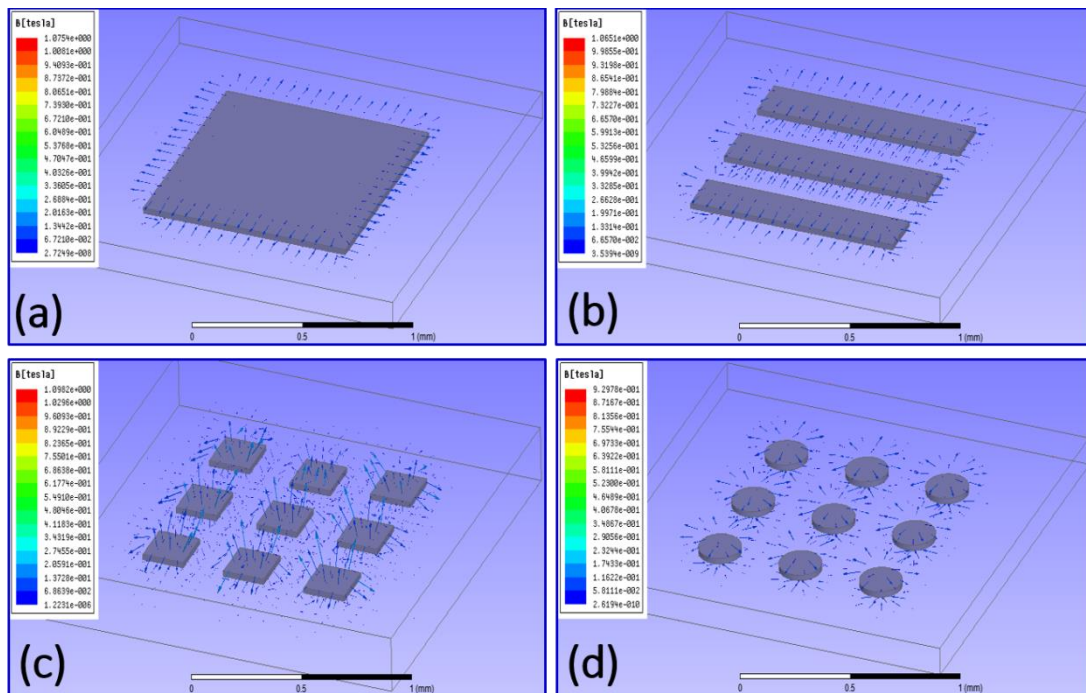
Fig. 8.16: FEM simulation of magnetic field from (a) whole block of thin film (b) stripe pattern structure (c) square pattern structure (d) circular pattern structure.

Magnetic Structure	Dimensions
(a) Single Block	Size - 5×5 mm^2; Thickness – 30 μm
(b) Stripe Patterns	Size - 5×0.05 mm^2; Interspace – 0.05 mm; Thickness – 30 μm
(c) Square Patterns	Size – 0.05×0.05 mm^2; Interspace – 0.05 mm; Thickness – 30 μm
(d) Circular Patterns	Size – (π/4)0.05 mm^2; Interspace – 0.05 mm; Thickness – 30 μm

Table 8.4: Different patterned structure dimensions for FEM simulations.
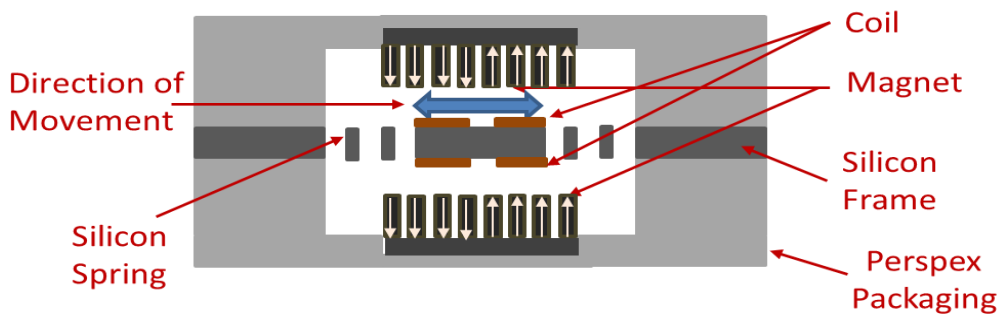
Fig. 8.17: Proposed device configuration with patterned magnetic structure.

Further simulation is conducted to estimate the effect of using a patterned magnetic structure in an integrated EM VEH device. For this purpose, a topology has been assumed whose cross-section is shown in Fig. 8.17. The device configuration is designed in such a way that it can be employed to vibrate in parallel to the device plane. Four oppositely polarized magnets are used to produce a large change of magnetic flux with the exception that a single magnet block is replaced by oriented film and patterned blocks in different cases for comparison. The natural frequency of the device is assumed to be 500 Hz. The coil used in the simulation is a micro copper coil with 144 turns and 190 ohm internal resistance. For comparison, the above mentioned dimensions of the magnets are used for each of the four oppositely polarized magnetic blocks. Using the above design, the maximum load power that is obtained for different patterns is shown in plot of Fig. 8.18 w.r.t. the total magnet volumes. It is observed that the maximum power is obtained for a square patterned magnet array compared to film or strip array due to the increase in the number of edges and consequently the stray magnetic field. For a circular array, the magnetic field is not as effective as the square pattern due to the aforementioned reason of shape anisotropy. The results are also compared to the case when the four oppositely

polarized magnets are conventional NdFeB magnets with dimension of $5 \times 5 \times 1$ mm^3. The resultant output power is two orders of magnitude higher than any of the patterned arrays. However, the magnetic volume is also greatly increased.
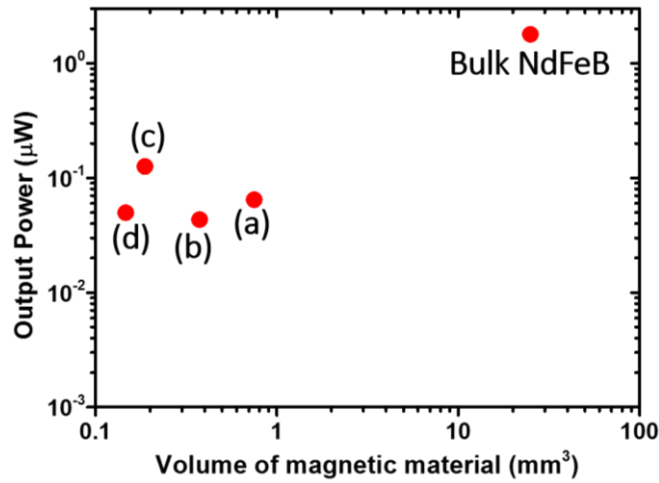
Fig. 8.18: Calculated output power for different magnetic structures and comparison with commercially available NdFeB magnet.
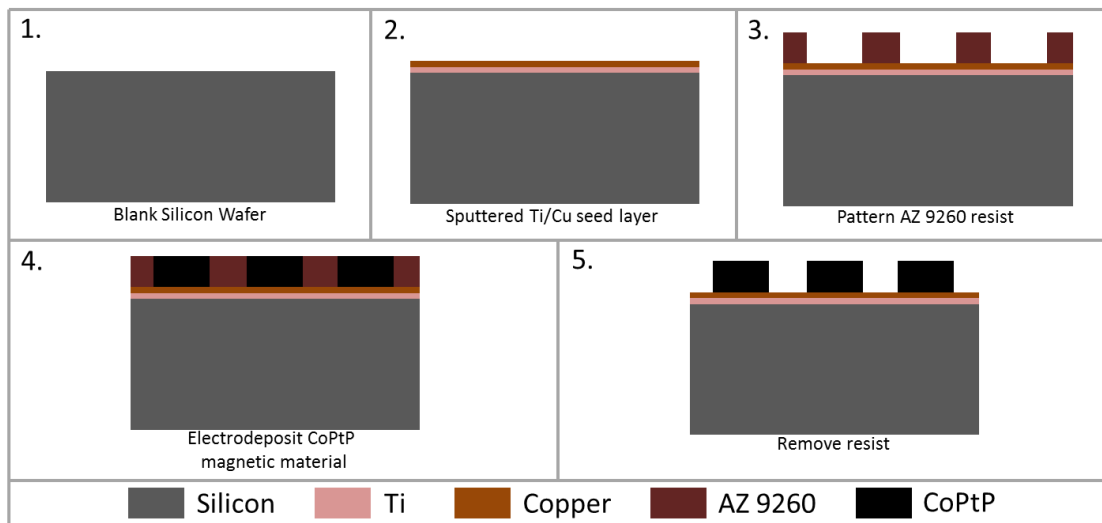
Fig. 8.19: Process flow for fabrication of patterned magnetic structure

This section provides a new methodology to develop an integrated EM VEH device where the magnet can also be integrated in a CMOS compatible process and yet the output power can be significantly improved. In the following section, different patterns of CoPtP hard magnetic material are described. However, a complete integration of such a patterned structure is not performed due to the limited time scale of the project and it can be pursued as future work.
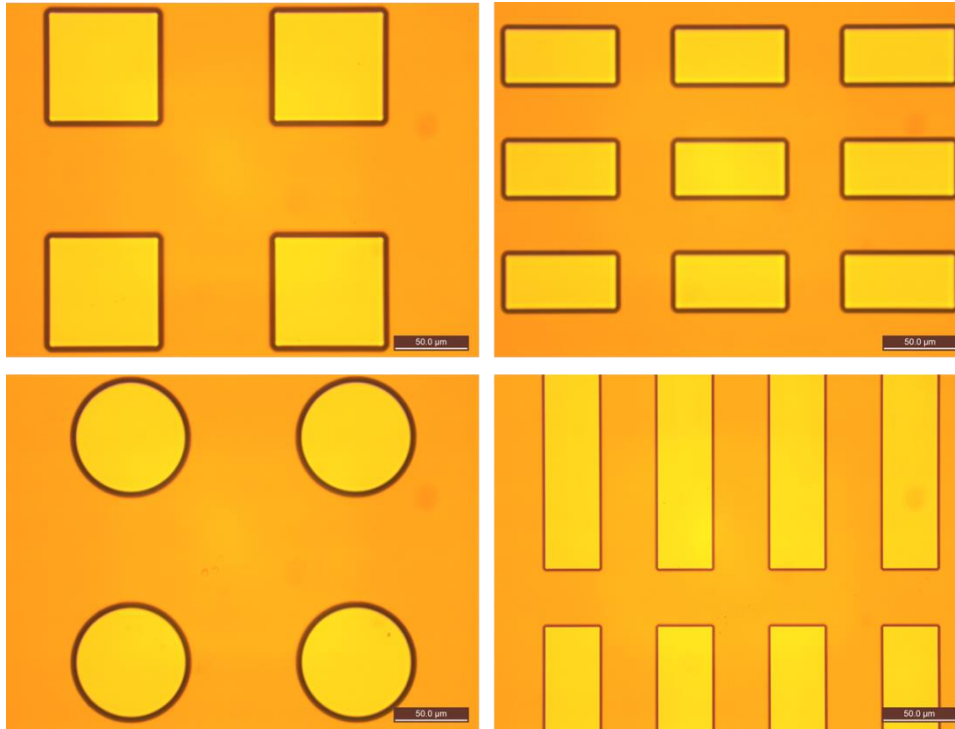
Fig. 8.20: Photoresist patterned structures. The deep yellow portions depict the resist whereas the light yellow portions are the openings for electrodeposition.

8.5.3. Fabrication of Micro-patterned CoPtP Hard Magnets: The process flow to develop patterned CoPtP magnets is shown in Fig. 8.19. The process starts by cleaning a blank silicon wafer in acetone, isopropyl alcohol and DI water. Then a Ti/Cu (20/200 nm) seed layer is sputtered on the wafer. AZ9260 positive photoresist is spun on the wafer and a 20 μm thick resist layer is developed using an optimized double spinning process. Patterns are generated on the wafer using a mask (Appendix V). The patterned Si wafer is shown in Fig. 8.20 which depicts different micro-patterns. After developing the resist, the wafer is diced into four equal pieces and CoPtP is electrodeposited in one of the pieces in a beaker containing 200 mL of the electrolytic bath using the PRP technique with the optimized deposition parameters described in the earlier section. Since the pH of the bath is 8, which is basic, it acts as a developer for the photoresist. It is observed that the resist profile is not maintained after long plating durations. Hence, in a future optimization of the process, either the mask (a bright field mask could be used for same resist) or an alternative resist could be used for developing thicker patterns of the hard magnetic material. The SEM images of the developed micro-patterned structures with a thickness of ~10 μm are shown in Fig. 8.21. Detailed characterization and integration of the patterned magnetic films in EM VEH devices may be pursued as future work.
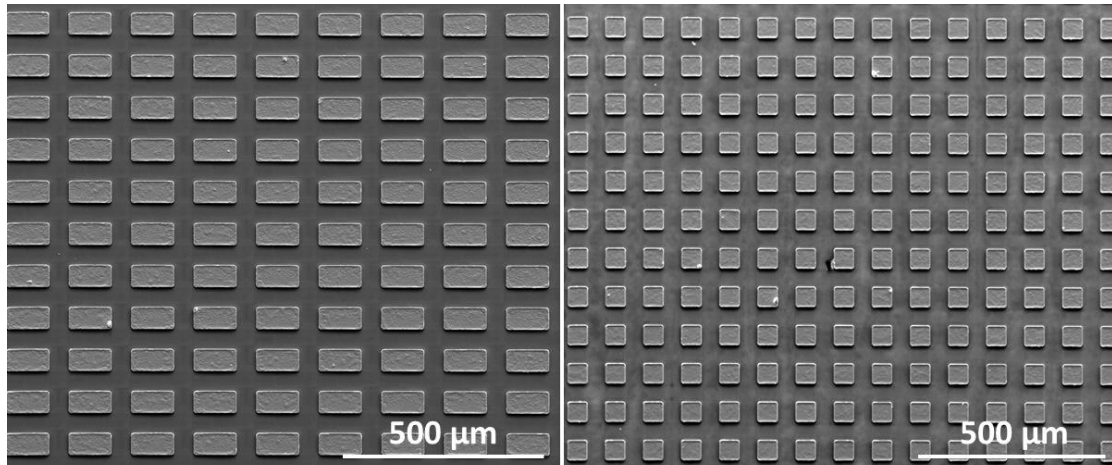
Fig. 8.21: Some of the fabricated micro-patterns of CoPtP magnetic material.

8.6. Conclusions:

In this chapter, the deposition technique and properties of thick Co-rich CoPtP films for use in electromagnetic power generators were discussed. The integration of permanent magnetic material in MEMS based EM VEH device is a major challenge in the field. Most of the commercial permanent magnets are deposited using a sintering technique, which requires high temperature processing. On the other hand, the permanent magnets which can be integrated using CMOS compatible processes requires either high temperature annealing or are limited in performance. Hence, to address this particular issue, a new method of electrodeposition is developed compared to the conventional DC plating; it involves a combination of forward and reverse pulses for optimized deposition of Co rich CoPtP hard magnetic material. This results in significant improvements in the microstructure of the developed films as the pulse reverse plated films are smooth, stress free and uniform. Such improvements in the structural properties are reflected in the hard magnetic properties of the material as well. The intrinsic coercivities of the pulse reverse deposited film are more than 6 times higher for both in-plane and out-of-plane measurement directions and the squareness of the hysteresis loops also improve for similar reasons.

Using a stabilization agent in the electrochemical bath, the deposition is made homogeneous for long durations. This makes it possible to develop thick (up to 26 μm) structures of CoPtP without any significant loss in the magnetic properties, which is suitable for MEMS applications like EM VEH. A maximum energy product of 45.9 kJ/m^3 is obtained for 0.9 μm film, which reduces to 27.1 kJ/m^3 for 26 μm thick film.

Further towards efficient integration of permanent magnets in an MEMS EM VEH topology, analytical and FEM calculations show that patterned magnetic structures produce denser stray fields compared to a thin block of magnet. Hence, efficient patterned magnetic structures are designed and their potential performance in a proposed topology are estimated and compared. Finally, patterned micro-magnets of developed Co rich CoPtP material are fabricated for a thickness up to 5 µm. However, the process needs further development to optimize its properties, to enable the magnets be integrated successfully in a MEMS topology.

Chapter 9

Conclusions and Future Works

9.1. Introduction:

In this work, wideband vibration energy harvesting is reported using electromagnetic transduction method for potential powering of the WSNs within the Internet of Things (IoT)' connected platform. Most of the reported works in the field of VEH consist of a linear resonant system that generates significant amount of power at resonance, however, the response drops drastically as the external vibration shifts slightly from resonant frequency. This is inevitable as most of the ambient vibrations are either random or frequency varying. Consequently, widening/tuning the operational frequency of the transducers is essential for efficient energy harvesting. The reported work here addresses three major challenges: i. wideband operation, ii. high output power generation, iii. integration using CMOS compatible MEMS fabrication processes (particularly challenging for EM transduction). The particular conclusions from the thesis are outlined below. Finally, suggestions toward further improvement/progress of the present work are reported.

9.2. Conclusions:

The conclusions drawn from different chapters of this thesis are given below:

9.2.1. Literature Review: An extensive amount work has been conducted over the last decade in the field of vibration energy harvesting. Researchers from various fields (such as mechanical engineering, mathematics and dynamics, electrical and electronics engineering, material science etc.) have contributed to this field with their respective focus. Much of the earlier reported generators are resonant or low frequency non-resonant, using various transduction mechanisms like electromagnetic, piezoelectric and electrostatic. The miniaturization of the devices while retaining useful power density has remained an open problem in this field. Particularly, scaling of the devices plays a critical

role in the case of EM VEH devices. Additionally, the integration of EM transducers is also very challenging due to the presence of permanent magnets and requirement of high efficiency micro-coils. An elaborate comparison of different reported MEMS scale (fully- or semi-integrated) EM VEH devices has shown that the power density available from such devices are considerably low compared to their meso-scale counter parts.

A major part of the initially reported devices are linear resonant. A number of approaches have been undertaken in the literature to broaden the frequency response of the VEH devices. These include (a) resonance frequency tuning, (b) multi-frequency/multi-modal generator development and (c) nonlinear energy harvesting. Resonance frequency has been tuned using both mechanical and electrical methods. However, real-time active tuning using mechanical methods is not straight forward. The tuning ranges of different tuning mechanisms are also not very high and require more energy to tune the frequency compared to the generated power. Multi-frequency generators are suitable for MEMS based approaches as different modes of the mechanical structure can be activated through proper design only. Therefore the fabrication of such generators is relatively easier. There has been a huge surge of research in nonlinear oscillator based VEH devices for their inherent wideband response. Nonlinear energy harvesting devices employing various potential functions, such as monostable, bistable and tristable, have been reported both in meso- and micro-scale. Often the reported devices are quite bulky and not suitable for MEMS integration. Presence of multiple states within a certain frequency range i.e. the hysteresis of the frequency response is a major concern which restricts operation of nonlinear generators in real applications.

Different power management schemes for EM VEH devices are also reported. Power management is as important as power generation for complete system development. Particularly for EM harvesters, where the generated voltage is low, AC/DC conversion is a major concern. Along with cold-start problem, optimal performance at steady state is addressed separately in literature.

9.2.2. Linear Generators and Bidirectional Electrical Tuning: Different EM harvesting devices are designed and fabricated on FR4 as the resonating spring material. FR4 has a low Young's modulus (Y=21 GPa), which enables low frequency operation in a smaller footprint without the need of additional mass, improving the reliability and applicability of the devices. The reported EM VEH devices (P1-4) differ in their spring configurations to operate at four different resonant frequencies: 58.6 Hz, 83.8 Hz, 162.9

Hz and 42.9 Hz respectively. In the untuned condition, the prototypes P1, P2, P3 and P4 produce 470 μW (at 0.3g), 350 μW (at 0.3g), 4.3 μW (at 0.3g) and 16.5 μW (at 0.3g) at respective optimum loads of 2400 Ω, 2100 Ω, 780 Ω and 900 Ω respectively. A bidirectional electrical tuning scheme for EM energy harvesters has also been developed using two different complex load topologies: capacitive load to tune in the lower frequency direction and inductive load to tune in the higher frequency direction respectively. A theoretical model has been derived for this tuning method and study shows that in case of capacitive tuning, the tuning range widens with increase in load resistance whereas the tuning range broadens with decrease in load resistance for inductive tuning. The bidirectional tuning has been implemented successfully on the four developed prototypes and the test results are found to agree well with theoretical predictions. A maximum capacitive tuning of 1.8 Hz, 1.75 Hz, 0.16 Hz and 0.16 Hz are achieved for P1 – P4 respectively whereas a maximum inductive tuning of 0.57 Hz, 0.6 Hz, 0.13 Hz and 0.13 Hz are obtained for the same devices. Results also show that output load power and load voltage drops with tuning as only 14% and 22.5% of the untuned power are obtained at the maximum tuned frequencies for capacitive and inductive tuning in case of P1 and 11.11% and 33.1% for P2. The tuning ranges could be modified by using different values of load resistance. Also, the tuning capability is largely dependent on the electromechanical coupling. Hence, this method could be very useful for high-Q, largely electromagnetically coupled EM harvesters. For MEMS based devices, where the aforementioned coupling is not very strong, further investigation involving complicated load electronics will be needed in order to efficiently tune the resonance frequency.

9.2.3. Multi-frequency MEMS EM Energy Harvesters: In this chapter, multi-frequency MEMS electromagnetic energy harvesters are reported employing two different topologies. The first system is single mass, where different fundamental modes are obtained within a close range through spring design innovation, realization of the spring architectures and by using a large magnetic proof mass. The second system is dual mass, which inherently has two major vibration modes corresponding to the movement of each of the masses. The output power is improved in the reported designs, in general, by using the bulk magnet as a proof mass compared to the reported MEMS scale EM generators and this high performance is benchmarked through normalized power density parameter. The spring structures are developed using Silicon-on-Insulator (SOI) substrate while voltage is induced on double layer electroplated copper coils. The 3D finite element

analysis on the devices shows that different modes are activated in the low frequency (< 300 Hz) region. The out-of-plane and torsional modes of the single mass systems are obtained at 188, 255.1 and 287.9 Hz, respectively whereas the first two modes of dual mass device are at 241.4 Hz and 419.6 Hz respectively. At 0.5g, the single mass device produces 0.37, 0.43 and 0.32 µW respectively in mode I, II and III whereas the dual mass device generates 0.22 and 0.02 µW in mode I and II respectively against a matched load. The experimental results are qualitatively explained using the simulation results and indicate a good potential in the development of multi-frequency energy harvesters for a number of practical applications.
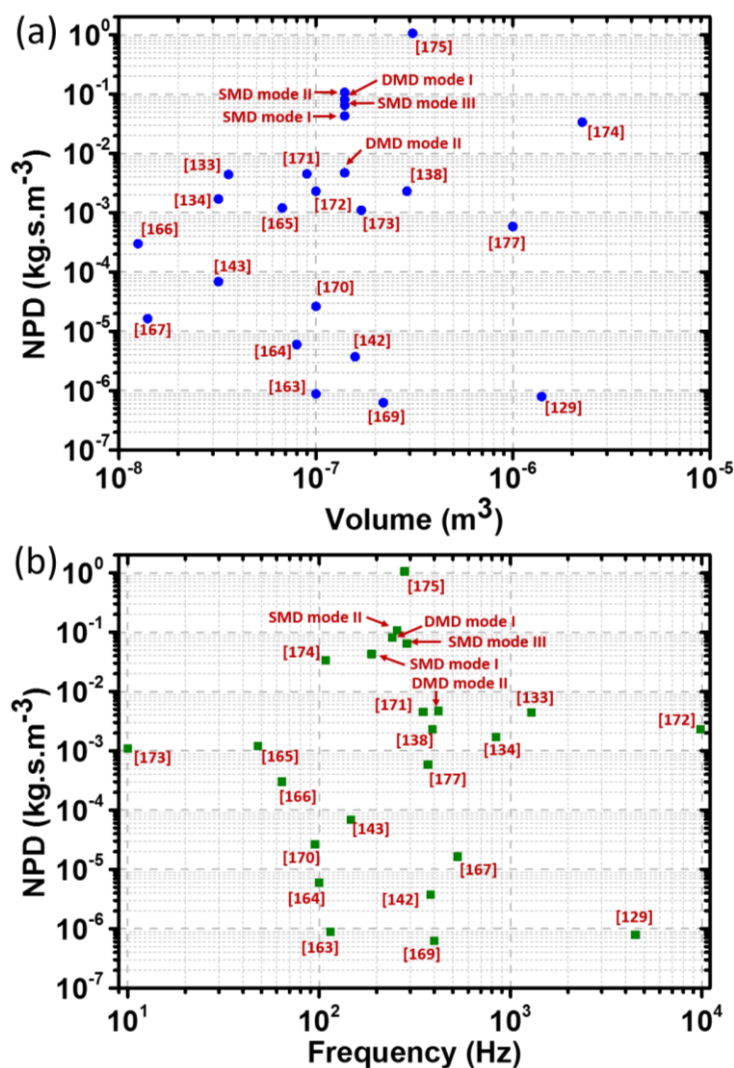
Fig. 9.1: Comparison of the Normalized Power Density (NPD) of the reported devices in different modes with the state-of-the-art MEMS EM VEH literatures in terms of (a) device volume and (b) operating frequency.

Comparing different VEHs is not straightforward as the amount of data presented in published works varies considerably in terms of their operating conditions such as input

acceleration and frequency. Hence, just comparing the output parameters like voltage, current or power is not justified. Beeby et al [62] derived a figure-of-merit for resonant VEH devices called, Normalized Power Density (NPD), which is simply the output power (P) of the device normalized w.r.t. input acceleration level (A) and volume (V) of the device. Frequency is not considered in the figure-of-merit as resonant generators are fixed in frequency whereas acceleration levels applied during testing can be varied. In Fig. 9.1, the NPD of different MEMS scale EM energy harvesters are compared w.r.t their operating frequency (Fig. 9.1 (a)) and device volume (Fig. 9.1 (b)). It is to be noted here, we have compared different MEMS scale VEH devices regardless of their operating principles, including resonant, multi-frequency and nonlinear energy harvesters. For wideband nonlinear devices, the peak power generated at the down jump frequency is considered which is not fully justified but makes the comparison easy. In terms of the level of integration, the fully integrated MEMS EM harvesters [163-167, 169-170] have lowest NPD due to the low efficiency of the integrated magnets. Thus in most of the reported literature [129, 133-135, 142-143, 172], bulk NdFeB magnets are used whereas the spring structure and pick-up coils are integrated using CMOS compatible MEMS techniques. Coils are mostly integrated on the vibrating elements while a single or an array of static magnets is used to create the varying magnetic field. The output power is found to be low in such cases due to poor magnetic flux linkage and smaller proof mass. In some reported literature [133-135, 142-143], a sputtered metallic coil is used to induce electrical voltage. Generally the thickness of the sputtered layers is quite low, which affects the final output. Silicon is the most commonly used material in MEMS devices due to their suitability with CMOS compatible fabrication processes and its mechanical robustness. But due to its large elastic modulus (Y=170 GPa), the operational frequency becomes high with miniaturization in size. Hence, many researchers have exploited other polymeric materials like PDMS [167, 174] and parylene [129, 173] for developing the spring structure in order to reduce the frequency within the same footprint. The low Young's modulus not only brings the resonance frequency to a lower value but also increases the displacement amplitude as the spring constant is reduced. However, reliability of these materials for long term applications is a concern which is yet to be verified in the reported literature.

In this reported work, a magnet proof mass architecture is used where a NdFeB bulk magnet is bonded on the silicon paddle to increase the mass vis-à-vis the output power.

The high performance obtained from the MEMS energy harvesters is also due to the development of integrated, double layer, and thick copper micro-coil, which enhances the electromagnetic coupling with the moving magnet. These factors lead to NPDs of 0.043, 0.11 and 0.064 kg.s/m^3 respectively in the first three vibration modes of SMD and 0.081 and 0.0047 kg.s/m^3 respectively in the first two modes of the DMD, which are among the higher values for MEMS scale EM VEH devices. The performances can be further improved through even more optimization of the different design parameters, as described in the theoretical model section of chapter 5.

9.2.4. Nonlinear Energy Harvesters: In chapter 6, the design, modelling and experimental validation of stretching strain based nonlinear EM Energy Harvesters are reported. An analytical formulation of large deformation of the spring arms shows that a cubic nonlinearity results from the contributions of stretching in addition to bending. This nonlinearity increases the operational bandwidth of the VEH significantly. Further, numerical investigation of a deterministic model based on a monostable Duffing oscillator supports this increase in bandwidth. Initially a proof-of-concept prototype is developed where up to 10 Hz bandwidth is obtained at 1g acceleration. However, the output power from the developed device is significantly low due to inefficient magnet-coil assembly. A qualitative discussion based on the numerical model shows that presence of dynamical noise in experimental system limits this bandwidth. Additionally, a non-characteristic secondary peak (at 196 Hz) was observed experimentally, where 110% of the peak power at the nonlinear jump point can be achieved at 0.5g acceleration. Almost three times more power is generated at this symmetry broken peak compared to the nearby symmetric states, showing high potential of dynamical symmetry breaking in generating more power compared to the symmetric states and this can be utilized by further optimization. A detailed examination of this secondary peak shows the symmetry breaking bifurcation at that particular position. It is inferred that the symmetry broken secondary resonance may appear due to the dynamic symmetry breaking of the oscillator or due to the inherent asymmetry of the built prototype. This work also shows the potential of FR4 based small footprint, wide bandwidth, nonlinear EM harvester generating useful amount of power, which can be increased significantly by further optimization of magnet coil assembly. Following this inference, a modified prototype is developed where the output power is significantly improved. A reasonably good bandwidth of 9.55 Hz is obtained with developed device among the reported macro

prototypes whereas the load power of 488.47 μW generated across a resistive load of 4000 Ω under 0.5g input acceleration at 77 Hz, which is also useful for practical applications. It is shown that bandwidth and the maximum power point (or jump-down frequency) can be modulated by changing either the input acceleration or the resistive load by contrast with a linear device.

Reference	Prototype Scale	Type of Transduction	Volume (cm^3)	Acceleration	Power Integral (μW-Hz)	NPID (Kg/m^3)
[141]	Macro	PZ	1.04	0.3g	640	68.38
[142]	MEMS	EM	0.032	3g	1.8	0.0625
[153]	Macro	EM	2.97	0. 5g	770	10.37
[324]	MEMS	PZ	0.016	0.6g	2.8	1744
[239]	MEMS	ES	0.042	1g (35V bias)	164	4.86
[144]	Macro	PZ	7.62	0.5g	1900	9.97
[325]	Macro	EM	11.19	2g	1800	0.4
First Prototype	Macro	EM	0.78	2g	17.33	0.05
Modified Prototype	Macro	EM	2.65	0.3g	3990	167.29
			2.65	0.5g	7560	114.11

PZ – Piezoelectric; EM – Electromagnetic; ES – Electrostatic.

Table 9.1: Comparison of power integral for different reported nonlinear energy harvesters with our work

In the literature, a number of nonlinear monostable energy harvesters have been reported where clearly two limiting cases of performances exist as macro prototypes with discrete components provide high output power mainly due to large transduction area whereas micro scale devices work over a large bandwidth due to the enhanced nonlinear stiffness. Stanton et. al. [141] reported a macro monostable system with piezoelectric transduction where magnetic end mass interacts with the field of oppositely poled stationary magnets to generate Duffing nonlinearity. For this device under hardening response, the value of 'Power Integral (P_f)' is approximately calculated to be 640 μW-Hz at 0.3g. Whereas Liu et al [142] demonstrated a micro electromagnetic energy harvester with spring hardening nonlinearity, which has an approximate P_f value of 1.8 μW-Hz under 3g input excitation. A more generalized figure of merit can be obtained by normalizing P_f w.r.t the volume of the device and the input accelerations, which can be defined as

$$Normalized\ Power\ Integral\ Density\ (NPID) = \frac{P_f}{Volume.Acceleration^2} \qquad (9.1)$$

Because of the above mentioned trade-off between the macro-scale and MEMS devices, P_f or NPID provides a more fair comparison between different nonlinear devices compared to the previous figure of merits. A more elaborated comparison of different state-of-the-art nonlinear energy harvesters with our system has been provided in Table 9.1. It is to be noted here that accurate information about the volume of the devices are not always clearly mentioned in literature. Hence, we have considered the volume of the active materials in some cases for comparison. In the reported device, the load resistance is optimized to generate P_f value of 3990 μW-Hz at 0.3g and 7560 μW-Hz at 0.5g, which is high for reported devices at this scale.

In the MEMS scale, wideband micro-electromagnetic energy harvesters employing two different nonlinear spring architectures are reported. Similar to the meso-scale prototypes, nonlinearity is introduced in the spring structures here, also by the stretching in addition to bending of the specially designed fixed-fixed configured spring arms. In first nonlinear architecture (A1), the fixed ends are orthogonal to each other with beam joint in the middle whereas the second nonlinear architecture (A2) is H-shaped. The realization of the spring architectures on the thin Silicon-on-Insulator substrate using MEMS processing technology activates different fundamental modes of the devices which further widens the output response. The devices are characterized at different level of MEMS integration to report a comparative result. Experimental results show that around 80 Hz of half power bandwidth is obtained for devices with A1 architectures due to nonlinear contributions from closely spaced vibration modes. On the other hand, devices with A2 spring structures have 60 Hz half power bandwidth due to strong nonlinear stiffness of the beams.

In Table 9.2, a comparative study of the reported MEMS based wideband energy harvesting devices is provided along with present work. For nonlinear energy harvesters, the peak power frequency is normally the same as the jump down frequency during up sweep. Since the operational bandwidth depends on the working frequency of the devices, the normalized bandwidth provides a fair comparison between the performances of different devices. The efficient nonlinear spring design in our device produces sufficient wideband response, which results in comparable normalized bandwidth and large power integral values. However, the performance can be improved by further optimizations. Another concern that can be raised is the relatively high frequency of operation of the

reported devices whereas most of the available vibration sources are low frequency (<100 Hz). However, there are a number of application scenarios where the available mechanical energy is located in the moderately high frequency (100-1000 Hz) region. In case of tire pressure monitoring system (TPMS), the vibration is distributed over the frequency range from 100 to 1000 Hz with quite high acceleration [327]. Similar high frequency application environment is available from aerospace vehicles during their take-off and landing [328]. The reported devices can be useful under such circumstances for harvesting useful electrical energy.

Reference	Type of Transduction	Volume (cm³)	Acceleration (g)	Output Power (μW)	Power Integral (μW-Hz)	NPID (kg/m³)
[172]	EM (MEMS Spring and coil)	0.158	1g	0.59×10^{-4}	0.02	0.0013
[141]	EM (MEMS Spring and coil)	0.032	3g	0.002	1.8	0.0625
[171]	EM (MEMS Spring and coil)	0.09	4.5g	0.82	98.4	0.54
[324]	PZ	0.016	0.6g	0.11	2.8	4.86
[239]	ES	0.042	1g (35V bias)	3.4	164	39.04
[326]	ES	0.144	0.42g (800V bias)	0.95	0.95 (approx.)	0.37
A1WC	EM (MEMS Spring)	0.14	0.5g	2.87	840	240
A1MC	EM (MEMS Spring and coil)	0.14	0.5g	0.41	123	35.14
A2WC	EM (MEMS Spring)	0.14	1g	1.05	225.75	16.13
A2MC	EM (MEMS Spring and coil)	0.14	1g	0.22	47.3	3.38

EM - Electromagnetic; PZ – Piezoelectric; ES – Electrostatic
Frequency values are approximated from figure unless mentioned explicitly

Table 9.2: Comparison of power integral for different reported MEMS nonlinear energy harvesters with our work

9.2.5. Electrical Switching in Nonlinear Energy Harvesters: Nonlinear oscillator based energy harvesters improve the off-resonance performance significantly due to their inherent wideband frequency response when compared with linear resonators. But the

applicability of such systems are restrained by the phenomenon of multi-stability and hysteresis in the dynamics of the devices. It implies that a number of stable steady states with different energy outputs may coexist. The device selects a stationary state depending upon the frequency schedule of the external excitation and the initial conditions. Hence, such devices will not be very useful under real application conditions unless there is some mechanism which can control the output states of the device and switch into the highest output power state for maximum efficiency. In chapter 7, it is demonstrated that a suitable electrical control signal switches the state of a nonlinear VEH from the Low Energy Branches (LEBs) to the High Energy Branch (HEB). The VEHs have an inherent connection between their mechanical and electrical degrees of freedom. This interplay is exploited in a very innovative way to supply a periodic electrical signal over a short period of time to the system to initiate the large amplitude mechanical motion when the system response is in the LEB. The proposed method is shown to work under fixed frequency, fixed amplitude as well as varying amplitude-frequency input vibrations. The method is successfully demonstrated for a MEMS scale EM harvester as well.

In principle, the control method can be applied to any device with nonlinear hysteresis, having different sizes and transduction methods, through required modifications. The presented underlying physics is generally applicable for other means of switching mechanism to control the coexisting states of the nonlinear oscillators which may find manifold of applications in different branches of science and engineering.

9.2.6. Development and Integration of Nano-structured CoPtP Permanent Magnets:

The integration of permanent magnetic material in an MEMS based EM VEH device is a major challenge in the field. Most of the commercial permanent magnets are deposited using sintering techniques which require high temperature processing. On the other hand, the permanent magnets which can be integrated using CMOS compatible processes require either high temperature annealing or are limited in performance. A simultaneous work was carried out on the development of stress-free, thick and nano-structured CoPtP hard micro-magnets for complete integration of the EM VEH devices. In chapter 8, the deposition technique and properties of thick Co-rich CoPtP films for use in electromagnetic power generators is discussed. A new method of electrodeposition is developed compared to the conventional DC plating, involving a combination of forward and reverse pulses, for optimized deposition of Co rich CoPtP hard magnetic material. This results in significant improvements in the microstructure of the developed films as

the pulse reverse plated films are smooth, stress free and uniform. Such improvements in the structural properties are reflected in the hard magnetic properties of the material as well. The intrinsic coercivities of the pulse reverse deposited film are more than 6 times higher for both in-plane and out-of-plane measurement directions and the squareness of the hysteresis loops also improve due to similar reasons. Using a stabilization agent in the electrochemical bath, the deposition is made homogeneous for long durations. This allows to develop thick (up to 26 μm) structures of CoPtP without any significant loss in the magnetic properties, which is suitable for MEMS applications like EM VEH. The maximum energy product of 45.9 kJ/m^3 is obtained for 0.9 μm film which reduces to 27.1 kJ/m^3 for 26 μm thick film.

Further towards efficient integration of permanent magnets in an MEMS EM VEH topology, analytical and FEM calculations show that patterned magnetic structures produce denser stray fields compared to a thin block of magnet. Hence, efficient patterned magnetic structures are designed and their application results in a proposed topology are estimated and compared. Finally, patterned micro-magnets of developed Co rich CoPtP material are fabricated for a thickness up to 5 μm. However, the process needs further development to gain the optimized properties, enabling them to successfully integrate in MEMS topology.

9.3. Highlights of the Work Presented in this Thesis:

Different innovations and novel outcomes from the works reported in this thesis are summarized as follows:

- Extensive use of FR4 (low Young's modulus, 21 GPa) for development of various linear resonance based meso-scale EM VEH devices. Development of compact, meso-scale nonlinear monostable energy harvester using FR4 as spring material.
- Demonstration of bidirectional electrical tuning for EM VEH devices using two complex load topologies.
- First reported experimental evidence of symmetry broken nonlinear secondary peak in a single potential well system. The presence of this secondary peak is useful in generating a significant amount of power compared to the symmetric states.
- Introducing a useful figure-of-merit for fairly benchmarking different wideband energy harvesters, called the 'power integral'. Addressing the trade-off between load

power and bandwidth of nonlinear generators, by using the 'power integral' optimization.

- Development of multi-frequency MEMS EM VEH devices with one of the highest reported normalized power densities. Development of MEMS scale nonlinear EM energy harvesters with one of the highest reported power integral values in the literature. Engaging different fundamental modes in a nonlinear MEMS spring topology to further widen the half-power bandwidth up to 80 Hz.

- First reported electrical control method to switch from the low to the high energy output branch of a nonlinear energy harvester, which is independent of device scale and transduction mechanism. Addressing the underlying physics of the proposed method using a modified Duffing oscillator model.

- Successful demonstration of the electrical control method to significantly improve the harvesting efficiency of a nonlinear energy harvester under amplitude-frequency varying environment.

- Development of stress-free, nano-structured CoPtP hard magnetic material using pulse reverse electrodeposition method for a thickness up to 26 μm, having coercivity up to > 3 kOe.

- Verification of the advantages of using micro-patterned permanent magnets for complete integration of EM VEH device using FEM analysis and fabrication of some of the micro-patterned CoPtP hard magnetic structures.

9.4. Future Works:

In this work, three major challenges of EM VEH devices are addressed i.e. i. wideband operation, ii. high output power generation and iii. complete integration. It is observed that, the power density falls down drastically with scaling and that fall of performance is even more severe for a completely integrated EM VEH devices, generating output power in the range of pW to nW which is of no use for practical applications. In chapter 8, it is shown that micro-patterned structures are more efficient for power generation than a whole block of thick, electrodeposited permanent magnet. But still for higher flux linkage it is necessary to develop patterned micro-magnets with multi-directional magnetizations similar to the Halbach array or alternately polarized array of magnets that are used in meso-scale devices. An approach to develop fine scale micro-magnetic pattern with alternate polarity could be using a magnetization mask.
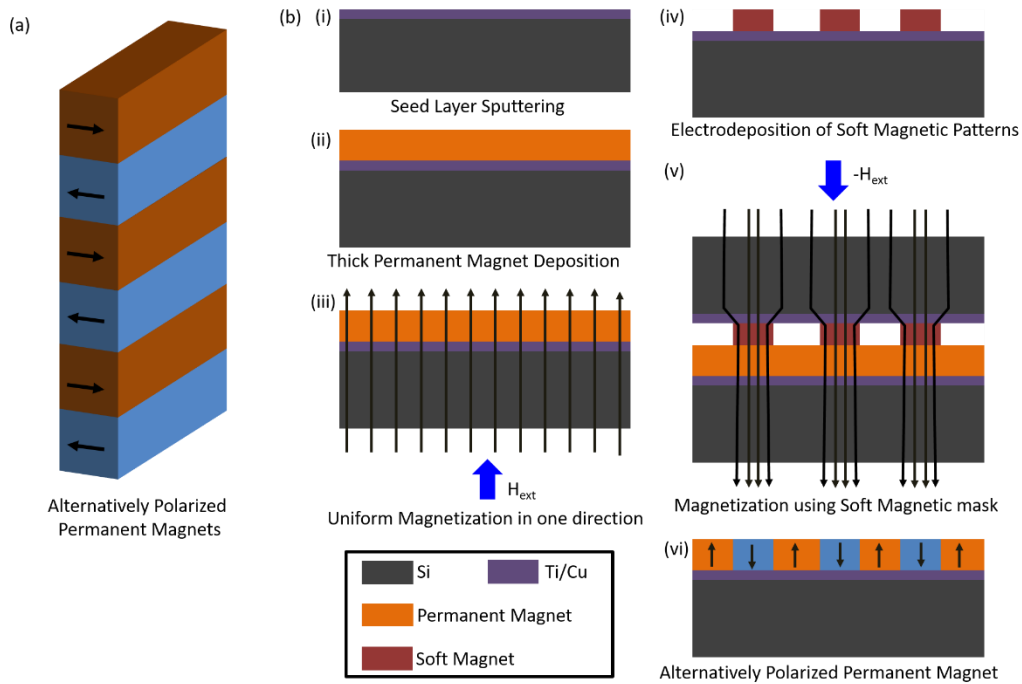
Fig. 9.2: (a) Alternately polarized permanent micro-magnets. (b) Proposed process flow using magnetization mask.

Fig. 9.2 shows the possible steps for developing such magnetic structure. First, an electroplated hard magnetic film will be pre-magnetized using a magnetizer to induce a magnetic polarization everywhere on the layer. A magnetizing mask (which has the desired pattern) will then be brought in contact with the developed magnetic film, and a pulsed magnetic field will be applied in the opposite direction. Because of the differences in relative permeability created by the features on the mask, the external reversal magnetic flux will be concentrated in the areas of the soft magnetic mask. Consequently, the magnetization of selected regions will get reversed, and the desired pattern will be transferred onto the hard magnetic layer. A major challenge that could arise in this process is that the magnetic flux lines might diffract from the soft magnetic mask and that could possibly change the magnetization map. Hence the process needs to be optimized before it can be taken to the device fabrication level.

Another challenge in this field is to work in the low/very low frequency region with a MEMS scale device. Silicon is the most used material in MEMS and microelectronics. But it has a high Young's modulus of 170 GPa. Hence, it is very difficult to develop miniaturized devices using silicon with very low (<10 Hz) operational frequency. Polymer materials like PDMS, parylene, etc., have been used in the literature to develop MEMS scale devices with low frequency operation. PDMS (Y = 750 kPa) is a

particularly good candidate for developing low frequency membrane structure using a low cost fabrication technique. Fig. 9.3 (a-b) shows the initial trial result of PDMS membrane which is spin coated on a blank silicon wafer and then peeled off. An initial experimental device is shown in Fig. 9.3 (c) which when tested (Fig. 9.3 (d)) showed a resonance frequency of 22 Hz. The PDMS thickness can be further reduced using spin coating optimization and different nonlinear mechanical structure can also be developed on the PDMS using photolithography technique to further widen the output response. The low Young's modulus not only reduces the frequency but also increases the amplitude of oscillation by reducing the spring constant. Therefore much higher output power can be obtained compared to a silicon based device having the same footprint.
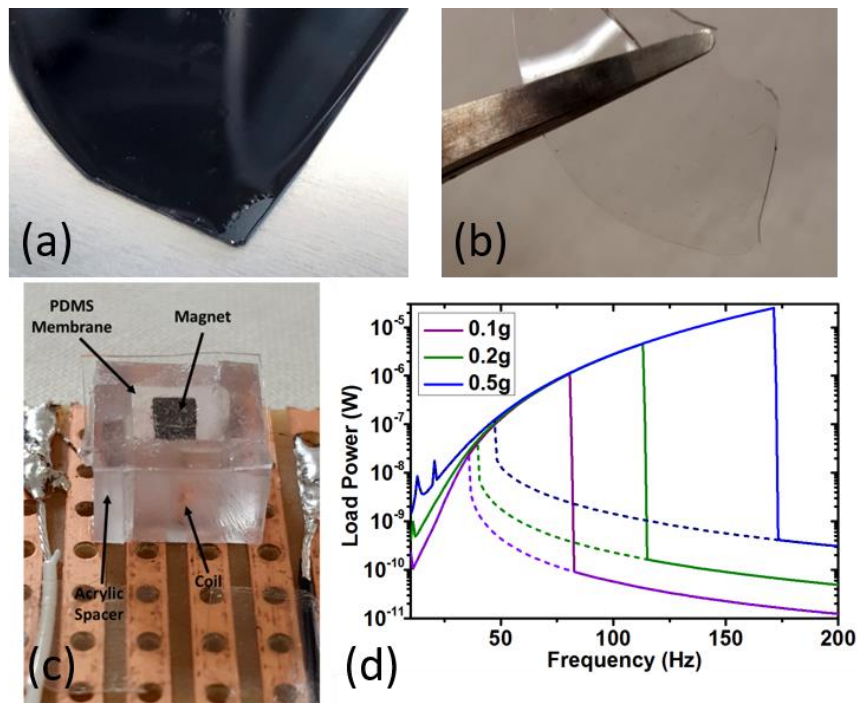
Fig. 9.3: (a) Spin coated PDMS on silicon. (b) Peeled off PDMS from the silicon substrate. (a) Initial trial device for experimentation. (d) Tested results under different input accelerations.

Other innovative aspect of the reported work is the demonstration of an electrical control method to switch from the low to the high energy output branch of a nonlinear generator. However, the technique has been demonstrated manually so far by employing a short duration electrical signal generated in the burst mode from a signal generator. However, for operation under real world applications, the mechanism needs to be automated. Two approaches can be used for this purpose. Firstly, a fraction of the energy generated from the device is saved from the device and the energy is fedback to the device at regular

intervals. In this method, lot of energy will be wasted as the device might not be within the hysteresis region at that particular instant. In the second approach, a circuit can be developed which will comprise of a voltage comparator to decide if the system is in low energy branch, an energy storage element to store the energy from the harvester itself, a triggering circuit and a voltage amplifier to generate a large amplitude signal. A low-power, completely automated electrical switching mechanism can really make the use of nonlinear energy harvesters in different applications widespread.

Finally, as was mentioned before, power management is as important as power generation for complete system development. To advance this part of the work, the meso-scale nonlinear harvesters will be demonstrated first with off-the-shelf power management circuit like LTC3588-1 which is reported in chapter 4. It is necessary to develop a highly efficient power management solution for low voltage sources like EM VEH devices. There are two major challenges: (i) activation in the discharged state (cold-start). (ii) Efficient operation in the steady state (MPPT requirement). A circuit designed for one of these requirements is not suitable for the other case. Hence it is important to come with a novel solution where a balance can be achieved between this trade-off. The circuit can be developed at first at board level using discrete components. Finally, the circuit can be fabricated to develop an Application Specific Integrated Circuit (ASIC) for EM VEH purpose.

9.5. Final Remarks:

The vision of billions of connected autonomous sensors for the monitoring of wellbeing of human health and the environment leading to the 'Internet of Things' is closing towards reality. While the other fields in sensors, computation and data transmission have improved significantly in the last decade or so, the area of powering these devices still requires more attention. Thus addressing the pertinent issues of miniaturized vibrational energy harvesters is of paramount importance both scientifically and commercially.

The reported work in this thesis has improved and advanced some of the issues related to the development of vibration energy harvesting technology. However, there is still scope for plenty of work that could enable an energy harvesting solution, which is capable of powering the billions of sensors under the IoT platform perpetually.

Appendix I: MATLAB Code for Bidirectional Tuning

Matlab Code for Inductive Tuning:

```
m=3e-3; %Kg
%b=10; %damping coefficient
%k=19720; %spring constant
%f0=11.25; % in Hz
wn=2*pi*100; %resonant frequency in rad/sec obtained through the
analytical formula k=181 N/m
%ke=1000; %flux linkage in Wb/m obtained from Ansoft solver
RC=1000; %coil resistance in ohm
RL=50; %load resistance in ohm
%CL=1e-6; %load capacitance
%a=0.5;%acceleration in m/sec2
ke=15;
Lm=(ke^2)/(m*(wn^2));
R=RL+RC;
f=2000;
wr=zeros(f,1);
L=logspace(-6,3,f);
for i=1:1:length(L)
wr(i)=sqrt((((sqrt((((R/wn)^2)-(L(i)^2)-
(L(i)*Lm))^2+4*((L(i)/wn)^2)*R^2))-(((R/wn)^2)-(L(i)^2)-
(L(i)*Lm)))/(2*(L(i)/wn)^2));
end
semilogx(L,wr/(2*pi),'m','linewidth',3)
```

Matlab Code for Capacitive Tuning:

```
m=3e-3; %Kg
%b=10; %damping coefficient
%k=19720; %spring constant
%f0=11.25; % in Hz
wn=2*pi*100; %resonant frequency in rad/sec obtained through the
analytical formula k=181 N/m
%ke=1000; %flux linkage in Wb/m obtained from Ansoft solver
RC=1000; %coil resistance in ohm
RL=1000; %load resistance in ohm
%CL=1e-6; %load capacitance
%a=0.5;%acceleration in m/sec2
K1=0.225;
r=RL/RC;
f=2000;
wr=zeros(f,1);
c=logspace(-12,-2,f);
for i=1:1:length(c)
%H=r/(((1+r)^2)+(wn^2)*(RL^2)*(CL^2));
%S=(CL*(r^2)*((K1*RC)/m))/(((1+r)^2)+(wn^2)*(RL^2)*(CL^2));
%O=(((1+r))+(wn^2)*(RL^2)*(CL^2))/(((1+r)^2)+(wn^2)*(RL^2)*(CL^2));
theta=(1+r)^2;
zeta=(c(i)*(r^2)*K1*RC)/m;
epsilon=(RL^2)*(c(i)^2);
wr(i)=sqrt((sqrt(((theta+zeta-
epsilon*(wn^2))^2)+4*epsilon*theta*(wn^2))-(theta+zeta-
epsilon*(wn^2)))/(2*epsilon));
end
semilogx(c,wr/(2*pi),'m','linewidth',3)
```

Appendix II: Mask for Spring Fabrication

Mask L1:
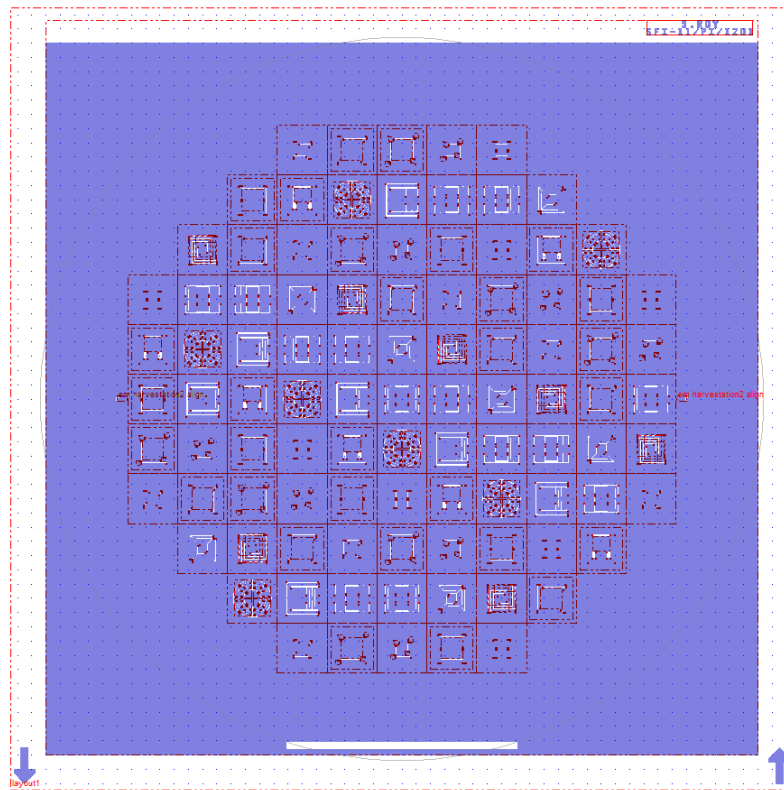
Mask BACK MASS:
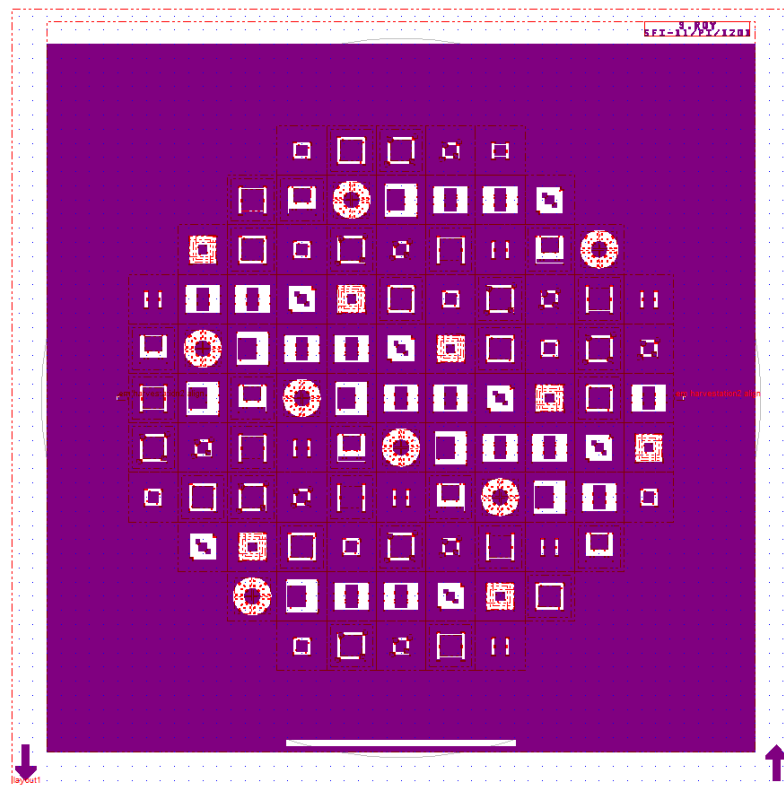
Mask Design for Linear MEMS EM VEH Spring Structure:
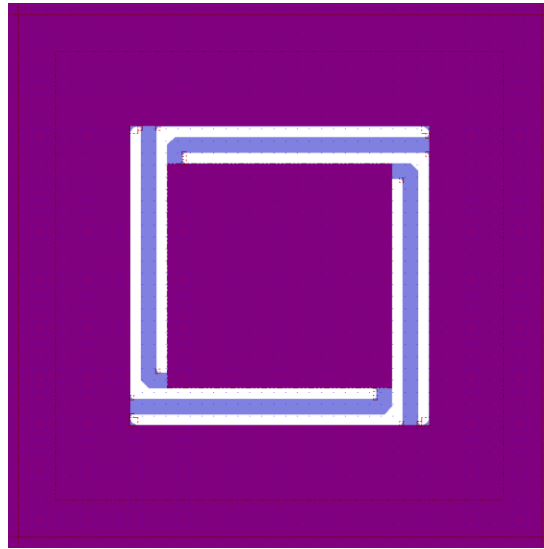
Front Lithography Mask:
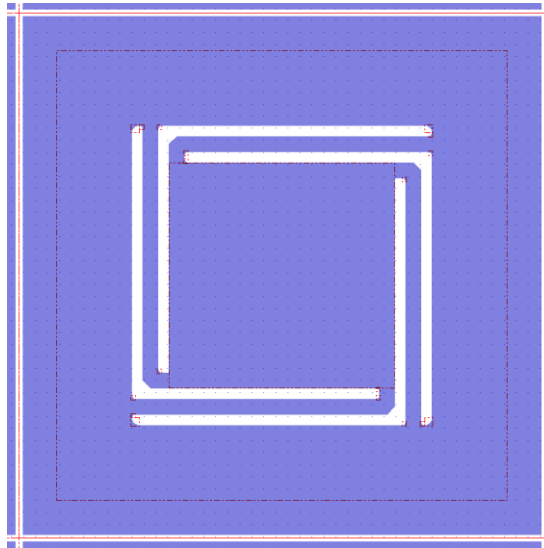
Back Lithography Mask:
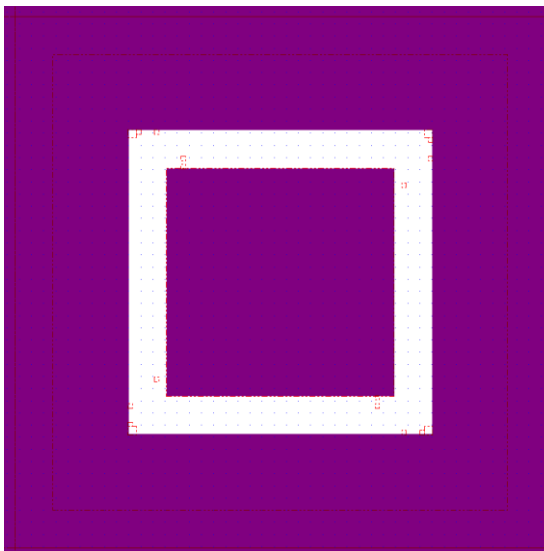
Appendix III: Mask for Double Layer Coil Fabrication
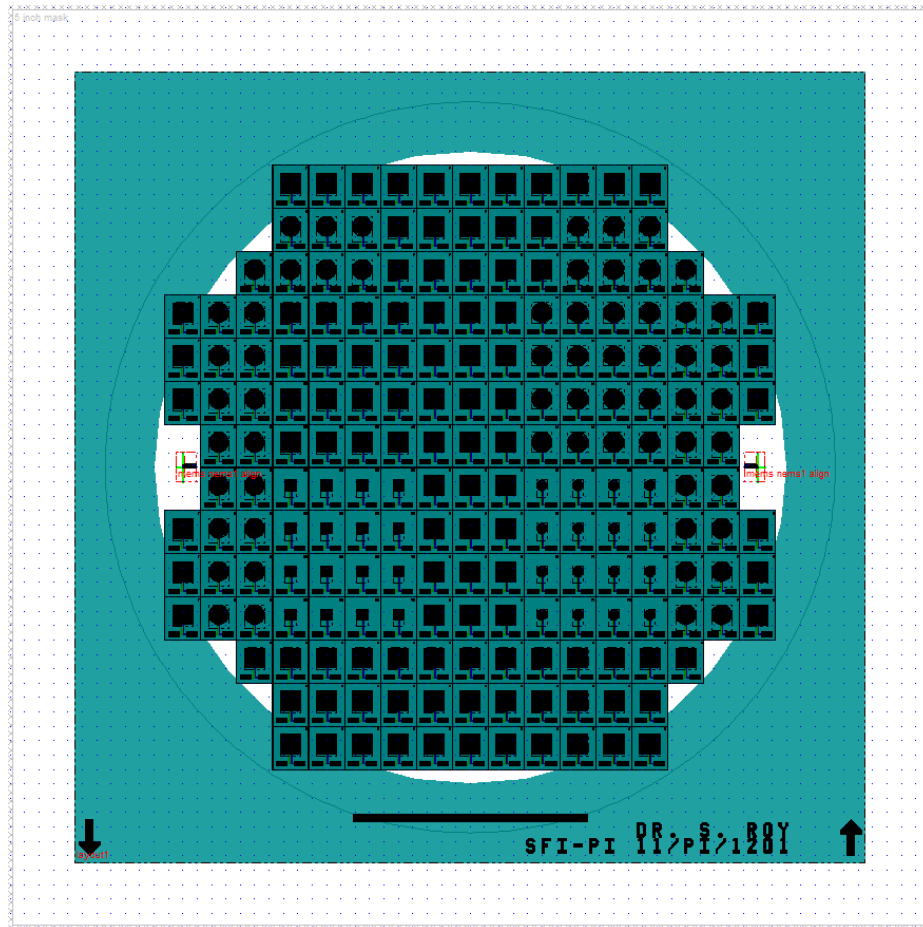
Bottom Layer Coil Mask:
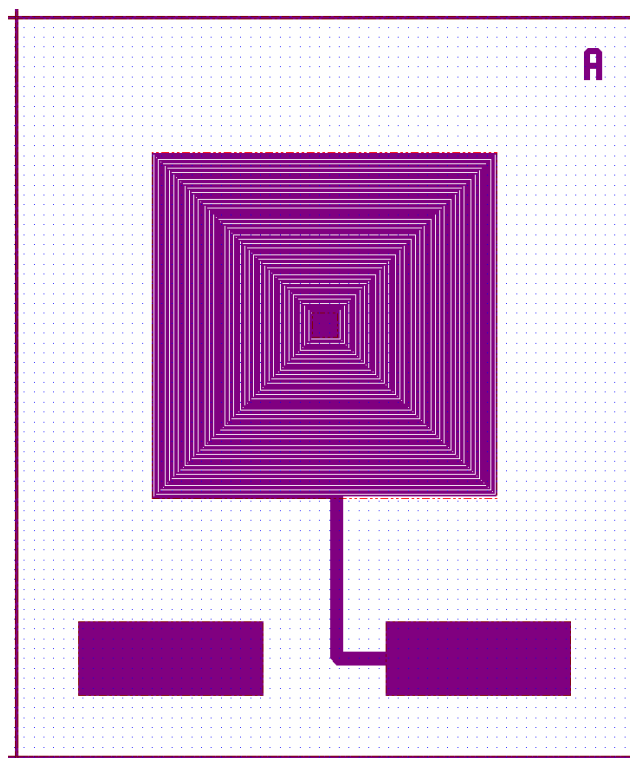
Via Layer Mask:
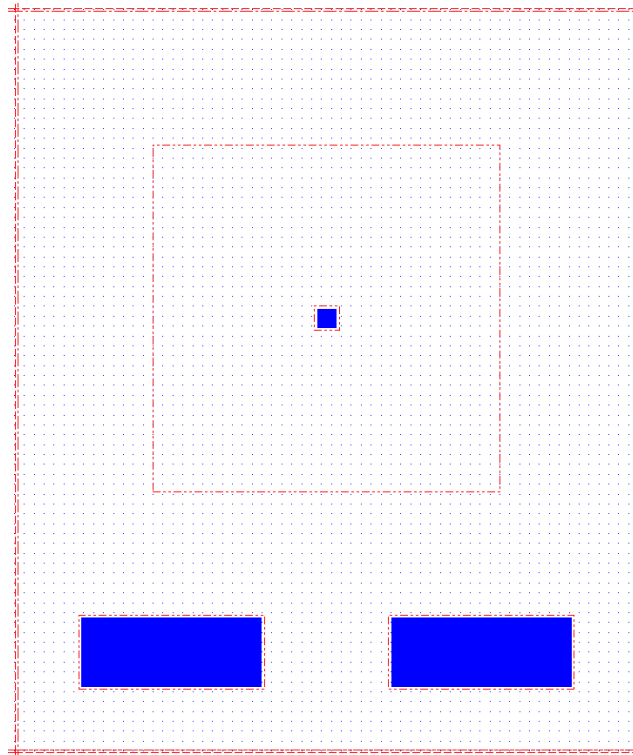
Top Layer Coil Mask:
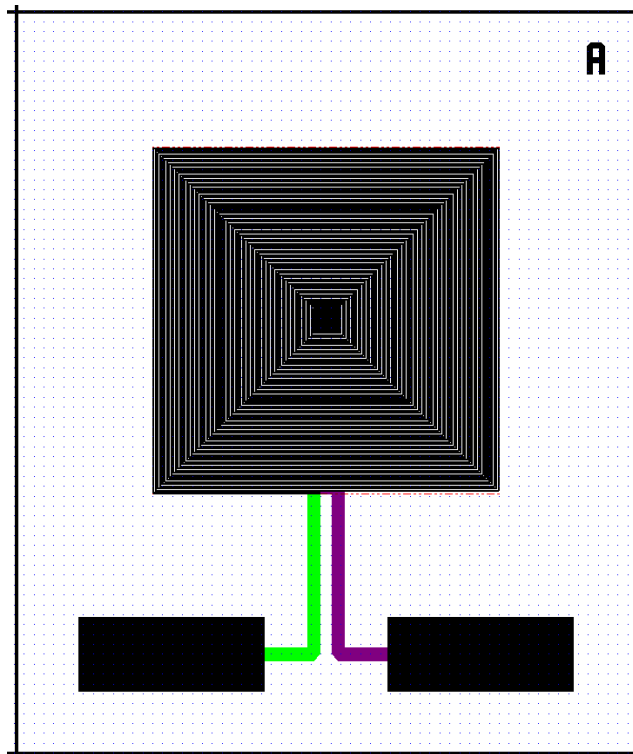
Appendix III: MATLAB Code for Duffing Oscillator

Matlab Code for Simulation of Non-dimensional Model:

```matlab
%Equation of motion
function pdot=Parlitz_time(t,p,w,f,d)
%f=2;
%d=0.2;
pdot=zeros(3,1);
pdot(1)=p(2);
pdot(2)=-d*p(2)-p(1)-p(1)^3+f*cos(p(3));
pdot(3)=w; %phase


%Frequency Response
s=200;
a=zeros(s,1);
b=zeros(s,1);
f=0.0019;
d=0.031;
%Front sweep
ww=linspace(0.9,2.1,s);
p0=[0 0 0];
for i=1:1:length(ww)
 [t,p]=ode45(@(t,p) Parlitz_time(t,p,ww(i),f,d),
linspace(0,100,1000), p0);
 x=max(p(:,2));
 %xrms=sqrt(mean(x));
 n=length(p(:,2));
 %avgp=(x(length(t))-x(round(length(t)/2)))/(t(length(t))-
t(round(length(t)/2)));
 a(i)=x;
 p0=p(n,:);
end
plot(ww,a,'b','Linewidth',2);
hold on;
% Back sweep
ww1=linspace(2.1,0.9,s);
for i=1:1:length(ww1)
 [t,p]=ode45(@(t,p) Parlitz_time(t,p,ww1(i),f,d),
linspace(0,100,1000), p0);
 y=max(p(:,2));
 %yrms=sqrt(mean(y));
 m=length(p(:,2));
 %avgpd=(y(length(t))-y(round(length(t)/2)))/(t(length(t))-
t(round(length(t)/2)));
 b(i)=y;
 p0=p(m,:);
end
plot(ww1,b,'--b','Linewidth',2);
xlabel('Frequency');
ylabel('Amplitude');
```

Bibliography

1. A. Lucas, Wind, Water, Work: Ancient and Medieval Milling Technology, Brill Publishers, p. 65., ISBN 90-04-14649-0.1 (2006).

2. Edelberg, Lennart, Schuyler Jones, Nuristan, Akademische Druck- u. Verlagsanstalt, Graz, Austria (1979).

3. Gies, Frances and Joseph, Cathedral, Forge, and Waterwheel: Technology and Invention in the Middle Ages, Harper Perennial, New York (1994).

4. Reynolds, S. Terry, "Medieval Roots of the Industrial Revolution," Scientific American, July pp.122-130 (1984).

5. R. W. Righter, Wind Energy in America: A History, 1st ed. University of Oklahoma Press (1996).

6. The World Wind Energy Association, 2014 Half-year Report. WWEA. pp. 1–8 (2014).

7. A. Chapius, E. Jaquet, The History of the Self Winding Watch, pp. 1770–1931, Geneva, Switzerland: Roto-Sadag (1956).

8. M. Hayakawa, 'Electric wristwatch with generator', U.S. Patent 5001685A, Mar. 1991.

9. P.D. Mitcheson, E.M. Yeatman, G.K. Rao, A.S. Holmes, T.C. Green, Energy harvesting from human and machine motion for wireless electronic devices, Proc. IEEE, 96:1454–1486 (2008).

10. J. Tiemann, 'Apparatus for converting vibratory motion to electrical energy', U.S. Patent 5578877A (1996).

11. S. Meninger, et al, IEEE transactions on VLSI systems, 9, No. 1, 64-76, (2001).

12. A. Chandrakasan, et al, Proc. Of the IEEE Int. Symp on circuits and systems, 604-607 (1998).

13. N. Okada et al., J. Of Multiple-valued logic and soft computing, 13 (4-6), 619-631 (2007).

14. O. Berkh et al, Microelectronic Engg., 84 (11), 2444-2449 (2007).

15. K. Ashton, 'That 'Internet of Things' Thing', RFID Journal, 22 June 2009.

16. Cisco IBSG, April 2011: http://www.cisco.com/c/dam/en_us/about/ac79/docs/innov/IoT_IBSG_0411FINAL.pdf

17. https://iot-analytics.com/10-internet-of-things-applications/

18. http://www.idc.com/getdoc.jsp?containerId=prUS25658015.

19. http://www.iec.ch/whitepaper/pdf/iecWP-internetofthings-LR-en.pdf

20. J. M. Gilbert, F. Balouchi, Comparison of Energy Harvesting Systems for Wireless Sensor Networks, Intl. J. Autom. Comp., 05(4):334-347 (2008).

21. A. Pfenniger, M. Jonsson, A. Zurbuchen, V. M. Koch, R. Vogel, 'Energy Harvesting from the Cardiovascular System, or How to Get a Little Help from Yourself', Annals of Biomedical Engineering, 41(11), pp 2248–2263 (2013).

22. S. Roundy, P.K. Wright, J. Rabaey, 'A Study of Low Level Vibrations as a Power Source for Wireless Sensor Nodes,' Computer Communications, vol. 26, no. 11, pp. 1131–1144 (2003).

23. M. Soliman, 'Wideband micro-power generators for vibration energy harvesting', PhD Thesis, University of Waterloo (2009).

24. C. C. Ho, J. W. Evans, P. K. Wright, 'Energy Storage', In S. P. Beeby, N. White (ed.), Energy Harvesting for Autonomous Systems, Artech House Publishers, pp. 212 (2010).

25. A. Somov, R. Giaffreda, 'Powering IoT Devices: Technologies and Opportunities', IEEE Internet of Things Newsletters, November (2015).

26. H. Chen, T. N. Cong, W. Yang, C. Tan, Y. Li, Y. Ding, 'Progress in electrical energy storage system: A critical review', Prog. Nat. Sci. 19(3): 291-312 (2009).

27. X. Jiang, J. Polastre, D. Culler, 'Perpetual Environmentally Powered Sensor Networks', IPSN 2005. Fourth International Symposium on Information Processing in Sensor Networks, 2005.

28. Imprint Energy's flexible battery, 2014. [Online]. Available: http://fashioningcircuits.com/?p=2550

29. L. Baggetto, R.A.H. Niessen, F. Roozeboom, P.H.L. Notten, 'High energy density all-solid-state batteries: A challenging concept towards 3D integration', Adv. Funct. Mater. 18:1057 (2008).

30. J. D. Morse, 'Micro-fuel cell power sources', Int. J. Energy Res., 31:576–602 (2007).

31. C. Knights, J. Davidson, S. Behrens, 'Energy Options for Wireless Sensor Nodes', Sensors, 8:8037-66 (2008).

32. G. Lu, C. Wang, T. Yen, X. Zhang, 'Development and characterization of a silicon-based micro direct methanol fuel cell', Electrochima Acta, 49:821–828 (2004).

33. X. Cheng, Z. Shia, N. Glass, L. Zhang, J. Zhanga, D. Song, Z-S Liu, H Wang, J. Shen, 'A review of PEM hydrogen fuel cell contamination: Impacts, mechanisms, and mitigation', J. Power Sources, 165(2): 739-756 (2007).

34. V. Mehta, J. S. Cooper, 'Review and analysis of PEM fuel cell design and manufacturing', J. Power Sources, 114(1): 32-53 (2003).

35. M. Winter, R. J. Brodd, 'What Are Batteries, Fuel Cells, and Supercapacitors?', Chem. Rev. 104:4245−4269 (2004).

36. D.J. Paul, Thermoelectric Energy Harvesting, in: G. Fagas, L. Gammaitoni, D. Paul, G. Abadal Berini (Eds.), ICT-Energy-Concepts Towards Zero-Power Information and Communication Technology, Intech pp. 49–78 (2014).

37. N. Muller, L. G. Frechette, 'Performance Analysis of Brayton and Rankine Cycle Microsystems for Portable Power Generation,' Proc. ASME International

Mechanical Engineering Congress and Exposition (IMECE), New Orleans, LA, November 2002.

38.   W. R. Corliss, D. G. Harvey, 'Radioisotopic Power Generation,' Prentice Hall: New Jersey, (1964).

39.   A. Lal, R. Duggirala, H. Li, 'Pervasive power: A radioisotope-powered piezoelectric generator,' IEEE Pervasive Comput., 4:53–61 (2005).

40.   S. Boisseau, G. Despesse and B. Ahmed Seddik, Electrostatic Conversion for Vibration Energy Harvesting, Small-Scale Energy Harvesting, Dr. Mickaël Lallart (Ed.), InTech, DOI: 10.5772/51360 (2012).

41.   T. Markvart, L. Castañer, 'Principles of Solar Cell Operation', In A. McEvoy, L. Castaner, T. Markvart (ed.), Solar Cells, Elsevier, doi:10.1016/B978-0-12-386964-7.01001-5 (2013).

42.   T. Wark, W. Hu, P. Corke, J. Hodge, A. Keto, B. Mackey, G. Foley, P. Sikka, M. Brunig, Springbrook: Challenges in Developing a Long-Term, Rainforest Wireless Sensor Network, In 4th International Conference on Intelligent Sensors, Sensor Networks and Information Processing, Sydney, Dec 2008.

43.   J. P. Thomas, M. A. Qidwai, J. C. Kellogg, 'Energy scavenging for small-scale unmanned systems', J. Power Sources, 159:1494–1509 (2006).

44.   S. Roundy, D. Steingart, L. Frechette, P. Wright, J Rabaey, 'Power Sources for Wireless Sensor Networks', In Holger Karl Andreas Willig Adam Wolisz (Eds.), Wireless Sensor Networks, First European Workshop, EWSN 2004 Berlin, Germany, January 19-21, 2004 Proceedings (Springer), pp 1-17 (2004).

45.   N. S. Hudak, G. G. Amatucci, 'Small-scale energy harvesting through thermoelectric, vibration, and radiofrequency power conversion', J. Appl. Phys. 103: 101301 (2008).

46.   D. Zhao, G. Tan, 'A review of thermoelectric cooling: Materials, modeling and applications', Appl. Therm. Engg. 66:15-24 (2014).

47.   L. E. Bell, Cooling, Heating, Generating Power, and Recovering Waste Heat with Thermoelectric Systems, Science, ol. 321, Issue 5895, pp. 1457-1461 (2008).

48.   Z.G. Wan, Y.K. Tan, C. Yuen, Review on energy harvesting and energy management for sustainable wireless sensor networks. In: Proceedings of the IEEE International Conference on Communication Technology (ICCT'11), pp. 317–362 (2011).

49.   U. Bergqvist, G. Friedrich, Y. Hamnerius, L. Martens, G. Neubauer, G. Thuroczy, E. Vogel, J. Wiart, Mobile telecommunication base stations – exposure to electromagnetic fields, report of a short term mission within COST-244bis. Technical report (2000).

50.   A. Sample, J.R. Smith, Experimental results with two wireless power transfer systems. In: Proceedings of the IEEE Radio and Wireless Symposium, pp. 16–18 (2009).

51.   R.J.M. Vullers, R.V. Schaijk, H.J. Visser, J. Penders, C.V. Hoof, Energy harvesting for autonomous wireless sensor networks. IEEE Solid-State Circuits Mag. 2 (2), pp. 29–38 (2010).

52. Y. Mao, Y. Luo, J. Zhang, K. B. Letaief, 'Energy harvesting small cell networks: feasibility, deployment, and operation', IEEE Comm. Mag., 53(6):94-101 (2015).

53. C. B. Williams, M. A. Shearwood Harradine, P. H. Mellor, T. S. Birch, R. B. Yates, Development of an electromagnetic micro-generator, IEE Proc. Circuits Devices Syst.148:337–42 (2001).

54. A. Badel, A. Benayad, E. Lefeuvre, L. Lebrun, C. Richard, D.Guyomar, 'Single crystals and nonlinear process for outstanding vibration-powered electrical generators', IEEE Trans. Ultrason. Ferroelectr. Freq. Control, 53:673–84 (2006).

55. S. Roundy, 'On the effectiveness of vibration-based energy harvesting', J. Intell. Mater. Syst. Struct., 16:809–23 (2005).

56. K. A. Cook-Chennault, N. Thambi, A. M. Sastry, 'Powering MEMS portable devices— a review of non-regenerative and regenerative power supply systems with special emphasis on piezoelectric energy harvesting systems', Smart Mater. Struct., 17:043001 (33pp) (2008).

57. P. Basset, E. Blokhina, D. Gayalko, 'Electroostatic kinetic energy harvesting', pp. 3, Wiley (2016).

58. G. Zhu, B. Peng, J. Chen, Q. Jing, Z. L. Wang, 'Triboelectric nanogenerators as a new energy technology: From fundamentals, devices, to applications', Nano Energy, 14:126–138 (2015).

59. Z. L. Wang, 'Triboelectric Nanogenerators as New Energy Technology for Self-Powered Systems and as Active Mechanical and Chemical Sensors', ACS Nano, 7 (11), pp 9533–9557 (2013).

60. H. Guo, Z. Wen, Y. Zi, Min-H. Yeh, J. Wang, L. Zhu, C. Hu, Z. L. Wang, 'A Water-Proof Triboelectric–Electromagnetic Hybrid Generator for Energy Harvesting in Harsh Environments', Adv. Energy Mater., 6:1501593 (2016).

61. A. Khaligh, P. Zeng, C. Zheng, Kinetic Energy Harvesting Using Piezoelectric and Electromagnetic Technologies—State of the Art, IEEE Trans. Indus. Elec., 57(3): 850-860 (2010).

62. S. P. Beeby, R. N. Torah, M. J. Tudor, P. Glynne-Jones, T. O'Donnell, C. R. Saha, S. Roy, A micro electromagnetic generator for vibration energy harvesting, J. Micromech. Microeng. 17:1257–1265 (2007).

63. M. Löhndorf, T. KvisterØy, E. Westby, E. Halvorsen, 'Evaluation of energy harvesting concepts for tire pressure monitoring systems', Proc. PowerMEMS 2007, pp 331–4 (2007).

64. H. Vocca, F. Cottone, Kinetic energy harvesting", in FAGAS G. (ed.), ICT – Energy – Concepts Towards Zero – Power Information and Communication Technology.

65. M. Deterre, B. Boutaud, R. Dalmolin, S. Boisseau, J-J. Chaillout, E. Lefeuvre, E. Dufour-Gergam, 'Energy Harvesting System for Cardiac Implant Applications', Proc. Symp. DTIP MEMS/MOEMS, pp. 387–391 (2011).

66. H. J. Pain, The Physics of Vibrations and Waves, 6th Edition,Wiley & Sons.

67. R. H. Olsson, K. E. Wojciechowski, M. S. Baker, M. R. Tuck, J. G. Fleming, 'Post-CMOS-Compatible Aluminum Nitride Resonant MEMS Accelerometers', J. Microelectromech. Syst., 18(3): 671-678.

68. A. A. Trusov, A. M. Shkel, 'Capacitive detection in resonant MEMS with arbitrary amplitude of motion', J. Micromech. Microeng., 17:1583–1592 (2007).

69. É. Colinet, J. Juillard, S. Guessab, R. Kielbasa, 'Actuation of resonant MEMS using short pulsed forces', Sens. Act. A: Phys., 115:118-125 (2004).

70. Q. Chen, D-J. Yao, C-J. Kim, G. P. Carman, 'Mesoscale actuator device: micro interlocking mechanism to transfer macro load', Sens. Act. A: Phys., 73:30-36 (1999).

71. S. Roundy, P. K. Wright, 'A piezoelectric vibration based generator for wireless electronics', Smart Mater. Struct. 13:1131–42 (2004).

72. P. Glynne-Jones, S. P. Beeby, N. M. White, 'Towards a piezoelectric vibration powered microgenerator,, IEE Proc.—Sci. Meas. Technol., 148:68–72 (2001).

73. D. Zhu, S. P. Beeby, M. J. Tudor, N. R. Harris, 'A credit card sized self-powered smart sensor node', 169(2): 317–325 (2011).

74. Y. B. Jeon, R. Sood, J.H. Jeong, S. G. Kim, 'MEMS power generator with transverse mode thin film PZT', Sens. Actuators A, Phys., 122(1):16–22, (2005).

75. IEEE Standards on Piezoelectricity, ANSI-IEEE 176-1987 (1987).

76. M. Marzencki, S. Basrous, B. Charlot, A. Grasso, M. Colin, L. Valbin, 'Design and fabrication of piezoelectric micro power generators for autonomous microsystems', in Proc. MEMS/MOEMS DTIP, pp. 299–302 (2005).

77. N. Jackson, R. O'Keeffe, F. Waldron, M. O'Neill, A. Mathewson, 'Evaluation of low-acceleration MEMS piezoelectric energy harvesting devices', Microsyst. Technol., 20:671–680 (2014).

78. A. Khaligh, P. Zeng, C. Zheng, Kinetic Energy Harvesting Using Piezoelectric and Electromagnetic Technologies—State of the Art, IEEE Trans. Indus. Elec., 57(3): 850-860 (2010).

79. N. S. Shenck, J. A. Paradiso, 'Energy scavenging with shoe-mounted piezoelectrics', IEEE Micro, 21(3):30–42 (2001).

80. M. J. Ramsay, W. W. Clark, 'Piezoelectric energy harvesting for bioMEMS applications', Proc. SPIE, 4332:429–438 (2001).

81. J. W. Sohn, S. B. Choi, D. Y. Lee, 'An investigation on piezoelectric energy harvesting for MEMS power sources', Proc. IMechE, J. Mech. Eng. Sci., 219(4):429–436 (2005).

82. C. Mo, L. J. Radziemski, W. W. Clark, 'Experimental validation of energy harvesting performance for pressure loaded piezoelectric circular diaphragms', Smart Mater. Struct. 19:075010 (2010).

83. M. A. Karami, D. J. Inman, 'Powering pacemakers from heartbeat vibrations using linear and nonlinear energy harvesters', Appl. Phys. Lett. 100:042901 (2012).

84. S. Meninger, J. Mur-Miranda, J. Lang, A. Chandrakasan, A. Slocum, M. Schmidt, R. Amirtharajah, 'Vibration to electric energy conversion', IEEE Trans Very Large Scale Integration (VLSI) Syst. 9:64–76 (2001).

85.   W. Ma, M. Wong, L. Ruber, 'Dynamic simulation of an implemented electrostatic power micro-generator', Proc. Design, Test, Integration and Packaging of MEMS and MOEMS pp 380–5 (2005).

86.   G. Despesse, T. Jager, J. Chaillout, J. Leger, A. Vassilev, S. Basrour, B. Chalot, 'Fabrication and characterisation of high damping electrostatic micro devices for vibration energy scavenging', Proc. Design, Test, Integration and Packaging of MEMS and MOEMS, pp 386–90 (2005).

87.   F. Wang, O. Hansen, 'Electrostatic energy harvesting device with out-of-the-plane gap closing scheme'.

88.   S. P. Beeby, D. Zhu, 'Vibration energy harvesting: fabrication, miniaturisation and applications', Proc. SPIE 9517, Smart Sensors, Actuators, and MEMS VII; and Cyber Physical Systems, 951703 (2015).

89.   C. Tsung-Shune, 'Permanent magnet films for applications in MEMS', J. Magn. Mag. Mat., 209:75‑79 (2000).

90.   C. B. Williams, R. B. Yates, 'Analysis of a micro-electric generator for microsystems', Proc. Transducers/Eurosensors IX, 1:369–372 (1995).

91.   C. Shearwood, R. B. Yates, 'Development of an electromagnetic microgenerator', Electron. Lett., 33(22) 1883–1884 (1997).

92.   R. Amirtharajah, A. P. Chandrakasan, 'Self-powered signal processing using vibration-based power generation', IEEE J. Solid State Circuits, 33(5):687–695 (1998).

93.   M. El-hami, P. Glynne-Jones, N. M. White, M. Hill, S. Beeby, E. James, A. D. Brown, J. N. Ross, 'Design and fabrication of a new vibrationbased electromechanical power generator', Sens. Actuators A:Phys., 92: 335–342, (2001).

94.   P. Glynne-Jones, M. J. Tudor, S. P. Beeby, N. M. White, 'An electromagnetic, vibration-powered generator for intelligent sensor systems', Sens. Actuators A: Phys., 110:344–349 (2004).

95.   J. Heit, D. Christensen, S. Roundy, A Vibration Energy Harvesting Structure, Tunable Over A Wide Frequency Range Using Minimal Actuation, Proceedings of the ASME 2013 Conference on Smart Materials, Adaptive Structures and Intelligent Systems, SMASIS (2013).

96.   S.P. Beeby, M. J. Tudor, R. N. Torah, S. Roberts, T. O'Donnell, S. Roy, 'Experimental comparison of macro and micro scale electromagnetic vibration powered generators', Microsyst. Technol., 13(11-12):1647-53 (2007).

97.   D. Zhu, S. Beeby, J. Tudor, N. Harris, 'Vibration energy harvesting using the Halbach array', Smart Mater. Struct., 21:075020 (2012).

98.   S. Roundy, E. Takahashi, 'A planar electromagnetic energy harvesting transducer using a multi-pole magnetic plate', Sens. Act. A: Phys., 195:98–104 (2013).

99.   E. Sardini, M. Serpelloni, 'An efficient electromagnetic power harvesting device for low-frequency applications', Sens. Act. A: Phys., 172 :475–482 (2011).

100. E. Bouendeu, A. Greiner, P. J. Smith, J. G. Korvink, "An efficient low cost electromagnetic vibration harvester," Proc. PowerMEMS 2009, December 01-04, 2009, Washington D.C., USA, 320-323 (2009).

101. C.R. Saha, T. O'Donnell, N. Wang, P. McCloskey, 'Electromagnetic generator for harvesting energy from human motion', Sens. Act. A: Phys., 147:248–253 (2008).

102. Q. Zhang, Y. Wang, E. S. Kim, 'Power generation from human body motion through magnet and coil arrays with magnetic spring', J. Appl. Phys. 115:064908 (2014).

103. D.F. Berdy, D.J. Valentinoc, D. Peroulis, 'Kinetic energy harvesting from human walking and running using a magnetic levitation energy harvester', Sens. Act. A: Phys., 222:262–271 (2015).

104. D. J. Apo, S. Priya, 'High Power Density Levitation-Induced Vibration Energy Harvester', Energy Harvesting and Systems 1(1-2): 79–88 (2014).

105. S. V. Palagummi, F-G. Yuan, 'An enhanced performance of a horizontal diamagnetic levitation mechanism–based vibration energy harvester for low frequency applications', J. Intell. Mat. Syst. Struc., 1045389X16651152, doi:10.1177/1045389X16651152 (2016).

106. M. Salauddin, M. A. Halim, J. Y. Park, 'A magnetic-spring-based, low-frequencyvibration energy harvester comprising a dual Halbach array', Smart Mater. Struct., 25:095017 (2016).

107. S-J. Jang, I-H. Kim, H-J. Jung, Y-P. Lee, 'A tunable rotational energy harvester for low frequency vibration', Appl. Phys. Lett., 99:134102 (2011).

108. S. D. Moss, G. A. Hart, S. K. Burke, G. P. Carman, 'Hybrid rotary-translational vibration energy harvester using cycloidal motion as a mechanical amplifier', Appl. Phys. Lett., 104:033506 (2014).

109. T. Ma, H. Zhang, 'Enhancing mechanical energy harvesting with dynamics escaped from potential well', Appl. Phys. Lett., 100:114107 (2012).

110. H. Yu, J. Zhou, X. Yi, H. Wu, W. Wang, 'A hybrid micro vibration energy harvester with power management 4 circuit', Microelec. Engg. 131:36-42 (2015).

111. Z. Xu, X. Shan, D. Chen T. Xie, 'A Novel Tunable Multi-Frequency Hybrid Vibration Energy Harvester Using Piezoelectric and Electromagnetic Conversion Mechanisms', Appl. Sci., 6(1):10 (2016).

112. A. Khaligh, P. Zeng, X. Wu, and Y. Xu, 'Hybrid energy harvesting topology for human-powered mobile electronics', in Proc. 34th Conf. IEEE Ind. Electron. Soc., Orlando, FL, Nov. 2008, pp. 448–453 (2008).

113. S. Roundy, Y. Zhang, 'Toward self-tuning adaptive vibration based micro-generators', Proc. SPIE., 5649:373–84 (2005).

114. D. Zhu, M. J Tudor, S. P. Beeby, 'Strategies for increasing the operating frequency range of vibration energy harvesters: a review', Meas. Sci. Technol., 21: 022001 (2010).

115. S. E. Leland and P. K. Wright, 'Resonance Tuning of Piezoelectric Vibration Energy Scavenging Generators Using Compressive Axial Preload', Smart Mater. Struct., 15:1413-20 (2006).

116. Y. Hu, H. Xue, H. Hu, 'A Piezoelectric Power Harvester with Adjustable Frequency Through Axial Preloads', Smart Mater. Struct., 16:1961-1966 (2007).

117. C. Eichhorn, F. Goldschmidtboeing, P. Woias, 'A Frequency Tunable Piezoelectric Energy Converter Based on A Cantilever Beam', in Proceedings of PowerMEMS, November 2008, Sendai, pp. 309-312 (2008).

118. X. Wu, J. Lin, S. Kato, K. Zhang, T. Ren, L. Liu, 'A Frequency Adjustable Vibration Energy Harvester', in Proceedings of PowerMEMS, November 2008, Sendai, pp. 245-248 (2008).

119. V. R. Challa, M. G. Prasad, Y. Shi, F. T. Fisher, 'A vibration energy harvesting device with bidirectional resonance frequency tenability', Smart Mater. Struct., 17 :015035 (2008).

120. T. Reissman, E. M. Wolff, E. Garcia, 'Piezoelectric Resonance Shifting Using Tunable Nonlinear Stiffness', Proc. SPIE, 7288:72880G (2009).

121. I. N. Ayala-Garcia, D. Zhu, M. J. Tudor, S. P. Beeby, 'A tunable kinetic energy harvester with dynamic over range protection', Smart Mater. Struct., 19:115005 (2010).

122. C. Peters, D. Maurath, W. Schock, F. Mezger, Y. Manoli, 'A Closed-loop Wide-range Tunable Mechanical Resonator for Energy Harvesting Systems', J. Micromech. Microeng., 19:094004 (2009).

123. M. Wischke, M. Masur, F. Goldschmidtboeing, F. P. Woias, 'Electromagnetic Vibration Harvester with Piezoelectrically Tunable Resonance Frequency', J. Micromech. Microeng., 20:035025 (2010).

124. D. Charnegie, 'Frequency tuning concepts for piezoelectric cantilever beams and plates for energy harvesting', MSc Dissertation, School of Engineering, University of Pittsburgh, USA (2007).

125. A. Cammarano, S. G. Burrow, D. A. W. Barton, A. Carrella, L. R. Clare, 'Tuning a resonant energy harvester using a generalized electrical load', Smart Mater. Struct., 19:055003 (2010).

126. D. Zhu, S. Roberts, T. Mouille, M. J. Tudor, S. P. Beeby, 'General model with experimental validation of electrical resonant frequency tuning of electromagnetic vibration energy harvesters', Smart Mater. Struct., 21:105039 (2012).

127. L. Tang, Y. Yang, C. K. Soh, 'Toward broadband vibration-based energy harvesting', J. Intell. Mater. Syst. and Struc., 21:1867 (2010).

128. H. Xue, Y. Hu, Q. Wang, 'Broadband Piezoelectric Energy Harvesting Devices Using Multiple Bimorphs with Different Operating Frequencies', IEEE Trans. Ultrason. Ferroelectr. Freq. Control, 55:2104-2108 (2008).

129. I. Sari, T. Balkan and H. Kulah, 'An electromagnetic micro power generator for wideband environmental vibrations', Sens. Actuators A, 145-146:405-13 (2008).

130. J-Q. Liu, H-B. Fang, Z-Y. Xu, X-H. Mao, X-C. Shen, D. Chen, H. Liao, B-C. Cai, 'A MEMS-based piezoelectric power generator array for vibration energy harvesting', Microelect. Journ., 39:802–806 (2008).

131. M. Ferrari, V. Ferrari, M. Guizzetti, D. Marioli, A Taroni, 'Piezoelectric Multifrequency Energy Converter for Power Harvesting in Autonomous Microsystems', Sens. Actuators, A: Phys, 142:329-335 (2008).

132. Y. Tadesse, S. Zhang, S. Priya, 'Multimodal Energy Harvesting System: Piezoelectric and Electromagnetic', J. Intell. Mater. Syst. Struct., 20:625-632 (2009).

133. H. Liu, B. W. Soon, N. Wang, C. J. Tay, C. Quan, C. Lee, 'Feasibility study of a 3D vibration-driven electromagnetic MEMS energy harvester with multiple vibration modes', J. Micromech. Microeng. 22:125020 (2012).

134. H. Liu, Y. Qian, C. Lee, 'A multi-frequency vibration-based MEMS electromagnetic energy harvesting device', Sens. Act. A: Phys., 204:37–43 (2013).

135. H. Liu, T. Chen, L. Sun, C. Lee, 'An Electromagnetic MEMS Energy Harvester Array with Multiple Vibration Modes', Micromachines, 6:984-992 (2015).

136. T. Petropoulos, E. M. Yeatman, P. D. Mitcheson, 'MEMS coupled resonators for power generation and sensing', Proc. Micromech. Europe, Leuven, Belgium (2004).

137. H. Wu, L. Tang, Y. Yang, C. K. Soh, 'A novel two-degrees-of-freedom piezoelectric energy harvester', J. Intell. Mat. Syst. Struc., 1045389X12457254 (2012).

138. K. Tao, J. Wu, L. Tang, X. Xia, S. W. Lye, J. Miao, X. Hu, 'A novel two-degree-of-freedom MEMS electromagnetic vibration energy harvester', J. Micromech. Microeng., 26:035020 (2016).

139. R. Ramlan, M. J. Brennan, B. R. Mace and I. Kovacic, 'Potential benefits of a non-linear stiffness in an energy harvesting device', Nonlinear Dyn., 59:545-58 (2010).

140. B. P. Mann and N. D. Sims, Energy harvesting from the nonlinear oscillations of magnetic levitation, J. Sound Vib., 319:515-30 (2009).

141. S. C. Stanton, C. C. McGehee, and B. P. Mann, 'Reversible hysteresis for broadband magnetopiezoelastic energy harvesting', Appl. Phys. Lett., 95:174103 (2009).

142. H. Liu, Y. Qian, N. Wang, C. Lee, 'An in-plane approximated nonlinear MEMS electromagnetic energy harvester', J. Microelectromech. Syst., **23**, 740-749 (2014).

143. H. Liu, K. H. Koh, C. Lee, 'Ultra-wide frequency broadening mechanism for micro-scale electromagnetic energy harvester', Appl. Phys. Lett., 104:053901 (2014).

144. G. Gafforelli, A. Corigliano, R. Xu, S. G. Kim, 'Experimental verification of a bridge-shaped, nonlinear vibration energy harvester', Appl. Phys. Lett., 105: 203901 (2014).

145. B. Marinkovic, H. Koser, 'Smart Sand—a wide bandwidth vibration energy harvesting platform', Appl. Phys. Lett., 94:103505 (2009).

146. D. S. Nguyen, E. Halvorsen, G. U. Jensen, A. Vogl, 'Fabrication and characterization of a wideband MEMS energy harvester utilizing nonlinear springs', J. Micromech. Microeng. 20:125009 (2010).

147. S A. Hajati and S-G Kim, 'Ultra-wide bandwidth piezoelectric energy harvesting', Appl. Phys. Lett. 99:083105 (2011).

148. M. F. Daqaq, 'Response of Uni-Modal Duffing-Type Harvesters to Random Forced Excitations', J. Sound Vib., 329:3621-3631 (2010).

149. M. F. Daqaq, R. Masana, A. Erturk, D. D. Quinn, 'On the Role of Nonlinearities in Vibratory Energy Harvesting: A Critical Review and Discussion', Appl. Mech. Rev., 66:040801 (2014).

150. A. Erturk, J. Hoffmann and D. J. Inman, 'A piezomagnetoelastic structure for broadband vibration energy harvesting', Appl. Phys. Lett., 94:254102 (2009).

151. F. Cottone, H. Vocca and L. Gammaitoni, 'Nonlinear energy harvesting', Phys. Rev. Lett., 102:080601 (2009).

152. B Ando`, S Baglio, C Trigona, N Dumas, L Latorre, P Nouet, 'Nonlinear mechanism in MEMS devices for energy harvesting applications', J. Micromech. Microeng., 20:125020 (2010).

153. P. Podder, A. Amann, S. Roy, A bistable electromagnetic micro-power generator using FR4-based folded arm cantilever, Sens. Actuators A: Phys. (2015), http://dx.doi.org/10.1016/j.sna.2015.03.043.

154. F. Cottone, P. Basset, H. Vocca, L. Gammaitoni and T. Bourouina, Bistable electromagnetic generator based on buckled beams for vibration energy harvesting, Journ. Intell. Mater. Syst. Struc. 25(12):1484-95 (2014).

155. S. D. Nguyen, E. Halvorsen, Igor Paprotny, 'Bistable springs for wideband microelectromechanical energy harvesters', Appl. Phys. Lett., 102:023904 (2013).

156. H. Kulah, K. Najafi, 'Energy Scavenging from Low-frequency Vibrations by Using Frequency Up-Conversion for Wireless Sensor Applications', IEEE Sens. J., 8:261-268 (2008).

157.   Y. Lu, F. Cottone, S. Boisseau, F. Marty, D. Galayko, P. Basset, 'A nonlinear MEMS electrostatic kinetic energy harvester for human-powered biomedical devices', Appl. Phys. Lett., 107:253902 (2015).

158.   S. Kaur, E. Halvorsen, O. Søråsen, E. M. Yeatman, 'Characterization and Modeling of Nonlinearities in In-Plane Gap Closing Electrostatic Energy Harvester', J. Microelectromech. Syst., 24(6):2071-82 (2015).

159.   Chapter 6: Scaling Laws in Miniaturization, Lectures on MEMS and Microsystems Design and Manufacture, http://www.engr.sjsu.edu/trhsu/ME189_Chapter%206.pdf.

160.   S. D. Moss, O. R. Payne, G. A. Hart, C. Ung, 'Scaling and power density metrics of electromagnetic vibration energy harvesting devices', Smart Mater. Struct., 24:023001 (2015).

161.   T. O'Donnell, C. Saha, S.P. Beeby, J. Tudor, 'Scaling effects for electromagnetic vibrational power generators', Microsyst. Technol., 13 (11-12):1637-1645 (2007).

162.   D. P. Arnold, 'Review of Microscale Magnetic Power Generation', IEEE Trans. Magn., 43(11):3940-51 (2007).

163.   Y. Jiang, S. Masaoka, T. Fujita, M. Uehara, T. Toyonaga, K. Fujii, K. Higuchi, K. Maenaka, 'Fabrication of a vibration-driven electromagnetic energy harvester with integrated NdFeB/Ta multilayered micro-magnets', J. Micromech. Microeng., 21: 095014 (2011).

164.   Y. Tanaka, T. Fujita, T. Kotoge, K. Yamaguchi, K. Sonoda, K. Kanda, K. Maenaka, 'Electromagnetic Energy Harvester by Using NdFeB Sputtered on High Aspect Ratio Si Structure', J. Phys.: Conf. Ser. 476:012095 (2013).

165.   M. Han, Z. Li, X. Sun, H. Zhang, 'Analysis of an in-plane electromagnetic energy harvester with integrated magnet array', Sens. Act. A: Phys., 219:38–46 (2014).

166.   M. Han, Q. Yuan, X. Sun, H. Zhang, 'Design and Fabrication of Integrated Magnetic MEMS Energy Harvester for Low Frequency Applications', IEEE J. Microelectromech. Syst., 23(1):204-212 (2014).

167.   N. Wang, D. P. Arnold, 'Fully batch-fabricated MEMS magnetic vibration energy harvesters', Proc. PowerMEMS 2009, Washington DC, USA, pp 348-51 (2009).

168.   K. Tao, G. Ding, P. Wang, Z. Yang, Y. Wang, 'Fully integrated micro electromagnetic vibration energy harvesters with micro-patterning of bonded magnets', IEEE 25th International Conference on Micro Electro Mechanical Systems (MEMS), Paris, pp. 1237-1240 (2012).

169.   Q. Zhang, E. S. Kim, 'Micromachined Energy-Harvester Stack with Enhanced Electromagnetic Induction Through Vertical Integration of Magnets', IEEE J. Microelectromech. Syst., 24(2):384-394 (2015).

170.   S. Miki, T.Fujita, T. Kotoge, Y.G. Jiang , M. Uehara, K. Kanda, K. Higuchi, K. Maenaka, 'Electromagnetic energy harvester by using buried NdFeB', IEEE 25th International Conference on Micro Electro Mechanical Systems (MEMS), Paris, pp. 1221-1224 (2012).

171.   Q. Zhang, E. S. Kim, 'Microfabricated Electromagnetic Energy Harvesters With Magnet and Coil Arrays Suspended by Silicon Springs, IEEE Sensor Journ., 16(3):634-641 (2016).

172.   S. Kulkarni, E. Koukharenko, R. Torah, J. Tudor, S. Beeby, T. O'Donnell, S. Roy,' Design, fabrication and test of integrated micro-scale vibration-based electromagnetic generator', Sens. Actuators A, 145–146:336–342 (2008).

173.   Ö. Zorlu, H. Külah, 'A MEMS-based energy harvester for generating energy from non-resonant environmental vibrations', Sens. Actuators A, 202:124–134 (2013).

174.   F. Khan, F. Sassani, B. Stoeber, 'Nonlinear behaviour of membrane type electromagnetic energy harvester under harmonic and random vibrations', Microsyst. Technol., 20:1323–1335(2014).

175.   P. Wang, H. Liu, X. Dai, Z. Yang, Z. Wang, X. Zhao, 'Design, simulation, fabrication and characterization of a micro electromagnetic vibration energy harvester with sandwiched structure and air channel', Microelectron. Journ., 43:154–159 (2012).

176.   X. Dai, X. Miao, L. Sui, H. Zhou, X. Zhao, and G. Ding, 'Tuning of nonlinear vibration via topology variation and its application in energy harvesting', Appl. Phys. Lett., 100:031902 (2012).

177.   F. Khan, F. Sassani, B. Stoeber, 'Copper foil-type vibration-based electromagnetic energy harvester', J. Micromech. Microeng. 20:125006 (2010).

178.   https://www.enocean.com/en/enocean_modules/eco-200/.

179.   http://www.perpetuum.com/resources/Vibration%20Energy%20Harvester_Data%20Sheet_21Oct13.pdf.

180.   https://www.microgensystems.com/products.asp.

181.   http://info.mide.com/piezo-products/download-piezo-products-datasheets.

182.   http://flexous.com/en/download/Energy_Harvester_HiPER-D_datasheet_V3-01.pdf.

183.   S. R. Anton, H. A. Sodano, 'A review of power harvesting using piezoelectric materials (2003–2006)', Smart Mater. Struct., 16:R1– R21 (2007).

184.   J. Dicken, P. D. Mitcheson, I. Stoianov, E. M. Yeatman, 'Power-Extraction Circuits for Piezoelectric Energy Harvesters in Miniature and Low-Power Applications', IEEE Trans. Pow. Elect., 27(11):4514-29 (2012).

185. G. D. Szarka, B. H. Stark, S. G. Burrow, 'Review of Power Conditioning for Kinetic Energy Harvesting Systems', IEEE Trans. Pow. Elect., 27(2):803-15 (2012).

186. S. Cheng, N. Wang, D. P. Arnold, 'Modeling of magnetic vibrational energy harvesters using equivalent circuit representations', J. Micromech. Microeng., 17:2328–2335 (2007).

187. L. Wang, T. Kazmierski, B. Al-Hashimi et al., 'An integrated approach to energy harvester modeling and performance optimization', in IEEE Behavioral Modeling and Simulation Conference (BMAS 2007), San Jos, California, Sep. 2007, pp. 121–125 (2007).

188. W. Q. Liu, Z. H. Feng, J. He, and R. B. Liu, 'Maximum mechanical energy harvesting strategy for a piezoelement', Smart Mater. Struct., 16:2130–2136 (2007).

189. E. E. Aktakka, R. L. Peterson, and K. Najafi, 'A self-supplied inertial piezoelectric energy harvester with power-management IC', in Proc. IEEE Solid-State Circuits Conf. Dig. Tech. Int., San Francisco, CA, Feb. 2011, pp. 120–121 (2011).

190. Y. K. Ramadass, A. P. Chandrakasan, 'An efficient piezoelectric energy harvesting interface circuit using a bias-flip rectifier and shared inductor', IEEE J. Solid-State Circuits, 45(1) 189–204 (2010).

191. M. Marzencki, Y. Ammar, S. Basrour, 'Integrated power harvesting system including a MEMS generator and a power management circuit', Sens. Actuat. A: Phys., 145–146: 363–370 (2008).

192. X. Cao, W. J. Chiang, Y. C. King, and Y. K. Lee, 'Electromagnetic energy harvesting circuit with feed forward and feedback DC-DC PWM boost converter for vibration power generator system', IEEE Trans. Power Electron., 22(2):679–685 (2007).

193. T. Galchev, J. McCullagh, R. L. Peterson, and K. Najafi, 'A vibration harvesting system for bridge health monitoring', in Proc. PowerMEMS Workshop, Leuven, Belgium 2010, pp. 179–182 (2010).

194. A. Rahimi, O. Zorlu, H. Kulah, and A. Muhtaroglu, 'An interface circuit prototype for a vibration-based electromagnetic energy harvester', in Proc. Int. Conf. Energy Aware Comput., Cairo, Egypt, Dec. 2010, pp. 1–4 (2010).

195. A. Rahimi, O. Zorlu, A. Muhtaroglu, and H. Kulah, 'A compact electromagnetic vibration harvesting system with high performance interface electronics', Eurosensors XXV, Athens, Greece, Sep. 2011, pp. 1–91 (2011).

196. M. Ghovanloo, K. Najafi, 'Fully integrated wideband high-current rectifiers for inductively powered devices', IEEE J. Solid-State Circuits, 39:1976–1984 (2004).

197. Y. H. Lam, W. H. Kim, and C. Y. Tsui, 'Integrated low-loss CMOS active rectifier for wirelessly powered devices', IEEE Trans. Circuits Syst., 53(12):1378–1382 (2006).

198. C. Peters, J. Handwerker, D. Maurath, Y. Manoli, 'A sub-500 mV highly efficient active rectifier for energy harvesting applications', IEEE Trans. Circuits Syst. I, 58(7):1542–1550 (2011).

199. H. Yan, J. G. Macias Montero, A. Akhnoukh et al., 'An integration scheme for rf power harvesting', in STW Annual Workshop on Semiconductor Advances for Future Electronics and Sensors, Nov. 2005, pp. 64–66 (2005).

200. R. Torah, P. Glynne-Jones, M. Tudor, T. O'Donnell, S. Roy, S. Beeby, 'Self-powered autonomous wireless sensor node using vibration energy harvesting', Meas. Sci. Technol., 19:125202 (2008).

201. P. D. Mitcheson, T. C. Green, E. M. Yeatman, 'Power processing circuits for electromagnetic, electrostatic and piezoelectric inertial energy scavengers', Microsyst. Technol. 13:1629–1635 (2007).

202. R. Dayal, L. Parsa, 'A new single stage AC-DC converter for low voltage electromagnetic energy harvesting', 2010 IEEE Energy Conversion Congress and Exposition, Atlanta, GA, 2010, pp. 4447-4452 (2010).

203. D. Maurath, P. F. Becker, D. Spreemann, Y. Manoli, 'Efficient energy harvesting with electromagnetic energy transducers using active low-voltage rectification and maximum power point tracking', IEEE J. Sol. Stat. Cir., 46(2):1369-80 (2012).

204. G. D. Szarka, S. G. Burrow, P. P. Proynov, B. H. Stark, 'Maximum Power Transfer Tracking for Ultralow Power Electromagnetic Energy Harvesters', IEEE Trans. Pow. Elect., 29(1):201-212 (2012).

205. https://www.comsol.com/comsol-multiphysics.

206. http://www.ansys.com/products/electronics/ansys-maxwell

207. https://en.wikipedia.org/wiki/Runge%E2%80%93Kutta_methods

208. Abbott, Charles, et al. "New techniques for laser micromachining MEMS devices." Proc. SPIE. Vol. 4760. 2002.

209. Tunna, L., et al. "Analysis of laser micro drilled holes through aluminium for micro-manufacturing applications." Optics and Lasers in Engineering 43.9 (2005): 937-950.

210. Plummer, James D. Silicon VLSI technology: fundamentals, practice, and modeling. Pearson Education India, 2009.

211. Madou, Marc J. Fundamentals of microfabrication: the science of miniaturization. CRC press, 2002.

212. Ohmi, Tadahiro. "Total room temperature wet cleaning for Si substrate surface." J. Electrochem. Soc., 143.9 (1996): 2957-2964.

213. Jansen, H. V., et al. "Black silicon method X: a review on high speed and selective plasma etching of silicon with profile control: an in-depth comparison between Bosch and cryostat DRIE processes as a roadmap to next generation equipment." J. Micromech. Microengg., 19.3:033001 (2009).

214. Brenner, Abner. Electrodeposition of alloys: principles and practice. Elsevier, 2013.

215. https://www.fei.com/products/sem/quanta-sem/

216. http://www.panalytical.com/XPert3-Powder.htm

217. M. McElfresh, 'Fundamentals of magnetism and magnetic measurements featuring quantum design's magnetic property measurement system', Quantum Design.

218. http://www.eplastics.com/G9-G10-FR4-glass-epoxy-sheet.

219. G. Hatipoglu, H. Urey, 'FR4-based electromagnetic energy harvester for wireless sensor nodes', Smart Mater. Struct. 19:015022 (2010).

220. W. Colone, T. McLyman, "Magnetic Materials and Their Characteristics", Transformer and Inductor Design Handbook, third Edition, CRC Press, pp 33 (2004).

221. M. S. M. Soliman, E. M. Abdel-Rahman, E. F. El-Saadany, R. R. Mansour, 'A wideband vibration-based energy harvester', J. Micromech. Microeng. 18:115021 (2008).

222. P. Podder, A. Amann, S. Roy, 'Combined bandwidth widening effect of bistability and mechanical impact in a nonlinear vibration energy harvester', IEEE Trans. Mechatron., 21(2):727-739 (2016).

223. J. Zou, C. Liu, J. Schutt-Aine, J. Chen, S. Kang, 'Development of a wide tuning range MEMS tunable capacitor for wireless communication systems', Electron Devices Meeting IEDM (2000).

224. http://www.willow.co.uk/TelosB_Datasheet.pdf.

225. http://cds.linear.com/docs/en/datasheet/35881fc.pdf.

226. S. P. Beeby, L. Wang, D. Zhu, A. S. Weddell, G. V. Merrett, B. Stark, G. Szarka, B. M. Al-Hashimi, 'A comparison of power output from linear and nonlinear kinetic energy harvesters using real vibration data', Smart Mater. Struct., 22:075022 (2013).

227. S. Renard, 'Industrial MEMS on SOI', J. Micromech. Microeng. 10: 245–249 (2000).

228. B. S. Doyle, S. Datta, M. Doczy, S. Hareland, B. Jin, J. Kavalieros, T. Linton, A. Murthy, R. Rios, R. Chau, 'High Performance Fully-Depleted Tri-Gate CMOS Transistors', IEEE Elect. Dev. Lett., 24(4):263-265 (2003).

229. M. Tachimori, 'SIMOX Wafers (Silicon wafers with a thin superficial silicon film separated from the body by implanted oxygen', Nippon Steel Technical Letters, 73 (1997).

230. P. Dallard, T. Fitzpatrick, A. Flint, A. Low, R. R. Smith, M. Willford, M. Roche, 'london millennium bridge: pedestrian-induced lateral vibration', J. Bridge Engg., 6(6):412-417 (2001).

231. J. Svoboda, Magnetic Techniques for the Treatment of Materials (Dordrecht: Kluwer) pp 260–3 (2004).

232. G. Sebald, H. Kuwano, D. Guyomar and B. Ducharne, Experimental Duffing oscillator for broadband piezoelectric energy harvesting, Smart Mater. Struct., 20: 102001 (2011).

233. D. A. W. Barton, S. G. Burrow, L. R. Clare, 'Energy harvesting from vibrations with a nonlinear oscillator', J. Vib. Acoust., Vol. 132:021009-1 (2010).

234. U. Parlitz and W. Lauterborn, 'Superstructure in the bifurcation set of the Duffing equation $\ddot{x} + d\dot{x} + x + x3 = f \cos(\omega t)$', Phys. Lett. 107A:8 (1985).

235. C. L. Olson, M. G. Olson, 'Dynamical symmetry breaking and chaos in Duffing's equation', Am. J. Phys. 59:907 (1991).

236. R. Masana and M. F. Daqaq, 'Energy harvesting in the super-harmonic frequency region of a twin-well oscillator', J. Appl. Phys. 111:044501 (2012).

237. T. Kalmar-Nagy and B. Balachandran, 'Forced harmonic vibration of a Duffing oscillator with linear viscous damping', in The Duffing Equation: Nonlinear Oscillators and their Behaviour, I. Kovacic and M. J. Brennan, Eds., pp. 139–174, John Wiley and Sons, (2011).

238. D. Mallick, S. Roy, 'Bidirectional Electrical Tuning of FR4 based Electromagnetic Energy Harvesters', Sens. Act. A: Phys., 226:154-162 (2015).

239. P. Basset, D. Galayko, F. Cottone, R. Guillemet, E. Blokhina, F. Marty, T. Bourouina, 'Electrostatic vibration energy harvester with combined effect of electrical nonlinearities and mechanical impact', J. Micromech. Microeng., 24: 035001 (2014).

240. R. Pratap, S. Mohite, Suhas A. K. Pandey, 'Squeeze Film Effects in MEMS Devices', Journ. Indian Institute of Science, 87 (1):75-94 (2007).

241. A. F. Arrieta, P. Hagedorn, A. Erturk, D. J. Inman, 'A piezoelectric bistable plate for nonlinear broadband energy harvesting', Appl. Phys. Lett. 97:104102 (2010).

242. S. Zhou, J. Cao, A. Erturk, J. Lin, 'Enhanced broadband piezoelectric energy harvesting using rotatable magnets', Appl. Phys. Lett., 102:173901 (2013).

243. P. Kim, J. Seok, 'A multi-stable energy harvester: dynamic modeling and bifurcation analysis', J. Sound Vib., 333:5525 (2014).

244. S. Zhou, J. Cao, D. J. Inman, J. Lin, S. Liu, Z.Wang, 'Broadband tristable energy harvester: Modeling and experiment verification', Appl. Energ., 133, 33 (2014).

245. S. Zhou, J. Cao, J. Lin, Z. Wang, 'Exploitation of a tristable nonlinear oscillator for improving broadband vibration energy harvesting', Eur. Phys J. Appl. Phys., 67, 30902 (2014).

246. M.P. Kennedy, L.O. Chua, 'Neural networks for nonlinear programming', IEEE Trans. Circuits Syst., 35 (5):554-562 (1988).

247. D. M. Gvozdic, M. M. Krstic, J. V. Crnjanski, 'Switching time in optically bistable injection-locked semiconductor lasers', Opt. Lett., 36:4200-4202 (2011).

248. H. Li, Y. Chen, J. Noh, S. Tadesse, M Li, 'Multichannel cavity optomechanics for all-optical amplification of radio frequency signals', Nat. Comm., 3:1091 (2012).

249. J. Foss, A. Longtin, B. Mensour, J. Milton, 'Multistability and delayed recurrent loops', Phys. Rev. Lett., 76, 708-711 (1996).

250. A. N. Pisarchika, U. Feudel, 'Control of multistability', Phys. Rep., 540:167-218 (2014).

251. B. E. Martinez-Zerega, A. N. Pisarchik, L. S. Tsimring, 'Using periodic modulation to control coexisting attractors induced by delayed feedback', Phys. Lett. A, 318:102-111 (2003).

252. L. M. Pecora, T. L. Carroll, 'Pseudoperiodic driving: eliminating multiple domains of attraction using chaos', Phys. Rev. Lett., 67:945-948 (1991).

253. W. Yang, M. Ding, H. Gang, 'Trajectory (phase) selection in multistable systems: Stochastic resonance, signal bias, and the effect of signal phase', Phys. Rev. Lett., 74:3955-3958 (1995).

254. O. Olusola, U. Vincent, A. Njah, 'Synchronization, multistability and basin crisis in coupled pendula', J. Sound Vib., 329:443-456 (2010).

255. A. Cammarano, A. Gonzalez-Buelga, S.A. Neild, S.G. Burrow, 'Bandwidth of a nonlinear harvester with optimized electrical load', Journ. Phys.: Conf. Ser., 476: 012071 (2013).

256. S. Zhou, J. Cao, D. J. Inman, S. Liu, W. Wang, J. Lin, 'Impact-induced high-energy orbits of nonlinear energy harvesters', Appl. Phys. Lett., 106:093901 (2015).

257. A. Masuda, T. Sato, 'Global stabilization of high-energy resonance for a nonlinear wideband electromagnetic vibration energy harvester', Proc. of SPIE, 9799, 97990K (2016).

258. E.J. Doedel, R.C. Paffenroth, A.R. Champneys, T.F. Fairgrieve, Y.A. Kuznetsov, B.E. Oldeman, B. Sandstede and X.-J. Wang. AUTO2000: Continuation and bifurcation software for ordinary differential equations. Technical report, Department of Computer Science, Concordia University, Montreal, Canada (2000). Available from http://indy.cs.concordia.ca.

259. D.P. Arnold, N. Wang, 'Permanent Magnets for MEMS', J. Microelectromech. Syst., 18(6): 1255-66 (2009).

260. D. Niarchos, 'Magnetic MEMS: key issues and some applications', Sens. Act. A 109:166–173 (2003).

261. C. Ó. Mathúna, N. Wang, S. Kulkarni, S. Roy, 'Review of integrated magnetics for power supply on chip (PwrSoC)', IEEE Trans. Pow. Elect. 27(11):4799-4816 (2012).

262. T. O'Donnell, N. Wang, S. Kulkarni, R. Meere, F. MF Rhen, S. Roy, S. C. O'Mathuna, 'Electrodeposited anisotropic NiFe 45/55 thin films for high-frequency micro-inductor applications', J. Magn. Mag. Mater., 322(9–12):1690–1693 (2010).

263. D. A. Thompson, J. S. Best, 'The future of magnetic data storage technology', IBM J. Resear. Dev., 44(3): 311 – 322 (2000).

264. Y. Jiang, S. Masaoka, T. Fujita, M. Uehara, T. Toyonaga, K. Fujii, K. Higuchi, K. Maenaka, 'Fabrication of a vibration-driven electromagnetic energy harvester with integrated NdFeB/Ta multilayered micro-magnets', J. Micromech. Microeng. 21(9):095014 (2010).

265. O. Gutfleisch, M. A. Willard, E. Brück, C. H. Chen, S. G. Sankar, J. P. Liu, 'Magnetic materials and devices for the 21st century: stronger, lighter, and more energy efficient', Adv. Mater., 23:821–842, 2011.

266. S. Guan, B. J. Nelson, 'Electrodeposition of low residual stress CoNiMnP hard magnetic thin films for magnetic MEMS actuators', J. Magn. Magn. Mater., 292:49–58 (2005).

267. S. Guan, B. J. Nelson, 'Pulse-reverse electrodeposited nano grain sized CoNiP thin films and microarrays for MEMS actuators', J. Electrochem. Soc., 152(4):C190–C195 (2005).

268. W. B. Ng, A. Takada, K. Okada, 'Electrodeposited Co-Ni-Re-W-P thick array of high vertical magnetic anisotropy', IEEE Trans. Magn., 41(10):3886–3888 (2005).

269. Y. Su, H. Wang, G. ding, F. Cui, W. Zhang, W. Chen, 'Electroplated hard magnetic materials and its application in microelectromechanical systems', IEEE Trans. Magn., 41(12):4380–4383 (2005).

270. C.H. Lee, R. F. C. Farrow, C. J. Lin, E. E. Marinero, C. J. Chien, 'MBE growth and magnetic properties of Co-Pt superlattices oriented along the (001), (110) and (111) axes of Pt', Phys. Rev. B 42 (7):11384–11386 (1990).

271. S. Jeong, Yu-Nu Hsu, D.E. Laughlin, M. E. McHenry, 'Magnetic properties of nanostructured CoPt and FePt thin films', IEEE Trans. Magn. 36 (5): 2336-2338 (2000).

272. D. Weller, A. Moser, L. Folks, M. E. Best, W. Lee, M. F. Toney, M. Schwickert, J. Thiele nd M. F. Doerner, 'High Ku Materials approach to 100 Gbits/in2', IEEE Trans. Magn., vol. 36(1): 10-15 (2000).

273. Y. H. Huang, H. Okumura, G. C. Hadjipanayis, D. Weller, 'CoPt and FePt nanowires by electrodeposition', J. Appl. Phys., 91:6869-6871 (2002).

274. F. M. F. Rhen, G. Hinds, C. O'Reilly, J. M. D. Coey, 'Electrodeposited FePt Films', IEEE Trans. Magn., vol. 39(5): 2699-2701 (2003).

275. F. M. F. Rhen, E. Backen, J. M. D. Coey, 'Thick-film permanent magnets by membrane electrodeposition', J. Appl. Phys. 97:113908 (2005).

276. O. D. Oniku, B. Qi, D. P. Arnold, 'Electroplated $L1_0$ CoPt thick-film permanent magnets', J. Appl. Phys. 115: 17E521 (2014).

277. A. Garraud, O. D. Oniku, D. P. Arnold, 'Influence of temperature on the magnetic properties of electroplated $L1_0$ CoPt thick films', J. Appl. Phys. 117: 17C718 (2015).

278. T. Homma, S. Wodarz, D. Nishiie, T. Otani, S. Ge, G. Zangari 'Fabrication of FePt and CoPt magnetic nanodot arrays by electrodeposition process' ECS Trans. 64(31):1-9 (2015).

279. T. Shima, K. Takanashi, Y. K. Takahshi and K. Hono, "Coercivity exceeding 100 kOe in epitaxially grown FePt sputtered films", Appl. Phys. Lett., 85(11): 2571-2573 (2004).

280. H. Yamane, K. Takeda, M. Kobayashi, 'Magneto-plasmonics on perpendicular magnetic CoPt–Ag nanostructures with ZnO intermediate thin layers', Appl. Phys. Lett., 106: 052409 (2015).

281. H. An, Q. Xie, J. Wang, T. Sannomiya, S. Muraishi, Z. Zhang, Y. Nakamura, Ji Shi, 'Highly (001) oriented L10-CoPt/TiN multilayer films on glass substrates with perpendicular magnetic anisotropy', J. Vac. Sci. Technol. A 33:021512 (2015).

282. B. Varghese, S. N. Piramanayagam, Y. Yang, S. K. Wong, H. K. Tan, W. K. Lee, I. Okamoto, 'Equiatomic CoPt thin films with extremely high coercivity', J. Appl. Phys. 115:17B707 (2014).

283. M. Nakano, S. Shibata, T. Yanai, and H. Fukunaga, "Anisotropic properties in Fe–Pt thick film magnets," J. Appl. Phys., 105(7): 07A732 (2009).

284. S. Thongmee, J. Ding, J. Y. Lin, D. J. Blackwood, J. B. Yi, J. H. Yin, 'FePt films fabricated by electrodeposition', J. Appl. Phys., 101(9): 09K519 (2007).

285. W. F. Liu, S. Suzuki, D. S. Li, K. Machida, 'Magnetic properties of Fe–Pt thick-film magnets prepared by RF sputtering', J. Magn. Magn. Mater., 302(1):201–205 (2006).

286. L. Callegaro, E. Puppin, P. L. Cavallotti and G. Zangari, "Electroplated, high Hc CoPt films: δM magneto-optical measurements", J. of Magn. Magn. Mater., 155, 190-192 (1996).

287. L. Vieux-Rochaz, C. Dieppedale, B. Desloges, D. Gamet, C. Barragatti, H. Rostaing, and J. Meunier-Carus, 'Electrodeposition of hard magnetic CoPtP materials and integration into magnetic MEMS', J. Micromech. Microeng., vol. 16, no. 2, pp. 219–224, Feb. 2006.

288. T.S. Ramulu, R. Venu, S. Anandakumar, V. Sudha Rani, S.S. Yoon, C.G. Kim, 'Structure, growth and magnetic property of hard magnetic CoPtP nanowires synthesized by electrochemical deposition', Thin Solid Films, 520:5508–5511 (2012).

289. N. Wang and D. P. Arnold, "Thick electroplated Co-rich Co–Pt micro magnet arrays for magnetic MEMS," IEEE Trans. Magn., vol. 44, no. 11, pp. 3969–3972, Nov. 2008.

290. T. M. Liakopoulos, W. Zhang, C. H. Ahn, 'Micromachined thick permanent magnet arrays on silicon wafers', IEEE Trans. Magn., 32(5): 5154-5156 (1996).

291. X. Sun, Q. Yuan, D. Fang, H. Zhang, 'Electrodeposition and characterization of CoNiMnP permanent magnet arrays for MEMS sensors and actuators', Sens. Act. A: Phys, 188: 190–197 (2012).

292. T. Budde, H. H. Gatzen, 'Thin film SmCo magnets for use in electromagnetic microactuators', J. Appl. Phys. 99:08N304 (2006).

293. J. Y. Wang, D. K. Sood, M. K. Ghantasala, N. Dytlewski, 'Characterization of sputtered SmCo thin films for light element contamination using RBS and HIERDA techniques', Vacuum 75(1): 17–23 (2004).

294.   T. Speliotis, D. Niarchos, V. Skumryev, Y. Zhang, G. Hadjipanayis, J. Magn. Mag. Mater., 272–276: E877–E879 (2004).

295.   A. Walther, K. Khlopkovc, O. Gutfleischc, D. Givorda, N.M. Dempsey, Evolution of magnetic and microstructural properties of thick sputtered NdFeB films with processing temperature, J. Magn. Mag. Mater., 316(2): 174–176 (2007).

296.   Z. Yang, I. Lisiecki, M. Walls, M-P Pileni, 'Nanocrystallinity and the Ordering of Nanoparticles in Two-Dimensional Superlattices: Controlled Formation of Either Core/Shell (Co/CoO) or Hollow CoO Nanocrystals', ACS Nano, 7 (2): 1342–1350 (2013).

297.   M. Casavola, A. Falqui, M. A. García, M. G Hernández, C. Giannini, R. Cingolan, P. D. Cozzoli, 'Exchange-Coupled Bimagnetic Cobalt/Iron Oxide Branched Nanocrystal Heterostructures', Nano Lett., 9 (1): 366–376 (2009).

298.   V. Neu, S. Sawatzki, M. Kopte, 'Fully Epitaxial, Exchange Coupled SmCo5/Fe Multilayers With Energy Densities above 400 kJ/m^3', IEEE Transactions on Magnetics, vol. 48, no. 11, pp. 3599-3602, Nov. 2012.

299.   W Liu, Z D Zhang, J P Liu, Z R Dai, Z L Wang, X K Sun, D J Sellmyer, 'Nanocomposite (Nd,Dy)(Fe,Co,Nb,B)5.5/α-Fe multilayer magnets with high performance', J. Phys. D: Appl. Phys. 36 No 17 (7 September 2003) L67-L70.

300.   S. Kulkarni, S. Roy, 'Development of nanostructured, stress-free Co-rich CoPtP films for magnetic microelectromechanical system applications', J. Appl. Phys., 101.9: 09K524 (2007).

301.   S. Kulkarni, S. Roy, 'Deposition of thick Co-rich CoPtP films with high energy product for magnetic microelectromechanical applications', J. Magn. Mag. Mater., 322 (2010) 1592–1596.

302.   Zeng, Hao, et al. "Exchange-coupled nanocomposite magnets by nanoparticle self-assembly." Nature 420.6914 (2002): 395-398.

303.   A. P. Roberts, R. P. Christopher, L. V. Kenneth, 'First- order reversal curve diagrams: A new tool for characterizing the magnetic properties of natural samples', J. Geophys. Resear.: Solid Earth 105.B12: 28461-28475 (2000).

304.   C. R. Pike, 'First-order reversal-curve diagrams and reversible magnetization', Phys. Rev. B 68.10: 104424 (2003).

305.   Tanaka et al., *IEEE GreenCom, iThings/CPSCom, IEEE ICCPSC*, Beijing, 2013, pp. 1656-1658.

306.   R. Skomski, J. M. D. Coey, 'Magnetic anisotropy—How much is enough for a permanent magnet?' Scripta Materialia 112: 3-8 (2016).

307.   W. F. Liu, S. Suzuki, D. S. Li, and K. Machida, "Magnetic properties of Fe–Pt thick-film magnets prepared by RF sputtering," J. Magn. Magn. Mater., vol. 302, no. 1, pp. 201–205, Jul. 2006.

308.   S. Thongmee, J. Ding, J. Y. Lin, D. J. Blackwood, J. B. Yi, and J. H. Yin, "FePt films fabricated by electrodeposition," J. Appl. Phys., vol. 101, no. 9, p. 09K519, May 2007.

309.   S. Sun, and C. B. Murray. "Synthesis of monodisperse cobalt nanocrystals and their assembly into magnetic superlattices." J. Appl. Phys., 85.8: 4325-4330 (1999).

310. N. V. Myung, D. -Y. Park, B. -Y. Yoo, and P. T. A. Sumodjo, "Development of electroplated magnetic materials for MEMS," J. Magn. Magn. Mater., vol. 265, no. 2, pp. 189–198, Sep. 2003.

311. Y. Su, H. Wang, G. ding, F. Cui, W. Zhang, and W. Chen, "Electroplated hard magnetic materials and its application in microelectromechanical systems," IEEE Trans. Magn., vol. 41, no. 12, pp. 4380–4383, Dec. 2005.

312. O. Berkh, Y. Rosenberg, Y. S. Diamand, E. Gileadi, "Electrodeposited near-equiatomic CoPt thick films," Electrochem. Solid-State Lett., vol. 11, no. 4, pp. D38–D41, 2008.

313. K. Leistner, J. Thomas, H. Schlörb, M. Weisheit, L. Schultz, and F.Fähler,"HighlycoerciveelectrodepositedFePtfilmbypostannealingin hydrogen," Appl. Phys. Lett., vol. 85, no. 16, pp. 3498–3500, Oct. 2004.

314. M. Nakano, S. Shibata, T. Yanai, and H. Fukunaga, "Anisotropic properties in Fe–Pt thick film magnets," J. Appl. Phys., vol. 105, no. 7, p. 07A732, Mar. 2009.

315. I. Zana, G. Zangari, and M. Shamsuzzoha, "Enhancing the perpendicular magnetic anisotropy of Co–Pt(P) films by epitaxial electrodeposition onto Cu(111) substrates," J. Magn. Magn. Mater., vol. 292, pp. 266–280, Apr. 2005.

316. O. Berkh, Y. Rosenberg, Y. S. Diamand, and E. Gileadi, "Deposition of CoPtP films from citric electrolyte," Microelectron. Eng., vol. 84, no. 11, pp. 2444–2449, Nov. 2007.

317. C. Prados, A. Hernando, G. C. Hadjipanayis, and J. M. Gonzalez, "Coercivity analysis in sputtered Sm–Co thin films," J. Appl. Phys., vol. 85, no. 8, pp. 6148–6150, Apr. 1999.

318. E. Pina, F. J. Palomares, M. A. Garcia, F. Cebollada, A. de Hoyos, J. J. Romero, A. Hernando, and J. M. Gonzalez, "Coercivity in SmCo hard magnetic films for MEMS application," J. Magn. Magn. Mater., vol. 290/291, pp. 1234–1236, Apr. 2005.

319. F. J. Cadieu, L. Chen, and B. Li, "Enhanced magnetic properties of nanophase SmCo5 film dispersions," IEEE Trans. Magn., vol. 37, no. 4, pp. 2570–2572, Jul. 2001.

320. K. Yamasawa, X. Liu, and A. Morisako, "Nd–Fe–B films with perpendicular magnetic anisotropy," J. Appl. Phys., vol. 99, no. 8, p. 08N302, Apr. 2006.

321. L. Castaldi, M. R. F. Gibbs, and H. A. Davies, "Effect of the target power and composition on RE-Fe-B thin films with Cu and Nb buffer and cap layers," J. Appl. Phys., vol. 100, no. 9, p. 093904, Nov. 2006.

322. N. M. Dempsey, A. Walther, F. May, D. Givord, K. Khlopkov, and O. Gutfleisch, "High performance hard magnetic Nd–Fe–B thick films for integration into micro-electro-mechanical systems," Appl. Phys. Lett., vol. 90, no. 9, p. 092509, Mar. 2007.

323. M. Nakano, S. Sato, H. Fukunaga, and F. Yamashita, "A method of preparing anisotropic Nd–Fe–B film magnets by pulsed laser deposition," J. Appl. Phys., vol. 99, no. 8, p. 08N301, Apr. 2006.

324. H. Liu, C. Lee, T. Kobayashi, C. J. Tay, C. Quan, Investigation of a MEMS piezoelectric energy harvester system with a frequency-widened-bandwidth

mechanism introduced by mechanical stoppers, Smart Mater. Struct. 21:035005 (2012).

325. N. S. Yuksek, Z. C. Feng, M. Almasri, Broadband electromagnetic power harvester from vibrations via frequency conversion by impact oscillations, Appl. Phys. Lett., 105, 113902 (2014).

326. K. Tao, S. W. Lye, J. Miao, L. Tang, X. Hu, "Out-of-plane electret-based MEMS energy harvester with the combined nonlinear effect from electrostatic force and a mechanical elastic stopper", J. Micromech. Microeng. 25:104014 (2015).

327. M. Löhndorf, T. KvisterØy, E. Westby, E. Halvorsen, "Evaluation of energy harvesting concepts for tire pressure monitoring systems", Proc. PowerMEMS 2007 (Freiburg, Germany), pp 331–4 (2007).

328. M. R. Pearson, M. J. Eaton, R. Pullin, C. A. Featherston, K. M. Holford, "Energy Harvesting for Aerospace Structural Health Monitoring Systems", Journ. Phys.: Conf. Ser. 382:012025 (2012).